IRAC Instrument Handbook

Spitzer Heritage Archive Documentation

IRAC Instrument and Instrument Support Teams

Version 2.1.2, November 2015

Table of Contents

1 Introduction

1.1 Document Purpose and Scope

The IRAC Instrument Handbook is one in a series of documents that explain the operations of the Spitzer Space Telescope and its three instruments, the data received from the instruments and the processing carried out on the data. Spitzer Space Telescope Handbook gives an overview of the entire Spitzer mission and it explains the operations of the observatory, while the other three handbooks document the operation of, and the data produced by the individual instruments (IRAC, IRS and MIPS). The IRAC Instrument Handbook is intended to provide all the information necessary to understand the IRAC standard data products, as processed by the online pipeline system, and which are retrievable from the Spitzer Heritage Archive (SHA). Besides the detailed pipeline processing steps and data product details, background information is provided about the IRAC instrument itself, its observational modes and all aspects of IRAC data calibration. It should be stressed that this Handbook is not intended to support interactive data analysis. For data analysis advice and suggested data processing procedures, please refer to the separate documentation available at the documentation website, including the Spitzer Data Analysis Cookbook. This Handbook serves as the reference for both the processing as well as the correct interpretation of IRAC data as available from the Spitzer Heritage Archive.

In this document we present information on:
- the IRAC instrument and its observing modes,
- the processing steps carried out on the Level 0 (raw) data,
- the calibration of the instrument,
- the artifacts, features and uncertainties in the data,
- and the final IRAC archival data products.

An overview of the IRAC instrument is given in Chapter 2. In Chapter 3 all the IRAC data taking modes are presented. The calibration is described in Chapter 4. Online pipeline processing is described in Chapter 5. The data products themselves are described in Chapter 6. Data features are presented in Chapter 7. A brief introduction into IRAC data analysis is given in Chapter 8. Several appendices are attached to give more detailed information on individual subjects.

1.2 Basic Definitions

This section contains a description of the most commonly used terms in this Handbook. A complete list of acronyms can be found in Appendix E.

An Astronomical Observing Template (AOT) is the list of parameters for a distinct Spitzer observing mode. There is one possible IRAC AOT for the cryogenic mission, and one for the warm mission. The observing parameters and modes are described in Chapter 3. A fundamental unit of Spitzer observing is

the Astronomical Observation Request (AOR), also referred to sometimes as "observation." It is an AOT with all of the relevant parameters fully specified. Each AOR is identified in the Spitzer Heritage Archive by a unique observation identification number known as AORKEY. An AOR consists of several Data Collection Events (DCEs), which can be thought of as single frame exposures. The data products consist of Level 0 products ("raw data") and Level 1 data products that are also called Basic Calibrated Data (BCD) and which are derived from the DCEs after pipeline processing. See Chapter 5 for more information about pipeline processing. BCDs (or in the case of IRAC, corrected BCDs or CBCDs) are designed to be the most reliable data product achievable by automated pipeline processing, and should be the starting point for further data processing. The pipeline also produces Level 2 data products or Post-BCD products, which are derived from data from the whole AOR (i.e., combination of several CBCDs). See Chapter 6 for more information about the data products.

1.3   IRAC Essentials

The most relevant software for IRAC data reduction is MOPEX (mosaicking and point source extraction). Documentation for it can be found in the data analysis section of the documentation website. See Chapter 8 for a brief introduction into IRAC data analysis. The separate Data Analysis section of the documentation website provides access to tools, user's guides and data analysis recipes.

Before you start using IRAC data, we recommend that you familiarize yourself very carefully with this document, and specifically Chapter 7, which discusses the various artifacts in IRAC data. Several of these artifacts are at least partially corrected in the pipeline, but you should still be aware of them. The CBCD frames contain the artifact-corrected observations, and should usually be a starting point for your further data reduction and analysis. However, you always have the option of going back to the BCD frames if you are not happy with how artifacts were corrected in the CBCDs, and perform your own corrections.

Please remember that IRAC flux calibration is only good to about 10% without additional corrections to the photometry. These are discussed in Chapter 4. You can achieve down to about a few percent flux accuracy if you carefully perform all the corrections to the data. Specifically, we recommend that you perform point source photometry using aperture photometry, unless your targets lie in an area of sky that has an extremely high surface density and/or a strongly variable background. The extended emission fluxes and especially surface brightnesses are not nearly as well calibrated, so please read our caveats about them in Chapter 4 and think carefully before you publish any results about extended emission fluxes and surface brightnesses.

1.4   Standard Acknowledgments for IRAC Publications

Any paper published based on Spitzer data should contain the following text: "This work is based [in part] on observations made with the Spitzer Space Telescope, which is operated by the Jet Propulsion Laboratory, California Institute of Technology under a contract with NASA." If you received NASA data analysis funding for your research, you should use one of the templates listed under

http://irsa.ipac.caltech.edu/data/SPITZER/docs/spitzermission/publications/ackn/. We also ask that you cite at least the seminal IRAC paper (*Fazio, G. G., et al. 2004, ApJS, 154, 10 [9]*) in your research paper, and other IRAC-related papers, as appropriate.

1.5 How to Contact Us

A broad collection of information about IRAC and IRAC Data Analysis is available on the Spitzer Documentation website, accessible via http://irsa.ipac.caltech.edu/data/SPITZER/docs/irac. In addition you may contact us at the helpdesk at http://irsa.ipac.caltech.edu/data/SPITZER/docs/spitzerhelpdesk.

2 Instrument Description

2.1 Overview

The InfraRed Array Camera (IRAC) was built by the NASA Goddard Space Flight Center (GSFC) with management and scientific leadership by the Smithsonian Astrophysical Observatory (SAO) under principal investigator Giovanni Fazio. The information in this Handbook is based on the design requirements and on the characterization of the flight instrument in pre-flight ground tests and on in-flight performance, including the In-Orbit Checkout (IOC)/Science Verification (SV) period in August–November 2003 and the IRAC Warm Instrument Characterization (IWIC) period in May – July 2009.
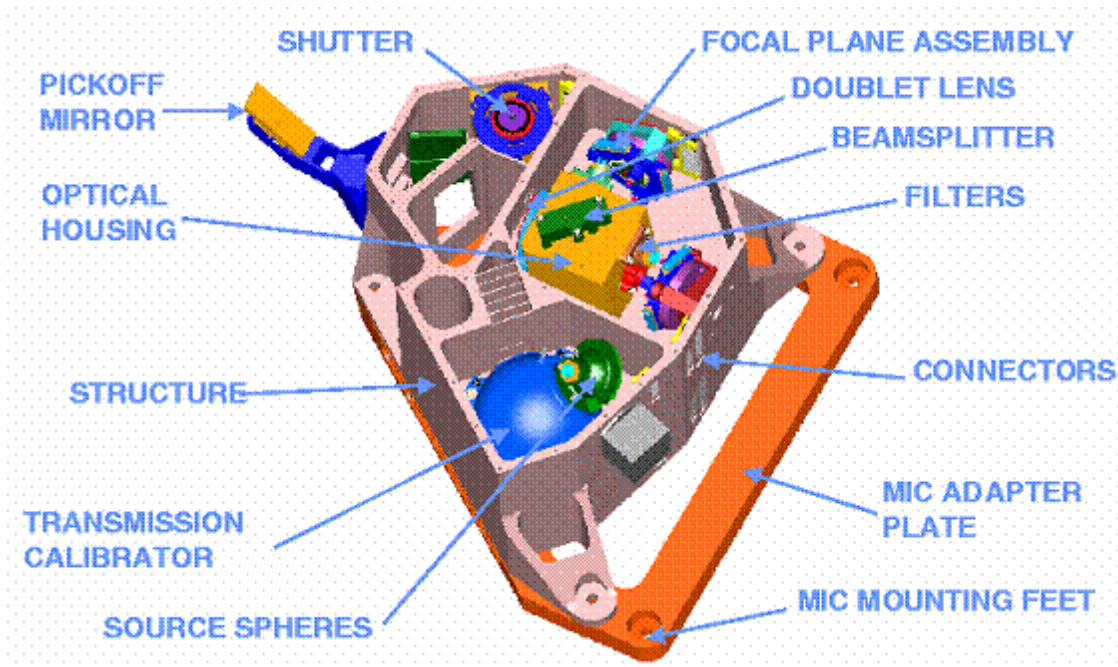
Figure 2.1. IRAC Cryogenic Assembly model, with the top cover removed to show the inner components.

A brief, high-level summary of IRAC for astronomers appeared in the ApJS Spitzer Special Issue, specifically the paper by *Fazio et al. (2004, ApJS, 154, 10, [9])* entitled "The Infrared Array Camera (IRAC) for the Spitzer Space Telescope" and in the paper by *Hora et al. (2004, SPIE, 5487, 244, [16])* entitled "In-flight performance and calibration of the Infrared Array Camera (IRAC) for the Spitzer Space Telescope." Copies of these papers are available on the Spitzer documentation website.

IRAC is a four-channel camera that provides simultaneous 5.2 arcmin × 5.2 arcmin images at 3.6, 4.5, 5.8, and 8 μm. Two adjacent fields of view are imaged in pairs (3.6 and 5.8 μm; 4.5 and 8.0 μm) using

dichroic beamsplitters. All four detector arrays in the camera are 256×256 pixels in size, with a pixel size of ~1.2 arcsec $\times$ 1.2 arcsec. The two short wavelength channels use InSb detector arrays and the two longer wavelength channels use Si:As detectors. The IRAC instrument was designed to address the four major scientific objectives defining the Spitzer mission. These are (1) to study the early universe, (2) to search for and study brown dwarfs and superplanets, (3) to study ultraluminous galaxies and active galactic nuclei, and (4) to discover and study protoplanetary and planetary debris disks. The utility of IRAC is in no way limited to these objectives, which we only mention to explain the scientific drivers for the instrument design. IRAC is a powerful survey instrument because of its high sensitivity, large field of view, mapping capabilities, and simultaneous four-color imaging.

IRAC consists of the Cryogenic Assembly (CA) installed in the Multiple Instrument Chamber (MIC) in the CTA, and the Warm Electronics Assembly (WEA) mounted in the spacecraft. Harnesses connect the detectors and the calibration subsystem in the CA to the WEA. The WEA communicates with the spacecraft over three RS-422 serial lines that allow receiving commands from, and sending acknowledgments and image data to, the spacecraft Command & Data Handling (C&DH) computer.

The IRAC Cryogenic Assembly, depicted in Figure 2.1, consists of the following major subassemblies: the Pickoff Mirrors; the Shutter; the Optics Housings, which hold the doublet lenses, beamsplitters, filters, and cold stops; the Focal Plane Assemblies (FPAs) that include the detector arrays and associated components; the Transmission Calibrator with its Source and Integrating Spheres; and the Housing Structure, consisting of the Main Housing Assembly and the wedge-shaped MIC Adapter Plate.

2.2 Description of Optics

2.2.1 *Field of View (FOV)*

The IRAC optical layout is shown in Figure 2.2 and Figure 2.3. Light from the telescope is reflected into the IRAC structure by the pickoff mirrors for the two fields of view (FOVs). Each pair of channels has a doublet lens which re-images the Spitzer focal plane onto the detectors. A beamsplitter reflects the short wavelength light to the InSb detectors (Channels 1 and 2) and transmits the longer wavelength light to the Si:As detectors (Channels 3 and 4). Channels 1 and 3 view the same telescope field (within a few pixels), and Channels 2 and 4 view a different field simultaneously. The edges of the two IRAC fields of view are separated by approximately 1.52 arcmin, with no overlap on the sky. The IRAC pixel scale is nearly the same in all channels (~1.2 arcsec per pixel), providing a 5.2 arcmin $\times$ 5.2 arcmin FOV.
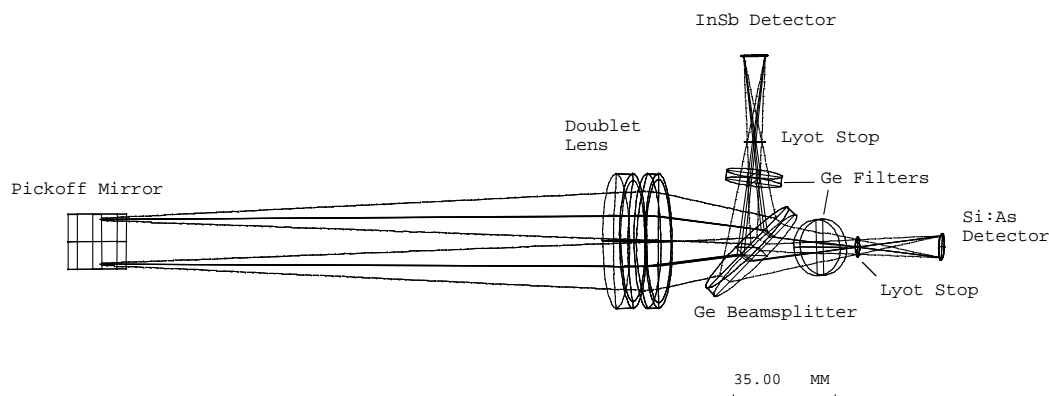
Figure 2.2. IRAC optical layout, top view. The layout is similar for both pairs of channels; the light enters the doublet and the long wavelength passes through the beamsplitter to the Si:As detector (Channels 3 and 4) and the short wavelength light is reflected to the InSb detector (Channels 1 and 2).
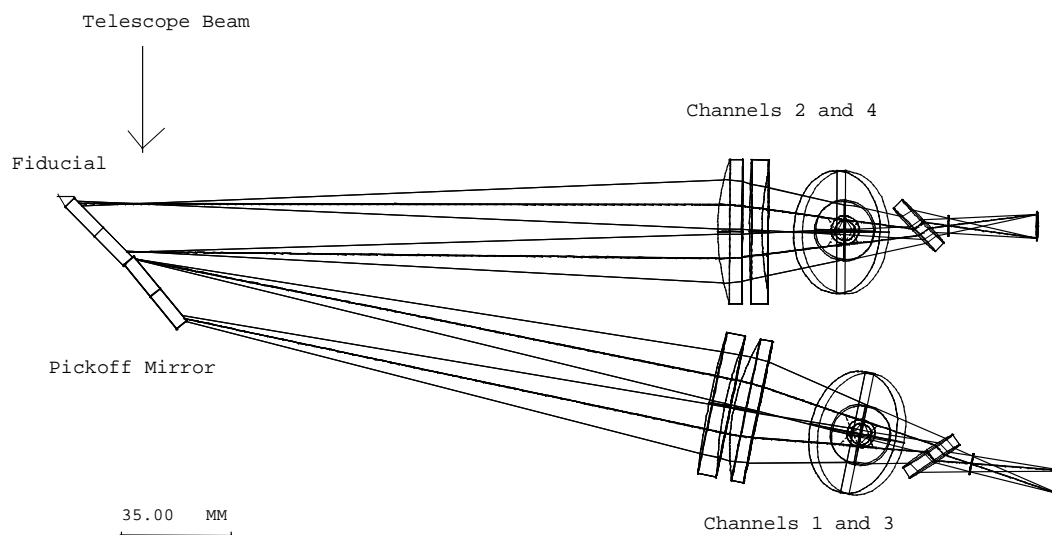
Figure 2.3. IRAC optics, side view. The Si:As detectors are shown at the far right of the figure, the InSb arrays are behind the beamsplitters.

2.2.2 IRAC Image Quality

The IRAC optics specifications limit the wavefront errors to $< \lambda/20$ in each channel. IRAC provides diffraction-limited imaging internally, and image quality is limited primarily by the Spitzer telescope. The majority of the IRAC wavefront error is a lateral chromatic aberration that is most severe at the corners of the IRAC field. The aberration is due to the difficulty of producing an achromatic design with a doublet lens over the large bandpasses being used. The effect is small, with the total lateral chromatic dispersion less than a pixel in the worst case. The sky coordinates of each pixel were accurately measured in the cryogenic mission using an astrometric solution from the ultra-deep GOODS Legacy data, resulting in

distortion coefficients that are in the world coordinate system of each image. The main effect is that the PSF and distortion may be slightly color-dependent, which may be detectable for sources with extreme color variations across the IRAC bands.

A much larger variation in the flux of sources measured in different parts of the array is due to the tilt of the filters, which leads to a different spectral response in different parts of the field of view. The flat field calibration is done with the zodiacal light, which is relatively red; blue sources have a flux variation of up to 10% from one side of an array to the other (see Section 4.5 in this Handbook for more details).

Table 2.1: IRAC image quality properties. The second set of numbers for channels 1 and 2 are for the warm mission, the rest of the numbers are for the cryogenic mission.

Channel	Noise pixels (mean)	FWHM (mean;")	FWHM of centered PRF (")	Central pixel flux (peak; %)	Pixel size (")	Maximum distortion (pixels relative to square grid)
1	7.0/7.22	1.66/1.95	1.44/1.78	42/37	1.221	1.3
2	7.2/7.33	1.72/2.02	1.43/1.80	43/34	1.213	1.6
3	10.8	1.88	1.49	29	1.222	1.4
4	13.4	1.98	1.71	22	1.220	2.2

Table 2.1 shows some properties relating to the IRAC image quality. These numbers were derived from in-flight measurements of bright stars. PRF is the "Point Response Function", further discussed in Section 4.7. The warm mission values were determined from the ~ 4000 observations (0.4s frames) of the calibration star that was used for the PRF/focus measurements in the warm mission after the final bias and temperatures were set. In the warm mission, the FWHM values were obtained from a Gaussian fit to the PSF profile and the peak central pixel fluxes were the average of stars that were within 0.09 and 0.15 pixels from being centered, in each channel.

The noise pixels column in Table 2.1 gives the equivalent number of pixels whose noise contributes to a linear least-squares extraction of the flux of a point source from a 13×13 pixel portion of an unconfused image and assuming the PRF is perfectly known. In more detail, the quantity is derived as follows.

Let the PRF in pixel i be P_i and the intensity of an image in pixel i be I_i. If a point source with flux F is present in the image, then $I_i = FP_i$. If we do a least-squares fit to determine F, then we minimize

$$\chi^2 = \Sigma \frac{(I_i - FP_i)^2}{\sigma_i^2}$$

where σ_i is the measurement uncertainty in pixel i. We will assume here that σ_i is independent of pixel and set $\sigma_i = \sigma$. Now we take the derivative of χ^2 with respect to the source flux and set it to zero to find the optimum value. We find

$$0 = \Sigma\left(I_i - FP_i\right)P_i$$

solving for F, we find

$$F = \frac{\Sigma I_i P_i}{\Sigma P_i^2}$$

Now we derive the uncertainty in the flux. Using the well-known theorem for propagation of errors

$$\sigma_F^2 = \Sigma\left(\frac{dF}{dI_i}\right)^2 ,$$

and applying it to the result above, we find that

$$\sigma_F^2 = \Sigma\left(\frac{P_i}{\Sigma P_i^2}\right)^2 \sigma^2 = \frac{\Sigma P_i^2 \sigma^2}{\left(\Sigma P_i^2\right)^2} = \frac{\sigma^2}{\Sigma P_i^2} ,$$

or, equivalently, $\sigma_F = \sigma\sqrt{N}$ where $N = \dfrac{1}{\Sigma P_i^2}$, which is the definition of noise pixels.

There are two columns for the full width at half-maximum (FWHM) of the PRF in Table 2.1. The mean FWHM is from observations of a star at 25 different locations on the array. The FWHM for "centered PRF" is for cases where the star was most closely centered in a pixel. The fifth column in Table 2.1 is the fraction of the flux in the central pixel for a source that is well centered in a pixel. It was determined from the images of the focus star (after the telescope was focused) that were the most symmetric and concentrated. These values for the flux in the central pixel can be used in the saturation predictions (see Section 2.4 below). The flux in the central pixel for a random observation is likely to be lower, because the Spitzer PRF is rather undersampled at the IRAC pixel scale.

2.2.3   Spectral Response

The IRAC system throughput and optical performance is governed by a combination of the system components, including the lenses, beamsplitters, filters, mirrors, and detectors. The system parameters are summarized in Table 2.2. The system response is based on measurements of the final in-flight system,

including the beamsplitter, filter, ZnS & ZnSe coating transmissions, mirror reflectance, BaF_2 and MgF_2 coating transmissions, and detector quantum efficiency.

Table 2.2: **IRAC Channel characteristics.**

Chan	Effective λ (μm)	Bandwidth (μm)	Average transmission (η_I)	Minimum in-band trans-mission	Peak trans-mission
1	3.550	0.750 (21%)	0.676	0.563	0.748
2	4.493	1.015 (23%)	0.731	0.540	0.859
3	5.731	1.425 (25%)	0.589	0.522	0.653
4	7.872	2.905 (36%)	0.556	0.450	0.637

At each wavelength, the spectral response curve gives the number of electrons produced in the detector per incoming photon. While the curves provided are best estimates of the actual spectral response, it is recommended that the curves are used in a relative sense for color corrections and the supplied photometric scaling (implicit in Level 1 products ["BCDs"] and described in *Reach et al. 2005, PASP, 117, 978, [24])* is used for absolute photometric calibration. Tests during IOC/SV showed that the out-of-band leaks are less than the astronomical background at all locations for sources of any temperature detectable in the IRAC bands.

The spectral response curves presented below reflect our best knowledge of the telescope throughput and detector quantum efficiency. The response curves use measurements of filter and beamsplitter transmissions over the range of angles of incidence corresponding to the distribution of incident angles across the fields of view of the IRAC detectors *(Quijada et al. 2004, Proc. SPIE, 5487, 244, [22])*.

We provide three sets of curves for each IRAC channel: an average response curve for the entire array, an average curve for the subarray field of view and a data cube of the response curves on a per pixel basis. The average curves are useful for making color corrections to photometry of well-dithered (four or more) observations. The response cubes can be used for more rigorous color corrections on per instance basis. For most purposes, the average curves are sufficient. A more detailed discussion of the spectral response curves is given by *Hora et al. (2008, [15]).* The derived IRAC spectral response curves are shown in Figure 2.4. The IRAC web pages contain links to the tabulated spectral response curves.
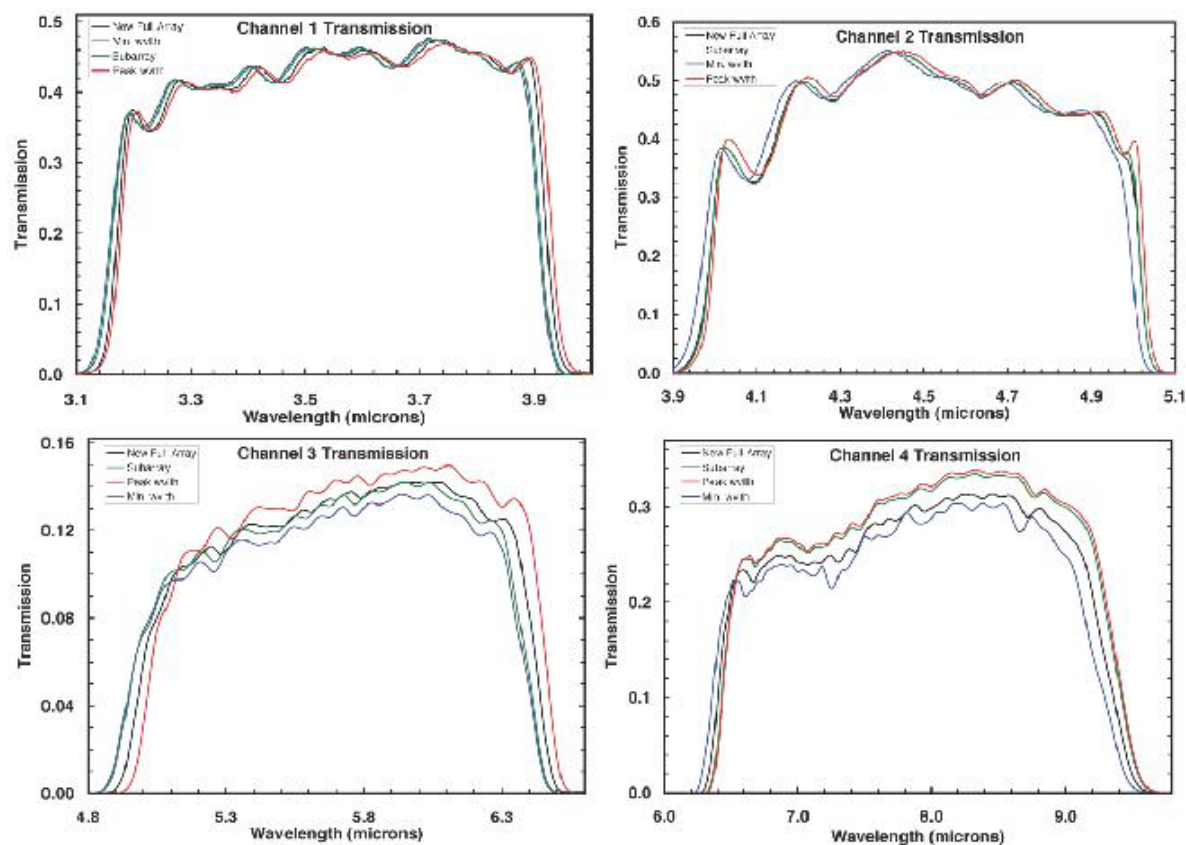
Figure 2.4. Spectral response curves for all four IRAC channels. The full array average curve is displayed in black. The subarray average curve is in green. The extrema of the full array per-pixel transmission curves are also shown for reference.
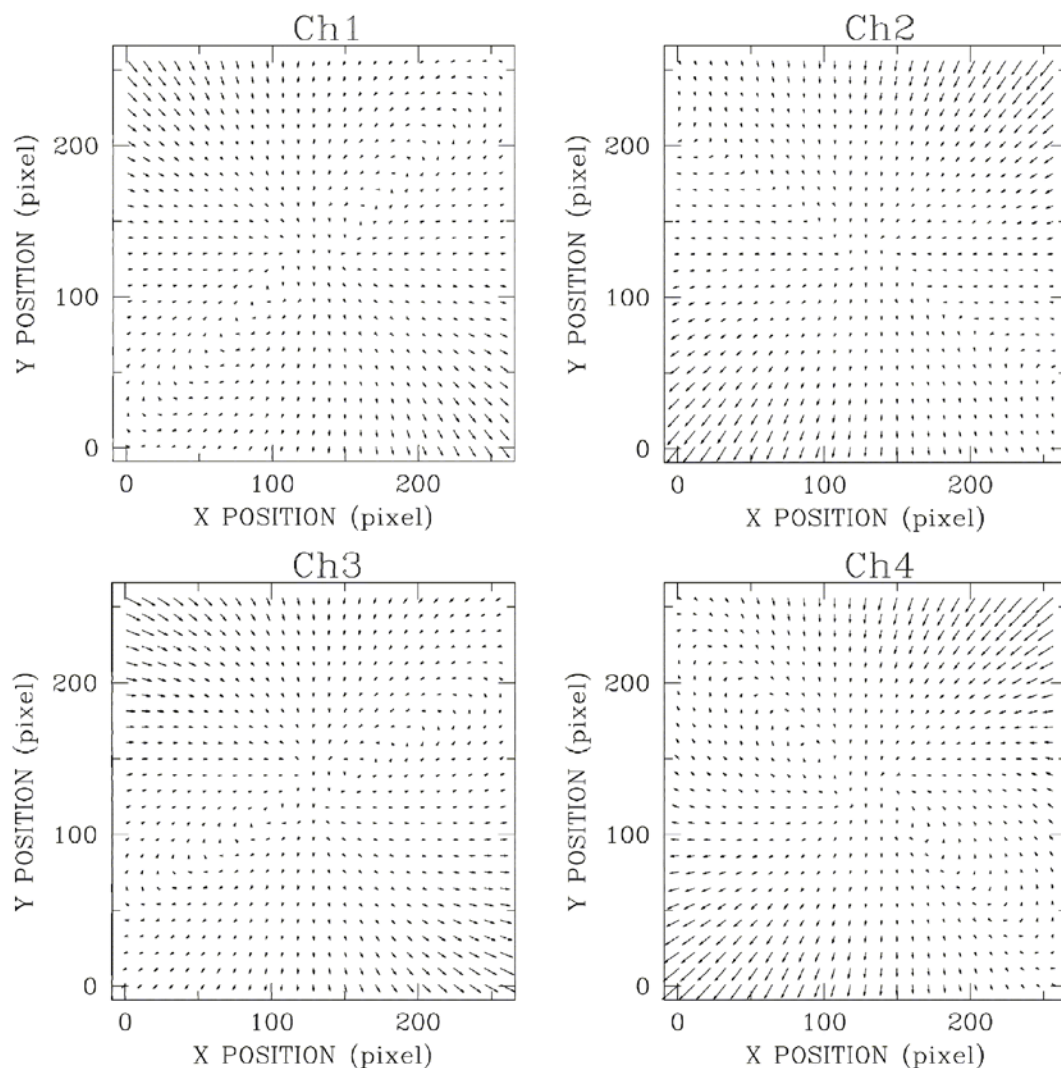
Figure 2.5. Optical image distortion in IRAC channels. The panels show the image distortions as calculated from a quadratic polynomial model that has been fit to in-flight data. The magnitude of the distortion and the direction to which objects have moved from their ideal tangential plane projected positions is shown with arrows. The length of the arrows has been increased by a factor of ten for clarity. The maximum positional deviations across the arrays for this quadratic distortion model are less than 1.3, 1.6, 1.4 and 2.2 pixels for channels 1−4, respectively. The derivation of the pixel scales that are listed in Table 2.1 fully accounted for the quadratic distortion effects shown here.

2.2.4 Distortion

Due to the off-axis placement of IRAC in the Spitzer focal plane, there is a small amount of distortion over the IRAC FOV. The maximum distortion in each IRAC band is < 2.2 pixels (compared to a perfectly regular grid) over the full FOV. Figure 2.5 shows the distortion across all four IRAC channels, as determined from data taken during IOC/SV.

2.3 Detectors

2.3.1 Design

The IRAC detector arrays were developed by the Raytheon/Santa Barbara Research Center (SBRC) in Goleta, CA, under contract to SAO *(Hoffman et al. 1998, [13]; Estrada et al. 1998, [8])*. Channels 1 (FPA desig. 48534/34 UR) and 2 (48975/66 GSFC) use InSb arrays operating at ~15 K, and channels 3 (30052/41 ARC) and 4 (30219/64 ARC) use Si:As detectors operating at ~ 6 K. Both array types use the CRC744 CMOS readout circuit, and the same physical pixel size of 30 μm. The arrays are anti-reflection coated with SiO (Channels 1, 2, and 3) and ZnS (Channel 4). The power dissipation for each array is <1 mW. The quantum efficiencies are 87%, 86%, 45% and 70% for channels 1–4, respectively. The quantum efficiencies and the well depths (below) are from pre-flight laboratory measurements. The operability or the percentage of the pixels that are within usable specifications was 99.97%, 99.9%, 99.99% and 99.75% for channels 1–4, respectively, during the cryogenic mission and 99.01% and 99.97% for channels 1 and 2, respectively, during the warm mission. The well depths were 145,000, 140,000, 170,000 and 200,000 electrons in channels 1–4, respectively, during the cryogenic mission and 110,000 and 125,000 in channels 1 and 2, respectively, during the warm mission (updated from the cryogenic values to match observed saturation limits). Table 2.2 gives the read noise values for IRAC channels 1–4 during the cryogenic mission and channels 1 and 2 during the warm mission.

Table 2.3. IRAC read noise. The first numbers in a cell are for cryogenic mission and lone or second numbers in a cell are for warm mission.

Ch.	Read noise for frame with specified frame time (electrons)											
	0.02s*	0.1s*	0.4s*	2s*	0.4s	0.6s	1.2s	2s	6s	12s	30s	100s
1	25.4	16.9/13.4	10.8	10.8	22.4	22.4	22.4	11.8/16	16	9.4/15	7.8/14.6	8.4/21
2	23.7	16.8/12.1	9.4	9.4	23.7	23.7	23.7	12.1/12.1	10	9.4/10.4	7.5/10.4	7.9/16
3		9.0						9.1		8.8	10.7	13.1
4		8.4						7.1		6.7	6.9	6.8**

* Per single subframe (1 of 64 planes in the BCD cube).
**Per 50 s frame.

2.3.2 Linearity

Both types of detectors have measurable nonlinearity. The InSb arrays are nearly linear until they reach saturation. The Si:As detectors are somewhat nonlinear over most of their operating range, and above half-well capacity this will contribute noticeably to the total error budget. However, all of the arrays are linearized to better than 1% up to approximately 90% of their full-well capacity (defined in electrons above, with the gain listed in Table 2.4, corresponding typically to 45,000-60,000 DN). The detector

linearity has been measured during ground testing and in flight. The laboratory linearity measurements, with the flight instrument, are shown in Figure 2.6. The arrays were illuminated with a constant flux, and successively longer exposures were taken. For a perfectly linear system, the flux would be directly proportional to the exposure time, and the graph would show a straight line. In fact, the arrays were driven past their saturation levels, and the shape of the curve up to 90% of the saturation level was fitted with a polynomial for the linearization module in the pipeline.

During IWIC, it was found that the non-linearity and well-depth varied as both a function of applied voltage on the arrays and the array temperature. Both of these were changed as a result of warm operations. Unfortunately, it was extraordinarily difficult to recalibrate the linearization in-flight with the accuracy of the ground-based cryogenic linearization.

The warm mission linearity calibration was derived using a combination of staring observations of bright galactic nebulae, and from the photometry of sources observed by the SERVS Exploration Science program, vs. the same sources observed by the SWIRE Legacy Science program during cryogenic operations. The warm mission linearity solution should be accurate at the level of better than 0.5%.

IWIC results indicated that the non-linearity at 27−28 K temperatures (warm mission) is more severe than at 15 K (cryogenic mission). Using the cryogenic calibration provides at least a partial correction. Note that the flux calibration is based on standard stars that are usually near 1/3−1/2 full well. Targets that are near this well depth will always have correct fluxes.

The other change in the warm linearization is the well depth that is defined by the point at which the pixel DN peaks is now roughly 30,000 DN in both channels, whereas it was closer to 44,000 DN in the cryogenic mission.
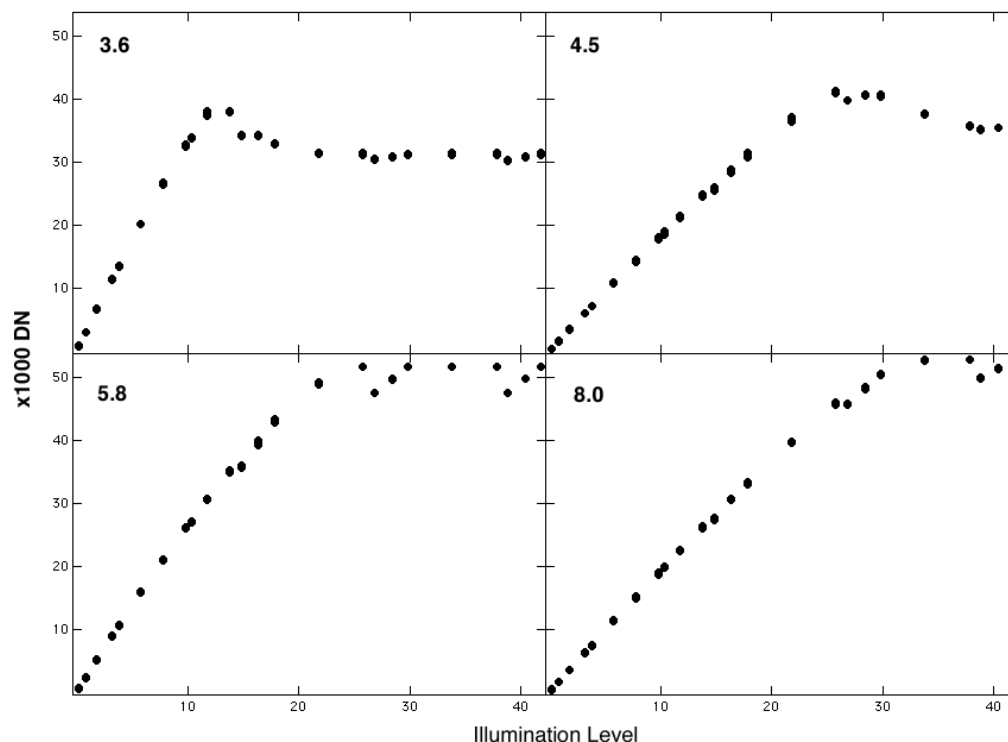
Figure 2.6 : Non-linearity curves for the IRAC detectors. The detector responses are fairly linear until saturation, where there is a steep drop-off in responsivity.

2.4 Electronics

2.4.1 Hardware

IRAC has no moving parts (other than the shutter, which was not operated in flight). The instrument takes data by staring at the sky and sampling the arrays between resets. IRAC was capable of operating each of its four arrays independently and/or simultaneously. All four arrays were used during normal, full-array operation.

2.4.2 Fowler Sampling

Multiple (Fowler) sampling is used to reduce the effective read noise. This mode of sampling consists of taking N non-destructive reads immediately after the reset, and another N non-destructive reads near the end of the integration. Differencing is performed in the IRAC electronics to generate one integer value per pixel per exposure to store on the spacecraft and transmit to the ground. The Fowler N used for an observation depends on integration time and was selected to maximize the S/N, based on in-flight performance tests.

2.4.3 Exposure Times and Frame Time

The relationship between the exposure time (T_{ex}) and frame time is shown in Figure 2.7. The exposure time is defined as the time elapsed between the first pedestal sample and the first signal sample. The Fowler samples are taken consecutively at 0.2-second intervals in each group (pedestal and signal samples). The frame time (T_f - T_i) is the total time elapsed between resets which could include multiple reads and dead time before and after Fowler sampling. The frames are commanded by specifying the number of Fowler samples for the pedestal (N_F) and the number of wait ticks in between the pedestal and signal frames (N_W); then the frame time is $T_F = (2N_F + N_W)\tau$, where τ is the readout time (0.2 sec for full array, 0.01 sec for sub-array mode). T_{ex} is simply $T_F - N_F\tau$. N_F values can be found in Table 2.6.
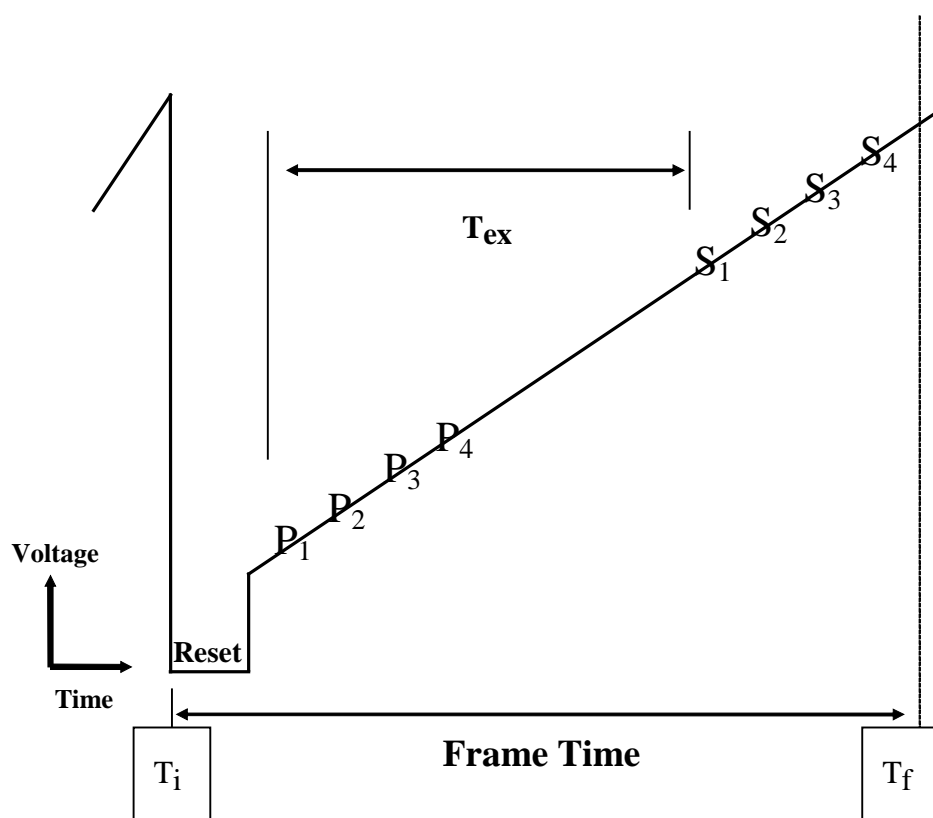
Figure 2.7: Fowler sampling times for one pixel (Fowler N=4). The P_n (n=1,2,3,4) show the "Pedestal" readouts, and the S_n show the "Signal" readouts. T_{ex} is the effective exposure time, and $T_f - T_i$ is the "frame time," or total time to obtain one IRAC image. The reset part of the sketch is not at the same time and voltage scale as the rest of the figure.

2.4.4   Subarray Mode

In subarray mode, only one corner, 32×32 pixels offset by 8 pixels from the edges, is read out from one array. Pixels (9:40, 9:40) in raw frame coordinates of the array are read out (thus in [C]BCD data the location is 9:40, 217:248 in channels 1 and 2). The subarray pixel size is the same as the full array pixel size (~1.2 arcsec). Fowler sampling is performed as in full array mode, but a set of 64 subarray images are generated and tiled into a single 256×256 image before data are sent from IRAC. In subarray mode, Fowler sampling is performed at 0.01 sec intervals. Subarray mode is useful for observing very bright sources and for obtaining high temporal resolution. No CBCDs are generated in the pipeline for subarray data but the pipeline produces simple stacks of 64 frames median-averaged together (*sub2d.fits). To make a mosaic of subarray data, users can use the *sub2d.fits images with corresponding uncertainty and maskfiles that are available with the BCD files. The *sub2d.fits images are median stacked two-dimensional combinations of the 64 plane BCD subarray frames. These frames can be used in MOPEX mosaicking software just as the full array (C)BCD frames.

2.4.5   Calibration Lamps

IRAC contains two types of internal calibration lamps. The transmission calibrator lamps were designed to illuminate all four arrays and provide an internal responsivity measurement. There are two transmission calibrator spheres, each of which contains two lamp elements. To illuminate the arrays, the shutter is closed, a transmission lamp is turned on, and the light from that lamp bounces off a mirror on the back of the shutter. The flood calibrators individually illuminate each detector. The flood calibrators could be controlled individually, and they could be used whether the shutter is open or closed. The flood calibrators were operated at the end of each IRAC campaign in the cryogenic mission and used as a consistency check. Calibration of IRAC observations is described in Chapter 4.

2.4.6   Firmware

The IRAC firmware controls the focal plane assemblies, calibration electronics, and warm electronics boards. Apart from autonomous fault protection, the IRAC firmware responds only to commands sent by the Spitzer Command & Data Handling (C&DH) computer. The C&DH sends setup commands to configure the electronics, requests for each telemetry packet, and integration commands to generate images. IRAC responds to each command with an acknowledgment. In the case of a command that requests telemetry, the acknowledgment consists of the telemetry packet, which is sent on the low-speed connection between IRAC and the C&DH. There are two types of engineering data: special engineering data, which are collected every 4 sec, and housekeeping data, which are collected every 30 seconds. Special engineering data are used for onboard communication between IRAC and the C&DH, while housekeeping data are used on the ground to monitor instrument performance. A command that generates images from the arrays is acknowledged on the low-speed line, and when the frame is complete, the data-ready signal is sent on the high-speed line. The frames (together with their ancillary data) are then transferred one at a time to the C&DH. The rate of transfer is 2 seconds per frame, which limits the data collection rate to a maximum of four frames every 8 seconds for IRAC observations with all four arrays.

Autonomous fault protection ensures that none of the monitored voltages or currents entered into a red limit. Fault protection is performed by a watchdog demon that is always running when the instrument is on. The red limits are stored in IRAC memory. If a voltage in the focal plane assembly goes into a red limit, IRAC will turn off the affected focal plane array. (The individual pixel values are not monitored, so a bright astronomical source does not trigger a red limit.) The command sequences would continue to execute; therefore, it is possible for normal completion of an IRAC observing campaign to occur with only three of the four arrays returning data. If a second focal plane assembly has a telemetry datum go into a red limit, then IRAC would send the C&DH (via the special engineering data on the low-speed line) a request to be turned off. If a telemetry point other than one affecting a single focal plane goes into a red limit, IRAC would also send the C&DH a request to be turned off.

2.5 Sensitivity and Saturation

2.5.1 *Sensitivity*

To estimate the sensitivity of IRAC in flight, where possible we use the measured properties of Spitzer and IRAC from IOC/SV and IWIC; otherwise we use the required performance based on the design specifications. The sensitivity to point sources (in flux density units) is based on the following formula:

$$\sigma = \frac{\sqrt{N_{pix}}}{ST_{ex}f_p}\sqrt{BT_{ex} + (BT_{ex}f_F)^2 + R^2 + DT_{ex}} \qquad (2.1)$$

where the scale factor is

$$S = \frac{Q\eta_T\eta_I A\Delta\lambda}{h\lambda} \qquad (2.2)$$

the background current is

$$B = SI_{bg}f_S\Omega_{pix}f_{ex} \qquad (2.3)$$

and the effective exposure time is

$$T_{ex} = T_F - 0.2 N_F \qquad (2.4)$$

In these equations, the spectral resolving power $\lambda/\Delta\lambda$ is from Table 2.3 ; the detector quantum efficiency Q (electrons per photon) is from Table 2.2; the instrumental throughput η_I is from Table 2.3; the telescope throughput η_T =[0.889, 0.902, 0.908, 0.914] for channels 1 to 4, respectively (with Be primary, Al-coated secondary, and 50 nm ice contamination); the telescope area (including obstruction) A=4636 cm^2; the equivalent number of noise pixels N_{pix} is from Table 2.1 (and defined in Section 2.2.2); h is the Planck constant; I_{bg} is the background surface brightness in MJy/sr; f_S=1.2 is the stray light contribution to the background; the dark current D is <0.1, 0.28, 1, and 3.8 e-/s for channels 1, 2, 3, and 4, respectively; the read noise R is from Table 2.2; Ω_{pix} is the pixel solid angle (see Table 2.1); f_p is the in-flight estimated throughput correction for point sources (Table 2.4); f_{ex} is the in-flight estimated throughput correction for the background (Table 2.4).

The "throughput corrections" f_p and f_{ex} were determined by comparing the observed to expected brightness of stars and zodiacal light. Stars were measured in a 10-pixel radius aperture, and the zodiacal light was measured in channels 3 and 4 for comparison to the COBE/DIRBE zodiacal light model. (This measurement was not possible in channels 1 and 2 because we could not use the shutter for absolute reference.)

Early in the mission, we found that the throughput in channels 3 and 4 was lower than expected, both for extended emission and point sources (but more so for point sources). Measurements of diffuse Galactic emission confirmed the deficit, and measurements of the PRF using bright stars showed that a considerable amount of stellar flux was being spread all across the arrays. The deficit in throughput from diffuse emission was due to the fact that the QE of the arrays had been overestimated. No reliable measurements of QE existed for channels 3 and 4, so the QE was based on a theoretical model that incorrectly assumed that all the flux was reflected at the front of the detector diode chip (the detector arrays are backlit). Some of the light that passes through the detector is scattered widely across the array. Measurements on a sister array confirmed this internal scattering, and showed that it is strongly wavelength dependent. There is considerable evidence that the "loss" of QE and the scattered light are not due to contamination, or damaged optical coatings, etc. Table 2.4 lists some useful combinations of IRAC instrument parameters.

Table 2.5 gives the background brightnesses, in useful units, for three nominal observing directions. The low-background model applies near the ecliptic pole; the high-background case is in the ecliptic plane; and the medium-background case is intermediate. The background model includes contributions from emission and scattering from zodiacal dust and emission from Galactic dust. The near-infrared cosmic infrared background radiation is not included because it was partially resolved by Spitzer.

Table 2.4: **Useful quantities for IRAC sensitivity calculations. The first number is for cryogenic mission, the second is for warm mission.**

Wavelength	3.6 μm	4.5 μm	5.8 μm	8 μm
Conversion factor (electrons/sec)/(MJy/sr)	25/29.5	29/25.3	14	29
S (electrons/sec)/(μJy)	0.77/0.84	0.89/0.73	0.42	0.91
Gain (electrons/DN)	3.3/3.7	3.7/3.7	3.8	3.8
f_p (throughput correction for point sources)	1.06/1	0.84/1	0.45	0.61
f_{ex} (throughput correction for background)	1	1	0.72	0.88

Table 2.5: **Background brightness in IRAC wavebands. The first number is for cryogenic mission, the second is for warm mission.**

	3.6 μm	4.5 μm	5.8 μm	8 μm
"low" background model				
$I_\nu f_S$ (MJy/sr)	0.093	0.32	1.7	6.6
F_ν^{BG} (μJy)	3.2	11	57	220
B (elec/sec)	2.5/2.7	9.9/8.9	18	184
"medium" background model				
$I_\nu f_S$ (MJy/sr)	0.15	0.44	2.3	9.3
F_ν^{BG} (μJy)	5.1	15	79	320
B (elec/sec)	4.1/4.4	14/11	25	260
"high" background model				
$I_\nu f_S$ (MJy/sr)	0.52	1.0	5.6	22
F_ν^{BG} (μJy)	18	35	190	750
B (elec/sec)	14/15	32/26	60	620

The quantity f_F is the flat field pixel-to-pixel variance, which depends on the observing strategy. In what follows, we will set $f_F =0$, which would apply strictly in the case of stable detectors with perfect flat field measurements, and should apply practically for highly-dithered observations. An observation with no dithering will be limited by the correlated noise. The accuracy of a flat field derived from a single observing campaign was measured to be 2.4, 1.2, 1.0, and 0.3% in channels 1, 2, 3, and 4, respectively, by comparing flats in several campaigns. Using combined flats ("superskyflat") from the entire cryogenic (warm) mission, the estimated f_F is 0.14% (0.17%), 0.09% (0.09%), 0.07%, and 0.01% in channels 1–4, respectively. Using these values for f_F in equation 6.1, single frames are dominated by background and read noise. When combining multiple frames to generate a mosaic, the background and read noises will average down (as square root of the number of frames), while the flat-field noise will only average down for dithered observations. For *N undithered* observations on the "medium" background, flat-field noise dominates when the total exposure time, $N \times T_{ex}$, exceeds approximately 420 sec (using individual

campaign flats) or 2.5 hrs (using the super sky flat). For dithered observations, the flat-field noise will also average down, and will only be important for the very deep observations of high background fields.

For the frame times used in IRAC operations in flight, Table 2.6 gives the readout mode and Fowler number. For full array readout mode, only the 2, 12, 30, and 100 sec (and initially 200 sec) frame times could be chosen in the IRAC AOT in the cryogenic mission, in the warm mission 0.4 and 6 sec frame times were added; the 0.6 and 1.2 sec frame times come as part of the "high dynamic range" (HDR) sequences. The 0.4 sec full frame time was only available for channels 1 and 2 in Stellar Mode in the cryogenic mission but is available in the regular full array mode in the warm mission. The 2 sec subarray frame time is only available in the warm mission. The frame sets that are taken for each pointing in HDR mode are shown in Table 2.7. Long frame times at 8 μm are background-limited. Therefore there is a maximum frame time of 50 sec at 8 μm, and the 100/200 sec frames were automatically converted into two/four repeats of 50 sec frames. The last column, T_h, gives the extra time spent taking the HDR frames (used in the observing time estimate equation below).

Table 2.6: Fowler numbers for IRAC frames. The first number is for cryogenic mission, the numbers in parenthesis are for channel 1 and 2 in the warm mission if different from cryogenic values.

Frame Time (sec)	Readout Mode	Fowler Number	Wait Ticks
200	Full	32	936
100	Full	16 (32/16)	468 (436/468)
50	Full (8 μm)	16	218
30	Full	16 (32/16)	118 (86/118)
12	Full	8	44
(6)	Full	(8/8)	(14/14)
2	Full	4	2
1.2	HDR	1 (2/2)	4 (2/2)
0.6	HDR	1	1
0.4	Stellar/Full	1	0
0.4	Subarray	8 (4/4)	24 (32/32)
0.1	Subarray	2	6
0.02	Subarray	1	0

Table 2.7: IRAC High-Dynamic-Range (HDR) framesets

Long Frame Time	List of frames taken	T_h (sec)
200	0.6, 12, 200	15
100	0.6, 12, 100	15
30	1.2, 30	3
12	0.6, 12	2
6[*]	0.6, 6	2

[*]**Warm mission only.**

Table 2.8, Table *2.9*, Table 2.10 and Figure 2.8, *Figure 2.9* and Figure 2.10 show the sensitivities for the four IRAC channels for each of the three background models. The sensitivities in the tables are for point sources extracted from single images (but perfectly flat-fielded). In the figures, the sensitivities are for point sources extracted from coadded images (perfectly registered). We do not include "confusion noise" (due to overlapping images of distant galaxies or other sources of background structure) in the sensitivity estimates. The detectors are assumed to perform according to the IRAC detector measurements of read noise, dark current, and quantum efficiency. The first 8 rows in each table show the sensitivity for full-array readouts, and the last four rows show the sensitivity for subarray readouts.

Table 2.8: IRAC point-source sensitivity, low background (1 σ, µJy). Numbers in parentheses are for warm mission.

Frame Time (sec)	3.6 µm	4.5 µm	5.8 µm	8 µm
200	0.40	0.84	5.5	6.9
100	0.60 (0.86)	1.2 (1.25)	8.0	9.8
30	1.4 (2.2)	2.4 (2.5)	16	18
12	3.3 (4.9)	4.8 (5.0)	27	29
6	(12.2)	(9.8)	-	-
2	32 (44)	38 (39)	150	92
0.6[a]	180 (185)	210 (222)	630	250
0.4[b]	360 (369)	430 (443)	1260	450
2[c]	(19)	(21)	-	-
0.4[c]	81 (102)	89 (102)	609	225
0.1[c]	485 (552)	550 (566)	2010	690
0.02[c]	7300 (8374)	8600 (8447)	25000	8100

Table 2.9: IRAC point-source sensitivity, medium background (1 σ, µJy). Numbers in parentheses are for warm mission.

Frame Time (sec)	3.6 µm	4.5 µm	5.8 µm	8 µm
200	0.49	0.97	6.4	8.2
100	0.73 (1.0)	1.4 (1.44)	9.3	12
30	1.6 (2.5)	2.8 (2.9)	18	21
12	3.6 (5.2)	5.3 (5.5)	31	34
6	(12.4)	(10.4)	-	-
2	32	38	150	110
0.6[a]	180 (185)	210 (222)	640	260
0.4[b]	360 (370)	430 (443)	1260	460
2[c]	(19)	(21)		
0.4[c]	82 (102)	89 (103)	610	250
0.1[c]	490 (553)	550 (567)	2020	720
0.02[c]	7300 (8374)	8600 (8447)	25000	8100

Table 2.10: IRAC point-source sensitivity, high background (1 σ, μJy). Numbers in parentheses are for warm mission.

Frame Time (sec)	3.6 μm	4.5 μm	5.8 μm	8 μm
200	0.89	1.5	9.8	12
100	1.3 (1.48)	2.1 (2.16)	14	18
30	2.5 (3.3)	4.1 (4.2)	27	32
12	4.8 (6.1)	7.1 (7.4)	44	52
6	(13.4)	(12.8)	-	-
2	34 (45)	41 (42)	180	156
0.6[a]	180 (186)	220 (224)	660	330
0.4[b]	360 (370)	430 (445)	1280	540
2[c]	21	24	-	-
0.4[c]	84 (104)	93 (106)	650	340
0.1[c]	490 (555)	560 (569)	2100	860
0.02[c]	7300 (8375)	8600 (8848)	25000	8200

[a] available only in high-dynamic-range mode.

[b] available only in stellar photometry mode in cryogenic mission, full array in warm mission.

[c] subarray mode (set of 64 32×32 images). Sensitivity is per frame, not the sensitivity of a 64-frame coadd.
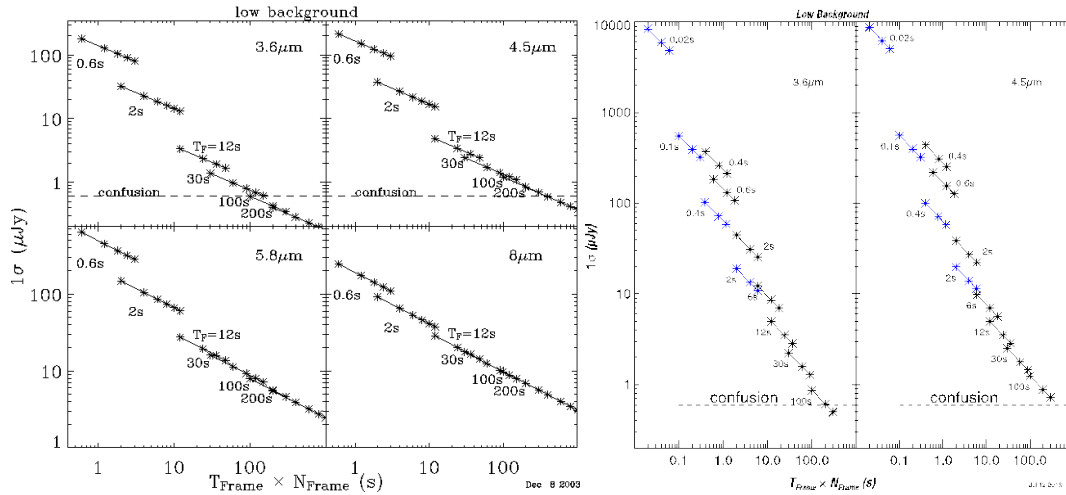
Figure 2.8: IRAC point source sensitivity as a function of frame time, for low background. Cryogenic values on the left, warm mission values on the right. To convert to MJy/sr, see equation 2.8.

Figure 2.8, Figure 2.9 and Figure 2.10 show the point source sensitivity as a function of integration time for each background model. The "time" axes in the plots represent the frame time for the images, which does not include time for moving the telescope. The IRAC full-array frame times are 0.4, 0.6, 2, 6, 12, 30, and 100 seconds (0.4 and 6 second frames were available only in the warm mission; 200 seconds was also

available in the early mission). Other times plotted below are assumed to use multiple exposures of those fixed times.

For bright sources, shot noise due to counting statistics in electrons from the source itself becomes the dominant source of noise. We can estimate the total noise by adding the shot noise in quadrature, so that

$$\sigma_{tot} = \sigma\sqrt{(1+(F/F_b))} \tag{2.5}$$
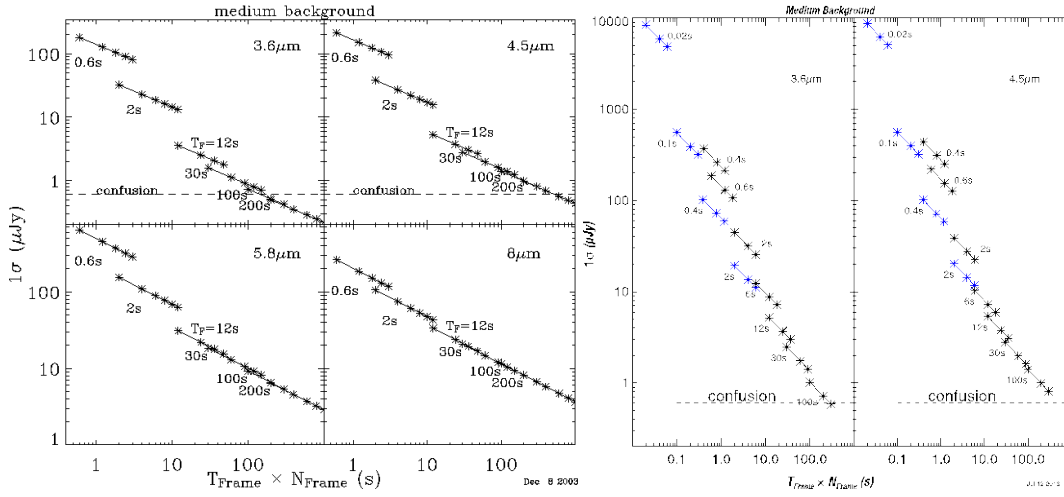
Figure 2.9: IRAC point source sensitivity as a function of frame time, for medium background. Cryogenic values on the left, warm mission values on the right. To convert to MJy/sr, see equation 2.8.

where σ is the noise from equation 6.1 and

$$F_b = f_p S T_{ex}\sigma^2 \tag{2.6}$$

In the bright source limit, $F \gg F_b$, then the signal-to-noise ratio becomes

$$S/N = \sqrt{f_p S T_{ex}F} \tag{2.7}$$

If the exposure time is in seconds and the source flux is in μJy, then for IRAC channels 1, 2, 3, and 4, respectively, *S/N* is 0.88 (0.86), 0.95 (0.85), 0.65, and 0.95 times $\sqrt{T_{ex}F}$. Warm mission values are in parentheses.
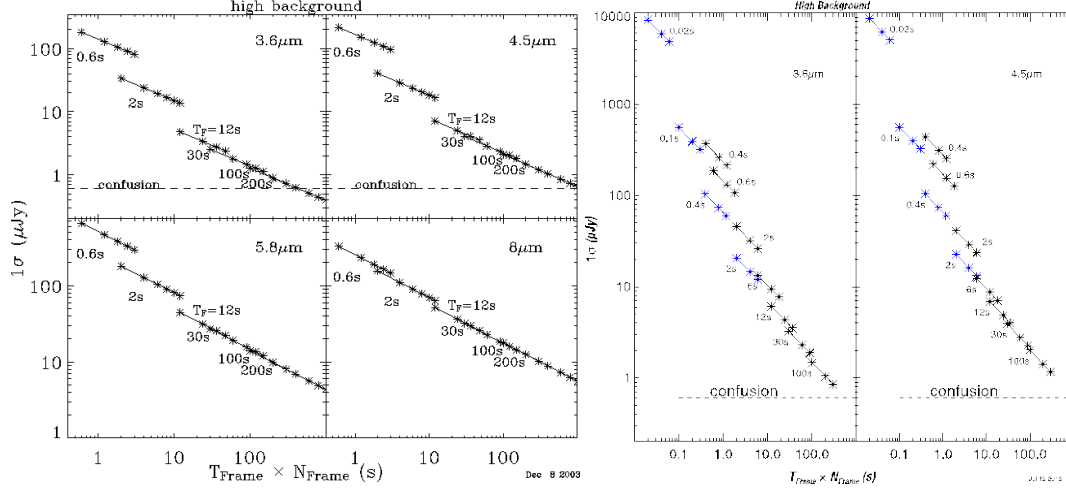
Figure 2.10: IRAC point source sensitivity as a function of frame time, for high background. Cryogenic values on the left, warm mission values on the right. To convert to MJy/sr, see equation 2.8.

In the sensitivity figures, the dashed line at 0.6 μJy is the confusion limit predicted by *Franceschini et al. (1991, [10])*. This does not represent a hard sensitivity limit, but rather indicates where source confusion affects reliability of source extractions for low background regions. Data from IOC/SV show noise decreasing as $\sqrt{N}$ to 0.25 μJy (channels 1 and 2) or 0.6 μJy (channels 3 and 4). Moderately deep source counts indicate that a source density equivalent to 36 beams/source is reached at 20.5 mag, or 1.8 and 1.1 μJy at 3.6 and 4.5 μm, respectively *(Fazio et al. 2004, [9])*. The confusion estimates by Franceschini et al. and Fazio et al. are for low background, extragalactic observations only. For observations of higher background or more "cluttered" regions (such as the Galactic Plane) the confusion noise will be much more significant.

For diffuse emission, the surface brightness sensitivity per pixel (in MJy/sr) is

$$\frac{0.03 f_p}{f_{ex}\sqrt{N_{pix}}} \times \text{ the point source sensitivity [in μJy]}. \tag{2.8}$$

The noise pixels, N_{pix}, is defined in Table 2.1.

2.5.2 Saturation

The saturation limit for IRAC is calculated as follows. Using the same notation as earlier in this section,

$$F_{sat} = \frac{Wf_w - BT_F f_{ex}}{ST_F f_{cen} f_p}$$

(2.9)

where W is the well depth (Table 2.2), $f_w = 0.9$ is the fraction of the well depth to which we can linearize the intensities, and f_{cen} is the fraction of the source flux falling onto the central pixel (Table 2.1). Table 2.11 shows the point source saturation limits of IRAC at each frame time. In an extremely bright area of sky, such as an H II region, the saturation limit is lower. Note that the saturation value is conservatively computed from the worst case in which the PSF is directly centered on a pixel. To apply Table 2.11 for extended sources,

$$I_{sat} = 28.6 \times f_{cen} F_{sat} \quad \text{for compact (diameter} < 30'') \text{ sources}$$

(2.10)

$$I_{sat} = 28.6 \times \frac{f_{cen} f_p}{f_{ex}} F_{sat} \quad \text{for more extended sources,}$$

(2.11)

where I_{sat}^{ext} is the total surface brightness (in MJy/sr) at which a pixel saturates; Ω_{pix} is the solid angle, in sr, subtended by the pixel; f_p, f_{cen}, and f_{ex} are as defined above, and F_{sat} is the saturating point source flux density (in mJy) from Table 2.11, appropriate for the channel and integration time. For 8.0 μm observations at low ecliptic latitude, an estimate of zodiacal light should be included in the surface brightness.

Table 2.11: Maximum unsaturated point source (in mJy), as a function of IRAC frame time. Values for the warm mission are given in parentheses.

Frame Time (sec)	3.6 um	4.5 μm	5.8 μm	8.0 μm
200	1.9	1.9	14	28
100	3.8 (2.8)	3.9 (3.5)	27	28
30	13 (10)	13 (12)	92	48
12	32 (25)	33 (30)	230	120
6	(50)	(60)		
2	190 (160)	200 (200)	1400	740
0.6	630 (~600)	650 (~750)	4600	2500
0.4*	950 (~1050)	980 (~1350)	6950	3700
2**	(150)	(180)		
0.4**	1000 (700)	820 (900)	3100	2300
0.1**	4000 (3000)	3300 (3700)	13000	9000
0.02**	20000 (~23000)	17000 (~31500)	63000	45000

*stellar mode (cryogenic), full array (warm); **subarray mode

The zodiacal background only makes a difference for long frames in channel 4 when observing near the ecliptic plane. If the bright extended source extends well beyond the 5.2 arcsec × 5.2 arcsec FOV, then the saturation brightness is *lower* by the factor f_s.

3 Operating Modes

The cryogenic and warm IRAC Astronomical Observation Templates (AOTs) consist of an (optional) dither pattern superposed on an (optional) rectangular-grid raster.

3.1 Readout Modes and Frame Times

In full-array readout mode, there were four selectable frame times: 2, 12, 30, and 100 sec (and a fifth, 200 sec, during the early mission). The warm mission added the 0.4 and 6 second frame times. To allow sensitive observations without losing dynamic range, there is a high dynamic range (HDR) option. When this option was selected, the IRAC AOT took extra frames, with frame times shorter than the selected frame time. The HDR frame times are given in Table 2.6. No spacecraft repositioning was done between frames, and the frames always were taken from shortest to longest. If dithers were selected, then the entire frame set was repeated at each dither position.

Stellar photometry mode was available for observations of objects much brighter in channels 1 and 2 than in 3 and 4 (typically stars) in the cryogenic mission. This mode took short exposures in channels 1 and 2, and long exposures in channels 3 and 4. Originally developed as engineering observations for taking calibration stars, this mode was available for all observers. Three framesets were available. The shortest set took a single 0.4 sec frame in channels 1 and 2, and a 2 sec frame in channels 3 and 4. The next set took two undithered 2 sec frames in channels 1 and 2, and a 12 sec frame in channels 3 and 4. The longest frame time combination took two undithered 12 sec frames in channels 1 and 2, and a 30 sec frame in channels 3 and 4. The sensitivities of each frame are identical to those in full array mode. Dithering and mapping were also available in this mode.

For very bright sources, a subarray mode is available. In this mode, only a small 32×32 pixel portion of the array was read out, so the field of view was only 38 arcsec $\times$ 38 arcsec. Mapping is not allowed in subarray mode. However, small maps can be made using a cluster target. In subarray readout mode, there were three selectable frame times: 0.02, 0.1, and 0.4 sec in the cryogenic mission. The warm mission added the 2 sec frame time. For one commanded image in subarray mode, a set of 64 Fowler-sampled frames are taken in succession, so that each time an image is commanded in subarray mode, a cube of $64\times32\times32$ pixel images are generated. This means that the durations of a single repeat at each of the three subarray frame times are 1.28, 6.4, 25.6 and 128 sec, respectively. The IRAC AOT moves the telescope to point to the subarray region of each requested channel at the target in turn. For the 0.02 sec frame time, data rate limitations allowed only data in the channel actually pointing at the target to be taken. For the 0.1, 0.4 and 2 (warm mission only) sec subarray frame times, data were taken in all four channels at each pointing position, although only one channel at a time pointed at the target.

3.2 Map Grid Definition

If "No mapping" was selected in the AOT, the map grid consisted of a single position at the coordinates specified in the Target section of the AOT. With "No mapping" selected, and selecting both fields of view, first the 4.8/8.0 μm field of view was pointed at the target, then the telescope repositioned so that the 3.6/5.8 μm field of view pointed at the target. In both cases, data from all 4 arrays were collected, whether they were pointed at the target or not. In the warm mission, the 5.8 and 8.0 μm (channels 3 and 4) arrays were not used to take data.

If the mapping mode is used, a rectangular map grid needs to be specified in either array or celestial coordinates. In array coordinates, the map grid is aligned with the edges of the array, such that the map rows and columns correspond to rows and columns of the array. Specifically, a column is along a line of constant solar elongation, and a row is along an ecliptic parallel (line of constant ecliptic latitude). It is worth noting that the two IRAC fields of view are at approximately constant solar elongation, so that a map with 1 column and several rows made a strip along the direction of the separation between the two fields of view and yields 4-array coverage along part of the strip (if it was long enough). In celestial coordinates the rows and columns correspond to J2000 right ascension and declination. A position angle, degrees E of N, can be specified to orient the raster in equatorial coordinates. Specifically, if the position angle is zero, a column is along a line of constant right ascension, and a row is along a parallel (line of constant declination). The map can be offset from the specified coordinates by giving a map center offset.

3.3 Dithering Patterns

For the full-array mode there are two types of dither patterns available. Five such patterns are fixed patterns, which were performed identically at each mapping position. The cycling pattern is a set of dither positions (also referred to as points), a different subset of which was performed at each map grid position.

Different patterns are available in subarray mode, as the angular scales covered by the arrays were quite different. Two fixed patterns are available for this mode.

The characteristics of the available dither patterns are given in Table 3.1. The Reuleaux Triangle patterns were designed with the idea of optimizing the Figure of Merit of *Arendt, Fixsen, & Moseley (2000, [3])*. They thus sample a wide range of spatial frequencies in a fairly uniform manner, and were well suited to the Fixsen least-squares flat fielding technique. The 9-point and 16-point patterns were designed to be the optimum size for 1/3 and ¼ subpixel dithering, respectively. The random 9 pattern is based on a uniform random distribution. The spiral 16 pattern was designed by R. Arendt to provide a pattern which is both compact and has a good figure of merit for self-calibration. The cycling patterns were designed for observations ("AORs") having many mapping/dithering pointings. The large and medium patterns are Gaussian distributions (with dithers >128 pixels removed). The small pattern is specifically designed for mapping, where only a few dithers were taken at each map position. It is also based on a Gaussian distribution, but the center is downweighted to decrease the fraction of small dithers in the pattern, and it is truncated at a maximum dither of 11 pixels to ensure that maps with up to 280" spacing have no holes,

even if there is only one dither per map point. All the patterns were constrained to have no pair of dithers closer than three pixels in any run of four consecutive points. The cycling dither table wraps around once the final (311th) element was reached. This pattern had a ½ sub-pixel sampling pattern superposed on it, starting with point 1 and repeating continuously every four points (at point 311, the final cycle is simply truncated early, thus patterns which wrap around the table miss a sub-pixel dither point). The five-point Gaussian pattern is a general use pattern suitable for shallow observations where the exact sub-pixel sampling is unimportant. It has a ½ subpixel pattern, with the 5th point at sub-pixel (¼,¼). Figure 3.1 shows the dither patterns at the default (large) scale. Figure 3.2 shows the cycling dither patterns and the distribution of both the dithers and of the separation between dithers for each scale.

Table 3.1: Characteristics of the dither patterns.

Dither Pattern	Scale	Max dither (pixels from (0,0))	Median dither separation (pixels)	Sub-pixel dither pattern
Cycling	Small	11	10.5	½ pixel
	Medium	119	53	½ pixel
	Large	161	97	½ pixel
5-point random	Small	26	23	½ pixel
	Medium	52	46	½ pixel
	Large	105	92	½ pixel
9-point random	Small	16	14	1/3 pixel
	Medium	34	28	1/3 pixel
	Large	69	59	1/3 pixel
12-point Reuleaux	Small	13	15	½ pixel
	Medium	27	30	½ pixel
	Large	55	59	½ pixel
16-point spiral	Small	16	12	¼ pixel
	Medium	32	23	¼ pixel
	Large	64	45	¼ pixel
36-point Reuleaux	Small	17	19	¼ pixel
	Medium	34	39	¼ pixel
	Large	67	78	¼ pixel

Each of the IRAC dither patterns is available in three sizes, large (default), medium, and small. For most of the patterns, the scaling of the large, medium, and small patterns is approximately in the ratio 4:2:1. Exceptions are the small cycling pattern, which is about 1/5 of the size of the large cycling pattern and has

a lower-weighted inner region to reduce the numbers of small separation dithers, and the 4-point subarray pattern where the scaling is 4:3:1.5. For all the patterns, the sub-pixel dithering is maintained, independent of scale.

Sub-pixel dithering, combined with the drizzle technique *(Fruchter & Hook 2002, [11])* to reconstruct the images, can improve the sampling of the mosaics that are obtained from IRAC (or any other) observations. Such strategies have been used for the WFPC2, NICMOS, ACS and WFC3 instruments on the HST for some time (for details see the HST MultiDrizzle Handbook). Dithering is also needed to calibrate intra-pixel sensitivity variations, and needed for programs requiring accurate photometry and astrometry *(Anderson & King 2000, [2])*. To be effective, however, accurate pointing and low image distortion are required. The offsetting accuracy of Spitzer is in the range 0.1"–0.4". This, combined with the image distortion in the IRAC arrays, places a limit of about ¼ pixel on the sub-sampling that is likely to prove useful in practice. For example, the distortion of the IRAC camera is < 1% (see Figure 2.5). Thus for the largest dither patterns, which typically offset up to ±64 pixels from the starting point, the offsets will be up to ±0.6 pixels from the nominal values. Thus only in the small scale patterns, where the offsets are less than ±16 pixels, will the sub-pixel sampling work well, though even on the larger scales some improvement of the images will probably be noticeable.
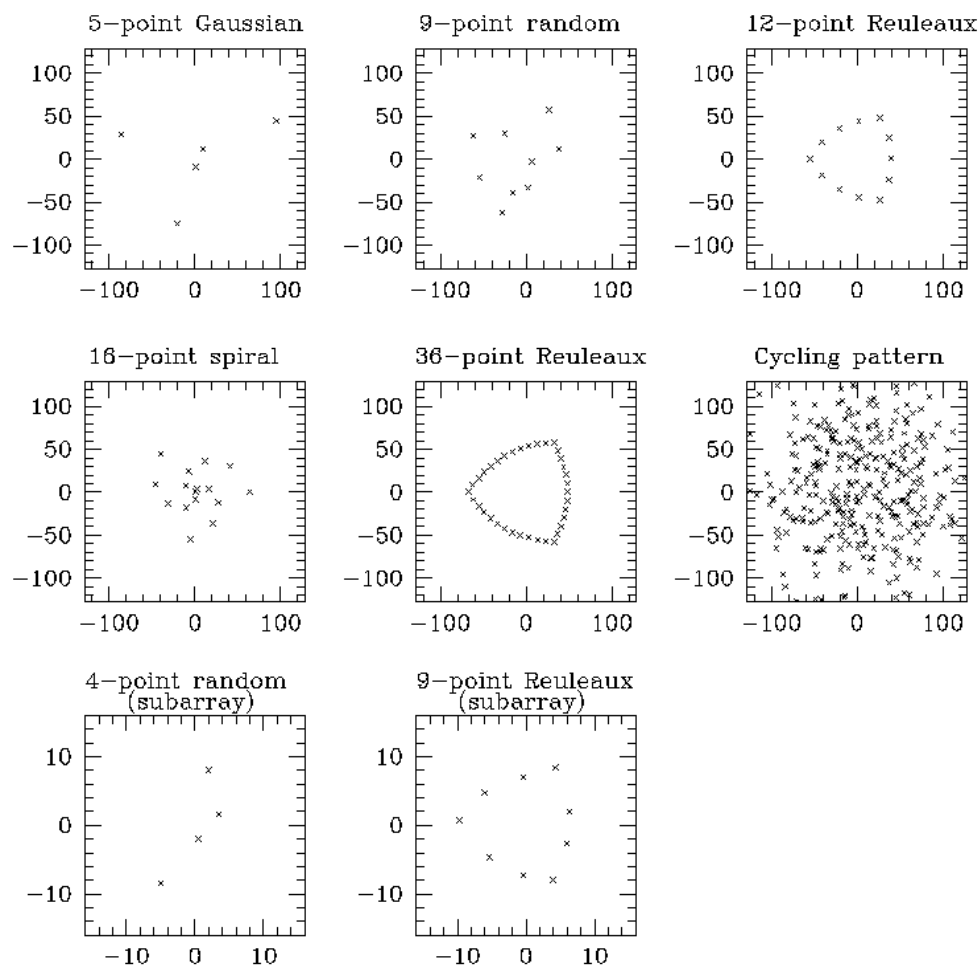
Figure 3.1 : IRAC dither patterns for the "large" scale factor.
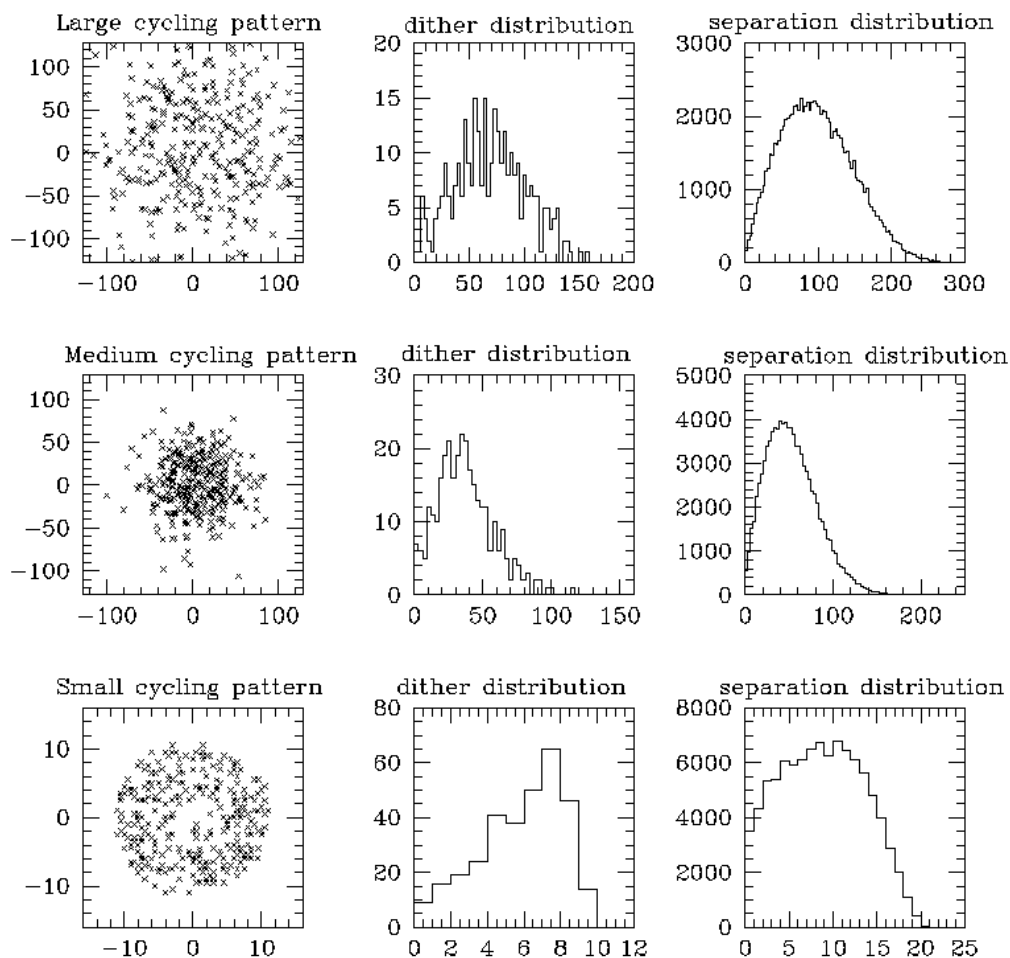
Figure 3.2: Characteristics of the cycling dither pattern, in pixels.

4 Calibration

The Spitzer Science Center (SSC) performs routine calibrations of IRAC using observations of standard stars and other astronomical objects. The data obtained in these observations are used to construct the necessary calibration inputs to the pipeline for the IRAC data processing of science observations. The calibration data files are available to the general user in the Spitzer Heritage Archive maintained by IRSA.

4.1 Darks

Dark current and bias offsets are calibrated via the standard ground-based technique of dark subtraction. As part of routine operations, the SSC observes a dark region of the sky (skydark) near the north ecliptic pole at least twice per campaign (at the beginning and end). These data are reduced and combined in such a way as to reject stars and other astronomical objects with size-scales smaller than the IRAC array. The resulting image (Figure 4.1) of the minimal uniform sky background contains both the bias and dark current. When subtracted from the routine science data, this eliminates both of these instrumental signatures. Naturally, this also subtracts a component of the true celestial background. The SSC includes a COBE-based model estimate of the true celestial background. Note that the lack of an isolated measurement of the dark current and bias offset during shutterless operations limits the ability of IRAC to measure the true celestial background.
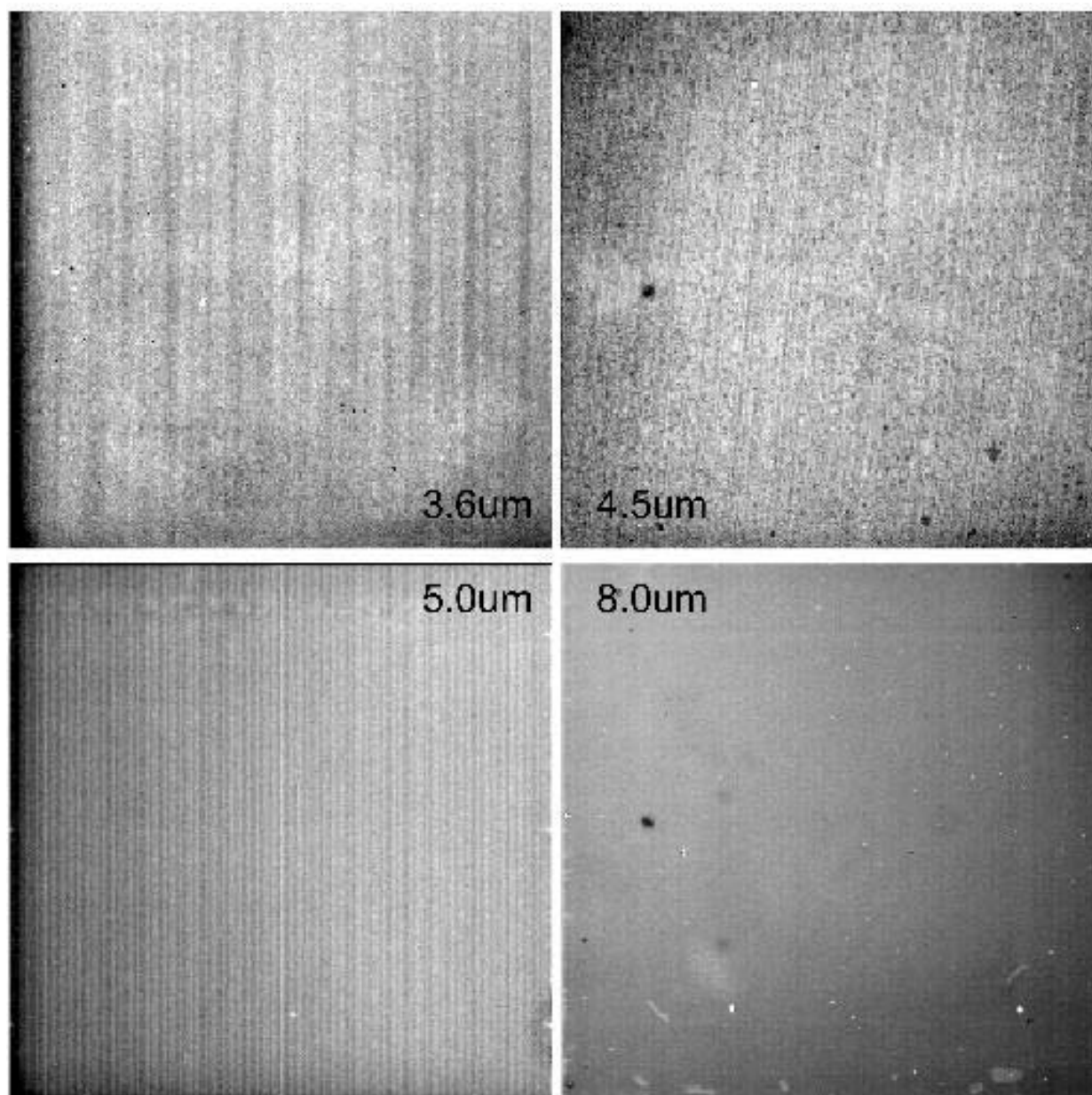
Figure 4.1: IRAC instrument dark current images. These measurements were made during a normal campaign producing a skydark with an exposure time of 100 seconds.

4.2 Flat Fields

Pixel-to-pixel relative gain variations are commonly know as the "flatfield". To get the most accurate measurement of the flatfield, including the effects of the telescope and the IRAC pickoff mirrors, one must use observations of the sky. Because the IRAC detectors are relatively large, there are few discrete astronomical objects large enough and bright enough to fill the detector field of view.

The flatfield was derived from many dithered observations of a network of 22 high zodiacal background regions of the sky in the ecliptic plane, which ensured a relatively uniform illumination with sufficient flux on all pixels such that the observations were relatively quick to perform. One such region was observed in every instrument campaign.

The data were combined with object identification and outlier rejection, creating an object-free image of the uniform celestial background, further smoothed by the dither pattern. An identical observation made at the north ecliptic pole (the "skydark") was subtracted, and the result normalized to create the flatfield. The resulting flatfield was divided into the science data. Pixel-to-pixel accuracy of the flat-fielding derived from a single observing campaign was typically 2.4%, 1.2%, 1.0%, and 0.3%, 1σ, for channels 1 through 4, respectively.

Analysis of the flatfield response on a campaign-wide basis showed that there were no changes throughout the cryogenic or warm missions. Based on this, all of the flatfield data were combined into a "superskyflat". The 1-sigma pixel-to-pixel accuracy of this cryogenic (warm) superskyflat flat is 0.14% (0.17%), 0.09% (0.09%), 0.07%, and 0.01% in channels 1–4, respectively. This is the flatfield used for all pipeline processed data. The superskyflats are available from the "IRAC calibration and analysis files" section of the archival documentation website.

Users should note that the flatfield data were generated from the zodiacal background, and are appropriate for objects with that color. There is a significant color term, of order 5%−10%, for objects with a Rayleigh-Jeans spectrum in the mid-infrared (such as stars); see Section 4.5 for more information. Note that for deep survey observations and other data sets with a large number of frames and a good dithering strategy, the system gain can be determined by the actual survey frames themselves, rather than using the standard set of dedicated observations of some other part of the sky.

During warm operations the flatfield was remeasured. While it is similar in overall appearance, details are sufficiently different that the warm and cold flats cannot be interchanged.
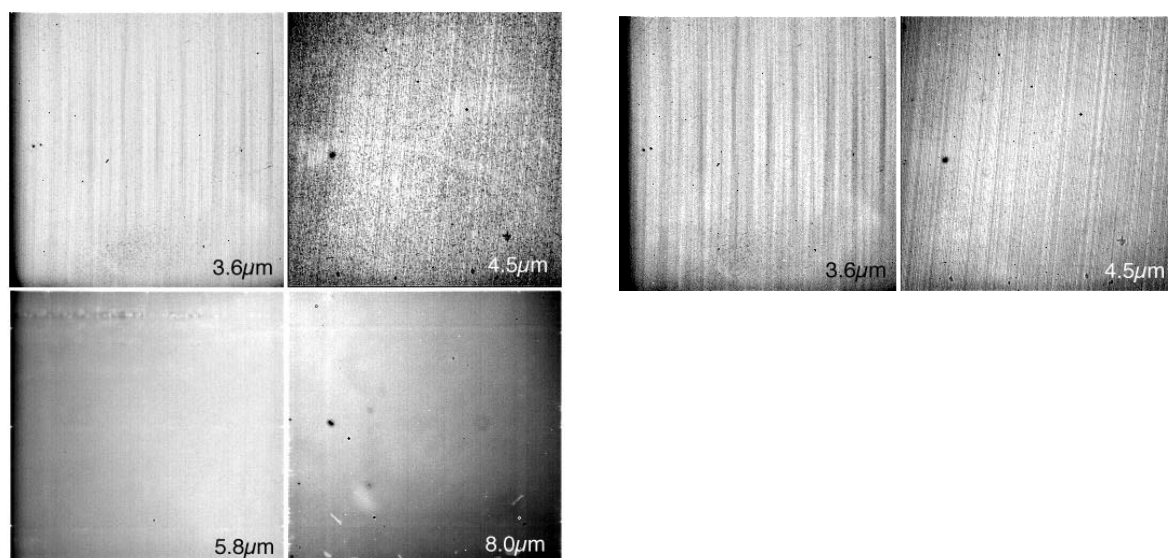
Figure 4.2: IRAC instrument cryogenic mission (left) and warm mission (right) super skyflats showing the flatfield response as measured onboard, for channels 1–4 in cryogenic mission, and channels 1–2 in warm mission.

.

4.3 Photometric Calibration

A number of astronomical standard stars were observed in each instrument campaign to obtain a valid absolute flux calibration. Stars with a range of fluxes were observed at a number of positions across the array and many times throughout the mission to monitor any changes that may have occurred. Calibration stars with measured spectral types and accurate absolutely calibrated fluxes in the IRAC bands have been determined. These absolute calibration stars were in the continuous viewing zone (CVZ) so that they could be observed at any time necessary and could be monitored throughout the mission.

Four stars were observed in the CVZ at the beginning and end of each instrument campaign. These standards remained the same throughout the cryogenic mission, and provide the absolute flux reference for IRAC. Additionally, a calibrator near the ecliptic plane (which was different for each campaign) was observed every twelve hours. Its placement in the ecliptic plane minimized telescope slews. This calibrator was used to monitor any short-term variation in the photometric stability.

Analysis of the flux calibrator data indicates that absolute flux calibration is accurate to 3% (reflecting mostly the uncertainty in the models). Repeatability of measurements of individual stars is better than 1.5% (dispersion), and can be as good as 0.01% with very careful observation design *(e.g., Charbonneau et al. 2005, [6])*. The absolute calibration is derived taking several systematic effects into account. The steps are described in detail by *Reach et al. (2005, [24])*. If this methodology is not applied, then point source photometry from the Level 1 products (BCDs) can be in error by up to 10%.

IRAC is calibrated using both so-called primary and secondary calibrator stars. The primary stars are used to monitor long-term variations in the absolute calibration. They number 11 stars, are located in the continuous viewing zone (CVZ), and were thus observable year-round. They were observed once at the beginning, and once at the end of each campaign, i.e., about every 10 days whenever the instrument was switched on in the cryogenic mission. The primary calibration stars are observed at the beginning of every two-week campaign in the warm mission. The primary calibrators (in decreasing brightness) are (J2000; with flux densities in mJy in channels 1–4, respectively):

NPM1+67.0536 = SAO 17718 = 2MASS J17585466+6747368 (K2III, Ks=6.4); 843.6, 482.3, 320.0, 185.3

HD 165459 = 2MASS J18023073+5837381 (A1V, Ks=6.6); 647.7, 421.3, 268.6, 148.1

NPM1+68.0422 = BD+68 1022 = 2MASS J18471980+6816448 (K2III, Ks=6.8); 580.4, 335.5, 223.2, 128.9

KF09T1 = GSC 04212-01074 = 2MASS J17592304+6602561 (K0III, Ks=8.1); 169.9, 104.7, 67.03, 38.75

NPM1+66.0578 = GSC 04229-01455 = 2MASS J19253220+6647381 (K1III, Ks=8.3); 140.9, 82.37, 54.54, 29.72

NPM1+64.0581 = HD 180609 = 2MASS J19124720+6410373 (A0V, Ks=9.1); 63.00, 41.02, 26.18, 14.40

NPM1+60.0581 = BD+60 1753 = 2MASS J17245227+6025508 (A1V, Ks=9.6); 38.21, 24.74, 15.74, 8.699

KF06T1 = 2MASS J17575849+6652293 (K1.5III, Ks=11.0); 13.92, 7.801, 5.339, 3.089

KF08T3 = 2MASS J17551622+6610116 (K0.5III, Ks=11.1); 11.77, 7.247, 4.642, 2.691

KF06T2 = 2MASS J17583798+6646522 (K1.5III, Ks=11.3); 10.53, 5.989, 4.050, 2.339

2MASS J18120956+6329423 (A3V, Ks=11.6) ; 8.681, 5.662, 3.620, 2.000

All of the calibration data taken with these stars are public and are available in the Spitzer Heritage Archive. The secondary calibrator stars were used to monitor short-term variations in the absolute calibration. To avoid slew overheads, they were observed close to downlinks and therefore had to be located near the ecliptic plane, in a tightly constrained window of about 20 degrees. Because of the motion of the Earth about the Sun this window constantly moved and so any one secondary calibrator was visible for only a campaign or two per year. In practice, the calibration values for IRAC appear to be quite temporally stable.

The data are calibrated by means of aperture photometry, using a 10 native pixel radius (~ 12 arcseconds) aperture. The background was measured using a robust average in a 12–20 native pixel annulus around the centroid of the star. Unfortunately, ground-based infrared calibrators were too bright to use as calibrators for IRAC. Therefore, one must use models to predict the actual flux for each channel as a function of spectral type *(Cohen et al. 2003, [7])*. Table 4.1 lists the calibration factors that are used in the final processing of all IRAC data. The absolute calibration is described in detail in *Reach et al. (2005,*

[24]), with further refinements at the 1%–3% level, based on better models for the calibration stars and a better estimate of the corrections to photometry (pixel phase, array-location dependent photometric correction, etc.).

Table 4.1: The photometric calibration and zero magnitude flux for IRAC. Values in parentheses are for warm mission.

λ (μm)	FLUXCONV (MJy/sr)/(DN/sec)	$F_{\nu 0}$ (Jy)
3.6	0.1088/01253	280.9±4.1
4.5	0.1388/0.1469	179.7±2.6
5.8	0.5952	115.0±1.7
8.0	0.2021	64.9±0.9

The absolute gain calibration is accurate to better than 3%. The stellar photometry is repeatable at the < 1% level. The absolute fluxes of the calibration stars are known to 2% – 3% *(Cohen et al. 2003, [7])*. To obtain photometry at this accuracy, photometric corrections for the location of the source within its peak pixel, and the location of the source within the array, must be made.

Note that IRAC is not an absolute background photometer, so the total brightness in IRAC images should be used with great caution. There was a cold shutter in the calibration assembly, but it was not operated in flight, in order to minimize mission risk. Therefore, the offset level in IRAC images is referred to laboratory measurements before launch, where the offset level was observed to change very significantly from one laboratory experiment to another.

In laboratory tests, the absolute offset of IRAC images was found to vary at levels that are comparable to the minimum celestial background in channels 1 and 2. Furthermore, the offset level changes depending on whether the detector was recently annealed. Thus, for diffuse surface brightness measurements, we recommend making differential measurements among at least two sky positions, preferably from the same campaign.

4.4 Color Correction

IRAC is a broad-band photometer. We describe here the method used for calibrating our data in specific surface brightness (MJy/sr) or flux density (Jy) units, and we provide the prescription for how to interpret the data for sources with spectral shapes other than the nominal one assumed in the calibration process.

The conventions used by IRAC are the same as those used by IRAS *(Beichman et al. 1988, IRAS Explanatory Supplement, §VI.C.3, [4])*, COBE/DIRBE *(Hauser et al. 1998, [12])*, and ISO *(Blommaert et al. 2003, [5])*. The basic idea is to quote a flux density $F_{\nu_0}^{quot}$ at a nominal wavelength $\lambda_0 = c/\nu_0$ that

would be accurate for a source with a nominal spectrum, νF_ν^{nom} =constant. Using this F_ν^{nom} is merely a matter of convention; in fact a wide range of spectra are expected, both redder (e.g., interstellar medium, asteroids) and bluer (e.g., stars) than nominal. The color correction tables given below allow observers to convert the nominally-calibrated data, $F_{\nu_0}^{quot}$ into more accurate estimates of the flux density at the nominal wavelength.

The number of electrons collected from the nominal source in a straight integration of duration t using a telescope with area A is

$$N_e^{nom} = tA \int \frac{F_\nu^{nom}}{h\nu} R d\nu; \tag{4.1}$$

where R is the system spectral response. The convention for R is that it is proportional to the number of electrons produced by a single photon with energy hν. If we define for convenience

$$\Delta\nu = \int (\nu/\nu_0)^{-2} R d\nu \tag{4.2}$$

then the number of electrons collected from a source with the nominal spectrum is

$$N_e^{nom} = tA \frac{F_{\nu_0}^{nom}}{h\nu_0} \Delta\nu \tag{4.3}$$

The calibration factor, by which the number of electrons, N_e from an arbitrary source must be divided in order to give the quoted flux density at the nominal wavelength, is

$$C = \frac{N_e^{nom}}{F_{\nu_0}^{nom}} = \frac{At\Delta\nu}{h\nu_0} \tag{4.4}$$

The calibration factor is measured using observations of a celestial calibrator source of known spectrum, F_ν^*. The number of electrons collected from the star is

$$N_e^* = tA \int \frac{F_\nu^*}{h\nu} R d\nu \qquad (4.5)$$

Combining with equation 4.4, we can express the calibration factor in terms of the observed number of electrons from the calibration source:

$$C = \frac{N_e^* \Delta \nu}{h\nu_0 \int \frac{F_\nu^*}{h\nu} R d\nu} \qquad (4.6)$$

We can now cast this in convenient terms as follows:

$$C = \frac{N_e^*}{F_{\nu_0}^* K^*} \qquad (4.7)$$

where $F_{\nu_0}^*$ is the flux density of the calibration source at the nominal wavelength, and K^* is the color correction factor for the calibration source spectrum.

The color correction factor for a source with spectrum F_ν is defined as:

$$K = \frac{\int (F_\nu / F_{\nu_0})(\nu / \nu_0)^{-1} R d\nu}{\int (\nu / \nu_0)^{-2} R d\nu} \qquad (4.8)$$

In this convention, the overall normalization of R is unimportant. Observers can correct the photometry to the spectrum of their source by either performing the integral in this equation or looking up the color corrections for sources with similar spectra. Note that our definition of the color correction looks slightly different from that in the *IRAS Explanatory Supplement [4]*, because we used the system spectral response R in electrons/photon, instead of ergs/photon.

We selected nominal wavelengths that minimize the need for color corrections, such that the quoted flux densities in IRAC data products are minimally sensitive to the true shape of the source spectrum. (This paragraph can be skipped by most readers; the table is given below.) First, let us expand the source spectrum in a Taylor series about the nominal wavelength:

$$F_\nu = F_{\nu_0}\left[1 + \beta\left(\frac{\lambda - \lambda_0}{\lambda_0}\right) + ...\right]$$ (4.9)

Using equation 4.8, the color correction for a source with spectrum F_ν is

$$K = \frac{1}{\Delta\nu}\int\left[1 + \beta\left(\frac{\lambda - \lambda_0}{\lambda_0}\right)\right](\nu/\nu_0)^{-1}Rd\nu$$ (4.10)

The choice of λ_0 that makes K minimally sensitive to β is the one for which

$$\frac{dK}{d\beta} = 0.$$

Solving for λ_0 we get

$$\lambda_0 = <\lambda> = \frac{\int\lambda(\nu/\nu_0)^{-1}Rd\nu}{\int(\nu/\nu_0)^{-1}Rd\nu} = C\frac{\int\nu^{-2}Rd\nu}{\int\nu^{-1}Rd\nu}$$ (4.11)

So the optimum choice of λ_0 for insensitivity to spectral slope is the weighted average wavelength. Using the nominal wavelengths from Table 4.2, the color corrections for a wide range of spectral shapes are less than 3%. Thus, when comparing IRAC fluxes to a theoretical model, placing the data points on the wavelength axis at λ_0 takes care of most of the potential color-dependence. To place the data points more accurately on the flux density axis, take the quoted flux densities derived from the images, and divide by the appropriate color correction factor in the tables below:

$$F_{\nu_0} = \frac{F_{\nu_0}^{quot}}{K}$$ (4.12)

Or, calculate the color correction using equation 4.8 together with the spectral response tables, which are available in the IRAC section of the documentation website.

Table 4.2: IRAC nominal wavelengths and bandwidths.

Channel	λ_0 (μm)	R_{max}	Eff. Width $\Delta\nu$ (Eq. 4.2; 10^{12} Hz)	Width $\Delta\nu / R_{max}$ (10^{12} Hz)	½-power wavelengths (μm) blue	red
1	3.550	0.651	7.57	16.23	3.18	3.92
2	4.493	0.736	6.93	12.95	4.00	5.02
3	5.731	0.285	1.93	11.70	5.02	6.43
4	7.872	0.428	3.94	12.23	6.45	9.33

Table 4.3 shows the color corrections for sources with power-law spectra, $F_\nu \propto \nu^\alpha$, and Table 4.4 shows the color corrections for blackbody spectra with a range of temperatures. The nominal spectrum has $\alpha = -1$, so the color corrections are unity by definition in that column. These calculations are accurate to ~ 1%. Note that the color corrections for a ν^{-1} and a ν^0 spectrum are always unity. This is in fact a theorem that is easily proven using equations 4.8 and 4.11.

Table 4.3: Color corrections for power-law spectra, $F_\nu \propto \nu^\alpha$

	Color correction for $\alpha =$				
Band	-2	-1	0	1	2
1	1.0037	1	1	1.0037	1.0111
2	1.0040	1	1	1.0040	1.0121
3	1.0052	1	1	1.0052	1.0155
4	1.0111	1	1	1.0113	1.0337

Table 4.4: Color corrections for blackbody spectra.

	Temperature (K)							
Channel	5000	2000	1500	1000	800	600	400	200
1	1.0063	0.9990	0.9959	0.9933	0.9953	1.0068	1.0614	1.5138
2	1.0080	1.0015	0.9983	0.9938	0.9927	0.9961	1.0240	1.2929
3	1.0114	1.0048	1.0012	0.9952	0.9921	0.9907	1.0042	1.1717
4	1.0269	1.0163	1.0112	1.0001	0.9928	0.9839	0.9818	1.1215

Table 4.5 gives the color corrections for the spectrum of the zodiacal light, which is the dominant diffuse background in the IRAC wavelength range. The first model is the COBE/DIRBE zodiacal light model as implemented in Spot. The zodiacal light is mostly due to thermal emission from grains at ~ 260 K over the IRAC wavelength range, except in channel 1 where scattering contributes ~ 50% of the brightness. The second zodiacal light spectrum in Table 4.5 is the ISOCAM CVF spectrum (5.6–15.9 μm; *Reach et al. 2003, [23]*) spliced with the COBE/DIRBE model at shorter wavelengths.

Table 4.5: Color corrections for zodiacal light spectrum.

Band	COBE/DIRBE model			ISOCAM+COBE/DIRBE		
	$I_{\nu_0} (MJy / sr)$	K	$I_{\nu_0}^{quot}$	$I_{\nu_0} (MJy / sr)$	K	$I_{\nu_0}^{quot}$
1	0.067	1.0355	0.069	0.40	1.0355	0.42
2	0.24	1.0835	0.26	1.44	1.0835	1.56
3	1.11	1.0518	1.16	6.64	1.0588	7.00
4	5.05	1.0135	5.12	25.9	1.0931	28.4

For sources with complicated spectral shape the color corrections can be significantly different from unity. The corrections are infinite in the case of a spectrum dominated by narrow lines, because there may be no flux precisely at the nominal wavelength, which only demonstrates that such sources should be treated differently from continuum-dominated sources. We calculated one illustrative example which may prove useful. The ISO SWS spectrum of NGC 7023 is dominated by PAH emission bands and a faint continuum over the IRAC wavelength range. Table 4.6 shows the color corrections using equation 4.8 and the ISO spectrum. The large value in channel 1 is due to the presence of the 3.28 μm PAH band, which dominates the in-band flux relative to the weak continuum at the nominal wavelength of 3.550 μm. Channel 2 is mostly continuum. Then channel 3 is dominated by a PAH band at 6.2 μm. Channel 4 has significant PAH band emission throughout, with prominent peaks at 7.7 and 8.6 μm. The values in this table can be used for comparison to IRAC colors of other sources by anti-color-correction, which gives the predicted colors for NGC 7023 in the same units as the SSC calibrated data: $F_{\nu_0}^{quot} = F_{\nu_0} \times K$, which is shown in the last column of Table 4.6. Thus, PAH-dominated sources are expected to have

$$F_{\nu_0}^{quot} (8\mu m) / F_{\nu_0}^{quot} (5.8\mu m) = 599 / 237 = 2.5 \quad\quad (4.13)$$

.

Table 4.6: Color corrections for NGC 7023 (PAH-dominated) spectrum.

Band	F_{ν_0}	K	$F_{\nu_0}^{quot}$
1	17.3	2.21	38.3
2	30.3	1.21	36.6
3	169	1.40	237
4	1021	0.59	599

For observations of sources dominated by spectral lines, the quoted flux densities should be converted into fluxes using

$$F = \frac{F_{\nu_0}^{quot} \Delta \nu \lambda_0}{R_l \lambda}$$

(4.14)

where λ is the wavelength of the spectral feature and R_l is the spectral response at that wavelength. Both λ_0 and effective width $\Delta \nu$ are in Table 4.2. The formalism used for continuum sources is inappropriate for spectral-line sources because it is likely that F_{ν_0} and $K = \infty$. It is important that the normalization of R used to determine $\Delta \nu$ and R_l is the same. In Table 4.2, the column $\Delta \nu$ (effective width) was calculated with the same normalization of response function as on the documentation website so it is the appropriate one to use. The maximum response, R_{max} is also given in that table, so the fluxes of lines in heart of the waveband can be estimated by simply multiplying the quoted flux densities by $\Delta \nu / R_{max}$, which is listed in the table in the column "Width."

4.5 Array Location-Dependent Photometric Corrections for Compact Sources with Stellar Spectral Slopes

Point source photometry requires an additional correction that arises from the way in which the data are flat fielded. Flat-fielding is a way of removing pixel-to-pixel gain variations. The IRAC flatfield is derived by imaging the high surface brightness zodiacal background. The way the IRAC flatfield is derived has a few consequences on making photometrical measurements using IRAC data.

First, the zodiacal background is extended and essentially uniform over the 5.2 arcmin x 5.2' arcmin IRAC field of view. The vast majority of objects seen by IRAC are not like this. Many are compact, being either stars or background galaxies. IRAC has significant scattering as well as distortion. As a result, the extended source effective gain is slightly different from the point source effective gain. IRAC point source photometry then requires a correction for the effective gain change between extended and point sources.

Second, the spectrum of the zodiacal background peaks redward of the IRAC filters. The vast majority of objects seen by IRAC are not like this. Many have spectral energy distributions in the IRAC filters more closely resembling stars. Stars (and many galaxies) have color temperatures that are fairly high, and peak blueward of the IRAC filters. Generally speaking, for these objects the IRAC filters are well on the Rayleigh-Jeans side of the blackbody spectrum. IRAC photometry of warmer sources then requires a correction for the spectral slope change between the zodiacal light and Rayleigh-Jeans spectra.

Lastly, there is a variation in the effective filter bandpass of IRAC as a function of angle of incidence, which in turn depends on the exact position of an object on the array *(Quijada et al. 2004, [22])*. As a

result of this, all objects in the IRAC field of view need to be corrected based on their location on the array.

All three of these effects can be directly measured and a correction derived. Stars (Rayleigh-Jeans, point sources) were sampled at many different locations on the array, and their flux was measured from the (C)BCD images (see Chapter 6 for the definition of the various types of data, including BCD and CBCD). The systematic variations in their measured fluxes were used to derive the corrections. The amplitude of this effect is sizeable. It may reach 10% peak-to-peak, depending on the detector array. This is larger than any other source of uncertainty in IRAC calibration. For well-dithered data, experiments have shown that this effect tends to average out so that the amplitude of the effect is very small (less than 1%). However, depending on the exact details of mapping and dithering, it is not uncommon to have small areas of data where the mean correction approaches the full 10%.

Correction images may be downloaded from IRAC instrument web pages. Note that the correction images for the cryogenic mission and the warm mission are different and users should use the appropriate mission corrections. Note the following:
• The correction images are oriented so that they apply multiplicatively to the (C)BCD images. Among other things, the channel 1 and 2 arrays are flipped around their vertical axis during the reduction by the BCD pipeline, hence these images cannot be directly applied to the raw data.
• The correction images are for compact, or point-like sources.
• The correction images are for a Rayleigh-Jeans (stellar, Vega-like) spectrum. Spectral indices differing from this will have different corrections. Generally, most IRAC objects have spectral slopes that are bracketed by the two extremes of the red zodiacal spectrum and the blue stellar spectrum, so the corrections will lie between zero and that in the correction image.
• Note that the existing flatfield flattens the zodiacal background. After correction, although the point sources may be correctly measured, the background will no longer be flat.

To apply the correction from these images to photometry on a single (C)BCD image, a) perform photometry on your (C)BCD image, b) measure the value from the correction images at the central pixel of your target for which you are performing photometry, c) multiply your photometrical flux measurement by the measured correction value for the central pixel of your target to obtain a corrected flux density value. To apply the correction from these images to photometrical measurements made on a mosaic image, you will need to first mosaic the correction images in the same way as the science images. Making the correction mosaic is now possible using the MOPEX tool. MOPEX can be found at http://irsa.ipac.caltech.edu/data/SPITZER/docs/dataanalysistools/tools/mopex/. You can also use the IDL script at http://irsa.ipac.caltech.edu/data/SPITZER/docs/files/spitzer/copy_photcorr_posns.pro
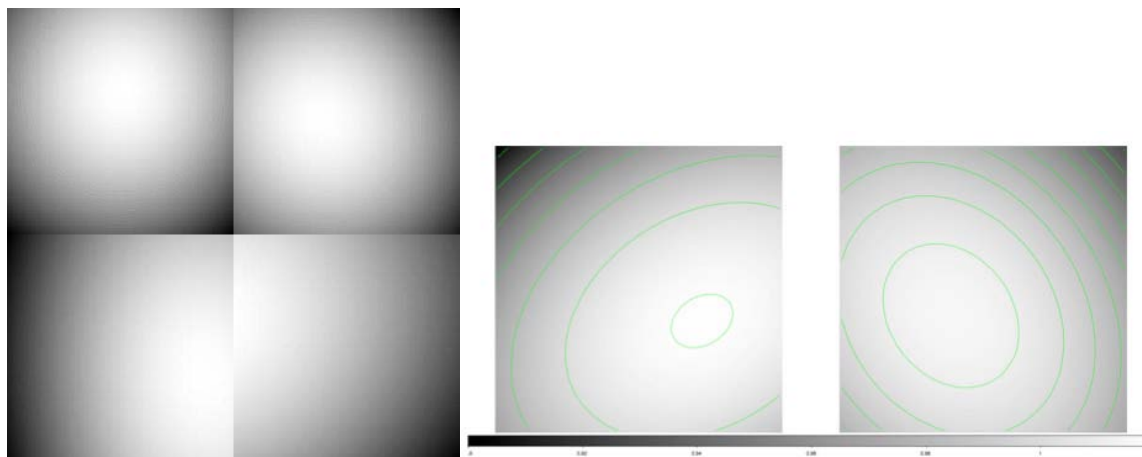
Figure 4.3. Array location-dependent photometric correction images. Cryogenic mission corrections are on the left, warm mission corrections on the right. In the cryogenic mission correction image, ch 1 is in the upper left, ch 2 in the upper right, ch 3 in the lower left and channel 4 in the lower right. In the warm mission correction image, ch 1 is on the left, ch 2 on the right.

A note on correction image filenames: The filenames for the cryogenic mission are in the pattern *ch[1–4]_photcorr_rj.fits* where "rj" means "Rayleigh-Jeans" and for the warm mission *ch[1–2]_photcorr_ap_5.fits*.

.

4.6   Pixel Phase-Dependent Photometric Correction for Point Sources

The flux density of a point source measured from an IRAC image depends on the exact location where the peak of the Point Spread Function (PSF) falls on a pixel. This effect is due to the variations in the quantum efficiency across a pixel, combined with the undersampling of the PSF. It is most severe in channel 1, partly due to the smallest (among IRAC channels) PSF angular size. The correction for this effect can be as much as 4% peak to peak. Early in the cryogenic mission, the point source aperture flux was fit with a radial function in pixel phase (Reach et al. 2005; [24]). Later, Mighell et al. (2008; [21]) found that the intra-pixel gain variation is better described by a two-dimensional function of (x,y) pixel phase, primarly because the peak of the response is not at the center of an IRAC Channel 1 pixel. The effect is graphically shown in Figure 4.4. These images are subsampled in 0.01 pixel increments, starting at -0.5 and ending at +0.5 (in both x_{phase} and y_{phase}), and may be interpolated to the phase of a given stellar centroid and multiplied by the measured aperture flux. Correction images (the inverse of the response) that can be applied (multiplied) to the data can be downloaded in FITS format from the Spitzer documentaton website at http://irsa.ipac.caltech.edu/data/SPITZER/docs/irac/.

Pixel Phase Response
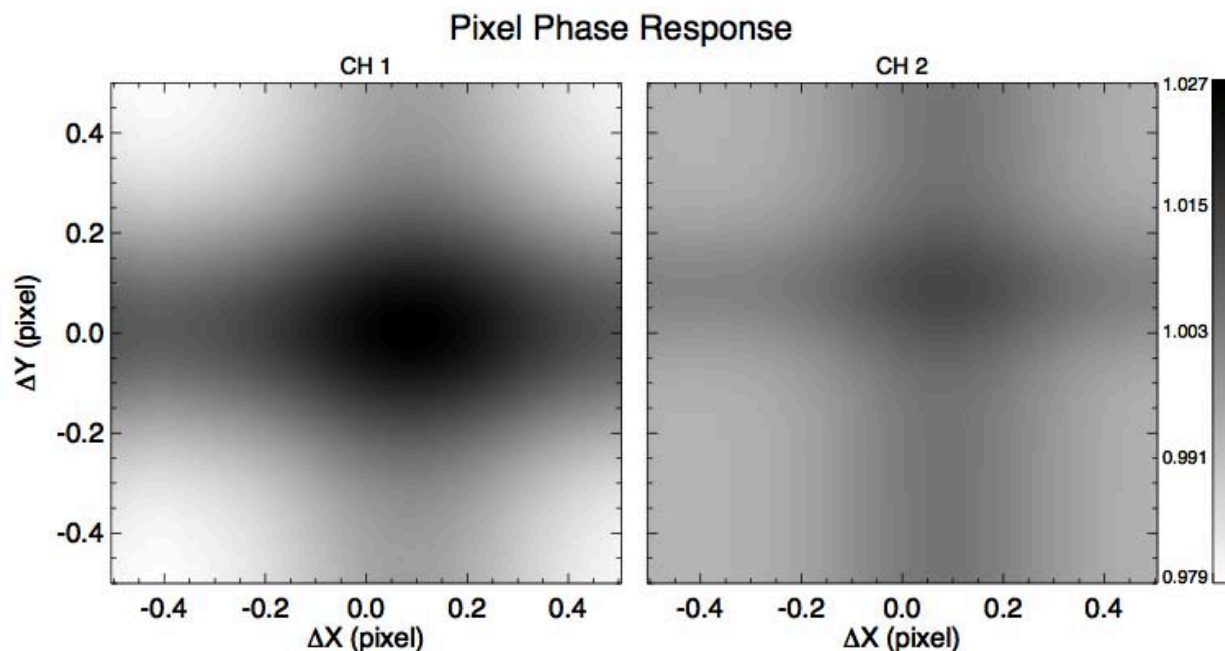
Figure 4.4: IRAC cryogenic pixel response model, showing intra-pixel gain variations as a function of pixel phase. Only channel 1 (3.6 μm) and channel 2 (4.5 μm) have significant variation.

At the beginning of the warm IRAC mission, we found that the pixel phase response peak-to-peak variation increased by a factor of about 2 in both channels 1 and 2. The larger dynamic range enabled us to model the intra-pixel gain in terms of the sum of gaussian functions in measured (x_{phase}, y_{phase}). See the warm IRAC documentation at http://irsa.ipac.caltech.edu/data/SPITZER/docs/irac/calibrationfiles/pixelphase/ for more details. See also the IDL code in the Contributed Spitzer software about performing a simultaneous pixel phase and array location-dependent photometric correction to the observed fluxes (cryogenic mission only).

4.7 IRAC Point Spread and Point Response Functions

Figure 4.5 shows the IRAC point response functions (PRF) reconstructed from images of a bright star obtained during IOC/SV. Here we use the language common in the optics field; the point spread function [PSF] is before sampling by the detector array, and the point response function [PRF] is after sampling by the detector array. The cryogenic PRFs in Figure 4.5, which are undersampled at the IRAC pixel scale, were generated by combining 108 individual IRAC images in each band. By offsetting each image by a fraction of a pixel width, fully sampled PRFs can be extracted from the data. The resulting PRFs are the optical point spread function projected onto the focal plane by the IRAC and telescope optics, convolved with the response function of a single detector pixel. The images were combined using a drizzle algorithm *(Fruchter & Hook 2002, [11])* to minimize smoothing of the PRF during the reconstruction process. The resulting pixel scale was ¼ the width of an IRAC pixel. Images of a bright star at the native IRAC pixel scale are also displayed for comparison.

FITS files of the IRAC PRFs are available in the IRAC section of the website at http://irsa.ipac.caltech.edu/data/SPITZER/docs/irac/calibrationfiles/psfprf/. The appropriateness of a given PRF is dependent on the observation sampling and the photometric reduction package used.
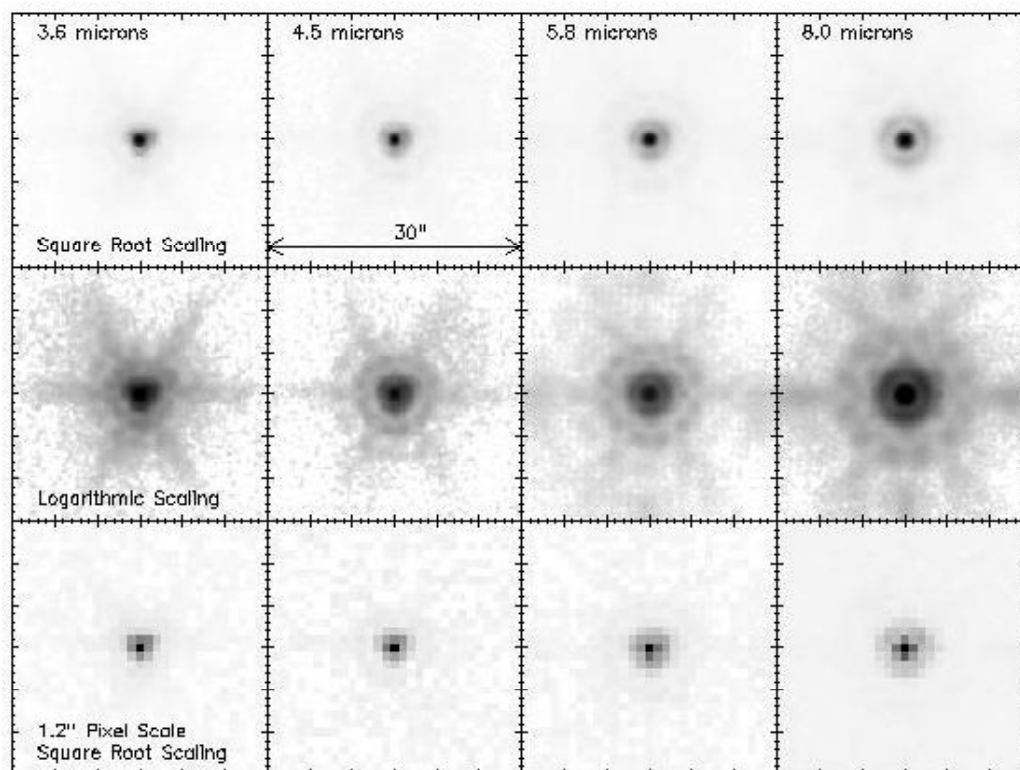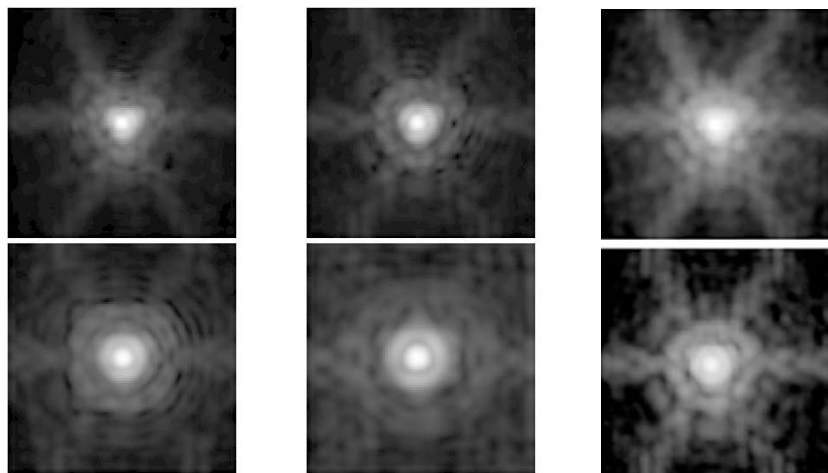
Figure 4.5. The in-flight IRAC cryogenic point response functions (PRFs) at 3.6, 4.5, 5.8 and 8 microns. The PRFs were reconstructed onto a grid of 0.3" pixels, ¼ the size of the IRAC pixel, using the drizzle algorithm. We display the PRF with both a square root and logarithmic scaling, to emphasize the structure in the core and wings of the PRF, respectively. We also show the PRF as it appears at the IRAC pixel scale of 1.2". The reconstructed images clearly show the first and second Airy rings, with the first Airy ring blending with the core in the 3.6 and 4.5 μm data.

Point source fitting to IRAC data has proven problematic as the PSF is undersampled, and, in channels 1 and 2, there is a significant variation in sensitivity within pixels (Section 4.6). To deal with these problems, we have developed Point Response Functions (PRFs) for IRAC. A PRF is a table (not an image, though for convenience it is stored as a 2D FITS image file) which combines the information on the PSF, the detector sampling and the intrapixel sensitivity variation. By sampling this table at regular intervals corresponding to single detector pixel increments, an estimate of the detector point source response can be obtained for a source centered at any given subpixel positition.

4.7.1 Core PRFs

The FITS files of the core PRFs are linked off the IRAC web pages. These core PRFs can be used for PRF-fitting photometry and source extraction in (C)BCDs for all but the brightest sources. We still recommend performing aperture photometry instead of PRF fitting in all instances except in crowded fields and regions with a strongly varying background, because aperture photometry is much simpler, straightforward and faster to do. In addition, especially in channels 1 and 2, the PSF is undersampled by the native IRAC pixel size, causing further uncertainty to PRF fitting. PRF fitting does not work in image mosaics where the information from the PSFs has been ``scrambled'' together. Aperture photometry is the correct way to perform point source flux density measurements in image mosaics.

The PRFs are provided in two different samplings, 1/5th and 1/100th native pixels. The 1/100th native pixel sampling PRFs have been created by interpolating the 1/5th sampled PRFs onto a finer grid. These PRFs are designed to work with the photometry extraction software APEX. The 1/5th pixel sampling versions are the originally derived versions and are appropriate for use with custom PRF-fitting software, but not APEX. For both versions of sampling, the PRFs are provided for 25 positions in a 5x5 grid upon the array for each channel. The PRFs are normalized such that the flux is unity within 12 arcsecond (10 pixel) radius around each point source with the zero pixel phase instance (centered on a pixel).

Figure 4.6. The IRAC cryogenic point response functions (PRFs) at 3.6 (upper left), 4.5 (middle, top row), 5.8 (left, bottom row) and 8.0 microns (middle, bottom row) and from warm mission at 3.6 (right, upper row) and 4.5 microns (right, bottom row). The PRFs were generated from models refined with in-flight calibration test data involving a bright calibration star observed at several epochs. Central PRFs for each channel are shown above with a logarithmic scaling to help display the entire dynamic range. The PRFs are shown as they appear with 1/5th the native IRAC pixel sampling of 1.2 arcseconds to highlight the core structure. The PRFs were calculated using the Simfit routine in Hoffmann et al. (2004; [14]).

4.7.2 Extended PSFs

The FITS files of the extended PSFs can be obtained using the links in the IRAC web pages. We will first address the cryogenic IRAC extended PSFs and then explain the procedure to generate the warm IRAC PSFs below. In order to gain high signal-to-noise out to the edge of the arrays, PSFs were generated from a combination of on-board calibration and science observations of stars with different brightness, joined together to produce extended high dynamic range (HDR) observational PSFs. These PSFs have two main components: a core HDR PSF created by the observations of a reference star, and the extended region from observations of a set of bright stars that saturated the IRAC array. They can be used to perform source extraction and PSF-fitting photometry of bright, highly saturated stars with extended wings. The core of the extended PSF was generated using the prf_estimate module of MOPEX which has been shown to be inadequate for making high-quality PSFs for IRAC. As a result, the extended PSF should not be used for PSF-fitting photometry and source extraction of non-saturated point sources. Instead, the core PRF in Section 4.7.1 is more appropriate for PSF-fitting photometry. Also, note that the detailed structure of the center of saturated sources fitted using the extended PSF will not be correct in detail.

These extended HDR PSFs have a pixel size of 0.2 IRAC pixels, or ~ 0.24 arcsec. The size of each PSF image is 1281x1281 pixels, covering an area of ~ 5.1 arcmin x 5.1 arcmin. The PSFs are centered within each image. The PSFs are calibrated in MJy/sr. The PSFs represent an unsaturated, very high S/N image of Vega, and the flux density contained within a 10 native IRAC pixel aperture radius (50 HDR PSF pixels), with the sky level estimated in a radial annulus from 12 to 20 native IRAC pixels, is equal to the flux density of Vega. The pedestal level of each image is set to zero in the corners of each PSF.

To produce the core portion of the HDR PSF, 300 HDR observations of a calibration star were obtained during three separate epochs, each observation consisting of short exposures (0.6 sec/1.2 sec) and long exposures (12 sec/30 sec). The HDR PSFs were generated by first combining short-exposure frames and long-exposure frames separately. The short frames enabled the cores to be constructed without a saturation problem, while the long exposures allowed the construction of a higher signal-to-noise PSF in the wings out to 15 arcseconds. The assembly required the replacement of any saturated areas in the long-exposure frames with unsaturated data from the same pixel area of the short-exposure frames. It also required the replacement of a few pixels in the long-exposure frames by the corresponding pixels in the short-exposure frames to mitigate the non-linear bandwidth effect in channels 3 and 4. The "stitching" of the two components of the HDR PSF was completed using a 1/r masking algorithm requiring a percentage of each frame to be added together over a small annulus two IRAC pixels in width just outside the saturated area. Each epoch was treated separately and then all three epochs were aligned and a median was taken to remove background stars.

Observations of the stars Vega, Epsilon Eridani, Fomalhaut, Epsilon Indi and Sirius were used in the construction of the extended portion of the PSF. Each star was observed with a sequence of 12 sec IRAC full frames, using a 12-point Reuleaux dither pattern with repeats to obtain the required total integration time (the stars were typically observed for $20 - 60$ minutes during each epoch). The images were aligned, rescaled to the observation of Vega, and then averaged together with a sigma-clipping algorithm to reject background stars.

The core HDR PSFs were aligned and rescaled to the extended portion of the PSF by matching their overlapping areas. The alignment was done at best to an accuracy of ~ 0.1 arcsec. The rescaling was made by forcing the cores to have the same flux density, that of Vega, within a 10 native IRAC pixel radius aperture. The stitching was made using a mask with a smooth 1/r transition zone, 2.4 arcseconds wide, between the core (contributing where the extended portion PSF data were missing due to saturation cutoff), and the extended portion of the PSF. The merged PSFs were then cropped to a final 5.1 arcmin x 5.1 arcmin size, and a pedestal level was removed in order to have a surface brightness as close as possible to zero in the corners of the images.

The warm mission extended PSFs were determined in a similar way, except that 22 A-M V stars (PID 40976) were used, along with 122 observations of NPM1 +67.0536 from the IRAC calibration observations. The original BCDs were corrected for pin-striping, and residual images were masked. Mosaics of each star were created with IRACproc (Schuster et al. 2006; [25]) on a 0.24 arcsec/pix scale. All pixels above 50% of the saturation level were masked, and the mosaics aligned to a common center (with a typical accuracy ~ 0.03 arcsec) using the diffraction spikes of the images. The pedestal level and normalization levels were then fit by minimizing the chi-squared value of the difference in the binned radial profiles between the observation and the Vega calibration measurement. The aligned and normalized mosaics were averaged with sigma-clipping to remove outliers (background stars, other artifacts) to produce a normalized PSF image. This procedure was repeated for the observations that were not saturated in the core, and the core and extended PSFs were aligned and smoothly merged to produce the final PSF for each channel.

All of the extended PSFs are available at the Spitzer/IRAC Documentation website at http://irsa.ipac.caltech.edu/data/SPITZER/docs/irac/calibrationfiles/psfprf/.
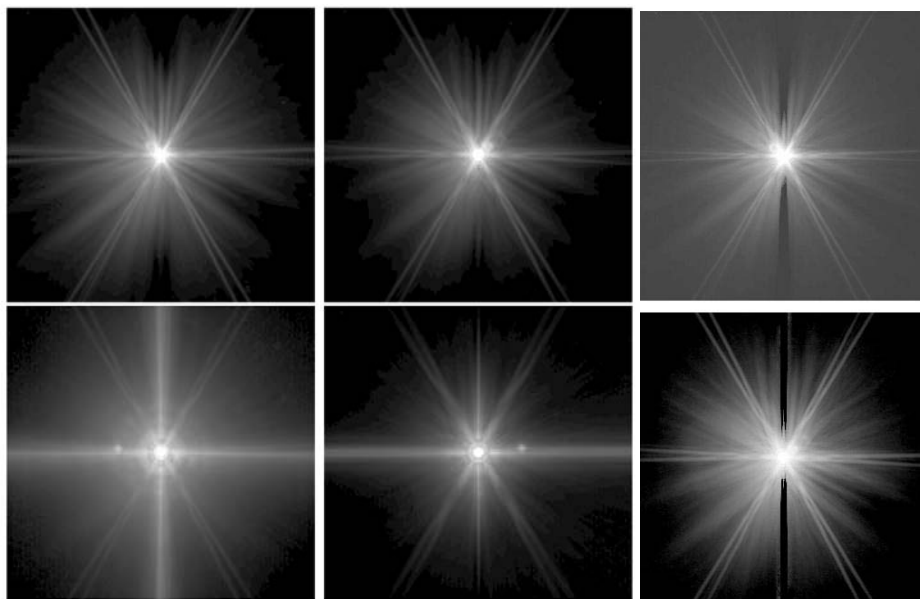
Figure 4.7. The IRAC extended PSFs. The cryogenic PSFs are shown on left, with channel 1 PSF upper left, channel 2 PSF middle (upper row), channel 3 lower left and channel 4 middle (lower row). The warm extended PSFs are shown on the right, with channel 1 on top and channel 2 at the bottom. See text for how these were constructed.

4.7.3   *Point Source Fitting Photometry*

The PRF is not an oversampled representation of a point source. Rather it is a map of the appearance of a point source imaged by the detector array at a sampling of pixel phases (positions of the source centroid relative to the pixel center). For that reason, performing aperture photometry directly on the PRF is not strictly correct.

IRAC provides diffraction-limited imaging internally. The image quality is limited primarily by the Spitzer telescope. The core PRFs are provided for 25 positions in a 5x5 grid on the array for each channel. Interpolating to the nearest position is needed. The extended PRFs have been created at the center of the array. Therefore these PRFs degrade as a function of distance from the center. The PRFs will vary with position on the array, including, but not limited to, the relative position of the optical ghosts in channels 1 and 2, and the diffraction spikes in all channels.

A step-by-step description of IRAC PRF-fitting photometry is given in Appendix C.

4.8   Calculation of IRAC Zmags

Some software packages, such as IRAF's "phot" task, require specifying "zmag". For IRAC data, you need to know the pixel size of the IRAC image being analyzed in order to convert surface brightness to

flux density. The zmag can be evaluated from $2.5 \times \log(F_0/C)$, where F_0 is the zero magnitude flux density in Jy for the relevant channel, tabulated in Table 4.1, and C is the conversion factor from MJy/sr to μJy/pixel, e.g., 8.461595 for $0.6'' \times 0.6''$ pixels (the value of C will be different depending on the pixel size).

To understand where the IRAC zmag comes from, you can start with the fundamental equation between magnitudes and flux densities. In one incarnation, it becomes

$$m - M_0 = -2.5 \times \log(F/F_0) \tag{4.16}$$

Here m is the magnitude of the source you want to measure, M_0 is the zero magnitude (= 0), F is the flux density in Jy of the source you want to measure and F_0 is the flux density of a zero magnitude source. For IRAC channel 1 in cryogenic mission, $F_0 = 280.9$ Jy. Expanded out, this becomes thus

$$m = -2.5 \times \log(F) + 2.5 \times \log(F_0) \tag{4.17}$$

Here $2.5 \ast \log(F_0)$ is the same as zmag. Now, since the IRAC images are in units of MJy/sr, we have to do some manipulation to get the equation to this form. Specifically, the measurable F that we have in IRAC images is the surface brightness, not the flux density. So therefore the equation becomes

$$m = -2.5 \times \log(SB \ast C) + 2.5 \times \log(F_0) \tag{4.18}$$

where SB is the measured surface brightness in the image in MJy/sr and C is a conversion factor from MJy/sr to Jy/pixel. For IRAC channel 1 mosaics with 0.6 arcsec x 0.6 arcsec pixels it equals C = 8.461595×10^{-6} Jy/pixel/(MJy/sr). Therefore the equation becomes

$$m = -2.5 \times \log(SB) + 2.5 \times \log(F_0/C) \tag{4.19}$$

where zmag now corresponds to the latter term, $+2.5 \times \log(F_0/C)$. Inserting the values of F_0 and C mentioned above, we get zmag = $2.5 \times \log(280.9/8.461595E\text{-}06) = 18.80$ mag in channel 1.

Please remember that this is true only for the 0.6 arcsec x 0.6 arcsec pixel scale mosaics. For other pixel scales you will get a different value. Also, please remember the required corrections (e.g., aperture

correction) that are needed for high accuracy photometry.

4.9   Astrometry and Pixel Scales

4.9.1   Optical Distortion

Optical distortion is a significant (measurable) effect in IRAC data. The ~ 1% distortion in all channels is due principally to being offset from the optical axis of Spitzer, with additional components from the telescope and camera optics. In addition to varying the effective pixel size, there are also higher-order terms such as skew (the two axes are not exactly perpendicular) and a difference in the pixel scales between the two axes. Failure to account for the distortion will lead not only to errors in photometry (described below), but also shifts in astrometric position approaching 1 arcsec near the array corners.

Optical distortion in each of the IRAC FOVs is described in the headers using a standard method described by *Shupe et al. (2005, [26])*. This method places the center of the distortion at the center of each detector array, in particular at CRPIX1 and CRPIX2. The linear terms and any skew are represented in the CD matrix header keywords (CD1_1, CD1_2, CD2_1, and CD2_2), while the distortion keywords provide the second and higher order terms. Importantly, these distortion corrections apply to the array coordinates, prior to the transformation to sky coordinates. This means that all IRAC data for a given detector share the same distortion keywords. In addition we also provide a separate set of keywords representing the "reverse" transformation from sky to array coordinates.

The form of the optical distortion that is encoded in the (C)BCDs is read properly by several "standard" tools available to the general astronomical community: (1) the Spitzer mosaicker (MOPEX), (2) WCSTOOLS by Doug Mink (SAO) and (3) DS9 (except for grid overlays).

The optical distortion is fit independently for each IRAC detector. Originally a second-order fit was used, but an improved fit to third order was derived from the GOODS data by S. Casertano. The (C)BCD coefficients remove the distortion to 0.1″ accuracy.

4.9.2   Pixel Solid Angles

As a result of the optical distortion described above, the detector pixels do not all subtend the same projected solid angle on the sky. The variation in projected pixel solid angle is roughly 1.5%.

This size variation is accounted for in the flat-fielding process because the flats are derived from actual sky measurements. As a result, after flat-fielding, the (C)BCD images are calibrated in units of true surface brightness (MJy/sr). This poses a difficulty because virtually all software assumes that the pixels are in units of flux per pixel, and simply sum the pixel values. In order to properly measure fluxes from an image in surface brightness units, one must multiply the pixel value by the pixel size. Failure to do so

could induce photometric errors at the 1% level, depending on location on the array. Unfortunately, only the newest photometry software can read the new FITS-standard WCS distortion keywords written in the (C)BCD headers and properly account for the sizes of the pixels.

The simplest solution to this problem is to reproject the images onto an equal area (or nearly so) projection system (such as TAN-TAN) using suitable software that can understand the distortion keywords in the WCS header (e.g., MOPEX). MOPEX also has the significant advantage that it understands how to properly handle surface brightness images during coaddition. After processing, the pixels will all subtend the same solid angle, and hence any standard photometry software can produce the correct result.

However, some observers may prefer alternative approaches, in particular if they wish to measure photometry directly from the (C)BCD images. Therefore, we supply maps of the pixel size in the "IRAC calibration and analysis files" section of the IRAC documentation website that can be used to correct the pixel solid angles in BCD images if any measurements are being directly made on them. Note that this correction is built into the "location-dependent photometric correction" image, also available on the website, so multiplying by this correction map (intended to provide correct photometry for point sources with stellar-like SEDs) will also produce the correct result.

4.10 Point Source Photometry

Please refer to Appendix B for a detailed description of how to achieve the highest possible accuracy when performing point source photometry. Appendix C summarizes the proper use of PRF fitting to obtain high accuracy point source photometry in a crowded field or in a field with highly varying background. Photometry using IRAC data is no different from that with any other high-quality astronomical data. Both aperture photometry and PRF-fitting work successfully. Aperture photometry is most commonly used, so we will discuss it briefly.

Aperture photometry measurements should be corrected by multiplying by the aperture correction, the array location-dependent correction, and the pixel phase correction. It is customary to perform the latter two corrections first. An IDL function can be found at http://irsa.ipac.caltech.edu/data/SPITZER/docs/dataanalysistools/tools/contributed/irac/iracaphotcorrcryo/ in the Spitzer documentation website (cryogenic mission only) to apply the latter two (position dependent) corrections. You will need to measure the centroid location in addition to the aperture flux. The corrections in the IDL function have been derived assuming first moment centroids. The link to the IDL function contains a code to derive first moment centroids as well.

The improvement in data quality after applying these corrections can be significant. We show in Figure 4.7 the cumulative distribution of the flux per cent difference from the mean (absolute value), for the original (BCD) and corrected data for calibration star NPM1p67.0536 (approximately 3000 data points). The corrected data have a factor of two smaller dispersion than the original data. The 68% confidence interval (1σ for a gaussian distribution) for the original data is about 2.5% in channel 1. In comparison,

the array location-dependent and intra-pixel gain corrected data have a 68% confidence interval of about 1.4%. The corrections available earlier, including the radial pixel phase correction, were only about half as good at reducing the scatter in the data, with 68% confidence interval of about 1.9%.
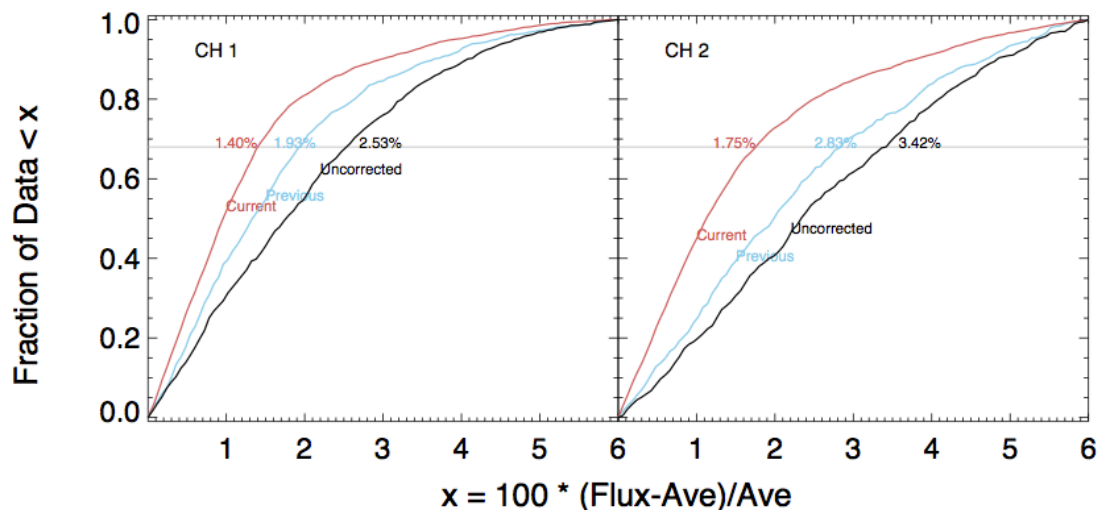
Figure 4.8: Correcting photometric measurements of NPM167.0536 using the pixel phase and array location-dependent correction. Black curves show the cumulative distribution of aperture photometry measurements throughout the cryogenic mission for which a value is within a given per cent of the mean. Blue curves show the distribution after correction using an earlier set of location-dependent functions. Red curves are the result of the new correction. A gray horizontal line at 68% (1σ for a gaussian distribution) is labeled with the corresponding spread in values for each of the three distributions.

Regarding aperture correction, the radius of the on-source aperture should be chosen in such a way that it includes as much of the flux from the star (thus, greater than 2 arcseconds) as possible, but it should be small enough that a nearby background annulus can be used to accurately subtract unrelated diffuse emission, and that other point sources are not contributing to the aperture. For calibration stars, an annulus of 12 arcseconds is used; such a wide aperture will often not be possible for crowded fields. The dominant background in regions of low interstellar medium (ISSA 100 μm brightness less than 10 MJy/sr) is zodiacal light, which is very smooth. In regions of significant interstellar emission, it is important to use a small aperture, especially in IRAC channels 3 and 4, where the interstellar PAH bands have highly-structured emission. For example, an aperture in a star-forming region might have a radius of 3 native pixels with a background annulus from 3 to 7 native pixels. The flux of a source can then be calculated in the standard way, taking the average over the background annulus, subtracting from the pixels in the on-source region, and then summing over the on-source region.

It is important to apply an aperture correction to flux densities measured through aperture photometry or PRF fitting, unless the exact same aperture and background radii and annuli were used as for the calibration stars. The IRAC data are calibrated using aperture photometry on a set of flux calibration stars. The calibration aperture has a 10 native pixel radius (12 arcsec) in all 4 channels. For flux density measurements in crowded fields, a much smaller on-source aperture should be used (or use PRF-fitting

photometry). And in the presence of extended emission, a small off-source annulus is normally used. The calibration aperture does not capture all of the light from the calibration sources, so the extended emission appears too bright in the data products we delivered. See the more detailed discussion under 4.11. Similarly, observers will often use smaller apertures and will want to correct their photometry to match the absolute calibration.

Users should note that the spatial extent of the PSF in channels 3 and 4 is much larger than the subarray area. In other words, a large amount of the total power in the PSF is scattered onto arcminute size scales. As a result, special care needs to be taken when measuring fluxes in these channels, since accurate measurement of the "background" is difficult. Proper application of aperture corrections is very important.

For photometry using different aperture sizes, the aperture correction can be estimated with Table 4.7. All distances in this table are in native pixels (~ 1.2 arcsec). Note that the post-BCD mosaics currently available from the Spitzer data archives use pixels that correspond to exactly 0.6 arcsec x 0.6 arcsec. The aperture corrections as written will INCREASE the flux measured by the listed method, i.e., your measured brightness should be MULTIPLIED by the aperture corrections in the table. The third decimal place in these numbers is included only to illustrate the trends; the accuracy of these corrections is presently ~ 1% - 2%. The aperture corrections in Table 4.7 are the modes of the distributions of aperture flux ratios measured using stars at several different positions covering the whole arrays. Standard deviations (including measurement errors and true variations across the array) are less than 0.5% for all entries except the smallest aperture, in which they are still less than 1%. The extended source (infinite) corrections in Table 4.7 come from *Reach et al. (2005, [24])*. The measured flux densities can then be converted to magnitudes, if desired, using the zero-points in Table 4.1.

Table 4.7: Cryogenic IRAC aperture corrections.

Radius on source (native ~1.2" pixels)	Background annulus (native ~1.2" pixels)	Aperture correction			
		3.6 μm	4.5 μm	5.8 μm	8.0 μm
infinite	N/A	0.944	0.937	0.772	0.737
10	12-20	1.000	1.000	1.000	1.000
8	12-20	1.011	1.013	1.011	1.017
6	12-20	1.032	1.036	1.030	1.051
5	12-20	1.047	1.048	1.054	1.064
5	5-10	1.060	1.063	1.063	1.084
4	12-20	1.070	1.080	1.076	1.087
3	12-20	1.112	1.112	1.118	1.213
3	3-7	1.125	1.120	1.135	1.221

2	12-20	1.208	1.220	1.349	1.554
2	2-6	1.215	1.233	1.366	1.568

.

4.11 Extended Source Photometry

The photometric calibration of IRAC is tied to point sources (calibration stars) measured within a standard aperture with a radius of 12 arcseconds. This point-source calibration is applied to all IRAC data products during pipeline processing to put them into units of MJy/sr (1 MJy/sr = 10^{17} erg s^{-1} cm^{-2} Hz^{-1} sr^{-1}). This method results in a highly accurate calibration for point sources. However, transferring this calibration to extended sources requires extra thought. The discrepancy between the (standard) point source calibration and the extended source calibration arises from the complex scattering of incident light in the array focal planes. Our best understanding is that there is a truly diffuse scattering that distributes a portion of the incident flux on a pixel throughout the entire array.

The surface brightness of extended emission in IRAC images will tend to appear BRIGHTER than it actually is. The reason for this is two-fold. First, photons that would normally scatter out of the PSF aperture used to measure a point source are instead captured by an extended source. The scattering depends on the convolution between the IRAC PSF and how the light is distributed across the focal plane, which is usually quite complex for extended sources (galaxies, ISM and nebulae). Second, photons are scattered into the aperture from the emission regions outside the aperture. As a thought experiment, one can imagine a single point source inside an aperture, which is easy to measure. But if four point sources are placed around it just outside the measurement aperture, each of them scatters light into the aperture, which leads to an overestimate of the real flux. For the extended source case, we can imagine the same experiment taken to the limit where all the regions have emitters in them.

For photometry of extended sources, the calculated flux inside an aperture must be scaled by the ratio of the extended and point source throughputs. The scaling factors (f_p/f_{ex}) to be used are given in Table 4.7 (the infinite aperture case). Note that these are not really "throughputs," in the sense that they have anything to do with the number of photons reaching the detector. It is more accurate to think of them as a special type of an aperture correction. The values in Table 4.7 are for a very extended, red source like the Zodiacal light.

The most challenging case of extended source photometry is of objects with sizes on arcminute scales, within apertures of similar size or smaller. Examples might be typical observations of nearby galaxies. In this case the aperture correction is related both to the aperture size and the underlying surface brightness distribution of the target. To derive a set of aperture corrections more appropriate to this case, a detailed analysis of early-type spheroidal galaxies (due to the relative ease of modeling the light profiles of these stellar-dominated sources), ranging in size from 20 arcseconds to several arcminutes, was carried out. A summary of the results is given below, including aperture correction curves that may be applied to

photometry of all types of well-resolved galaxies. These extended source aperture corrections are somewhat larger than the infinite aperture corrections given in Table 4.7.

A commonly encountered problem is that of measuring the total flux of extended objects that are still smaller than the standard aperture size used for the photometric calibration. For example, the background galaxies seen in all IRAC images are often slightly extended on size-scales of a few arcseconds. PRF-fitting photometry of such objects will obviously underestimate their fluxes. One methodology for handling such sources was developed by the SWIRE project; readers are referred to the data release document for SWIRE, available from the Spitzer documentation website under Legacy projects. Detailed analysis by SWIRE has indicated that Kron fluxes, with no aperture corrections applied, provide measurements of small extended sources that agree closely with hand-measured fluxes. Kron fluxes are provided as one of several flux measures in the popular "SExtractor" software. Note that it is important to determine that an object actually is extended before using the Kron flux, as it is ill-defined otherwise. This may be determined by using the stellarity and isophotal area as defined by the SExtractor software. Selecting limits on these parameters based on their breakdown as a function of signal-to-noise ratio generally will mimic SExtractor's own "auto" function.

To measure **absolute** flux on large scales (sizes of order the field of view), consider all the sources of flux that go into each pixel. The IRAC images are in surface-brightness units. The flux of an extended object is the integral of the surface brightness over the solid angle of the object. The value of a pixel in an IRAC BCD is the real sky value plus a contribution from the zodiacal light minus the dark current value at that pixel. The dark current value is made from observations of a low background region at the north ecliptic pole and so it contains some small amount of flux of astrophysical origin. The darks have also had an estimate of zodiacal light subtracted from them before use. The (theoretically) estimated zodiacal light brightness during an observation is in the BCD header keyword ZODY_EST, and that for the sky dark observation is listed as SKYDRKZB. While it is possible using the above keywords to recover something similar to the absolute sky surface brightness, this brightness estimate is still limited by the accuracy of the underlying model of the zodiacal emission.

In practice, most extended source photometry will usually be performed with respect to a background region within the image (for example, large aperture photometry of galaxies, nebulae, etc.) and one does not attempt to measure the absolute sky brightness on large scales (like the zodiacal cloud). The median value of the pixels located in user-selected background regions is generally a reasonable estimator of the background.

4.11.1 Best Practices for Extended Sources

Resolved galaxies with apertures centered on the nucleus:
- For sources < 8–9 arcsec in size, treat as point source (small aperture photometry, with local annular background subtraction)
- For sources > 8–9 arcsec in size, apply extended source aperture corrections (see below).

Emission knots, embedded resolved sources

- If the source is small (compact), treat as point source (small aperture photometry, with local annular background subtraction)
- If the source is large and fuzzy, use the extended source aperture corrections (see below). Beware that background structure will introduce large uncertainties (~10%)

Surface Brightness (pixel-to-pixel measurements)

- For very extended sources (> 300 arcseconds) or flat, low surface brightness sources (e.g., Magellanic-type galaxies), use the *maximum scaling factors* given below.

Cross-comparing IRAC images (e.g., channel 1 versus channel 4), we recommend that you first cross-convolve the images. For the example above, convolve the channel 4 image with the channel 1 PSF, and convolve the channel 1 image with the channel 4 PSF. This operation will reduce the deleterious effects of the light scattering, but will not completely eliminate them. Be very conservative in interpreting colors as surface brightness measurements can be off by 5%–10% in the short-wavelength channels and 30% in the long-wavelength channels.

4.11.2 Extended Source Aperture Correction

The following aperture corrections are intended to correct the photometry of extended sources (e.g., galaxies) whose absolute calibration is tied to point sources. These corrections not only account for the "extended" emission from the IRAC PSF itself, but also from the diffuse scattering of the emission across the IRAC focal plane. The curves were derived from detailed analysis of elliptical galaxies (see related notes in Section 4.11.4). The curves may be applied to all types of galaxies, but beware that significant departures can be expected for sources that are morphologically different from elliptical galaxies (e.g., late-type LSB galaxies; see surface brightness recommendations above).
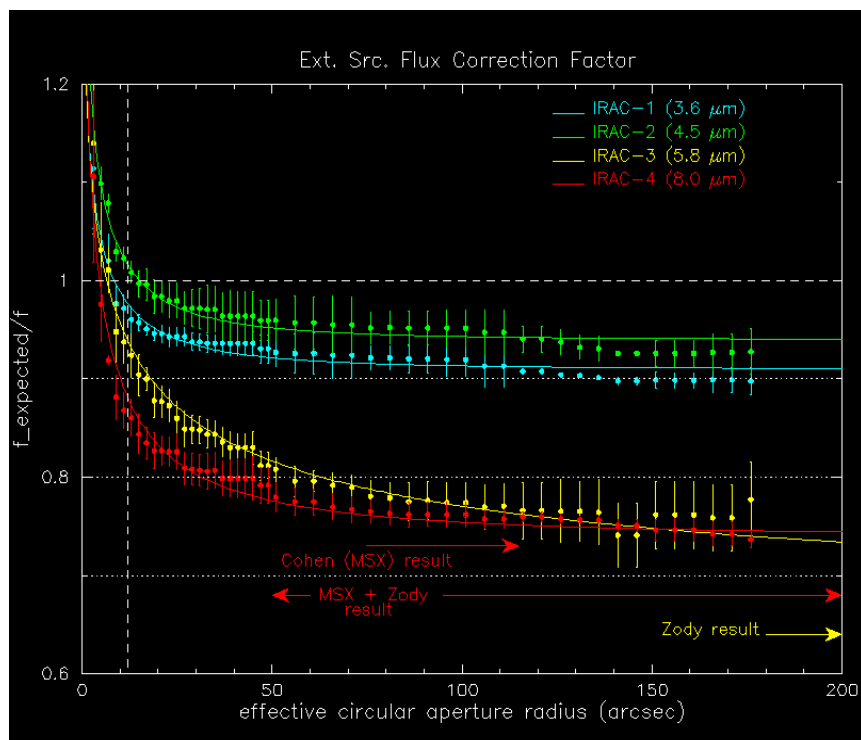
Figure 4.9. Extended source flux correction factors; solid lines represent exponential function fits to the data. Also indicated are correction factors derived from zodiacal light tests, and Galactic HII region tests (e.g. Martin Cohen's GLIMPSE vs. MSX, private communication).
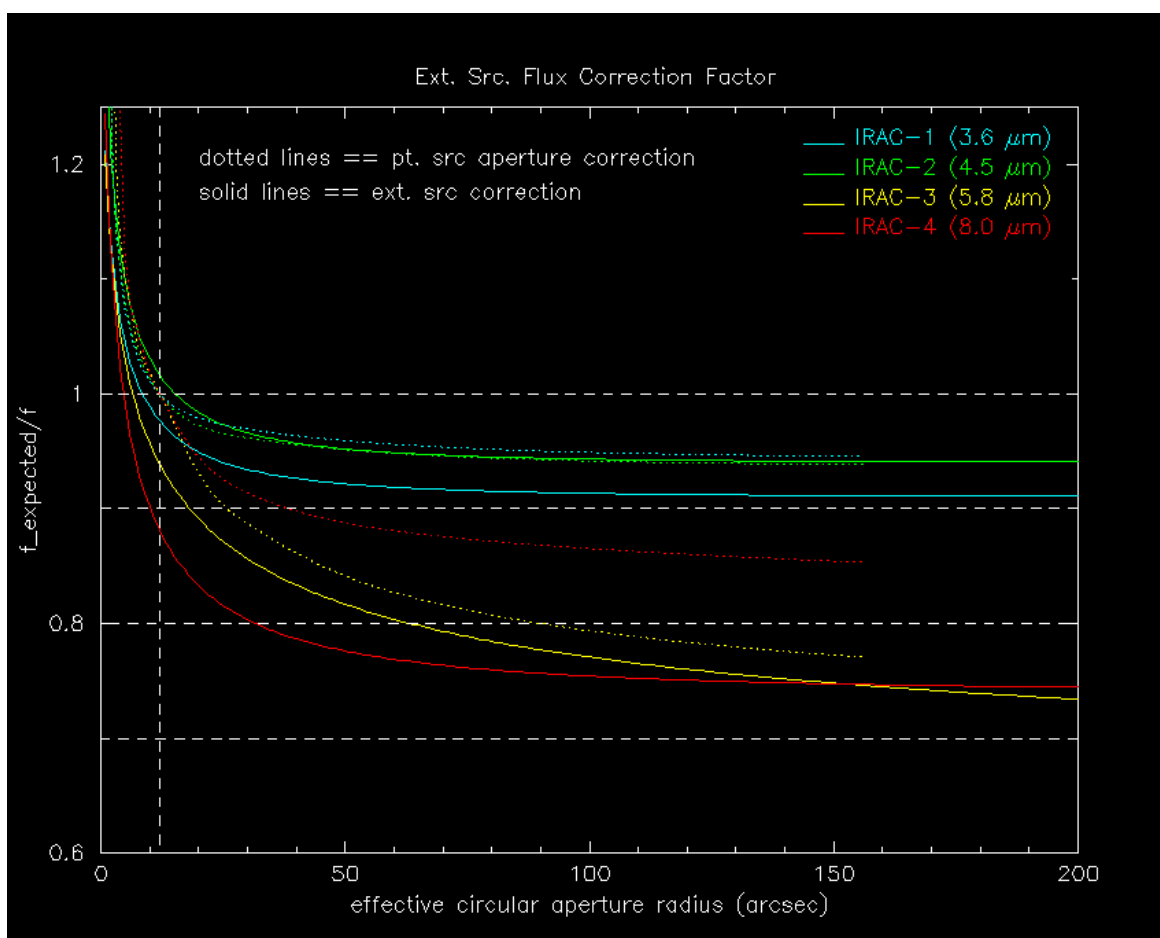
Figure 4.10. Extended source flux correction factors for galaxies (solid lines) versus the PSF aperture correction factors (dotted lines). The main difference between the two is the truly diffuse scattering internal to the array.

Aperture photometry should also include background subtraction; we recommend that you use an annulus that is located just outside the boundary of your galaxy. Circular or elliptical apertures may be used.

The procedure for correcting extended source photometry is to apply the correction factor to the integrated flux measured from the IRAC image (subject to the standard or point source calibration). The correction factor is a function of the circular aperture radius or the effective circular aperture radius (if using ellipses). These corrections should be good to 10%. For convenience, we have converted the empirical curves into a functional form:

integrated flux (radius) = measured flux (radius) x correction_factor (radius)   (4.20)

$$\text{correction\_factor (radius)} = \text{true\_flux} / \text{flux} = [A \times \exp(-\text{radius}^B)] + C \qquad (4.21)$$

where radius is in arcsec, and A, B and C are the best fit coefficients tabulated below:

Table 4.8: IRAC extended source photometrical correction coefficients.

IRAC	A	B	C
3.6 μm	0.82	0.370	0.910
4.5 μm	1.16	0.433	0.94
5.8 μm	1.49	0.207	0.66
8.0 μm	1.37	0.330	0.740

The coefficient "C" represents the infinite, asymptotic value.

4.11.3 Low Surface Brightness Measurements and the Maximum Scaling Factors

Photometry of diffuse emission or low surface brightness objects is also subject to a large calibration correction in the IRAC 5.8 and 8.0 μm channels. The way to think about "flat" extended objects is that any aperture you use to measure the integrated flux (or surface brightness) is equivalent to an infinitely large aperture applied to a point source (or galaxy). Hence, the appropriate aperture correction (or equivalently, surface brightness factor) is the large radius case of the above aperture corrections:

Table 4.9: IRAC surface brightness correction factors.

IRAC	Surface Brightness Correction Factor
3.6 μm	0.91
4.5 μm	0.94
5.8 μm	0.66–0.73
8.0 μm	0.74

Surface Brightness = measured surface brightness x correction_factor, where the correction factors represent the infinite aperture value. Note that for IRAC channel 3 the recommended correction is somewhere between 0.66 and 0.73, depending on the downward curvature of the aperture corrections (which is highly uncertain). These aperture corrections should be good to 10%.

Examples of LSB objects: large, late-type galaxies (e.g., NGC 300); Magellanic-type galaxies (e.g., NGC 6822); diffuse dwarf galaxies (e.g., M81 DwA); HII regions that are larger than ~100 arcseconds and not very centrally condensed.

4.11.4 Caveats & Cautionary Notes

At small radii, r < 7–8", the extended source aperture corrections should not be used. Instead, we recommend using the point source aperture corrections for small radii.

It remains uncertain how much the spectral shape of the extended object determines the flux corrections; the aperture corrections presented here were derived using relatively "old" spheroidal galaxies. To first order, the extended source aperture corrections apply to most types of galaxies.

Likewise with the spectral color caveat, it remains uncertain how much the spatial distribution of the light determines the flux corrections; these corrections were derived using relatively high surface brightness spheroidal galaxies; it is unknown whether these corrections apply to lower surface brightness galaxies (e.g., late-type spirals; irregulars; Magellanic-types).

4.11.5 Faint Surface Brightness Behavior

Note that the discussion in this section applies only to warm IRAC data. For more detailed information, please see *Krick et al. (2011, [17])*.

4.11.5.1 Binning

Binning data by essentially making larger "pixels" should reduce the noise in the image linearly with binning length. Figure 4.10 and Figure 4.11 show a plot of noise versus binning length for a set of deep mapping data in the Virgo cluster (PID 60173). These data have been carefully corrected for the first frame effect using the data themselves. The measured noise does not achieve the expected linear relation with binning length.
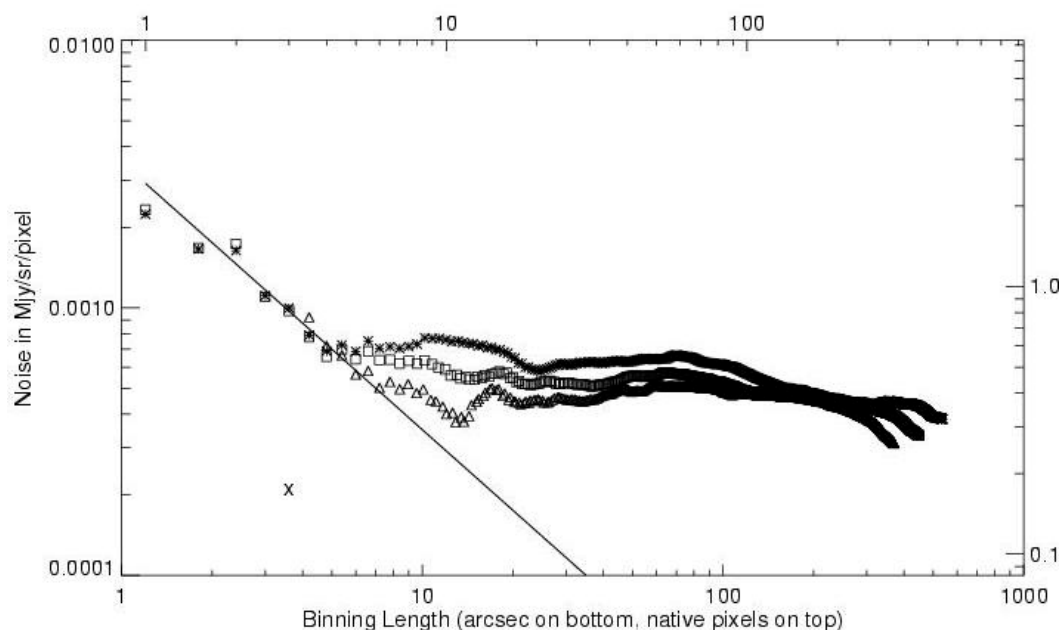
Figure 4.11. Noise versus binning length in channel 1. To make this plot the surface brightness was measured in nine regions across an object-masked mosaic. These regions are not near the bright galaxies, stars, or diffuse plumes. The noise is defined as the standard deviation of those nine regions. The box size is incrementally increased until the box length is many hundreds of pixels. For reference the solid line shows the expected linear relation.
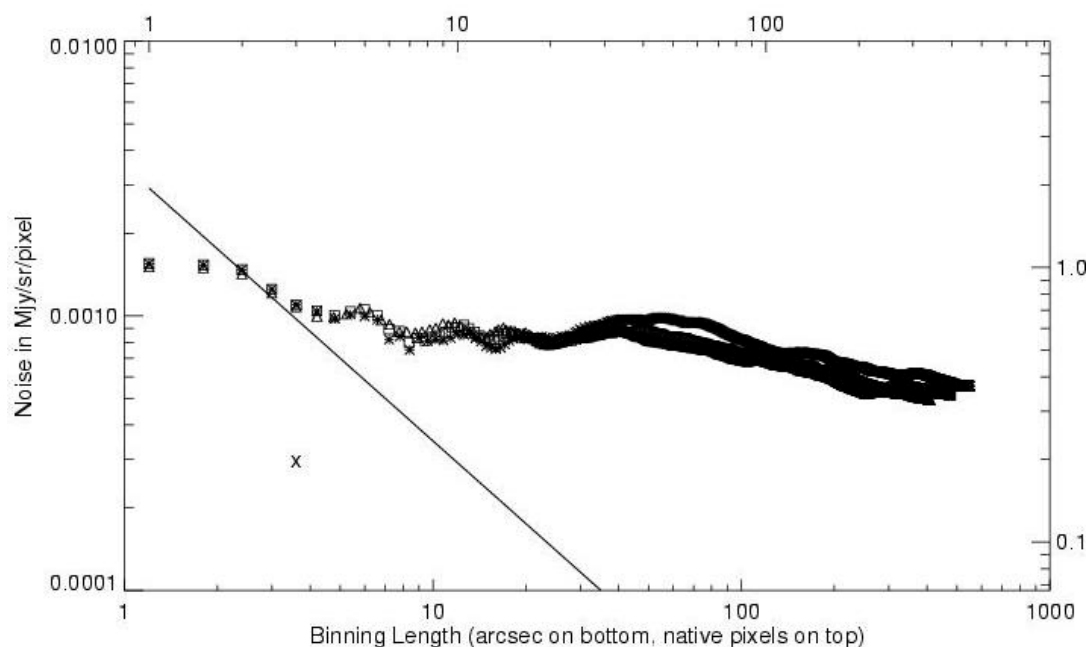
Figure 4.12. Noise versus binning length in channel 2. To make this plot the surface brightness was measured in six regions across an object-masked mosaic. These regions are not near the bright galaxies, stars, or diffuse plumes. The noise is defined as the standard deviation of those six regions. The box size is incrementally

increased until the box length is many hundreds of pixels. For reference the solid line shows the expected linear relation.

4.11.5.2 Small Scales

There is a discrepancy between the expected linear behavior and the data at short binning length scales of just a few pixels (mosaics only). This discrepancy occurs because we have correlated noise on a mosaicked image on small pixel scales (a few pixels), so the noise does not bin down appropriately.

4.11.5.3 Medium Scales

On 5"–30" scales much of the extra noise is due to sources in the image. The first level of masking used the SExtractor segmentation map as a mask. The resulting noise properties are shown with asterisks. Increasing the size of the masks to 1.5 (2.0) times the SExtractor-determined object radii produced noise properties shown with a square (triangle) symbol. Further increases in mask size are inconsequential. The discrepancy between the observed and expected behaviors in this binning length regime is dominated by noise from the wings of galaxies that are improperly masked. Even after increasing the mask sizes, extra sources of noise remain which prevent detection of ultra-low surface brightness. There appears to be a floor to the noise at roughly 0.0005 MJy/sr at 3.6 μm and 0.0008 MJy/sr at 4.5 μm.

4.11.5.4 Large Scales

Some of the large-scale noise is caused by the mapping pattern used for the observations. On scales of roughly half a field of view there are differences in the total exposure time and hence the total number of electrons detected (not a dominant source of noise). There are remaining sources of noise on the large scales, both instrumental and astronomical, which are very hard to disentangle. Uncertainties in the flat-fielding and removal of the first frame effect are two instrumental effects that are contributing to the noise on large scales. The first frame effect has a column-wise dependence that requires special calibration data to measure. Astrophysically, there is real structure in the zodiacal light and Galactic cirrus. There is also documented diffuse intracluster light in the Virgo cluster itself, and a small signal from the extragalactic background light that are both adding to the noise at low levels. There is potentially also noise due to the blue infrared color of intracluster light, while the zodiacal light from which the flats are made is red in near-IR (see Section 4.2). Differentiating between all of these sources of noise is difficult.

4.11.5.5 Increasing exposure time

The IRAC dark field was used to study whether the noise decreases with the square root of exposure time, as expected. The dark field has extremely low zodiacal light and low Galactic diffuse emission. Using all the warm mission dark calibration data through 2010, a mosaic was made from 300 dark frames (each with 100 second frame time). Object masking was made with the SExtractor segmentation image. The

noise on the distribution of pixel values is the standard deviation of the Gaussian fit to that distribution. Each distribution has > 750 pixels in it. For comparison the same analysis was performed on the dark field mosaics from the first year of the cryogenic mission. The results from both are in Figure 4.12 and Figure 4.13.
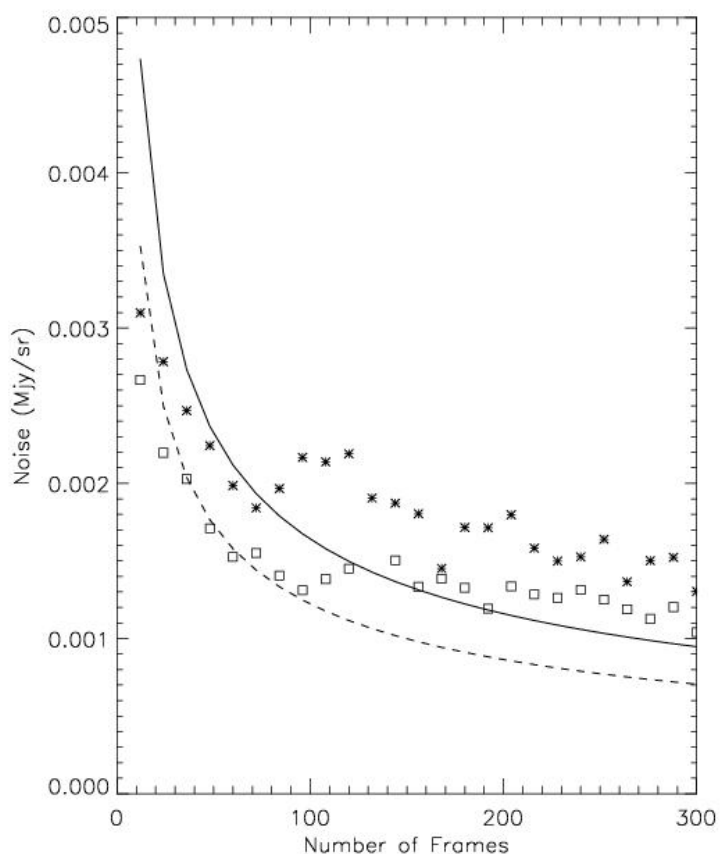
Figure 4.13. Noise as a function of exposure time (number of frames) in channel 1. The results from the warm mission data are shown with x's and the expected behavior with the solid line. The results from the cryogenic mission are shown with open squares and the expected behavior with the dashed line.
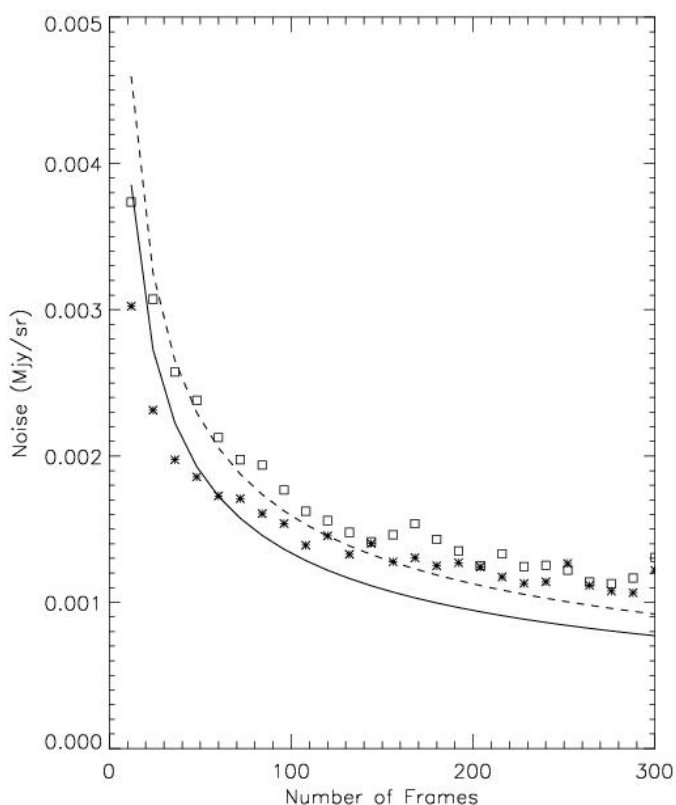
Figure 4.14. Noise as a function of exposure time (number of frames) in channel 2. The results from the warm mission data are shown with x's and the expected behavior with the solid line. The results from the cryogenic mission are shown with open squares and the expected behavior with the dashed line.

These plots show that background noise in IRAC channels 1 and 2 does decrease roughly as expected with exposure time. The slight deviation at larger exposure times is likely caused by the first frame effect and by residual source wings.

4.12 Pointing Performance

Pointing is controlled by Spitzer's Pointing Control System (PCS). This uses a combination of a star tracker and gyros to locate and control the attitude of the spacecraft. Absolute pointing is controlled by the star tracker, through a filter (known as the "observer") which smooths the raw star tracker output. Slews under control of the observer take ~ 10 seconds to settle, so only the initial slew and cluster slews in celestial coordinates are carried out using the observer. Once the observatory has taken the initial frame at the starting position, attitude control is handed over to the gyros. Mapping and dithering slews are made under gyro control with a shorter (~ 5 sec) settle time. The price to be paid for the shorter settle time is that the spacecraft attitude will slowly drift with respect to the observer attitude, at a rate ~ 1 mas/sec.

For long integrations (100 sec frame time), attitude control is returned to the observer after 80 seconds to halt the drift.

Table 4.10: Pointing uncertainties.

Pointing Effect	Characteristic Amplitude [arcsec]	Characteristic Timescale
Accuracy	0.07	N/A
Wobble	0.07	~ 40 minutes
Initial drift	0.5	~ 30 minutes
Long-term drift	0.3	~ 1 day
Low frequency jitter	0.07	~ 2 minutes
High frequency jitter	0.03	< 0.02 seconds

In addition, attitude resets were performed regularly (about every 30 minutes) to return the spacecraft attitude to the observer attitude. The system is designed to ensure that any motion to return the spacecraft attitude to that of the observer does not take place during an IRAC integration, to avoid smearing the images. Throughout the first 18 months of the mission the PCS system and the corresponding parts of the IRAC AOT were being adjusted for optimal performance. Below is a guide to the astrometric accuracy and image quality that can be expected from a typical observation.

4.12.1 Pointing Accuracy

Slews under observer control settle to the accuracy to which the star tracker to IRAC pointing offset is known, about 0.5". Offsets between dither/mapping moves are accurate to 0.1" relative to the commanded move for small moves (~ 10"), and for large moves (~ 0.5 deg) the accuracy is ~ 0.5" (though this was improved as of Spring 2005, and should be only ~ 0.2" thereafter). An additional pointing error comes from the gyro drift which can accumulate over the 30 minute period between attitude resets. This error is typically ~ 2" for a "worst case" frame just before a reset. The pointing uncertainties due to various effects are summarized in Table 4.10.

The pointing of each frame as reported in the header keywords CRVAL1 and CRVAL2 is an average of the observer attitude during the frame, and is typically accurate to ~ 0.5" (though it may be slightly worse for short frames where the observer has not fully settled). Other header keywords related to pointing

include RA_RQST and DEC_RQST, the requested R.A. and Dec. of the frame, and PTGDIFF, the difference between the requested and actual pointing. USEDBPHF should be T for all frames, if not, then pointing transfer has failed for the frame.

The Level 2 (Post-BCD) pointing refinement module is run by default in the post-BCD pipeline to refine the pointing to 2MASS accuracy (~ 0.15"), and will be successful if there is a sufficient number of 2MASS stars in the data. The module operates by matching common stars between frames ("relative refinement") and a fiducial set of stars from 2MASS ("absolute refinement"). The (R.A., Dec.) position and twist of each frame is then adjusted until a global minimum in the residuals is found. Application of this to the Extragalactic IRAC First Look Survey (FLS) data results in a mean position error for high signal-to-noise stars with respect to 2MASS positions of 0.25".

The pointing refinement module writes several new keywords to the header. RFNDFLAG is true if pointing refinement was run and produced a refined solution. The refined position is given by keywords RARFND and DECRFND, and rotation by CT2RFND. A new version of the CD matrix, given by keywords CD11RFND, etc., is also written to reflect the new rotation angle (note that the pixel scale and distortion are not changed by pointing refinement). If pointing refinement fails, then the header keyword RFNDFLAG will be false and RARFND, DECRFND and CT2RFND will be set to CRVAL1, CRVAL2 and CROTA2, respectively. Note that the refined solution may be poor if the number of astrometry stars in the frame, NASTROM, is low (i.e., 0, or only a few stars). The refined pointing keywords are used by the post-BCD software if USE_REFINED_POINTING = 1 in the namelists (but see next paragaph). To use the refined pointing with other software, copy the non-standard keywords to their FITS standard equivalents, e.g., RARFND to CRVAL1, CD11RFND to CD1_1 etc. Pointing refinement works well on most channel 1 and 2 data, though short frames in fields near the Galactic poles in channels 3 and 4 will frequently have too few stars for a good solution.

All data have a "superboresight" correction applied. Users wishing to make use of the superboresight solutions need to set USE_REFINED_POINTING = 0 in MOPEX, as the superboresight pointing is contained in the standard CRVAL1, CRVAL2 and CD matrix keywords (this is the recommended pointing to be used when making mosaics etc.). Data which have had this correction applied will also have the ORIG_RA and ORIG_DEC keywords present which contain the initial (uncorrected) pointing estimate.

4.12.2 Jitter and Drift

Jitter is typically 0.1". It has been measured on timescales ~ 0.04 seconds to 5 minutes. In addition to high frequency jitter, there are modulations ~ 0.1" on timescales of 200–400 seconds. These are not expected to noticeably affect the IRAC PSF. Gyro drift occurs for the first 80 seconds of IRAC integrations, but again this should result in only ~ 0.1" of motion. Some amount ($<$ 0.4") of image smearing is expected in short frames due to settling motions. Other instances of pointing glitches occur when one of the four reaction wheels goes through zero velocity. To reduce stiction when the speed actually hits zero, the wheels are given a small "bump" in torque at this point, which has been seen to result in a small (~ 0.05"),

short duration (~ 10 seconds) pointing glitch. On average, only about one crossing per hour occurs, and they are thought to mostly happen during slews, so they are not expected to affect many IRAC images.

One manifestation of settling, jitter and drift during integrations is that the pointing of HDR short, medium (for 100 sec HDR) and long frames are slightly different (the same is also true of repeats taken in the same position). These differences are usually ~ 0.1 arcseconds, so they should not be a problem for most observers, but they are large enough to show up as residuals in difference images.
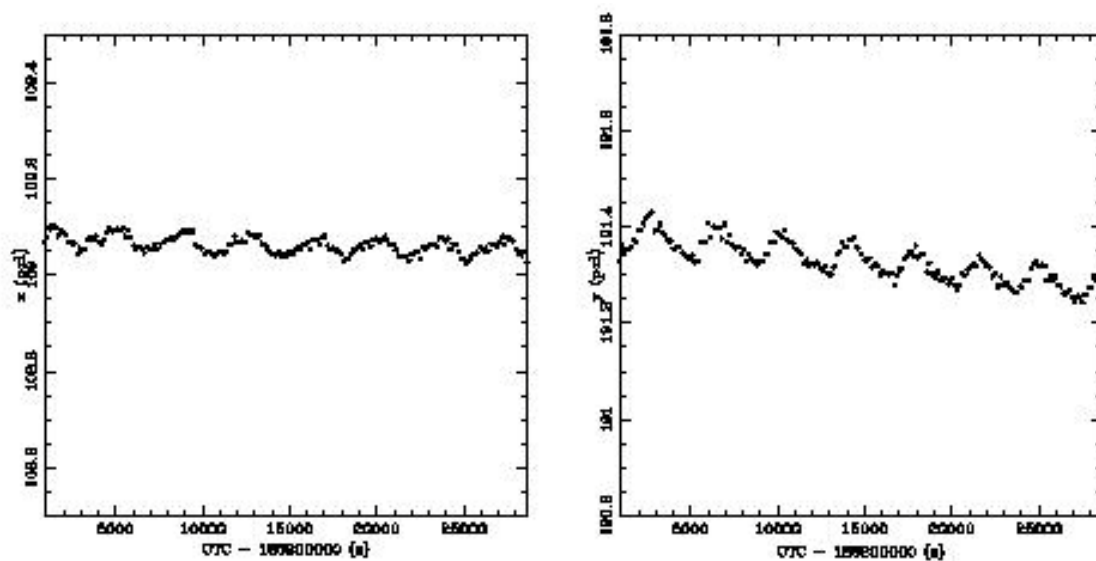
Figure 4.15: Position of a star in the x (left) and y (right) axes of IRAC during a long (8 hr) observation. The ~ 3000 sec oscillation is superposed on a slow drift of the Star Tracker to telescope alignment.

A slowly varying pointing oscillation is seen in long staring observations. This oscillation has an amplitude of 0.1" and a period ~ 3000 sec (Figure 4.14). It is believed to be related to battery heating and cooling cycles influencing the mechanical link between the Star Tracker and the telescope. There is also a steady drift of the pointing, ~ 0.01"/hr due to other changes in the Star Tracker to telescope alignment. The accumulated drift is removed using regular Star Tracker-to-telescope boresight calibrations every ~ 12 hours.

5 Pipeline Processing

5.1 Level 1 (BCD) Pipeline

The IRAC Level 1 (BCD; Basic Calibrated Data) pipeline is designed to take a single Level 0 ("raw") image from a single IRAC detector and produce a flux-calibrated image which has had all well-understood instrumental signatures removed. The following describes the data reduction pipeline for science data. Similar pipelines are used for reducing calibration data.

The IRAC pipeline consists of two principal parts: the data reduction software modules and the calibration server. The individual modules each correct a single instrumental signature. They are written as standalone code executable from the UNIX command line. Each uses FITS files and text configuration files as input and produces one or more FITS files and log files as output. These modules are strung together with a single PERL script. The actual calibration data needed to reduce a given DCE is produced via "calibration pipelines." A raw IRAC DCE is thus "passed" between successive modules, and at each step becomes closer and closer to a finished, fully reduced image. The following sections describe the reduction steps used to produce the BCD data.

5.1.1 SANITY DATATYPE (parameter checking)

Before data proceeds through the pipeline, it is checked to ensure that it is of the type of data expected. In particular, ancillary keywords are checked against their expected values to ensure that they are in range and of the expected logical state. These include the shutter state (open/closed), transmission and flood calibrator lamp status (on/off), and read mode (full/subarray).

5.1.2 SANITY CHECK (image contents checking)

Before pipeline processing continues, the actual image contents are checked to ensure that they contain values expected for actual image data. These tests include checking to insure that the image is not all zeros, that the pixels are not all identical, or that areas of the image do not have an abnormal data range.

5.1.3 TRANHEAD (header processing)

The FITS headers delivered by JPL/FOS are translated into a more readable format. For example,

```
A0612D00= 14478455 / AINTBEG
A0612E00= 1.4478455E5 / [Sec]
A0614D00= 8 / AFOWLNUM
A0614E00= / [NONE]
A0615D00= 44 / AWAITPER
```

A0615E00= / [NONE]
A0657D00= 14479495 / ATIMEEND
A0657E00= 1.4479495E5 / [Sec]

is translated to:

AINTBEG = 144784.55 / [Secs since IRAC turn-on] Time of integ. start
ATIMEEND= 144794.95 / [Secs since IRAC turn-on] Time of integ. end
AFOWLNUM= 8 / Fowler number
AWAITPER= 44 / [0.2 sec] Wait period
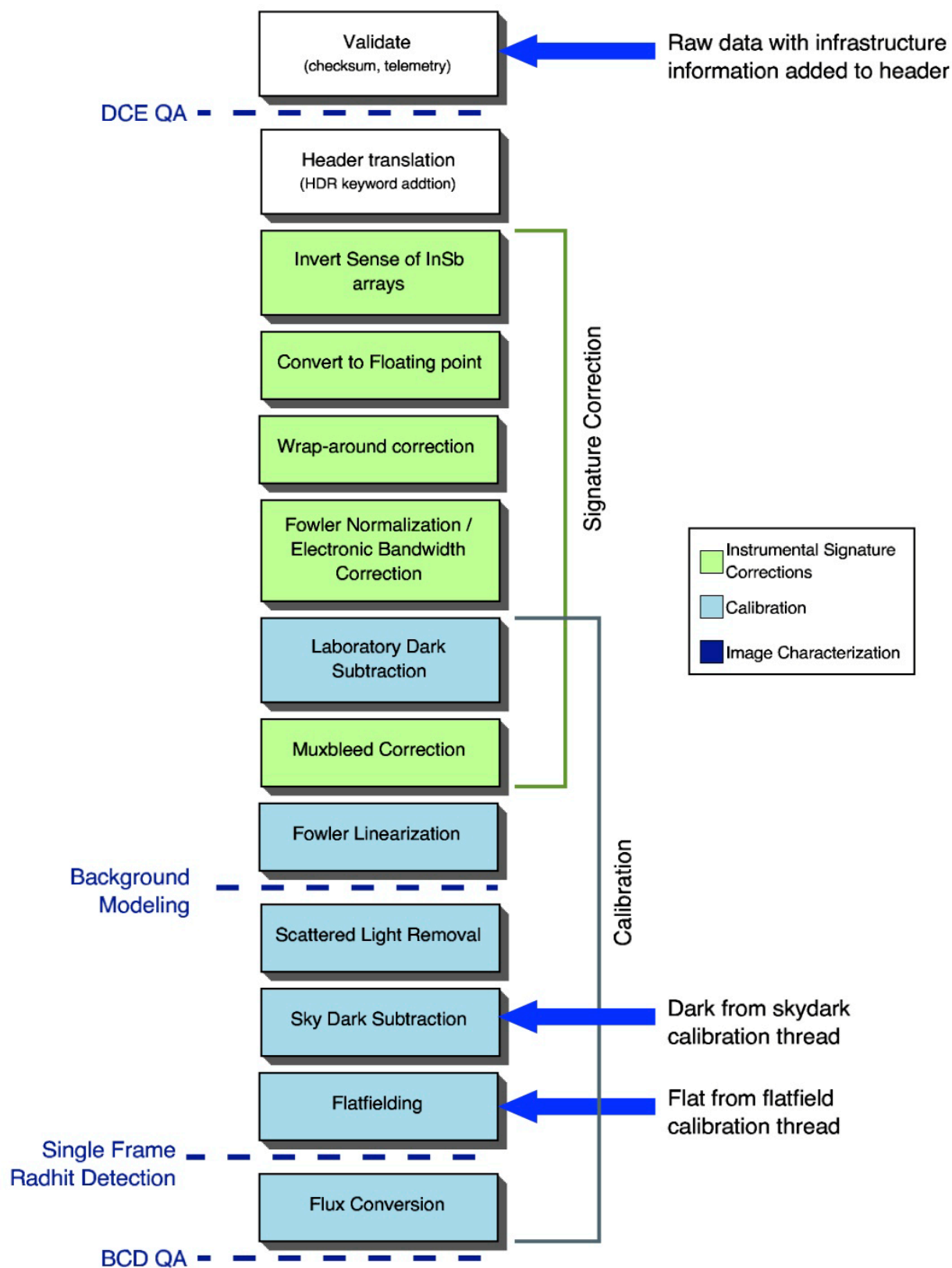
Figure 5.1: Data flow for processing a raw IRAC science DCE into a BCD that is described in this Chapter.

It is also at this stage that "derived" parameters, most notably the integration time, are added to the headers. The integration time is related to the Fowler number (AFOWLNUM) and the number of wait periods (AWAITPER) via

$$EXPTIME = mode * (AWAITPER + AFOWLNUM) \qquad (5.1)$$

The integration time is stored in the header in the keyword EXPTIME. Another timescale of importance is the frame time. This is the actual length of time that the observation was integrating on the sky, and is equal to

$$FRAMTIME = mode * (AWAITPER + 2 * AFOWLNUM) \qquad (5.2)$$

The factor "mode" is equal to 0.2 seconds for full-array mode, and 0.01 seconds for subarray mode. The read-mode is determined by the least significant bit of the ancillary keyword AREADMOD. If AREADMOD is 0 (or even) then the mode is full-array. If it is 1 (or odd) then the image is sub-array.

Note that because of TRANHEAD processing, the headers of the raw data and the final BCD data products are not identical. In general, users should only need to read the BCD headers. However, if it becomes somehow necessary to examine any of the camera telemetry (voltages, currents, etc.), then they can be read from the complete raw data header.

5.1.4 INSBPOSDOM (InSb array sign flipping)

The IRAC InSb arrays (channels 1 and 2) were operated in such a way that flux appears "negative" in the raw data (Figure 5.2). That is, data numbers start at 65,535 (16-bit max) for zero light levels and become increasingly close to 0 as light levels increase. The INSBPOSDOM module rectifies this so that increasing DN yields increasing flux (0 to 65,535), as is more common. This is done by

$$A_{out} = (65,535 - A_{in}) \qquad (5.3)$$

where A is the pixel intensity in DN for the two InSb arrays (ACHANID = 1 or 2). ACHANID is turned into CHNLNUM in the BCD header by the last step in the pipeline.
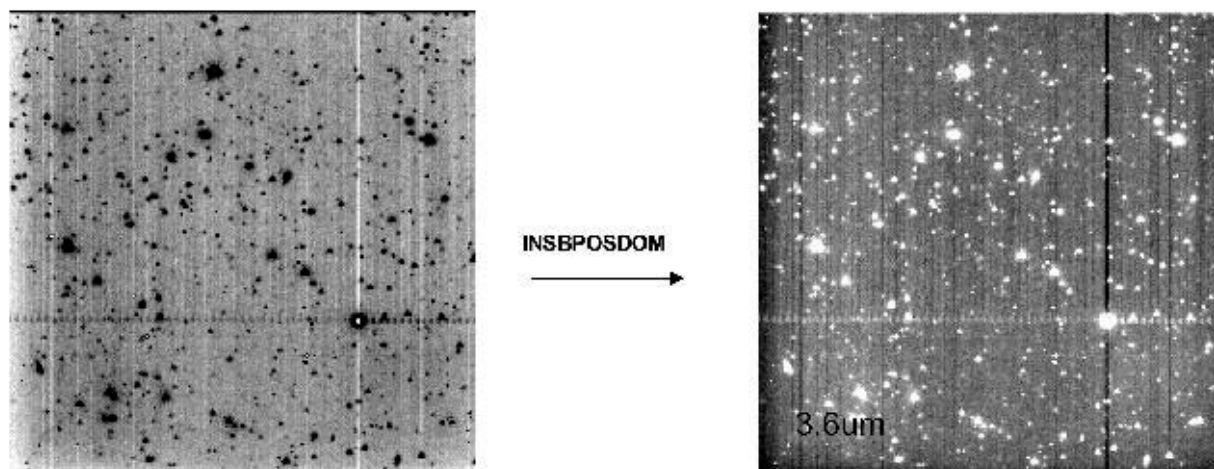
Figure 5.2: INSBPOSDOM works only on the two InSb arrays (Channels 1 & 2) and reverses the sense of intensities.

5.1.5   CVTI2R4 (byte type changing)

Data are converted from the native unsigned 16-bit format used by IRAC to the 32-bit floating point format used in astronomical calculations. At this point, the following DN is added to all pixels in order to account for the bias introduced by the spacecraft on-board bit truncation.

$-0.5 \times (1 - 2^{-ABARREL})$ for channels 1 and 2
$+0.5 \times (1 - 2^{-ABARREL})$ for channels 3 and 4

Here, "ABARREL" is the barrel-shift number keyword where the bit truncation occurs (see Section 5.1.7). Also, if the header indicates that any rows or columns are blank (usually due to data loss during transmission from Spitzer to the ground), then those pixels are set equal to NaN's.
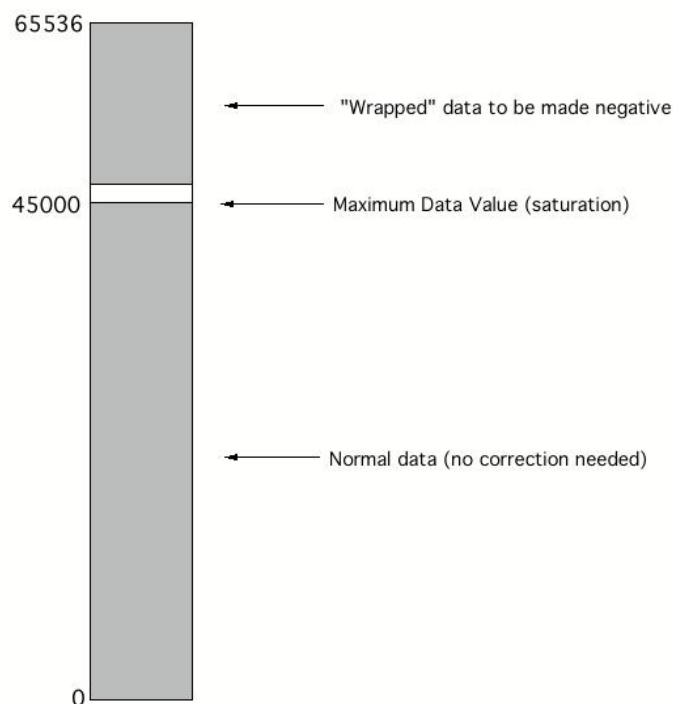
Figure 5.3: Diagram of the wrapping of negative values due to truncation of the sign bit.

5.1.6   *Wraparound Correction: IRACWRAPDET AND IRACWRAPCORR*

IRAC suffers from two kinds of "wraparound" errors, wherein DN values are actually multi-valued. That is, a given DN actually corresponds to more than one possible flux level.

IRACWRAPDET (sign truncation wraparound)
As a means of data compression, IRAC discards the sign bit of its data before transmission to the ground. This creates an ambiguity in that negative numbers appear in the raw data as very large positive numbers. However, by design the detector reaches physical saturation before "electronic" (A/D) saturation (Figure 5.3). That is, the maximum physical values the detectors ever have are around 45,000 DN for the InSb arrays and 60,000 DN for the Si:As arrays, which are less than the maximum 16-bit value of 65,535. IRAC uses the 2s-complement storage system for negative numbers. In this system negative numbers are denoted by setting the sign bit and then complementing (i.e., flipping) all the remaining bits. For example, in 2s-complement storage, −1 is represented by 65534 in unsigned integer form. Therefore, values higher than the maximum saturation levels must be "wrapped" negative numbers. For each array a set of maximum values has been chosen such that no pixel will be erroneously identified as wrapped. The module then flags any pixels lying in the "wraparound" DN region. Observers are strongly cautioned to check for possible saturation problems by examining the structure in their data. If a user finds that any

part of their image is near the saturation value (typically either 45,000 DN in channels 1 and 2 or 60,000 DN in channels 3 and 4) then they should suspect surrounding pixels of being near saturation.

IRACWRAPCORR (wraparound correction)
This module uses the flag bits set by the previous module and attempts to correct the wraparound problem (Figure 5.4). Note that both the sign truncation and the non-linearity wraparound, i.e., doughnuts, are corrected in the pipeline. The sign truncation correction is made by

$$A_{corrected} = A_{uncorrected} - 65535. \tag{5.4}$$

5.1.7 IRACNORM (Fowler sampling renormalization)

IRAC data are taken with Fowler (multi) sampling in order to reduce read noise. This is done by non-destructively reading the array multiple times (set by the Fowler number), and accumulating the sum into an internal register. Since these reads are summed, the result must be divided by the number of reads in order to get the actual number of DN. Additionally, when data are transmitted to the ground, a variable number of least significant bits are discarded as a means of data compression (Figure 5.5). In order to correct for the effects of bit-truncation and Fowler sampling the data are transformed by

$$A_{out} = \frac{A_{in} \times 2^{ABARREL}}{AFOWLNUM} \tag{5.5}$$

where ABARREL is the barrel-shift keyword and AFOWLNUM is the Fowler number keyword. Note that in normal usage the Fowler number and barrel shift actually used and commanded by the science center are such that they cancel, i.e.,

$$\frac{2^{ABARREL}}{AFOWLNUM} = 1 \tag{5.6}$$

and hence observers should not be surprised if this module normally appears to do nothing.
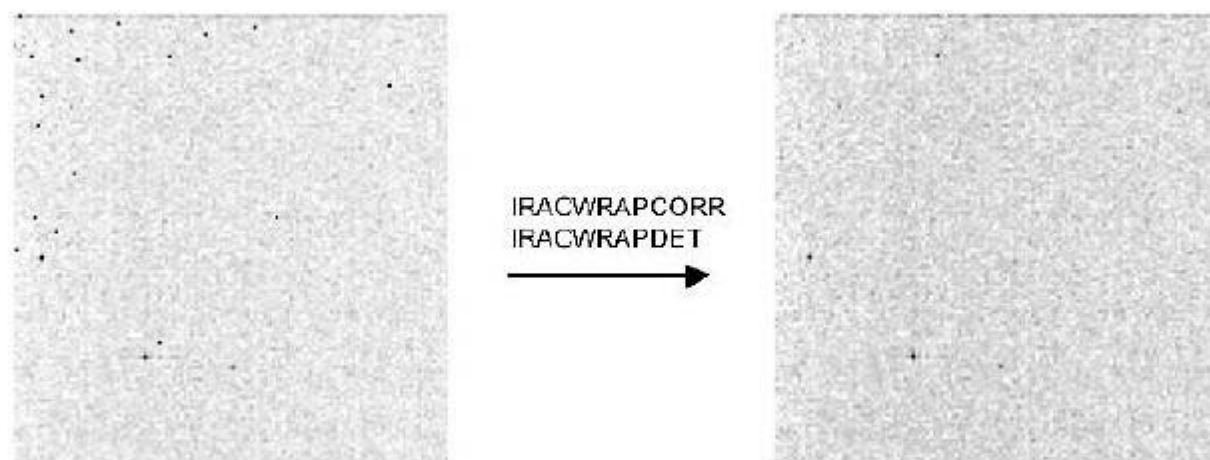
Figure 5.4: Application of IRACWRAPCORR to Channel 1 data. The many apparently "hot" pixels are actually wrapped negative values, which are detected on the basis of their vastly exceeding the physical saturation value for the detectors, and corrected by subtracting the appropriate value. Real hot pixels do not exceed the physical saturation value, and hence are not changed.
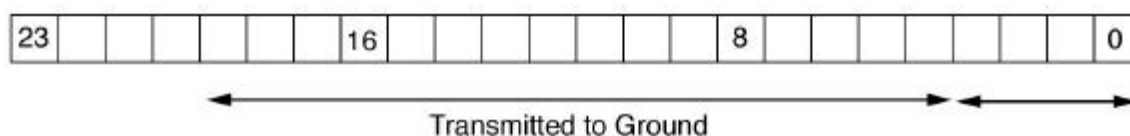
Figure 5.5: Illustration of bit truncation used by IRAC for ground transmission, necessitating IRACNORM. The internally stored 24-bit word is truncated to 16 bits, with a sliding window set by the barrel shift value. Illustrated is the case for ABARREL=4.

5.1.8 *SNESTIMATOR (initial estimate of uncertainty)*

The module SNESTIMATOR calculates the uncertainty of each pixel based on the input image (here, the input image is the output of IRACNORM). The uncertainty for each pixel is estimated as the Poisson noise in electrons and the readout noise added in quadrature. The formula for the calculation is as follows:

$$\sigma^2 = \sigma^2_{readnoise} + \sigma^2_{poisson} \tag{5.7}$$

To obtain an expression in DN, σ is divided by Gain. This uncertainty image will be carried through the pipeline, and additional uncertainties (e.g., dark and flat uncertainties) will be added in quadrature when appropriate.

5.1.9 IRACEBWC (limited cable bandwidth correction)

The cables that connect the IRAC Cold Assembly (the detectors) to the Warm Electronics Assembly (the readout electronics) have a characteristic time constant similar to the rate at which individual pixels are read. As a result, all pixels have an "echo" or ghost in the following readout pixel (Figure 5.6). Since the pixels are contained in four readout channels, the "next" pixel is actually four pixels to the right. The first pixel read out in an IRAC image is the first data byte in the image, and is situated in the lower left corner in most astronomical display software. This effect is corrected for by using the known readout order of the pixels. Starting at the first pixel, we correct the following pixel, and so on. An additional wrinkle is that the time required to go from the end of one row to the beginning of the next is slightly longer (by 75%) than the time to go from one column to the next in the same row. As a result, a slightly different coefficient must be applied. The task is simplified by two things. First, the effect is so small that it is only necessary to correct the following pixel, as the next echo is below $1e^{-5}$th of the original in intensity. Second, the time of the effect is much faster than the decay time. Thus, the problem needs only to be solved in one direction. The current bandwidth coefficients are given in Table 5.1. They are applied using

$$A_{n+4} = A_{n+4} - \kappa A_n \qquad (5.8)$$

where A is the pixel intensity in DN and κ is the correction coefficient for a given readout channel (of 4). A different value of κ is used for correcting the first 4 pixels in a row, based on the pixel values of the last four pixels of the previous row.

Table 5.1: Bandwidth correction coefficients.

Channel 1				
Readout	1	2	3	4
κ	1.58e-3	2.17e-3	2.33e-3	1.64e-3
κ(end of row)	1.2e-5	2.1e-5	2.4e-5	1.3e-5
Channel 2				
Readout	1	2	3	4
κ	1.71e-3	3.63e-3	1.06e-3	1.11e-3
κ (end of row)	1.4e-5	5.2e-5	6.0e-5	6.6e-5
Channel 3				
Readout	1	2	3	4
κ	3.19e-3	1.04e-2	3.3e-3	2.09e-3
κ (end of row)	4.2e-5	3.3e-4	4.4e-5	2.0e-5
Channel 4				
Readout	1	2	3	4
κ	3.74e-3	3.74e-3	3.74e-3	3.74e-3
κ (end of row)	5.5e-5	5.5e-5	5.5e-5	5.5e-5

5.1.10 Dark Subtraction I: FFCORR (first frame effect correction) or LABDARKSUB (lab dark subtraction)

The true dark current in the IRAC detectors is actually very low – the most notable dark current features are the electronic glows seen in the Si:As arrays (channels 3 & 4). However, the IRAC arrays experience considerable pedestal offsets which are commonly of the order of tens of DN. These offsets are dependent on the Fowler sampling, exposure time, and operation history of the arrays, and are believed to be due to very small thermal changes in the internal IRAC cold electronics. The most significant of these offsets is the "first-frame" effect: the laboratory measurements show that the dark patterns and DC levels change as a function of the time elapsed between the end of the previous frame and the start of the current frame (called "delay time"). The first frame of a series of exposures is most affected, and therefore this effect is

called "the first-frame effect". Figure 5.7 shows how the DC levels of darks change as a function of delay-time.
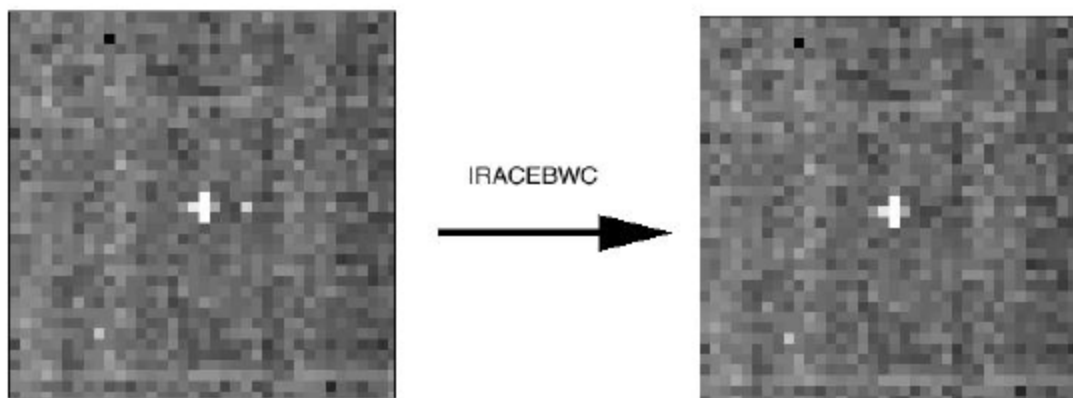
Figure 5.6: Correction of cable-induced bandwidth error by IRACEBWC. The illustrated data show a cosmic ray hit.

Due to the decision not to use the photon-shutter on the IRAC for dark and flat measurements, we have a somewhat sophisticated dark subtraction procedure. There will be two steps for the dark subtraction, one using a dark from the ground-based laboratory measurements (called, "lab darks"), and another using a delta dark which is the difference between the lab dark and the sky dark measured at the low zodiacal light region.

In the first step of dark subtraction, we subtract a calibrated lab dark from the data at this point in the processing. This lab dark subtraction occurs before the linearization of the array, so that we can linearize the data as well as possible. The labdark subtraction will be handled by a combination of modules including LABDARKSUB and FFCORR depending on which kind of labdark data are needed. In some observing modes (subarray mode, shortest frames within the HDR mode and the first frame of an observation or AOR), not enough data are available to construct delay-time dependent darks. In such cases, a single mean dark has been computed using 30 sec as a delay time, and it is used as a labdark. The LABDARKSUB module subtracts this mean labdark. The correction of the first-frame effect for all other frames is handled by the FFCORR module, which interpolates the library of labdarks taken at different exposure times with different delay times, and creates a labdark corresponding to the particular delay time of the frame being calibrated. These delay-time dependent darks are then subtracted from the IRACEBWC-processed frame. Therefore, FFCORR requires a number of different labdarks taken with different delay times to calibrate properly. These were taken pre-launch and have been loaded into the calibration database. The IRAC pipeline determines the delay time (header keyword INTRFRDLY), and the lab dark file (header keyword LBDRKFLE) that was subtracted is placed within the header keywords of the BCD.
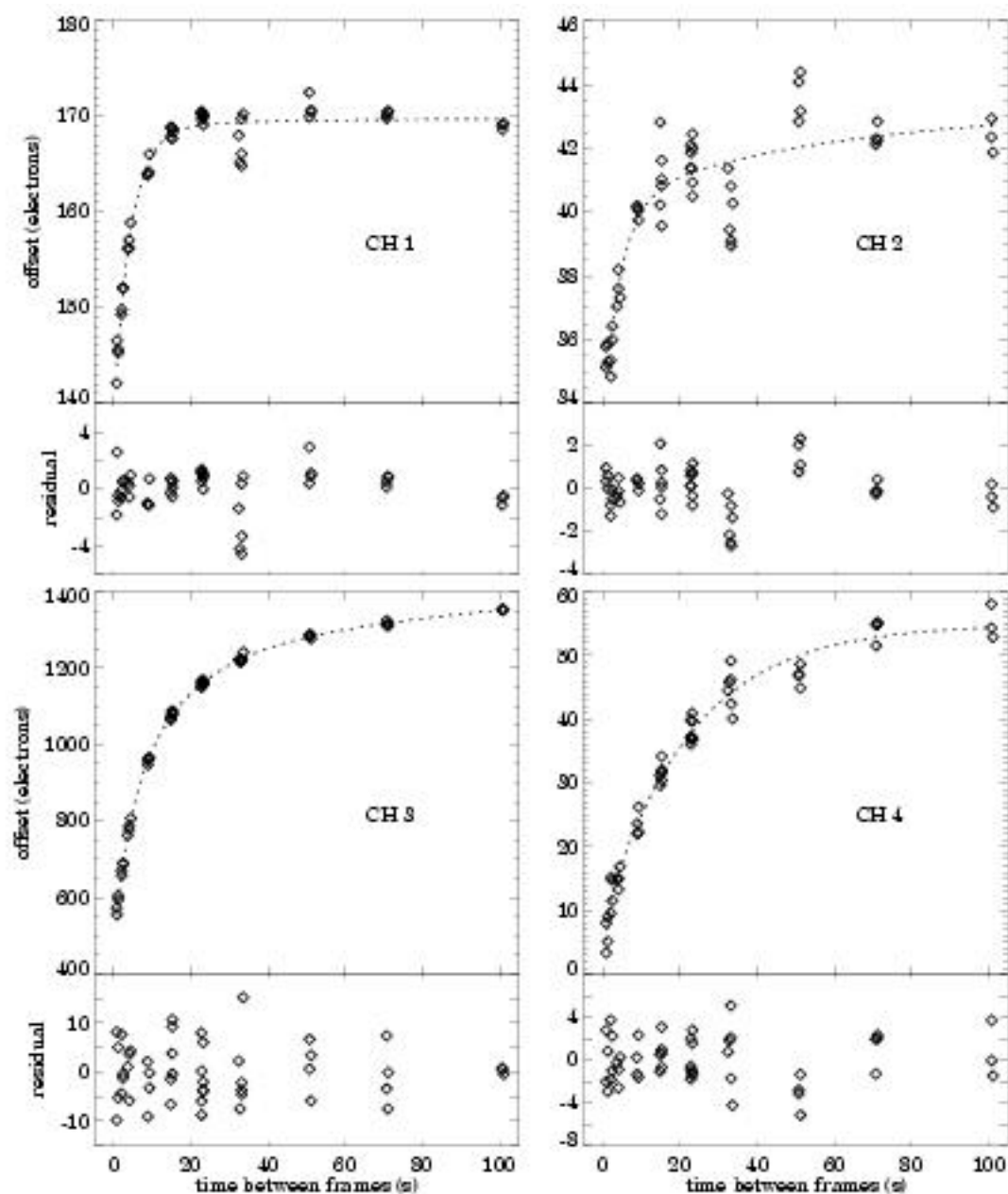
Figure 5.7: First-frame effect. Dark counts as a function of interval between frames. This figure is for a 30 second exposure frame.

The second step of the dark subtraction uses a delta-dark found in the SKYDARKSUB module described below. This "skydark", described in Section 4.1, is subtracted from the IRAC image after the linearization

and should take away any additional dark features which are not present in the labdarks, but exist in the flight data. Note that the delta-dark includes the sky background around the low-zody region.

5.1.11 MUXBLEEDCORR (electronic ghosting correction)

The InSb arrays suffer from an effect known as "muxbleed". This is believed to be a result of operating the arrays at unusually cold temperatures. When a bright source is read out, the cold electronics do not return to their quiescent state for a considerable length of time. The result is a ghosting along the pixel readout channels, sometimes referred to as "ant trails" (Figure 5.8). The effect is easily noticeable against a low background (such as a dark current measurement), and can extend the full length of the array. The muxbleed flux is not real – it is not "borrowed" from the actual source and as such needs to be accounted for, or removed, unlike CTE smearing in CCDs.
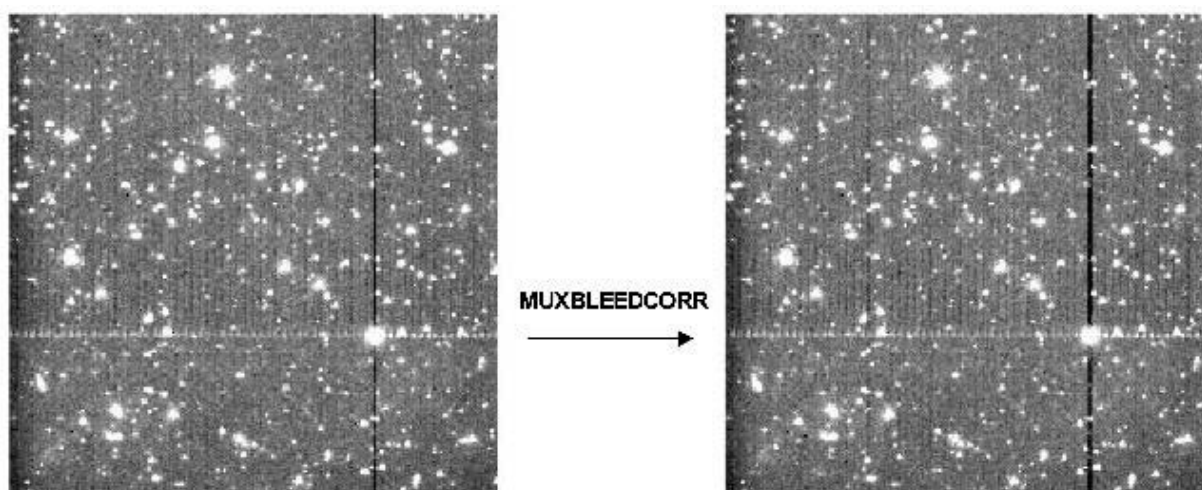
MUXBLEEDCORR

Figure 5.8: Correction of pseudo-muxbleed for channel 1. Shown is a bright source within a calibration AOR and a background of sources under the muxbleed limit.

This effect is complicated. It appears that a pixel bleeds only as a result of the light falling onto it, and not as the sum of the value of the pixel plus the bleeding from previous pixels. Since we know the readout order of the pixels, we can start by correcting all pixels downstream from the first pixel, and then move on to the next pixel. The exact shape of the mubleed pattern, obtained after examining hundreds of muxbleed incidences is summarized as a modified polynomial:

$$Log(MuxbleedIntensity) = 3.1880 - 2.4973x + 1.2010x^2 - 0.2444x^3 \tag{5.9}$$

where

$$x = \log_{10}(\text{pixel number} + 1) \qquad (5.10)$$

Pixel numbers are counted along the detector readout direction, starting from the muxbleed causing pixel (pixel number zero). The muxbleed pattern appears to be independent of readout channel, Fowler sampling, etc. Furthermore, the pattern seems to be applicable to both the channel 1 and channel 2 muxbleed, with a slightly different scaling factor. The severity of muxbleed depends on the brightness of the bleeding pixel. Muxbleed scaling laws as a function of the bleeding pixel were obtained for channels 1 and 2. They are

$$ScalingFactor = A \cdot \exp\left(-\frac{1}{2} \left(\frac{x - B}{C} \right)^2 \right) \qquad (5.11)$$

where

$$x = \log_{10}(\text{bleeding pixel intensity in DN}). \qquad (5.12)$$

For channel 1, A = 0.6342, B = 5.1440 and C = 0.5164. For channel 2, A = 0.3070, B = 4.9320 and C = 0.4621. Both the scale factors and the muxbleed pattern are fixed for all pixels in a given array. Muxbleed from triggering pixels with brightnesses below 10,000 DN is not corrected, because the corrections in these cases would be just a few times the read noise. Muxbleed is also not corrected in the subarray observations.

Observers should note that calibration darks are not muxbleed corrected. Muxbleed occurs in these images due to the presence of hot pixels. However, this occurs equally both in the darks and in the science frames and has been found to subtract noiselessly from the science data. Thus, any dark frame muxbleed is simply considered a feature of the darks.

Note that the muxbleed correction decribed here does not correct 100% of the muxbleed effect.

5.1.12 DARKDRIFT (``readout channel'' bias offset correction)

Each IRAC array is read out through four separate channels. The pixels read out by these channels are arranged vertically, and repeat every four columns. Small drifts in the bias levels of these readouts, particularly relative to the calibration dark data, can produce a vertical striping called the "jailbar" effect.

This is mostly noticeable in very low background conditions. This is corrected by adding to the individual readout channels a common mean offset. For any image, the flux in a pixel is assumed to be

$$A_{i,j} = S_{i,j} + B + D_{C_{i,j}} + D_{O_{i,j}} \tag{5.13}$$

where i is the readout channel number (1–4), j is the row number, A is the detected intensity in DN, S is the incident "science flux" (celestial background + objects), B is a constant offset in the frame, D_C is the standard calibration dark, and D_O is the dark offset. The first dark varies on a pixel by pixel basis, whereas the offsets are assumed to vary on a readout channel basis. It can be assumed that the mean $S_{i,j}$ is the same for all readout channels i, and therefore there is a mean estimator function M for each readout channel

$$M_i = \text{MeanEstimator}(S_{i,0}...S_{i,n}) \tag{5.14}$$

The corrected image (post dark-subtraction) is then

$$A_{i,j}' = A_{i,j} - (M_i - \frac{1}{4}\sum_{i=1}^{4} M_i) \tag{5.15}$$

5.1.13 FOWLINEARIZE (detector linearization)

Like most detectors, the IRAC arrays are non-linear near full-well capacity. The number of read-out DN is not proportional to the total number of incident photons, rather it becomes increasingly small as the number of photons increases. In IRAC, if fluxes are at levels above half full-well (typically 20,000–30,000 DN in the raw data), they can be non-linear by several percent. During processing the raw data are linearized on a pixel-by-pixel basis using a model derived from ground-based test data and re-verified in flight. The software module that does this is called FOWLINEARIZE. FOWLINEARIZE works by applying a correction to each pixel based on the number of DN, the frame time, and the linearity solution. For channels 1, 2 and 4, we use a quadratic solution, i.e., we model the detector response as

$$DN_{obs} = kmt - Ak^2t^2 \qquad (5.16)$$

The linearization solution to the above quadratic model is:

$$DN = \frac{-1 + \sqrt{1 - 4L\alpha DN_{obs}}}{2L\alpha} \qquad (5.17)$$

where

$$L = \frac{\alpha}{n(w+n)^2}\left[\left(\sum_{n+w+1}^{2n+w} i^2 - \sum_{1}^{n} i^2\right) - 2(1 - \frac{t_d}{t_c})n(n+w)\right], \qquad (5.18)$$

and $\alpha = \dfrac{A}{m^2}$, n is the Fowler number, and w is the wait period. The above expression for L is the

correction required to account for multi-sampling. This is required because the multi-sampling results in the apparent time spent integrating not actually being equal to the real time spent collecting photons. Note that t_d is the time between the reset and the 1st readout of the pixel. For channel 3, we use a cubic linearization model:

$$DN_{obs} = Ckt^3 + Akt^2 + kmt \qquad (5.19)$$

For the cubic model, the solution is derived via a numerical inversion.

5.1.14 BGMODEL (zodiacal background estimation)

For this module, a spacecraft-centric model of the celestial background was developed. For each image, the zodiacal background will be estimated (a constant for the entire frame) based on the pointing and time that the data were taken. This value is written to the header keyword ZODY_EST in units of MJy/sr. The zodiacal background is also estimated for the subtracted skydark (see next module) and placed in the header keyword SKYDRKZB.

5.1.15 Dark Subtraction II: SKYDARKSUB (sky "delta-dark" subtraction)

This module, the second part of dark subtraction, strongly resembles traditional ground-based data reduction techniques for infrared data. Since IRAC did not use the photon-shutter for its dark measurement, a pre-selected region of low zodiacal background in the north ecliptic cap is observed in order to create a "skydark". At least twice during each campaign a library of skydarks of all Fowler numbers and frame times were observed, reduced, and created by the calibration pipeline. The skydarks have had the appropriate labdark subtracted in their DARKCAL pipeline and are therefore a "delta-dark." These skydarks are then subtracted from the data in the pipeline within this module, based on the exposure time, channel and the time of the observation. Note that there is a problem with the skydark subtraction from the 58th frame in the subarray observations which leaves the background level in that frame different from the rest. While this should not affect photometric measurements, users may want to choose to leave the 58th subarray frames out from their analysis.

5.1.16 FLATAP (flatfielding)

Like all imaging detectors, each of the IRAC pixels has an individual response function (i.e., DN/incident photon conversion). To account for this pixel-to-pixel responsivity variation, each IRAC image is divided by a map of these variations, called a "flatfield."

Observations are taken of pre-selected regions of high-zodiacal background with relatively low stellar content located in the ecliptic plane. They are dithered frames of 100 seconds in each channel. These observations are processed in the same manner as science data and then averaged with outlier rejection. This outlier rejection includes a sophisticated spatial filtering stage to reject the ever-present stars and galaxies that fill all IRAC frames of this depth. The result is a smoothed image of the already very uniform zodiacal background. This "skyflat" is similar to flatfields taken during ground-based observations. The flatfields are then normalized to one. The flatfield calibration pipeline produces a library of the flat fields throughout each campaign since a flatfield is taken at the beginning and end of an observing campaign. We have found that there is no difference in flatfields from campaign to campaign, so a "super skyflat," composed of five full years worth of data and therefore of very high S/N, is used for processing science data in the BCD pipeline. It should be noted that this flatfield is generated from a very red target, i.e., the zodiacal background. There is considerable evidence for a spatially-dependent color term in the IRAC calibration (which is roughly a quadratic polynomial function across the array). Objects that have color temperatures radically different from the zodiacal background require an additional multiplicative correction of order 5%–10%. This is not treated by the flat-fielding stage.

Software module FLATAP applies the flats generated by the calibration server. This operation is equivalent to division by the flat.

5.1.17 IMFLIPROT

IRAC utilizes beamsplitters to redirect the incoming light for a given FOV through each of the two filters. As a result, although for a given FOV two filters such as for channel 1 and 3 view the same piece of sky, the detectors see (and hence read out) mirror images of each other. An image transposition is applied to ensure that the two filters for each FOV are in the same orientation (**Figure 5.9**). Note that the *images are not de-rotated*, that is, each is now correct relative to the other filter for a given FOV, but all of the images still have the effects of spacecraft rotation.

$$A_{x,y}^{flipped} = A_{x,255-y}^{original} \qquad (5.20)$$
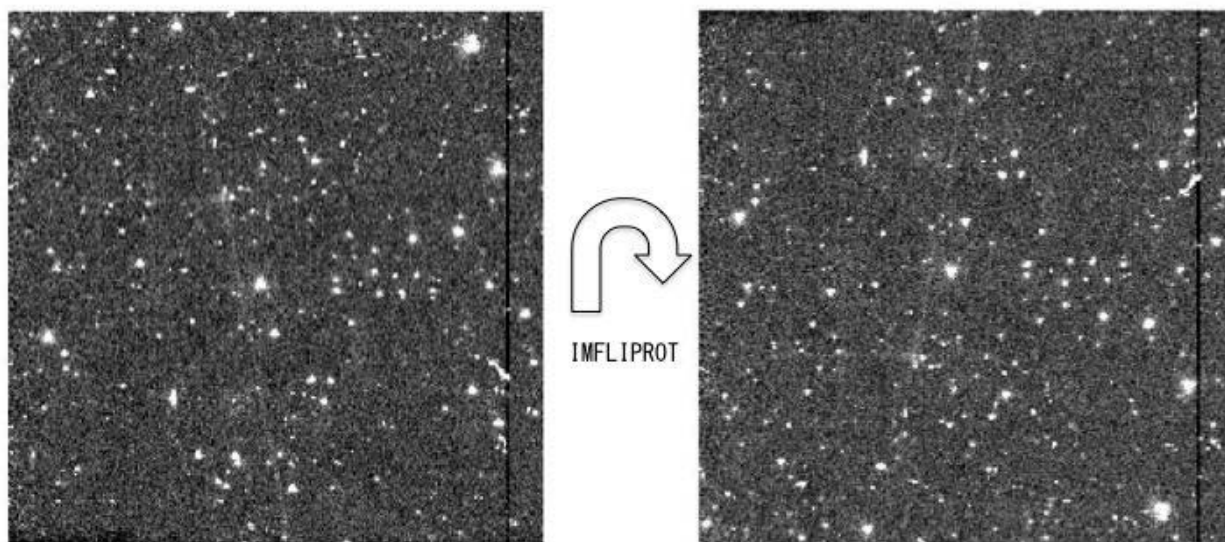
Figure 5.9: Transposition of an IRAC channel 1 dark image by the IMFLIPROT module.

Currently, channels 1 & 2 are flipped about their vertical axis, which is illustrated by the equation above. The image flip of these two channels provides an array orientation with the E axis located to the left of N for all channels. Since this image transposition is applied after skydark subtraction and flatfielding, those calibration files do not have such an orientation.

5.1.18 DETECT-RADHIT (cosmic ray detection)

Within this module, individual frames are analyzed for probable radiation hits (cosmic rays), and the results appear as a flag in the imask file. This is computed by a median filtering technique. Input images are read in, and a median filter is applied. The difference between the input image and the median-filtered image is then computed. Pixels above a specified threshold (i.e., are "pointier" than is possible for a true

point source) are then flagged in a mask image (bit 9 of imask is set when a pixel is suspected to be hit by a cosmic ray).

5.1.19 DNTOFLUX (flux calibration)

IRAC flux calibration is tied to a system of celestial standards measured at regular intervals during each campaign. The IRAC IST provides the calibration server with calibration files based upon these measurements. Because the flux calibration is determined from stellar point sources, the calibration for extended sources is somewhat different. For details of the photometric calibration and correction factors, see Chapter 4. The IRAC data are calibrated in units of MJy/sr in this module. This is accomplished by multiplying the data image by a conversion factor provided by the calibration server. This conversion factor is written to the data header as:

```
                / PHOTOMETRY
COMMENT 1 blank line
BUNIT = 'MJy/sr '            / Units of image data
FLUXCONV= 0.2008            / Flux Conv. factor (MJy/sr per DN/sec)
GAIN = 3.8                  / e/DN conversion.
```

5.1.20 Pointing Transfer (calculation of pointing information)

The Pointing Transfer pipeline is a separate script from the actual data reduction pipeline script, designed to insert raw-pointing and distortion information into the FITS headers of BCDs. Like the reduction pipeline, it executes on a per-BCD basis. Pointing data was acquired by the spacecraft star-tracker at a rate of 2 Hz, transferred to the boresight onboard, and down-linked every 12 hours as a Boresight Pointing History File (BPHF). The BPHF is received via a separate telemetry stream from the science data. The first step in pointing transfer is to acquire the portion of the BPHF which spans the integration time of the BCD (getPH module). The 2 Hz sampled data are then transferred to the specific channel-dependent science FOV using a set of Euler transformations handled by the "BORESIGHTTRAN module". The Euler angles relating the boresight and FOV positions have been determined in-flight and are stored in a configuration file.

The pointing samples are then averaged and combined by the "ANGLEAVG" module to compute the raw-pointing for the BCD: CRVAL1 (RA), CRVAL2 (Dec) and PA (position angle). These, along with uncertainties and reference pixel coordinates (CRPIX1, CRPIX2), are inserted as keywords into the FITS header of the BCD. The module also computes a CD matrix and transfers distortion coefficients (represented in the pixel coordinate frame) from a calibration file to the FITS header. The default projection type for the celestial reference system (CTYPE keyword) is "TAN-SIP". This is a tangent (TAN) projection modified to make use of the Spitzer Imaging (distortion) Polynomials (SIP) in coordinate mappings.

The Final Product Generator (FPG) is executed at the end. This reformats the FITS header and adds additional keywords, which are most useful to the user, from the database. An example of a BCD header containing pointing and distortion information is given below.

```
SIMPLE  =                       T / Fits standard
BITPIX  =                     -32 / FOUR-BYTE SINGLE PRECISION FLOATING POINT
NAXIS   =                       2 / STANDARD FITS FORMAT
NAXIS1  =                     256 / STANDARD FITS FORMAT
NAXIS2  =                     256 / STANDARD FITS FORMAT
ORIGIN  = 'Spitzer Science Center' / Organization generating this FITS file
CREATOR = 'S18.7.0 '              / SW version used to create this FITS file
TELESCOP= 'Spitzer '             / SPITZER Space Telescope
INSTRUME= 'IRAC    '             / SPITZER Space Telescope instrument ID



            / TARGET AND POINTING INFORMATION


OBJECT  = 'NGC7479 '             / Target Name
OBJTYPE = 'TargetFixedSingle'    / Object Type
CRPIX1  =                    128. / Reference pixel along axis 1
CRPIX2  =                    128. / Reference pixel along axis 2
CRVAL1  =     346.229408109806 / [deg] RA at CRPIX1,CRPIX2 (using Pointing Recon
CRVAL2  =      12.3406747724052 / [deg] DEC at CRPIX1,CRPIX2 (using Pointing Reco
CRDER1  = 3.47278123674643E-05 / [deg] Uncertainty in CRVAL1
CRDER2  = 3.44327670377712E-05 / [deg] Uncertainty in CRVAL2
RA_HMS  = '23h04m55.1s'          / [hh:mm:ss.s] CRVAL1 as sexagesimal
DEC_DMS = '+12d20m26s'           / [dd:mm:ss] CRVAL2 as sexagesimal
RADESYS = 'ICRS    '             / International Celestial Reference System
EQUINOX =                   2000. / Equinox for ICRS celestial coord. system
CD1_1   = 0.000165673336023108 / Corrected CD matrix element with Pointing Recon
CD1_2   = -0.000296839887227466 / Corrected CD matrix element with Pointing Reco
CD2_1   = -0.000296695378233646 / Corrected CD matrix element with Pointing Reco
CD2_2   = -0.00016538074830257 / Corrected CD matrix element with Pointing Recon
CTYPE1  = 'RA---TAN-SIP'         / RA---TAN with distortion in pixel space
CTYPE2  = 'DEC--TAN-SIP'         / DEC--TAN with distortion in pixel space
PXSCAL1 =    -1.22334117768332 / [arcsec/pix] Scale for axis 1 at CRPIX1,CRPIX2
PXSCAL2 =     1.22328355209902 / [arcsec/pix] Scale for axis 2 at CRPIX1,CRPIX2
PA      =      -119.12383984174 / [deg] Position angle of axis 2 (E of N) (was OR
UNCRTPA = 0.000467418894131902 / [deg] Uncertainty in position angle
CSDRADEC= 1.31286126610331E-06 / [deg] Costandard deviation in RA and Dec
SIGRA   =    0.0965180263226379 / [arcsec] RMS dispersion of RA over DCE
SIGDEC  =    0.0477081433171542 / [arcsec] RMS dispersion of DEC over DCE
SIGPA   =     0.627707783301654 / [arcsec] RMS dispersion of PA over DCE
PA      =      -119.12383984174 / [deg] Position angle of axis 2 (E of N) (was OR
RA_RQST =     346.229439557555 / [deg] Requested RA at CRPIX1, CRPIX2
DEC_RQST=      12.3408384725542 / [deg] Requested Dec at CRPIX1, CRPIX2
PM_RA   =                      0. / [arcsec/yr] Proper Motion in RA (J2000)
PM_DEC  =                      0. / [arcsec/yr] Proper Motion in Dec (J200)
RMS_JIT = 0.00561943353954093 / [arcsec] RMS jitter during DCE
RMS_JITY= 0.00415225189801845 / [arcsec] RMS jitter during DCE along Y
RMS_JITZ= 0.00378640165338011 / [arcsec] RMS jitter during DCE along Z
SIG_JTYZ= -0.000574938554882557 / [arcsec] Costadard deviation of jitter in YZ
PTGDIFF =    0.599601238096299 / [arcsec] Offset btwn actual and rqsted pntng
PTGDIFFX=    0.460985501941048 / [pixels] rqsted - actual pntng along axis 1
PTGDIFFY=   -0.383877068036649 / [pixels] rqsted - actual pntng along axis 2
RA_REF  =     346.235833333333 / [deg] Commanded RA (J2000) of ref. position
DEC_REF =     12.3227777777778 / [deg] Commanded Dec (J2000) of ref. position
USEDBPHF=                      T / T if Boresight Pointing History File was used
```

Pipeline Processing   **92**   Level 1 (BCD) Pipeline

```
BPHFNAME= 'SBPHF.0773452800.031.pntg' / Boresight Pointing History Filename
FOVVERSN= 'BodyFrames_FTU_14a.xls' / FOV/BodyFrames file version used
RECONFOV= 'IRAC_Center_of_3.6umArray' / Reconstructed Field of View
ORIG_RA =      346.229614257812 / [deg] Original RA from raw BPHF (without pointi
ORIG_DEC=      12.3407106399536 / [deg] Original Dec from raw BPHF (without point
ORIGCD11=        0.0001656730165 / [deg/pix] Original CD1_1 element (without point
ORIGCD12=       -0.0002968400659 / [deg/pix] Original CD1_2 element (without point
ORIGCD21=       -0.0002966955653 / [deg/pix] Original CD2_1 element (without point
ORIGCD22=       -0.0001653804356 / [deg/pix] Original CD2_2 element (without point



              / DISTORTION KEYWORDS

A_ORDER =                      3 / polynomial order, axis 1, detector to sky
A_0_2   =            2.9656E-06 / distortion coefficient
A_0_3   =            3.7746E-09 / distortion coefficient
A_1_1   =            2.1886E-05 / distortion coefficient
A_1_2   =           -1.6847E-07 / distortion coefficient
A_2_0   =           -2.3863E-05 / distortion coefficient
A_2_1   =            -8.561E-09 / distortion coefficient
A_3_0   =           -1.4172E-07 / distortion coefficient
A_DMAX  =                 1.394 / [pixel] maximum correction
B_ORDER =                      3 / polynomial order, axis 2, detector to sky
B_0_2   =              2.31E-05 / distortion coefficient
B_0_3   =           -1.6168E-07 / distortion coefficient
B_1_1   =           -2.4386E-05 / distortion coefficient
B_1_2   =           -5.7813E-09 / distortion coefficient
B_2_0   =            2.1197E-06 / distortion coefficient
B_2_1   =           -1.6583E-07 / distortion coefficient
B_3_0   =           -2.0249E-08 / distortion coefficient
B_DMAX  =                 1.501 / [pixel] maximum correction
AP_ORDER=                      3 / polynomial order, axis 1, sky to detector
AP_0_1  =           -6.4275E-07 / distortion coefficient
AP_0_2  =           -2.9425E-06 / distortion coefficient
AP_0_3  =            -3.582E-09 / distortion coefficient
AP_1_0  =           -1.4897E-05 / distortion coefficient
AP_1_1  =            -2.225E-05 / distortion coefficient
AP_1_2  =            1.7195E-07 / distortion coefficient
AP_2_0  =            2.4146E-05 / distortion coefficient
AP_2_1  =             6.709E-09 / distortion coefficient
AP_3_0  =            1.4492E-07 / distortion coefficient
BP_ORDER=                      3 / polynomial order, axis 2, sky to detector
BP_0_1  =           -1.6588E-05 / distortion coefficient
BP_0_2  =           -2.3424E-05 / distortion coefficient
BP_0_3  =             1.651E-07 / distortion coefficient
BP_1_0  =           -2.6783E-06 / distortion coefficient
BP_1_1  =            2.4753E-05 / distortion coefficient
BP_1_2  =            3.8917E-09 / distortion coefficient
BP_2_0  =            -2.151E-06 / distortion coefficient
BP_2_1  =               1.7E-07 / distortion coefficient
BP_3_0  =            2.0482E-08 / distortion coefficient
```

5.1.21 PREDICTSAT (HDR saturation processing)

PREDICTSAT is used to process data taken in the High Dynamic Range (HDR) mode by identifying saturated pixels using the information obtained from the shorter exposure time frames. Specifically, if the shorter frame is frame 1 and the longer frame is frame 2, and they have Fowler numbers F, wait periods W, pixel values DN, and saturation values of DN_{sat}, then if

$$\frac{DN_1(2F_2 + W_2)}{F_1 + W_1} > DN_{sat} \tag{5.21}$$

for any pixel, then that pixel is masked as saturated in the longer frame 2. Optionally, surrounding pixels may also be masked. This information is used in the post-BCD pipeline by the mosaicker when coadding frames to a priori reject saturated pixels before applying any other outlier rejection. High dynamic range data are received as separate DCEs by IRAC. No co-addition is done of these frames at the BCD level, but they are received by the user as separate BCDs.

5.1.22 LATIMFLAG (residual image flagging)

The IRAC pipeline detects and flags residual images left from imaging bright objects. A model of the charge decay is used to build a time history of the DCEs and sets a mask bit to indicate that a given pixel in the DCE is contaminated by a residual. Currently, the algorithm works the following way: Starting with the first image in each observation or AOR, LATIMFLAG computes what is called a "latent-trap" image at the end of its exposure. This specifies the amount of trapped charge in every pixel. The charge-trap decays and appears as a residual in subsequent images. The latent-trap image is effectively an image of the number of filled traps, which we label $N_F(t)_i$. The subscript i refers to the "trap-species" or type of latent trap distinguished by a characteristic decay-time and trap filling efficiency. The latent-trap image is propagated forward in time, and updated with each consecutive image in the sequence. The images with pixels sustaining and exceeding a threshold above the background noise from image to image within the decay time are flagged in the imask (bit 5).

5.2 The Artifact-Corrected BCD Pipeline

There are several artifacts commonly seen in IRAC images. For a complete description, see Chapter 7 in this Instrument Handbook. To mitigate the commonly found artifacts of stray light, saturation, muxstripe, column pulldown, and banding, an artifact correction pipeline was created. It performs the artifact correction on the BCD files. The pipeline then creates a product called a Corrected BCD, or CBCD. The CBCDs are used to create the pipeline mosaic. The user receives the BCD and CBCD files in case the artifact correction was not completely successful or it needs to be run again more conservatively.

At each step, an attempt is made to identify the artifacts in the BCDs, adjust the imask pixel values according to the identified artifact, and correct the artifact, with CBCD files being the corrected files. The history of these artifact changes is recorded within the imask file headers. The user can find all of the artifact correction modules on the contributed software section of the Spitzer website, and replicate or improve the corrections using the BCD and imask files as input.

5.2.1   Stray Light

The IRAC stray light masker was written by Mark Lacy of the IRAC Instrument Support Team with help from Rick Arendt of the IRAC Instrument Team and adapted for the artifact mitigation pipeline. The program is designed to mask out stray or scattered light from stars outside the array location as well as filter ghosts from bright stars. The module will alter each imask, corresponding to each BCD file, with pixels likely to be affected by stray light, by turning bit 3 on for those pixels that are likely to be affected by scattered light. The program turns imask bit 2 on for those pixels likely to be affected by filter ghosts.

The module first queries the 2MASS database, producing a table of sources that are likely to produce scattered light within the field of view. Using the BCDs and the 2MASS table, including the flux of the bright sources, possible stray light affected areas are calculated. These pixel positions are then turned on within the imask. When the CBCDs are combined to a mosaic, the corresponding pixels in the CBCDs will not be used to produce the mosaic, thereby "masking out" the input pixels possibly affected by scattered light.

IRAC data users are reminded that observations that were not adequately dithered (such as the ones made with the small-scale dither patterns) will have gaps if the stray light mask is used. In these cases, the stray light masking program can be downloaded from the Spitzer website and run on the BCDs in an unaggressive mode by setting a keyword. This disables the production of the larger masks for very bright stars (which produce diffuse scattered light over a large fraction of the array), avoiding gaps in mosaics. More information about stray light can be found in Section 7.3.1.

5.2.2   Saturation

Many of the following artifact corrections need knowledge of the offending source's flux to work correctly. For observations of very bright sources, the signal (and even pedestal) reads can be saturated. Therefore, the next step in the artifact mitigation process is the saturation correction.

For a bright, strongly saturated point source, the DN will increase from some low number away from the source to some maximum value between 35,000 and 47,000 DN, and then decrease to a small, usually negative number, at the center. The image looks like a bright doughnut with a dark center. This inverted "crater" peak profile indicates that a significant fraction of the light from the bright star may have been lost due to saturation. Recovery, or flux rectification, is possible if the point-spread-function, or PSF, of the star is known. The PSF can then be scaled in flux until the the non-saturated pixels in "wings" of the stellar profile can be fit correctly.

There are several steps to rectify the inner region of the saturated star. First, the exact position of the saturated star is identified using the "craters". The program then creates a sub-image around the saturated star, and that is resampled on a finer grid to match the 0.24 arcsecond resampled PSF. Remaining artifacts, such as banding and muxbleed, are masked out. The PSF is then matched pixel-by-pixel, the PSF flux wings are scaled to the target wings, mean flux ratios are computed, and the best fit outside the inner saturated region is determined. The "lost flux" is then calculated and the star is rectified by replacing the inner, saturated pixels with flux determined from the PSF profile.

The IRAC PRF in channel 1 was found to be too narrow for stars, and so a "puffed up" version was empirically derived and found statistically to be more accurate by testing it on stars with known flux. Also, the program will fail in fitting a PSF to saturated stars that are closer than 20 pixels to the edge of the image. Such saturated stars are not corrected.

A star that is saturated, or predicted to be saturated, has bit 13 flipped on in the corresponding imask. After this module has corrected the saturation, it will turned off bit 13 and turn on bit 4, meaning that the pixel was saturated, but has now been rectified. More information about saturation can be found in Section 7.2.1.

5.2.3 Sky Background Estimation

The remaining artifacts are caused by the flux in a pixel reaching a set threshold (documented in Chapter 7). Once the saturated stars have been corrected, all of the point sources that have fluxes over the respective artifact flux thresholds are detected and flagged. Each pixel that is potentially affected by the artifacts triggered by these high fluxes is flagged in the corresponding imask file (column pulldown has bit 7 set and banding has bit 6 set).

An estimated truth image of the sky background is created. To replace the masked pixels, a 5x5 pixel box around the corrupted pixel is used to create a weighted average for the pixel value to be replaced using a Gaussian-weighted interpolation from the pixels within the box. If there are not enough pixels in the 5x5 pixel area around the affected pixel due to masking, then an 11x11 pixel area is used in the calculation.

5.2.4 Column Pulldown

In all four arrays, a bright pixel will trigger a bias shift within its respective column, creating a lower background value throughout the entire column than in the surrounding columns. The imask will have bit 7 set, denoting the column pulldown artifact, as mentioned above.

In this module, the "truth image" of the sky background is used, and for each column, a robust weighted DC offset is determined. This is a simple offset between the affected column and the estimated background value. This offset is determined separately above and below the triggering source. The offset is then applied to the affected column and saved into the CBCD image, thereby removing the bias shift

from all the pixels in the column. More information about column pulldown can be found in Section 7.2.4.

5.2.5 *Banding Correction (Channels 3 and 4)*

The banding effect manifests itself as the rows and columns that contain a bright source having an enhanced level of flux. This happens only in the Si:As arrays (channels 3 and 4) and has been shown to be due to internal optical scattering (inside the array). Both bright stellar sources and bright extended sources cause banding. It is clearly different from the optical diffraction patterns and the column pulldown effect.

Again, the "truth image" of the background is used to compute a robust weighted DC offset. The banding artifact is extra flux above the background and it will be subtracted out and saved into the CBCD image. The IRAC pipeline does not model the flaring of banding towards the edges of the array. Therefore, the pipeline correction is not always perfect. More information about banding can be found in Section 7.3.2.

5.2.6 *Muxstripe Correction (Channels 1 and 2)*

For a very bright source, muxbleed is accompanied by a pinstripe pattern ("muxstripe"; every 4th column from the bright source is affected) that may extend over part of the image preceding or following the bright pixel (for example, see Figure 7.3 and Figure 7.4). Stars, hot pixels, and particle hits can generate muxbleed and muxstripe. In the artifact correction pipeline, a procedure was developed to mitigate the muxstripe in the image.
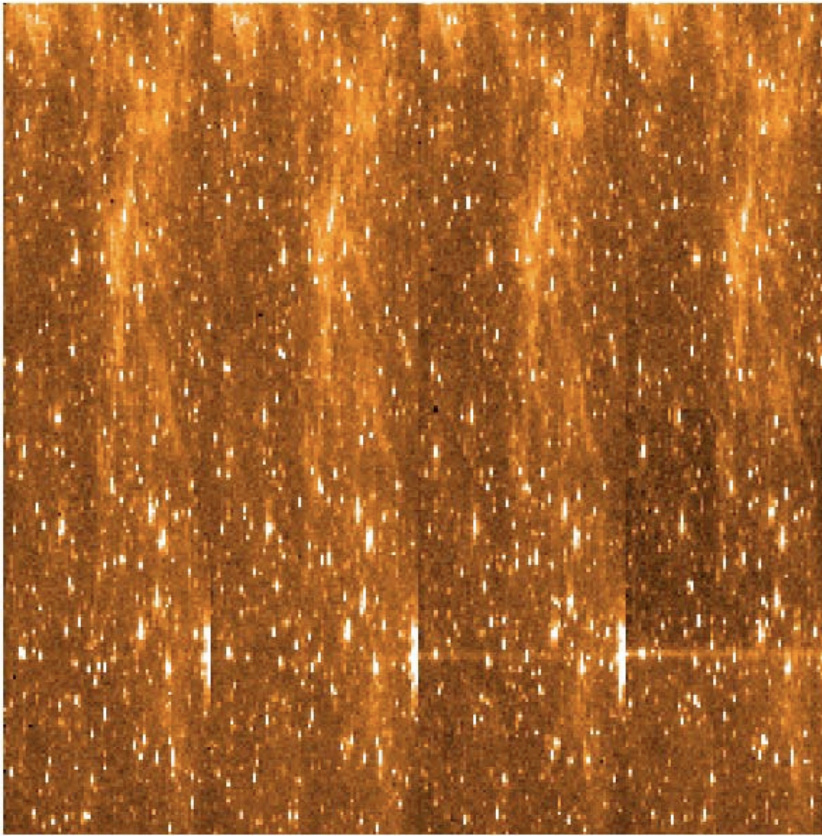
Figure 5.10. An image showing all four readout channel images side by side. These have been obtained by rearranging the columns in the original image. Muxbleed is apparent in the bottom right of the 4th readout channel image.

The algorithm involves converting the BCD image into 256X64 pixel arrays (each of the four readout channels into a separate image; every fourth column is read out by the same channel; see Figure 5.10). The muxstripe for one source contaminates only one readout channel, and therefore only one of these separate arrays. The median of the four arrays is created and subtracted from each array, which allows deviation from the normal background to stand out.
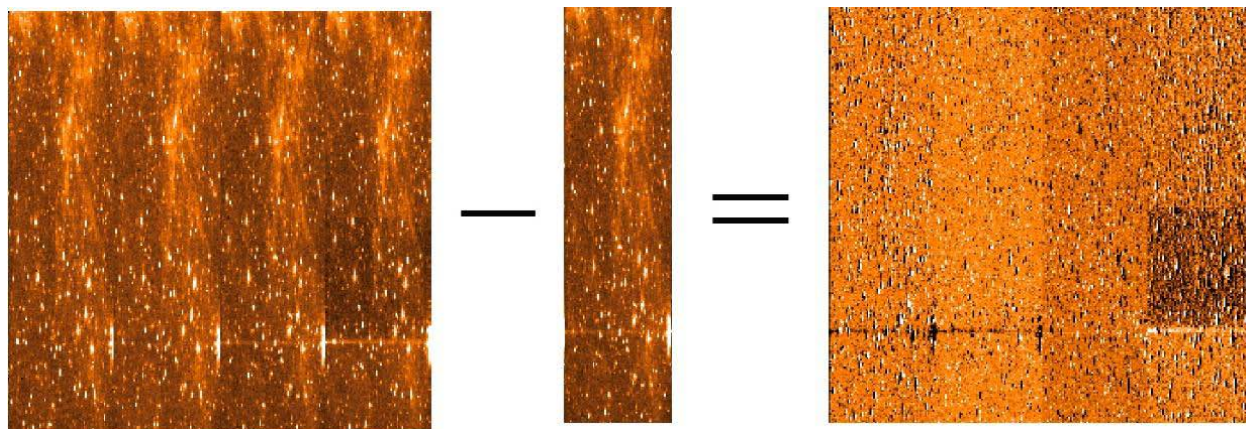
Figure 5.11. Subtraction of the median background from the readout channel images. This makes the muxstripe much more apparent in the 4th readout channel image (on the right).
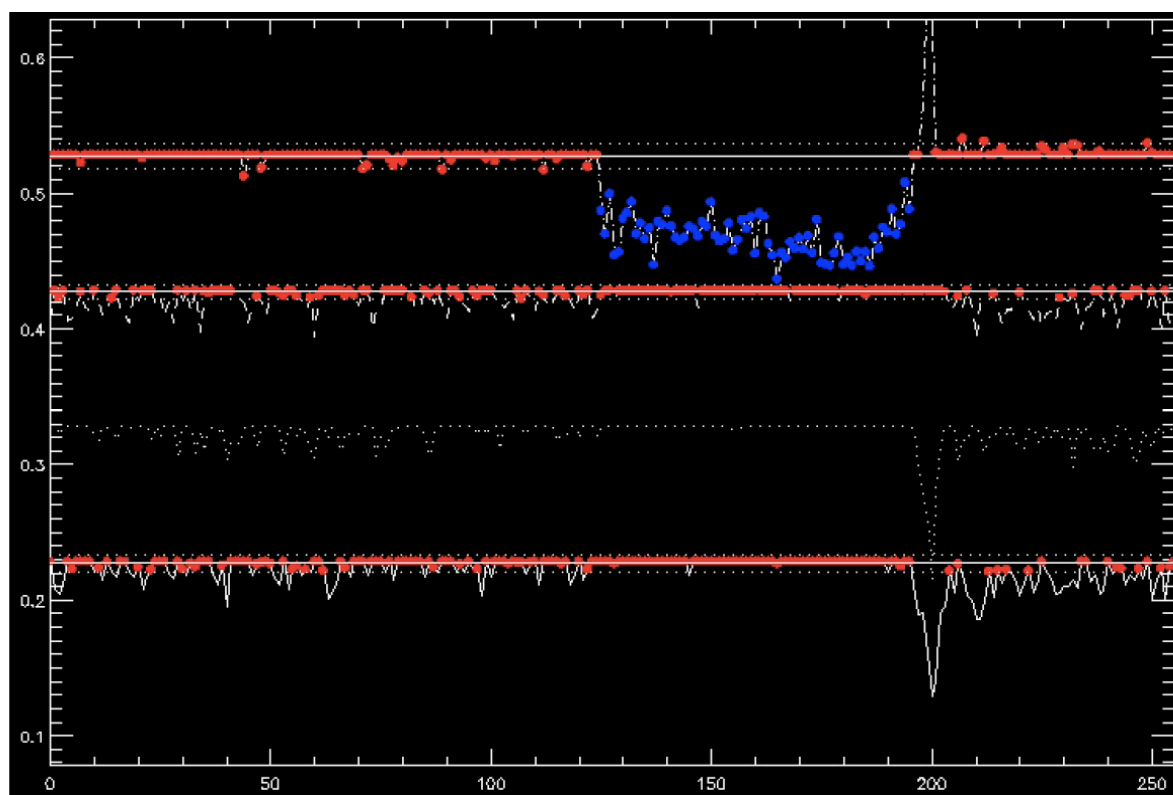
Figure 5.12. Profiles showing the column median versus row values for identifying muxstripe. The muxstripe is now identifiable between rows 125 and 200 (significantly lower values than the median background).

From each of these median-subtracted arrays, a one-dimensional array of the values along each row is then created, simply by combining the pixel values along the X-dimension. A profile that represents the

median versus row is created. For each profile, statistics arre calculated to identify any muxstripe. It will be identified as a deviation larger than 3% of the median value for several rows. This will miss the weakest muxstripe or a case where all readout channels have muxstripe in the same position (cluster of very bright stars), but this will be rare. The subset of pixels that are affected by the muxstripe is identified and this column is corrected using the difference of the median of the 'clean' pixels and the median of the affected pixels. The readout channel arrays are then read back out to recreate the original image, and the corrected image is written to the CBCD file. More information about muxstriping can be found in Section 7.2.2.

5.3 Level 2 (Post-BCD) Pipeline

Pipeline processing of IRAC data also includes more advanced processing of many individual IRAC frames together to form more "reduced" data products. Known by the generic title of "post-BCD" processing, this extended pipeline refines the telescope pointing, attempts to correct for residual bias variations and produces mosaicked images. We do not attempt to improve (relative to the BCD) the point source or extended emission flux calibration by automatically comparing to a reference source catalog. The mosaic only includes data from a single observation or AOR.

All IRAC BCD images contain a pointing estimate based on the output of the Spitzer pointing control system (star tracker and gyros), i.e., the boresight pointing history file. This initial pointing estimate is accurate to about 0.5". The post-BCD pipeline performs additional pointing refinement for all IRAC frames. This is achieved by running the SSC point source detector on channel 1 and 2 frames and comparing the resultant list of point sources to the 2MASS catalog. The results are then averaged, and the known focal plane offsets between all four channels are applied to produce a "superboresight" pointing history file, which is then applied to the data during end-of-campaign reprocessing. This improves the pointing accuracy of the frame to better than about 0.3". This refined RA, Dec appears in the header as the CRVAL1, CRVAL2 keyword values.

The pipeline SSC mosaicker produces a single image (one per band) from many input images. First, the BCDs are corrected for overlap consistency. The parts of the images that overlap are forced to have the same background value via addition of an offset. Then a "fiducial frame" is derived. This is the definition for the output frame in terms of its physical size, projection, and orientation. Because IRAC has such a large field of view, projection effects are non-negligible, and the mosaicking and coadding process must reproject the data. The fiducial frame finder seeks to minimize the amount of "blank" area in the output mosaic by rotating the output projection such that it is aligned with the map axes. This is useful for long thin maps, where potentially the output mosaic could be very large, but with a great deal of empty space. The mosaicker then reprojects all of the input data onto the output projection. It reads the SSC WCS, which contains the field pointing center, rotation, scale, and instrument distortion, and reprojects this onto a standard TAN FITS projection. In the process, the data are undistorted. The reprojected images are interpolated onto the fiducial image frame with outlier rejection, rejecting radiation hits that happen in overlapping observations. The outlier rejection scheme is specifically designed to work well in the case of

intermediate coverage and may not be adequate for all observations and science programs. In addition to a sky map (in units of surface brightness), a noise image and coverage map are also produced.

The post-BCD pipeline modules have been made available for general public use as part of the MOPEX tool. They consist of a number of C-modules connected via PERL wrapper scripts. Namelists are used for input. In most cases their operation simply consists of supplying the software with a list of input image files; by default they read and understand the IRAC image headers.

5.3.1   *Pointing Refinement*

To improve the ~ 0.5" blind pointing, a pointing refinement is run in which the point sources are identified in the IRAC frames and astrometrically correlated with stars near the source position in the 2MASS catalog. The pointing refinement typically improves the positional error to < 0.3" and removes any systematic offsets.

First, point sources are extracted from the pipeline-processed mosaics and transformed to RA and Dec using the transformations derived from the current pointing. If there are less than five sources in an image, then there will be no refinement for that BCD.

A comparison is made of the position and flux of each point-source match found in the 2MASS point-source catalog. The new translational and rotational reference frame can be computed from the differences and uncertainties, and a refinement is made of the celestial pointings and angles of each BCD in the observation or AOR used for the mosaic. These refined values are written to the end of the FITS headers as RA_RFND, DEC_RFND, including many others with RFND as an indicator of "refined" pointing.

5.3.2   *Superboresight Pointing Refinement*

Pointing refinement operates on each IRAC channel independently. This often results in poor pointing solutions for channels 3 and 4, in which stellar fluxes are lower and the background higher than in channels 1 and 2. We have therefore developed a technique which combines the results of pointing refinement in channels 1 and 2 and applies it to all four channels using the known offsets between the IRAC fields of view. This improved pointing solution is derived during campaign reprocessing. The results of the pointing refinement from the first run of the post-BCD pipelines are averaged, and the correction derived from this is applied to the boresight pointing history file (which contains the pointing estimate derived from the spacecraft telemetry and which provides our initial pointing estimate). This corrected pointing history file (the "superboresight" file) is then applied to the BCD at the pointing transfer stage of the BCD pipeline. The superboresight RA and Dec estimates are recorded in the CRVAL1 and CRVAL2 FITS keywords, and the position angle estimate is recorded in the CD matrix keywords. The uncorrected RA and DEC are retained, but called ORIG_RA, ORIG_DEC, as is the

pointing refinement solution for each frame (as RARFND and DECRFND). Note that to use the superboresight solution, USE REFINED POINTING = 0 should be set in the MOPEX namelists.

Superboresight was implemented as a patch to the S13 software build, thus most (but not all) data processed with S13 or subsequent pipeline versions will have it. Users should check for the presence of the ORIG_RA, ORIG_DEC keywords to see if it has been applied to their data. From S14 onwards, the HDR data have the long frame RA, Dec solution copied to the short frames, as the short frame pointing solutions are less accurate. Neither superboresight nor pointing refinement are run on the subarray data.

.

5.3.3   *Mosaicking and Coaddition*

Using the refined coordinates, individual IRAC BCDs from a given observation (AOR) are reconstructed onto a larger field (mosaicking), and overlapping frames are averaged together to achieve a higher S/N. Outlier rejection is performed on sets of overlapping pixels. Because Spitzer observations cover such a large area, individual BCDs are remapped onto a common grid with a technique similar to "drizzle" *(Fruchter & Hook 2002, [11])*. The pixel size in the mosaics produced by the pipeline is exactly 0.6 arcseconds x 0.6 arcseconds in the final data processing. The masks are used in the coaddition in such a way that the pixels previously flagged as bad (for example, hot or dead pixels) are rejected before the averaging process. Cosmic rays are rejected at this point via the outlier rejection algorithm. Users will receive a single coadded image per channel, and per observation (AOR). It will be accompanied by a coverage map and an uncertainty file per channel per exposure time.

6 Data Products

This section describes the basic data products the observer will receive from the Spitzer Heritage Archive. The available data products consist of Level 0 (raw) data, Level 1 (BCD) data, calibration files, log files, and Level 2 (post-BCD) data. IRAC data are supplied as standard FITS files.

Each file consists of a single data collection event (i.e., a single exposure), and contains one image corresponding to one of the four IRAC arrays (the exception being post-BCD products, described below). The FITS headers are populated with keywords including (but not limited to) physical sky coordinates and dimensions, a photometric solution, details of the instrument and spacecraft including telemetry when the data were taken, and the steps taken during pipeline processing.

6.1 File-Naming Conventions

Table 6.1 lists the IRAC data files produced by the IRAC data reduction pipelines, together with brief descriptions of these files. The Basic Calibrated Data (BCD) are the calibrated, individual images. These are in array orientation and have a size of 256 x 256 pixels for the full array images, and 64 planes times 32 x 32 pixels for the subarray images. These data are fully calibrated and have detailed file headers. The Post-BCD pipeline combines the BCD images into mosaics (per wavelength and per frame time). Calibration observations designated as darks or flats go through a similar but separate pipeline that generates the products listed in the last section of Table 6.1.

Note that because of the "first frame effect," the first frame of every Astronomical Observation Request (AOR) has a different delay time and it cannot be calibrated correctly. Therefore, the first frame of every AOR with a frame time greater than 2 seconds is taken in HDR mode which causes the first frame to be 0.6 seconds or 1.2 seconds in duration instead of the full frame time. This first frame usually has a name such as *SPITZER_I1_11111111_0000_0000_2_bcd.fits* and has no associated cosmic ray mask (brmsk file). The observer is encouraged not to use this first short frame. The pipeline mosaicker does not use it either when building the mosaic.

The BCD uncertainty files (listed below) are rough uncertainty estimations and do not include all of the systematic effects associated with IRAC detectors, nor do they include the absolute flux uncertainty. These uncertainty images are generated as follows. They begin as an estimate of the read noise (one number in electrons for the whole image) and the shot-noise due to the sky (proportional to the square-root of the number of electrons in the image). Then each module propagates the uncertainty image forward, including the uncertainties in dark and flat calibration files. The pipeline modules use the uncertainty image as a way to quantitatively estimate the quality of the sky estimate given by the value of a pixel. In the end, the uncertainty images overestimate the formal uncertainty of the image, because the net propagated uncertainty is much higher than the observed pixel-to-pixel fluctuations in the images. We therefore recommend that the uncertainty images only be used for relative weights between pixels, for example when performing outlier rejection or making a weighted mosaic that combines multiple input frames that view the same sky mosaic pixel.

Please note that all of the calibration products (specifically, skydarks, skyflats, and linearity curves) are in the raw reference frame. Hence, the subarrays are located at pixel coordinates 9:40, 9:40. In the BCDs, the subarrays are located in pixel coordinates 9:40, 9:40 in channels 3 and 4, and in pixel coordinates 9:40, 217:248 in channels 1 and 2. Also note that those coordinates are for the case in which the first pixel is indexed as 1,1 (i.e., IRAF convention). E.g. IDL pixel indices start from 0,0.

Table 6.1 Sample IRAC file names.

Brief Description	
Basic Calibrated Data (BCD)	
SPITZER_I1_0008845056_0031_0000_01_dce.fits	Raw data (in units of DN)
SPITZER_I1_8845056_0031_0000_1_bcd.fits	BCD data (in units of MJy/sr)
SPITZER_I1_8845056_0031_0000_1_bcd.log	BCD pipeline log
SPITZER_I1_8845056_0031_0000_1_bunc.fits	BCD uncertainty file
SPITZER_I1_8845056_0031_0000_1_bimsk.fits	BCD Imask file
SPITZER_I1_8845056_0031_0000_1_brmsk.fits	Rmask images
SPITZER_I1_8845056_0031_0000_1_ptn.log	BCD Pointing log
SPITZER_I1_8845056_0031_0000_1_sub2d.fits	2D BCD image (subarray only)
SPITZER_I1_8845056_0031_0000_1_unc2d.fits	2D BCD uncertainty file (subarray only)
SPITZER_I1_8845056_0031_0000_1_msk2d.fits	2D BCD Imask file (subarray only)
SPITZER_I1_8845056_0031_0000_1_cov2d.fits	2D BCD coverage file (subarray only)
Artifact-Corrected BCD Processing (CBCD)	
SPITZER_I1_8845056_0031_0000_1_cbcd.fits	Artifact-corrected BCD data
SPITZER_I1_8845056_0031_0000_1_cbunc.fits	Artifact-corrected BCD uncertainty file
Post-BCD Processing	
SPITZER_I1_8845056_0000_1_E123458_maic.fits	Mosaic
SPITZER_I1_8845056_0000_1_A2987651_munc.fits	Mosaic uncertainty file
SPITZER_I1_8845056_0000_1_A2987653_mcov.fits	Mosaic coverage file
SPITZER_I1_8845056_0000_1_A2987653_mmsk.fits	Mosaic mask file
SPITZER_I1_8845056_0000_1_A2987654_maicm.fits	HDR intermediate frame time mosaic
SPITZER_I1_8845056_0000_1_A2987655_muncm.fits	HDR intermediate frame time mosaic uncertainty file
SPITZER_I1_8845056_0000_1_A2987656_mcovm.fits	HDR intermediate frame time mosaic coverage file
SPITZER_I1_8845056_0000_1_A2987657_mmskm.fits	HDR intermediate frame time mosaic mask file
SPITZER_I1_8845056_0000_1_A2987658_maics.fits	HDR short frame time mosaic
SPITZER_I1_8845056_0000_1_A2987659_muncs.fits	HDR short frame time mosaic uncertainty file
SPITZER_I1_8845056_0000_1_A2987660_mcovs.fits	HDR short frame time mosaic coverage file
SPITZER_I1_8845056_0000_1_A2987653_mmsks.fits	HDR short frame time mosaic mask file
SPITZER_I1_8845056_0000_1_A26871875_irsa.tbl	List of 2MASS stars for pointing refinement
SPITZER_I1_8845056_0000_1_A26871873_refptg.tbl	Table of pointing refinement information
Calibration pipeline data files	
SPITZER I1_13450853_0000_1_C92523_ sdark.fits	Skydark
SPITZER I1_13450853_0000_1_A210654_ scmsk.fits	Skydark mask file
FUL_2s_2sf4d1r1_ch[1-4]_v1.2.0_dark.fits	IRAC labdark image (full array)

FUL_2s_2sf4d1r1_ch[1-4]_v1.2.0_dark_noise.fits	IRAC labdark noise image
HDR_30s_1.2sf1d1r_ ch[1-4]_v1.2.0_dark.fits	IRAC labdark image (HDR short frame)
HDR_30s_30sf16d1r_ ch[1-4]_v1.2.0_dark.fits	IRAC labdark image (HDR long frame)
SUB_0.1s_0.1sf2d1r1_ch[1-4]_v1.2.0_dark.fits	IRAC labdark image (subarray)
irac_b[1-4]_[fa/sa]_superskyflat_finalcryo_091004.fits	IRAC superskyflat image
irac_b[1-4]_ [fa/sa]_superskyflat_finalcryo_091004_cmask.fits	IRAC superskyflat mask file
irac_b[1-4]_[fa/sa]_20020921_lincal.fits	linearization calibration image
irac_b[1-4]_[fa/sa]_20020921_lincal_cmask.fits	linearization calibration mask
irac_b[1-4]_[fa/sa]_cdelt12_distort.tbl	Array distortion table
irac_b[1-4]_[fa/sa]_16_118_muxbleed_coeff_112003	Muxbleed correction coefficients
irac_b[1-4]_[fa/sa]_16_118_muxbleed_lut_100102	Muxbleed correction look-up table
[month][year]_ch[1-4]_pmask_[subarray].fits	Pmask (nearest in time)
[month][year]_ch[1-4]_fa_pmask[subarray]_flip.fits	Flipped pmask (nearest in time; not in use)
irac_b[1-4]_fa_slmodel_v1.0.1.fits	Subtracted scattered light model
irac_b[1-4_fluxconv_10112010.tbl	Flux conversion file used
instrument_FOV.tbl	IRAC array locations in Spitzer FOV
irac_b[1-4]_mosaicPRF.fits	PRF file used for pointing refinement
irac_b[1-4]_PRF.tbl	PRF used for the four quadrants of the image
SPITZER_I1_21752576_0000_5_A41882936_avg.fits	Average image of all BCDs in an AOR
SPITZER_I1_21752576_0000_5_A41882938_avmed.fits	Average image of all HDR intermediate frames
SPITZER_I1_21752576_0000_5_A41882937_ashrt.fits	Average image of all HDR short frames
SPITZER_I1_21752576_0000_5_C8232029_mdn.fits	Median image of all BCDs in an AOR
SPITZER_I1_21752576_0000_5_A41882940_mdmed.fits	Median image of all HDR intermediate frames
SPITZER_I1_21752576_0000_5_A41882939_mshrt.fits	Median image of all HDR short frames

6.2 IRAC Specific Header Keywords

Here we describe some of the important header keywords. A complete IRAC image header description is included in Appendix D.

AORLABEL is the name of the AOR as it was defined by the user in Spitzer Observation Planning Tool Spot when the observations were requested. The P.I. of a program under which the data were taken will be listed as the OBSRVR of each project. AORKEY is a unique identification number or "digit sequence" for each observation; it is also part of the filename for each BCD. EXPID is an exposure counter incremented within a given AOR for each data-taking command. Most data-taking commands generate multiple files: one per array in full array mode. The DCENUM is a counter of individual frames (per wavelength) from an individual command; it can be used to separate frames generated with internal repeats. The only observations with non-zero DCENUM are channel 4 BCDs for 100/200 second frame time (taken as two/four 50 second frames). In high dynamic range mode, the long and short exposures are generated with independent commands and have different EXPIDs. Thus, for example, data from 12-second high dynamic range observations can be separated into long and short frames using the `odd' or

`even' EXPIDs. DATE_OBS is the time at the start of the AOR. Other times in the header include the time since IRAC was turned on (both for the beginning and end of the frame). FRAMTIME is the duration of the frame including Fowler sampling, and EXPTIME is the effective integration time. UTCS_OBS is the start of IRAC data taking sequence. ET_OBS is the beginning time of the observation (DCE) in barycentric dynamical time (TDB) seconds since J2000 or January 1, 12 hours, 2000 (JD 2451545.0). SCLK_OBS is the Spitzer Spacecraft clock time at the beginning of the observation (DCE) since 0000 UT, January 1, 1980. Modified Julian date is in keyword MJD_OBS and the corresponding heliocentric modified Julian date in HMJD_OBS. There is also a Solar System barycentric modified Julian date in BMJD_OBS. Note that BMJD_TDB = BMJD_OBS + (ET_OBS - UTCS_OBS) at the start of the DCE. In IER observations where several IERs are taken successively in a "staring" mode, only the first IER contains good requested pointing information that is used in calculations of HMJD and BMJD, and therefore these keywords are not reliable in these successive IERs. ATIMEEND is the correct time of an integration end. HDRMODE tells you if the frame was taken in the high dynamic range mode.

BUNIT gives the units (MJy/sr) of the images. For reference, $1 \text{ MJy/sr} = 10^{-17} \text{ erg s}^{-1} \text{ cm}^{-2} \text{ Hz}^{-1} \text{ sr}^{-1}$. FLUXCONV is the calibration factor derived from standard star observations; its units are (MJy/sr)/(DN/s). The raw files are in "data numbers" (DN). To convert from MJy/sr back to DN, divide by FLUXCONV and multiply by EXPTIME. To convert DN to electrons, multiply by GAIN.

The predicted background (using the same model as what was implemented in Spot, evaluated for the wavelength, date, and coordinates of observation) is contained in three keywords: ZODY_EST, ISM_EST, CIB_EST. These are not based on the actual data from Spitzer. SKYDRKZB is the zodiacal background prediction for the skydark that was subtracted from the science image in the reduction pipeline. Thus the predicted background in the BCD data is ZODY_EST – SKYDRKZB. DS_IDENT is a journal identification number for the Astrophysics Data System (ADS) to keep track of papers published from these data.

Absolute pointing information is contained in the following keywords. ORIG_RA and ORIG_DEC give the coordinates of the image center constructed from the telemetry using the Boresight Pointing History File, as indicated by the Boolean keyword USEDBPHF, and the file is listed in BPHFNAME. When pointing telemetry is not available, due to a telemetry outage, the commanded positions are inserted instead, USEDBPHF is false, and the coordinates will be less certain. RARFND and DECRFND are the refined positions derived by matching the brightest sources in the image with the 2MASS catalog. PA_RFND is the refined position angle of the +y axis of the image, measured east from north (CROTA2 is the same position angle but measured west from north). CRVAL1 and CRVAL2 give the coordinates of the image center, derived from the refined positions in all channels, and are usually the most accurate coordinates available.

Sometimes a bad pixel value (zero) was inserted in the data field. These pixels are detected and shown in raw frame header where ABADDATA assumes the value of 1. In the BCD FITS header you will then find header keyword BADTRIG set to "T" (true) and the number of zero pixels in the frame listed in header keyword ZEROPIX. If there is only one bad pixel, the pipeline fixes the problem and gives the bad pixel position in header keyword ZPIXPOS.

The BCD +x-axis (bottom, or horizontal axis) is in the direction of the telescope +Y-axis, and the BCD -y-axis (left side or vertical axis) is in the direction of the telescope +Z-axis.

Next we give an example of how an AOR file translates into final data products. A Spitzer observation is specified by a small list of parameters that are listed in the ".aor" file. This file was generated when the observation was designed (using Spot). The ".aor" file for a planned or performed observation can be retrieved using the "view program" feature of Spot. (You will be prompted for the program name or ID, which can be obtained from the image header keywords PROGTITLE and PROGID). Here is an example AOR file:

```
# Please edit this file with care to maintain the
# correct format so that SPOT can still read it.
# Generated by SPOT on: 5/9/2003 12:10:9

HEADER: FILE_VERSION=7.0, STATUS = PROPOSAL


AOT_TYPE: IRAC Mapping
AOR_LABEL: IRAC-FLS-CVZ-a
AOR_STATUS: new
MOVING_TARGET: NO
TARGET_TYPE: FIXED SINGLE
TARGET_NAME: FLS-CVZ
COORD_SYSTEM: Equatorial J2000
POSITION: RA_LON=17h13m05.00s, DEC_LAT=+59d10m52.0s
OBJECT_AVOIDANCE: EARTH = YES, OTHERS = YES
          READOUT_MODE: FULL_ARRAY
                 ARRAY: 3.6_5.8u=YES, 4.5_8.0u=YES
             HI_DYNAMIC: NO
             FRAME_TIME: 12.0
         DITHER_PATTERN: TYPE=Cycling, N_POSITION=5, START_POINT=1
           DITHER_SCALE: small
   N_FRAMES_PER_POINTING: 1
MAP: TYPE=RECTANGULAR, ROWS=7, COLS=6, ROW_STEP=277.0, COL_STEP=280.0,
     ORIENT=ARRAY, ROW_OFFSET=0.0,COL_OFFSET=440.0,N_CYCLE=1
SPECIAL: IMPACT = none, LATE_EPHEMERIS = NO,SECOND_LOOK = NO
RESOURCE_EST: TOTAL_DURATION=5848.4, SLEW_TIME=1089.0, SETTLE_TIME=1045.0,
SLEW_OVERHEAD=180.0, SPECIAL_OVERHEAD=0.0, UPLINK_VOLUME=9026,
DOWNLINK_VOLUME=59065440, VERSION=S7.0.B2
INTEGRATION_TIME: IRAC_3_6=60.0,IRAC_4_5=60.0,IRAC_5_8=60.0,IRAC_8_0=60.0
```

For this AOR, there are 210 files (6 columns x 7 rows x 5 dither positions) of each type for each channel. The final data products from this AOR in channel 2, provided it got assigned the AORKEY 6213376, are as follows:

SPITZER_I2_0006213376_0000_0000_01_dce.fits

SPITZER_I2_6213376_0000_0000_1_bcd.fits

SPITZER_I2_6213376_0000_0000_1_cbcd.fits

SPITZER_I2_6213376_0000_0000_1_bcd.log

SPITZER_I2_6213376_0000_0000_1_bunc.fits

SPITZER_I2_6213376_0000_0000_1_cbunc.fits

SPITZER_I2_6213376_0000_0000_1_bdmsk.fits

SPITZER_I2_6213376_0000_0000_1_bimsk.fits

SPITZER_I2_6213376_0000_0000_1_brmsk.fits
SPITZER_I2_6213376_0000_0000_1_ptn.log

....
SPITZER_I2_0006213376_0209_0000_01_dce.fits
SPITZER_I2_6213376_0209_0000_1_bcd.fits
SPITZER_I2_6213376_0209_0000_1_cbcd.fits
SPITZER_I2_6213376_0209_0000_1_bcd.log
SPITZER_I2_6213376_0209_0000_1_bunc.fits
SPITZER_I2_6213376_0209_0000_1_cbunc.fits
SPITZER_I2_6213376_0209_0000_1_bdmsk.fits
SPITZER_I2_6213376_0209_0000_1_bimsk.fits
SPITZER_I2_6213376_0209_0000_1_brmsk.fits
SPITZER_I2_6213376_0209_0000_1_ptn.log

After the name of the telescope, the first partition gives the instrument ("I" = IRAC), and the number after the "I" gives the channel (in this case, 2). The next part gives the AORKEY, then we have the EXPID, DCENUM, and the version number (how many times these data have been processed through the pipeline). One should generally use only the data from the highest version number, in case multiple versions have been downloaded from the archive. To verify that the data are from the latest pipeline version, check the CREATOR keyword in the header (S18.18 for the final cryogenic IRAC data processing). Finally, there is a group of letters that specify what kind of data are in the file (see Table 6.1 above), and the file type (usually "fits" or "log"). The post-BCD file names include telescope name (SPITZER), "I" (for "IRAC"), the channel number, the productid (not the same as the AORKEY), the DCENUM, the (pipeline) version, "ensemble product id," the type of the data and the suffix. In the case of an ensemble product, "DCENUM" in the filename refers to the first DCE that was used in the ensemble creation, and "version" refers to the version of that first DCE. The letter "C" stands for "calibration" product: in the case of a calibration product, "DCENUM" refers to the first DCE that was used in the calibration creation, (pipeline) "version" refers to the version of that first DCE, and the number after the "C" letter is the "calibration number". Note that for a given AORKEY of science data being retrieved, the AORKEY for the associated calibration products is different.

A list of 2MASS sources for the field of the IRAC observation is included in the data delivery as *irsa.tbl*. Note that the 2MASS magnitudes given in the *irsa.tbl* file are not meant for scientific use. For scientific use of the 2MASS data, query the 2MASS catalog directly from IRSA, and take into account the flux quality flags.

7 Data Features and Artifacts

The common artifacts in IRAC data are discussed in this chapter. Most of these have been mitigated by the pipeline processing, which produces artifact-corrected images ("CBCDs"). Further mitigation is often possible by a judicious quality inspection of the data, and/or further processing of the BCDs. Note that many of these artifacts are quite commonly seen in IRAC images.

The most common artifacts are as follows. Stray light from point sources should be masked by hand. Persistent images usually come from a bright source observed as part of the observation. In some cases, however, persistent images from a preceding observation may be found. One way to check this is by inspecting a median of all the images in an observation (AOR). Another possible flaw in the observations would be an exceptionally high radiation dosage. The nominal rate is 1.5 hits per array per second, and the radiation hits range from single pixels to connected streams (and occasionally small clouds of secondaries). High particle hit rates occurred following one solar flare during the In-Orbit Checkout, and one in Nominal Operations. In the latter event, several hours of science data were rendered useless because of the large number of hits in the images. Objects that are bright enough leave muxbleed trails and can generate pinstripe patterns over large parts of the image, and offsets along the columns and rows containing the bright source. Ghosts from internal reflections within the filters can be seen in almost every channel 1 or 2 BCD, and more ghosts in all channels are noticeable from bright objects.

We begin with a discussion of the basic characteristics of the dark frames and flatfields that affect every image. We follow with a discussion of electronic artifacts. These effects arise from the inherent nonlinearity of the detector diodes and saturation of either the detector well, transistors in the mux, or the analog-to-digital converter (ADC) in the warm electronics; crosstalk within the mux or warm electronics; or from inductive coupling to currents in spacecraft cables. Most electronic effects have a short persistence, but image persistence, which is also nonlinear in photon fluence, can last seconds, minutes, hours, or even weeks. Next we have a section on optical artifacts, which include stray light or ghosts from sources within or outside the FOV. Finally, we discuss the effects of cosmic rays and solar protons on IRAC observations. Please note that asteroids may be "contaminants" in the data as well, especially when the target is close to the ecliptic plane. Asteroids can most effectively be rejected from datasets that have been taken at least several hours apart, so that the asteroids have moved in the data and can be masked out by temporal outlier rejection routines.

7.1 Darks, Flats, Missing Data and Bad Pixels

The true median dark currents, due to nonzero leakage resistance or recombination in reverse-biased detector diodes, are very small compared to the current from the background at the darkest part of the celestial sphere. Labdarks, which were measured with the cold IRAC shutter closed, with zero photon flux, are not zero, and have significant pixel-dependent offsets, usually positive, that depend on the frame time and the Fowler number, as well as the history of readouts and array idling over the previous several hours. Channel 3 is by far the most extreme case, in which, for example, a 100 second (Fowler-16) frame can be offset as much as 370 DN (median), or the equivalent of 1400 electrons at the integrating node,

with no light incident on the array. The signal from the darkest background in a 100 second frame in channel 3 is only about 1000 electrons. Channel 1 has much smaller offsets, but the sky is so dark that the offsets are often larger than the background signal. Channel 2 has very small offsets, which are less than the background signal except in short frames or certain frames immediately following a change in integration time. The background in channel 4 is so large that the offsets are almost negligible except in very short integrations. There is no measureable excess noise from the offset itself: the noise is not the square root of the equivalent number of charge quanta on the integrating node. This is because the offset arises from the redistribution of charge within the mux in which the associated currents and capacitance are much greater than in the detector diodes. However, imperfect correction of this "first-frame" effect does increase the uncertainties in BCD frames. The uncertainty scales with the size of the offset and its small-scale spatial nonuniformity. Only in channel 3 does it significantly increase the total pixel noise.

We can break down the offset into contributions beginning with the largest spatial scale down to the smallest. In this view, the largest part of the offset is uniform over the array, followed by the contribution of a few spatial gradients, and some pinstriping that repeats every four columns (due to the four array outputs), with a few columns with odd offsets (due to hot pixels or parts of the mux), and weakest of all, pixel-to-pixel dependent offsets.

There are some very obvious features imposed on the true offset, due to a relatively small number of hot pixels, and mux glow. Hot pixels usually appear bright, and in such cases one can see a trail of muxbleed (in raw images) or a pinstripe pattern in InSb arrays, or the bandwidth effect (in Si:As arrays) following the hot pixel. These pixels have high dark currents and are usually isolated, but sometimes in a clump. "Dead" pixels are really just very hot pixels, so hot that they saturate before the first pedestal sample. In a BCD image, hot pixels do not appear bright because they have been canceled by the labdark or skydark subtraction. Most hot pixels appeared after launch and are the result of hits by energetic nuclei. By annealing the arrays, we restored most pixels that got activated. Some of them cannot be restored, and thus they became "permanent" hot pixels. Some pixels jumped randomly from normal to high dark current and back, dwelling in one state for anywhere from a few minutes to weeks, so they may not be canceled by a skydark subtraction. These are IRAC's "rogue pixels." The IRAC "static" bad pixel masks were updated when significant changes in the permanent bad and/or hot pixels occurred.

Areas of mux glow are visible in the labdark and images. Electrons and holes recombine in diodes in the mux, allowing current to flow. Photons emitted in the recombination are detected in the InSb or Si:As detector above or near the source of the glow. Most prominent is the glow from the four output FETs visible only in Channels 3 and 4 (the Si:As arrays). These are semicircular areas about 17 pixels in radius located near column 256, row 30 at the right edge of the images. The glow is most obvious in long frames. Another glow region is visible along the last few rows in all 4 channels; it comes from the unit cell FETs. Currents flow through all the unit cell FETs in the last row which is left selected during the integration, so the glow is particularly bright in the last row itself. The 3rd and faintest glow region is along the left edge (column 1) of channel 3. Detected glows have shot noise, which can exceed the background noise along the last row and in the brightest parts of the semicircular areas. Pixels are masked in these areas where the noise significantly degrades sensitivity in 100-second frames.

Table 7.1: Definition of bits in the "pmask".

Bit	Condition
0	Not set
1	Not set
2	Not set
3	Not set
4	Not set
5	Not set
6	Not set
7	Dark current highly variable
8	Response to light highly variable
9	Pixel response to light is too high (unacceptably fast saturation)
10	Pixel dark current is too excessive
11	Not set
12	Not set
13	Not set
14	Pixel response to light is too low (pixel is dead)
15	[reserved: sign bit]

7.1.1   Bad Pixels

Included with the BCD data are three masks, a semi-static mask (the "pmask") which contains permanent or semi-permanent bad pixels and regions, and which is the same for all BCDs in a given AOR and channel, the "imask" which contains bad pixels specific to any one BCD, and the "rmask" which contains outliers masked by the post-BCD pipeline. All of the bits set in the imask indicate pixels that have been compromised in some fashion. Not all of the imask bits are set by the BCD pipeline, but some bits are placeholders for post-BCD processing of data artifacts. The higher the order of bit set in the imask, the more severe the effect on data quality. Mask values are set as powers of two, and summed together for each pixel. Any pixel with a bit set in the pmask is suspect.

Several sets of pmasks have been produced. At the start of the mission, sets were produced at 3–6 month intervals. As the bad pixel behavior has been shown to vary little with time, these intervals were extended to 12–18 months. The masks are made from calibration data spanning three campaigns, allowing some short-term bad pixels to anneal out, while retaining the ones persistent on timescales of weeks or more. Pixels consistently noisy in the darks and/or flats in these three campaign sets are flagged. The regions of amplifier glow are also flagged (with bit 10). Combined masks are also available, with bit 0 set to indicate

a suspect pixel. The "OR" masks contain all pixels which have been flagged in any pmask set during the mission, and the "AND" masks contain only those pixels set in every pmask set. Table 7.1 and Table 7.2 show what each bit value corresponds to. The DCE Status Mask Fatal Bit Pattern = 32520 (bits 3, 8-14; to be used with the MOPEX software).

Table 7.2: Definition of bits in the "imask".

Bit	Condition
0	reserved for boolean mask (or if best practice bits set, data quality)
1	reserved for future use
2	optical ghost flag (set by post-BCD tool)
3	stray light flag (set by post-BCD tool)
4	saturation corrected in pipeline
5	muxbleed flag in ch 1,2; bandwidth effect in ch 3,4 (set by post-BCD tool)
6	banding flag (set by post-BCD tool)
7	column pulldown flag in ch 1,2; vertical banding flag in ch 3,4 (set by post-BCD tool)
8	crosstalk flag
9	radhit (single frame radhit detection)
10	latent flag (not functional in IER observations)
11	not flat-field corrected
12	data not very linear
13	saturated (not corrected in pipeline), or predicted to be saturated in long HDR frames
14	data bad and/or missing
15	[reserved: sign bit]

7.1.2   Flatfield

Individual pixel-to-pixel gain variations are corrected by means of a pixel-to-pixel gain map commonly known as a "flatfield." IRAC flats are derived by making highly dithered observations of one of approximately 20 fixed locations in the ecliptic plane, specifically chosen to be as free of stars and extended cirrus emission as possible, and in which the zodiacal light provides a uniform illumination. The data are processed much like science data and then averaged with outlier rejection. Additionally, since stars, asteroids and galaxies are a significant contaminant in the data, an object detector is used to find and then explicitly reject them during the averaging. The flats are normalized to a median of one. New flat field measurements are made every time the instrument is turned on.

Analysis of data from the first two years of operations has shown that the flatfield response of IRAC is unchanging at the limit of our ability to measure. As a result, so-called "super skyflats" were generated from the first two years of data. The super skyflats are shown in Figure 7.1.

These flats are extremely low-noise, with stochastic pixel-to-pixel uncertainties of 0.14% (0.17%), 0.09% (0.09%), 0.07%, and 0.01% in channels 1 through 4, respectively, where the values in parentheses refer to warm mission. This is smaller in amplitude than the intrinsic pixel-to-pixel scatter in the gain. Furthermore, because the super skyflats are derived from data over many parts of the sky, with many dithers and rotations of the telescope, they are substantially free of errors arising from gradients in the zodiacal background, or from residual contamination by stars and galaxies. Currently all IRAC data are reduced with the same set of super skyflats.

Large-scale gradients corrected by the flats are on the order of 10%−15%. Systematic errors in the flats are due to the gradient in the zodiacal background and straylight removal errors. The former is expected to be very small based on results from other missions *(Abraham et al. 1997 [1]*, ISOPHOT 25 μm). Diffuse stray light is a significant contaminant in the raw images at the ∼ 5%−10% level. This diffuse light looks like a "butterfly" across the top of the InSb detectors in channels 1 and 2, or a "tic-tac-toe" pattern in channels 3 and 4. It is always present, resulting from scattering of the zodiacal background onto the detectors. In both the skyflats and the science data, a model of the straylight has been subtracted, but this leaves a residual pattern on the order of 1% which contaminates the flats. These errors are substantially ameliorated by dithering (errors will decrease as $\sqrt{N}$, where N is the number of dithers, and will quickly become very small relative to other uncertainties).
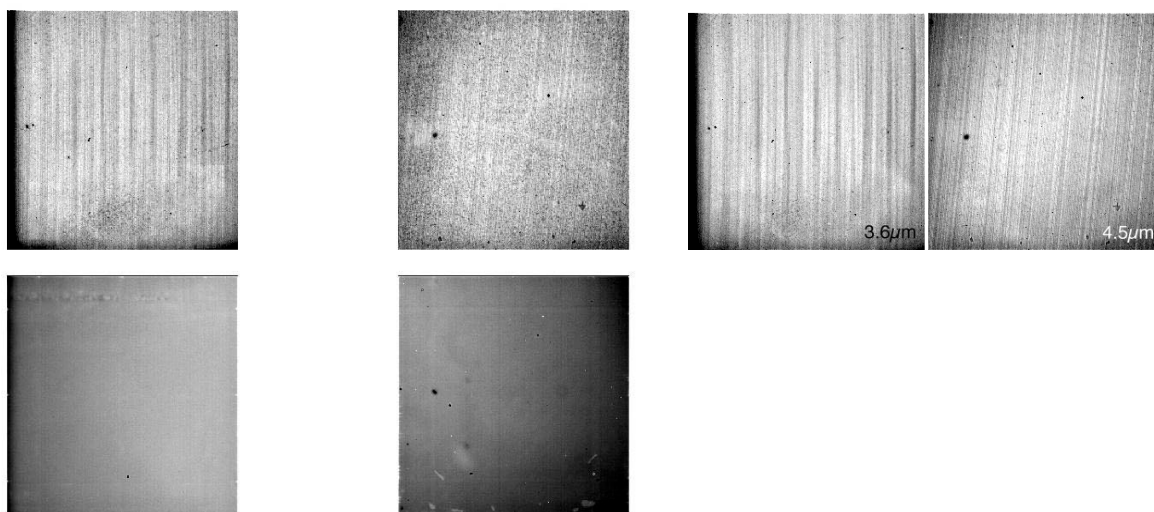
Figure 7.1: Super skyflats for IRAC. The cryogenic flats are shown on the left, ch1 at the upper left, channel 2 to the right of it, channel 3 at lower left and channel 4 to the right of it. The warm flats are shown on the right. These were made by combining the flat fields from the first five years of operations. The dark spot in channel 4, near the left side and about half way up, and the dark spot in about the same place in channel 2, are due to the same speck of contamination on the channel 2/4 pickoff mirror. The darkest pixels in the spot

are 20% below the surrounding area in channel 2, and 32% in channel 4. Flat-fielding in the pipeline fully corrects for these dark spots in the data.

The left edges of channels 1 and 3 are vignetted due to misalignment of IRAC optics with the telescope. The darkest pixels have 50% of the mean throughput in channel 1, and 70% in channel 3. The vignetting only extends for 10-15 pixels. The vignetting is compensated for by the flat-fielding, and results primarily in an increase by at most $\sqrt{2}$ of the noise in the affected pixels.

Finally, one should note that the flat fields are generated from a diffuse, extremely red emission source. While the resulting flats perfectly flatten the zodiacal background, they are not accurate for compact objects with different spectral slopes, the most obvious examples being stars. Please see the section on array location-dependent corrections (Section 4.5).

7.1.3   Missing Data

In some cases, there may be sections of data that are missing. These are usually marked in both the raw and (C)BCD data headers in the header keywords MISSDATA = T (both full array and subarray data) and MSLC1 (start of gap; raw only), NMSD1 (number of missing lines, raw only), MISS_LCT (total missed line count in the current FITS file; raw only) and MANCPKT =T (if ancillary data are missing; raw only). An example of missing full array data in a CBCD is shown in Figure 7.2. In subarray the data are stored in blocks of 4x256 pixels and missing frames may, for example, make an object completely disappear in a subframe. The corresponding mask image should show a flag revealing that the data are bad, and the header keywords should also indicate a missing line problem.
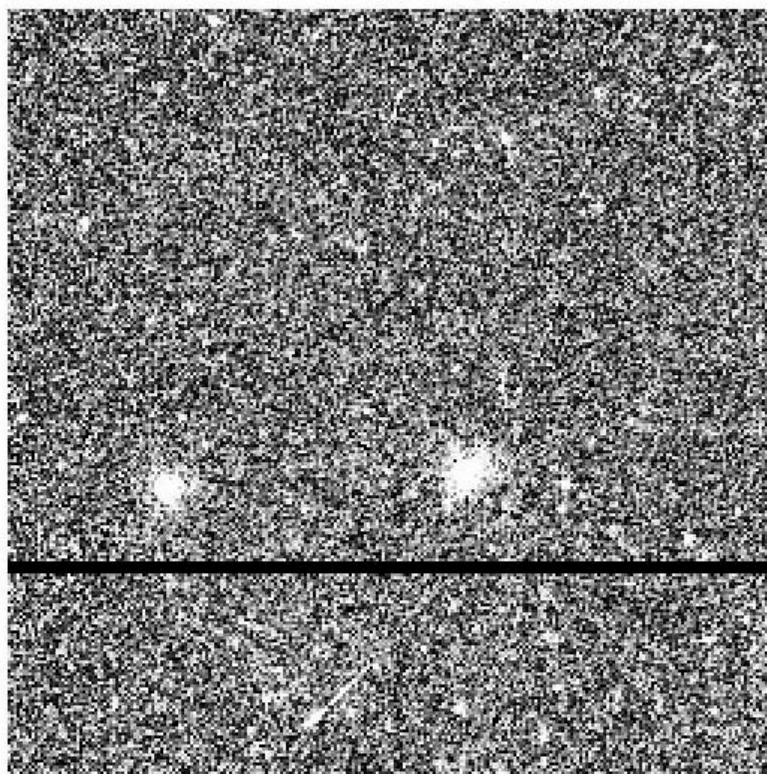
Figure 7.2: Full array CBCD image showing rows of missing data (dark band across the image). This observation is in channel 2, 12 second HDR frame, program pid = 80254, AORKEY 44050944.

7.2 Electronic Artifacts

7.2.1 Saturation and Nonlinearity

The IRAC detector pixels are limited in the number of photons (actually, electrons) they can accurately accumulate and detect. Once this maximum number is reached, the detector pixel is "saturated" and additional photons will not result in an increase in read-out data numbers. Prior to this, the detector becomes effectively less sensitive as more photons are received, an effect referred to as "non-linearity."

The saturation value varies slightly pixel-to-pixel, and substantially from detector to detector. The IRAC InSb (3.6 and 4.5 microns) detectors typically have saturation values of approximately 44,000 DN in the raw data. The Si:As detectors (5.8 and 8 microns) have saturation values closer to 52,000 DN. The IRAC pipeline automatically detects pixels that exceed a pre-defined threshold and marks them in the data mask. Unfortunately, IRAC uses a Fowler-sampling scheme where the returned DN are the difference between a set of readouts at the end of the integration (signal reads) and a set at the beginning (pedestal reads). Thus, once a pixel has saturated the signal reads, the DN for that saturated pixel will actually start to decrease,

and as a result of this double-valued nature the DN value alone is not a reliable saturation indicator. Examining the images containing very bright sources is necessary in order to evaluate saturation based on the observed spatial structure of the source. Very bright sources, for example, will appear to plateau or even develop a dark hole in the center. For point sources, a rough estimate of the flux in the saturated pixels can be made by fitting the wings of the PSF to the linearized pixels in the BCD image. If the data were taken in the high dynamic range mode, the IRAC pipeline will automatically identify pixels in the long frametimes that are saturated based on the observed flux in the short frame times. The short frame time data can then be used to recover saturation in the long frame time data (this is not done automatically). This replacement is accurate to about 10% at the peak of bright sources as the ~ 0.1 arcsecond jitter of the telescope coupled with pixel phasing in channels 1 and 2 and charge diffusion in all channels will cause the measured flux densities between short and long frames to vary.

The IRAC arrays are slightly nonlinear at all signal levels. At levels above 30,000 DN (in the Level 0 raw data) the response is low by several percent. As part of pipeline processing, the data are linearized based on ground calibrations (which have been verified in flight) of this effect. The BCD data are linear to better than 1% up to about 90% of full well, which is defined to be the level where we no longer can fully linearize the data, and at which saturation, by definition, begins. Below 20% of full well the nonlinearity in the raw data is negligible.

In detail, there are four places in the electronics where a pixel may saturate: the detector diode, the unit cell source-follower in the Read-Out Integrated Circuit (ROIC), the output source-follower in the ROIC, and the analog-to-digital converter (ADC) in the warm electronics. In most cases, it is the ADC that saturates first, at 0 or 65,535 units. ADC saturation produces a discontinuity in the second derivative of the measured Fowler DN versus the flux. The other saturations are smooth, with no discontinuity. In the other cases, depending on the channel, the detector diode may saturate before or after the source-followers.

In principle, for any source for which we already know the spatial variation of its intrinsic surface brightness, we can determine whether the pixel is above or below saturation, and therefore, its flux. In practice, we do not know the gains of the source-followers very well near saturation, nor do we know enough about the detector diode saturation, to make a good estimate of the flux. Therefore, we flag pixels which are above the range of our linearization correction.

The users should note that the pipeline does a saturation correction for bright point sources (see Section 5.2.2). In some cases of a bright and variable background, such as the center of a globular cluster, the pipeline may be fooled to insert an artificial "star" into the CBCD image. Users are encouraged to carefully examine the CBCD images in such cases and use the BCD images if any new artificial-looking features are found in the CBCD images.

7.2.2   Muxbleed (InSb)

Multiplexer bleed, or "muxbleed," appears in IRAC channels 1 and 2 (3.6 and 4.5 μm). It looks like a decaying trail of pixels, repeating every 4th column, with enhanced output level trailing a bright spot on the same array row. The effect can wrap around to subsequent rows, but it does not wrap from the last

row to the first. Since columns are read simultaneously in groups of four, one for each mux output, the next pixel read out on any single output is four pixels to the right, in array coordinates. As the BCDs for channels 1 and 2 are flipped in the y-direction when compared to the raw images, the read direction is top to bottom for BCDs and muxbleed-triggering pixels will affect rows beneath the source. Muxbleed is usually accompanied by a pinstripe pattern (every 4th column) that may extend over part of the image preceding or following the pixel. It is caused by a slow relaxation of the mux following the momentary disequilibrium induced when a bright pixel's voltage is placed on an output FET during pedestal and signal reads. Although the pixel rise and fall times are fast (2.6 and 1.0 μsec, respectively) compared to the 10 μsec time to clock the next pixel onto an output, longer relaxation times are involved for an output FET to fully recover after the voltage from a bright pixel is briefly impressed on its gate. The decaying trail has a time constant of tens of μsec, and the pinstripe, tens of seconds. In BCDs produced by pipeline versions prior to S13, the pinstripe pattern from muxbleed was complicated by a de-striping step in the pipeline in the darkdrift module. This often caused pinstriping to appear over an entire image. In data processed by pipeline version S13, we turned off the de-pinstriping in channels 1, 2, and 4, but left it on for channel 3. It was subsequently noticed that the vertical striping affects all four channels, and the destriping step, the so-called "jail-bar correction," was turned on in all four channels beginning with pipeline version S14.

Stars, hot pixels, and particle hits can generate muxbleed, and the characteristics of the pinstripe depend on frame time and Fowler number. Hot pixels may show muxbleed in a raw image, but in the BCD the muxbleed induced by hot pixels may not be present because it was canceled in either the labdark subtraction or in the skydark subtraction. The pinstripe pattern is nearly constant in areas of a single image that do not contain a saturating star, particle hit, or hot pixel. The characteristics of muxbleed from particle hits depend on when the hit occurs within the frame.

Muxbleed was characterized long before the launch of Spitzer, but it is reasonably well understood and it is fully corrected in the final IRAC pipeline. The pinstripe is strongest in channel 2, particularly in 12 second frames. In channel 2 mosaics, even with overlap correction, there may appear to be bright and dark patches everywhere, about the size of one frame or part of a frame. Upon close inspection, though, individual patches are revealed as areas of nearly constant pinstripe pattern that runs between the edges of the array, bright stars, hot pixels, and particle hits. A systematic and automated pinstripe correction scheme has been implemented in the pipeline.
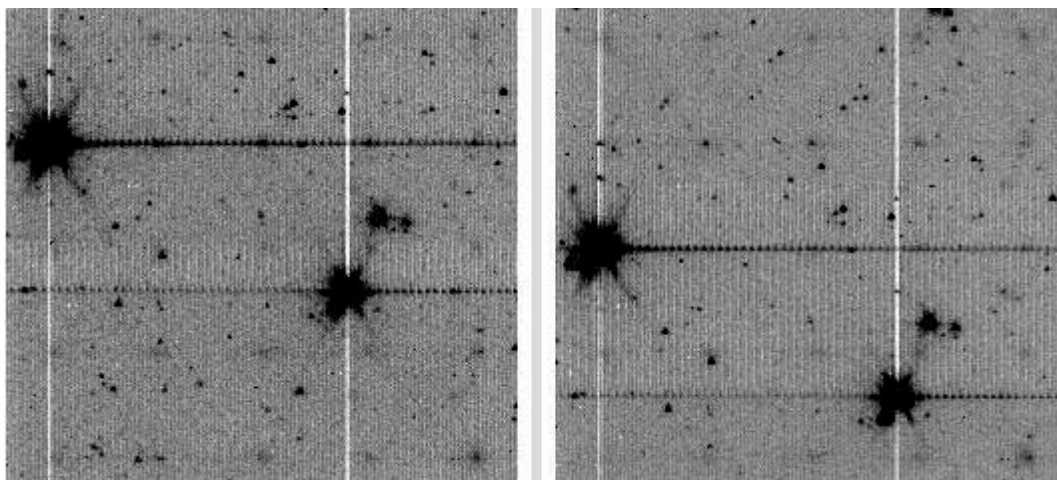
Figure 7.3: Images showing the muxbleed effect (the horizontal line on both sides of a bright stellar image). The pixels on the left side of the bright source are pixels on rows following the row in which the bright source was located (and have wrapped around in the readout order of the array). The vertical (white) lines are due to the so-called "column pull-down" effect. These are 12-second BCD frames in IRAC channel 1, taken from IRAC program pid = 618, AORKEY = 6880000.

The amplitude of the effect decays as one moves away from the bright spot, and this decrease can be nicely described by a simple function. In general, the muxbleed decays rapidly within 5–10 reads and plateaus at a roughly constant value. The functional form of the muxbleed is frame time independent. However, the amplitude does not scale linearly with the flux at the brightest pixel or the integrated flux of the triggering source, and this often leaves over/undercorrection of muxbleed in BCD frames. For this reason, an additional muxbleed correction by fitting the functional form of the muxbleed pattern to the actual muxbleed incidence is performed after the BCD frame creation (i.e., CBCD frames) and this will correct muxbleed below the rms noise level of the image.
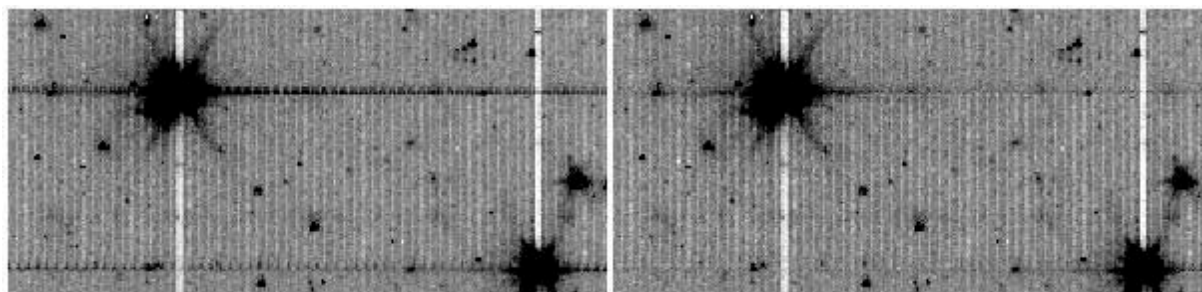
Figure 7.4: Demonstration of the S18 pipeline muxbleed removal. The image on the left is before and the one on the right is after the correction. These are First Look Survey channel 1 data, taken from AORKEY =

4958976. Note that the brightest star in the upper-left corner is heavily saturated and the current muxbleed scheme can correct muxbleed from a saturated source also.
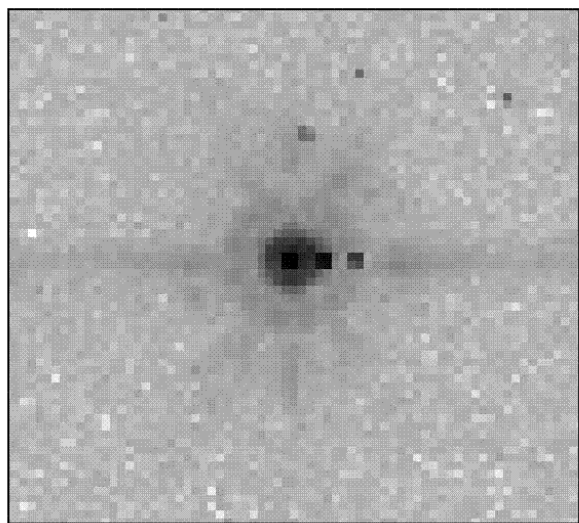
Figure 7.5: A typical bandwidth effect trail in channel 4, in a 30 second frame. These data were taken from program pid=1154, AORKEY = 13078016.

An example of the current (S18) muxbleed correction is shown in Figure 7.4. It can be seen that at least cosmetically the effect can be greatly reduced without introducing new artifacts. With an additional correction to residual muxbleed during the CBCD pipeline, resultant images should be nearly muxbleed free.

7.2.3   Bandwidth Effect (Si:As)

The bandwidth effect appears in IRAC channels 3 and 4 (5.8 and 8.0 μm). It looks like a decaying trail of pixels 4, 8, and 12 columns to the right of a bright or saturated spot. Only in the most highly saturated cases is the effect visible 12 columns to the right. A typical case for a star is shown in Figure 7.5. The effect is due to the fact that inside the ROIC the maximum voltage slew rate is limited, so charge on the output bus can not be drained fast enough for the output to settle to the value for a dark pixel that follows a bright pixel, or vice versa, in the 10 μsec or 20 μsec at which times the next two pixels (4 and 8 columns to the right) are read out. A smaller, additional delay comes from charging or discharging the cables from the array to the warm electronics. The effect is nonlinear except in the weakest cases. The output FETs in the Si:As arrays do not have the long recovery time that causes the long muxbleed trails and pinstriping in the InSb arrays, in part because the voltage swings have the opposite sign. The bandwidth effect presumably affects the first two or three pixels read out after a bright pixel in the InSb arrays as well, but for InSb, we have included the bandwidth effect as part of the overall "muxbleed" effect. It is much better behaved in InSb because the voltage swings are smaller and the slew rates are faster. A rare case which gives rise to a bizarre image is shown in Figure 7.6. Here, an extremely saturated star saturates an area in the last 4 columns. The bandwidth effect appears in the first 12 columns, making it appear as if the right edge of the image was cut and pasted onto the left side of the image.

Because of the details of the array clocking, part of the unsettled signal appears in both the same row and the next row.
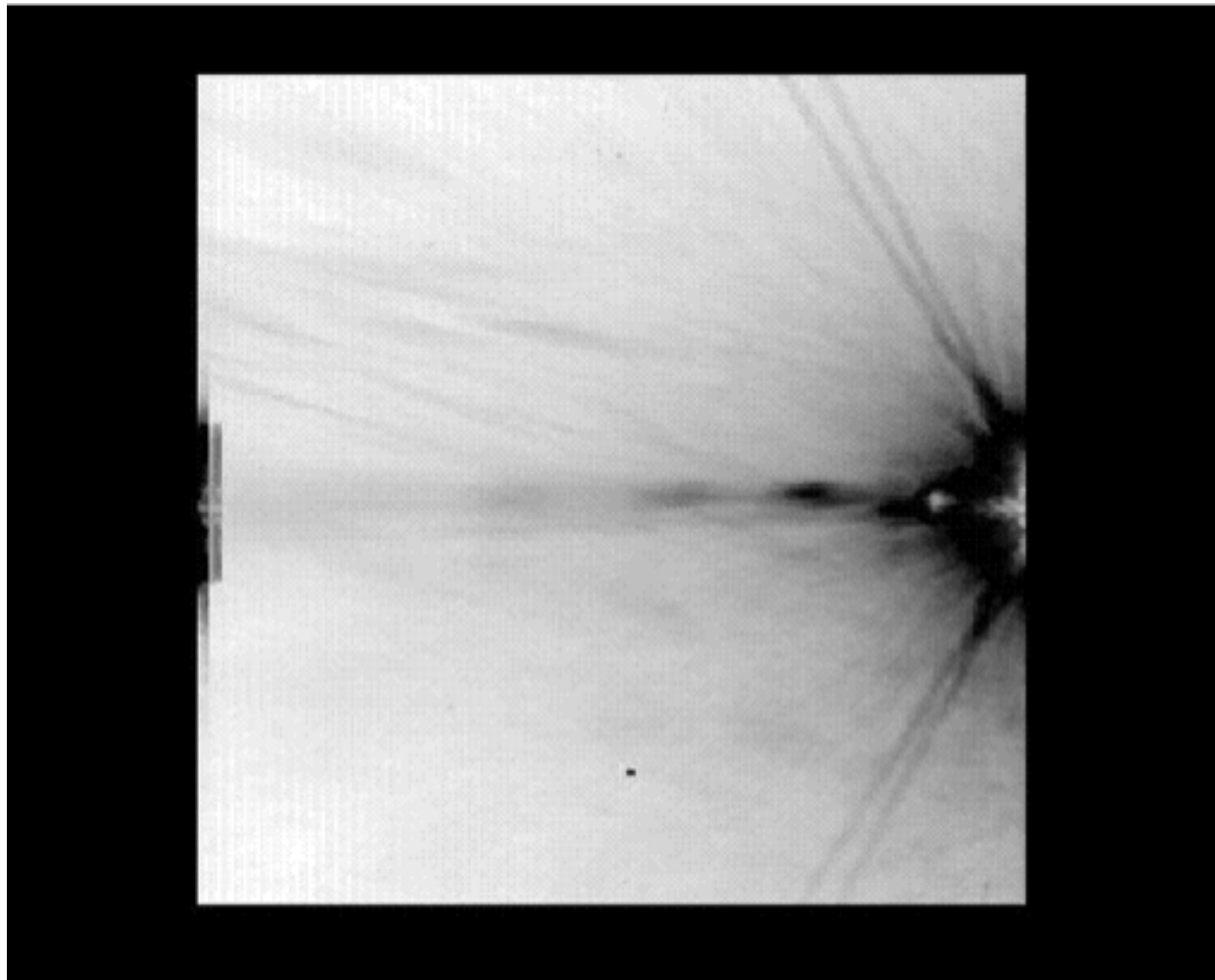
Figure 7.6: The bandwidth effect when a bright object is in the last 4 columns. IRC+10216, strongly saturated, is just off the right side of the channel 3 array. Even the filter ghost is saturated. The bandwidth effect appears on the left side of the array. These data were taken from program pid = 124, AORKEY = 5033216.

7.2.4   Column Pull-Down/Pull-Up

When a bright star or cosmic ray on the array reaches a level of approximately 35,000 DN, there is a change in the intensity of the column in which the signal is found. In channels 1 and 2, the intensity is reduced throughout the column (thus the term "column pull-down"); see Figure 7.7. When the effect occurs, it shifts the intensities of the pixels above and below the position of the "guilty" source, within the same column. This effect is limited to the brightest sources. The amplitude of the column pull-down does not scale linearly with the flux of the source or the brightest pixel. The effect appears to be constant on

either side of the source and algorithms which fit separate DC offsets above and below the source should be effective. Cosmetic corrections are partially successful. One, provided by the GOODS Legacy team, takes the median of each column, identifies columns that deviate from the local average by more than some threshold, and then adds back in a constant to the apparently affected columns. The code does not currently work in fields with extended emission. A more general algorithm which estimates the "true" sky value for affected pixels and fits DC offsets is also available for observations of more structured emission. This algorithm is implemented in the BCD pipeline.
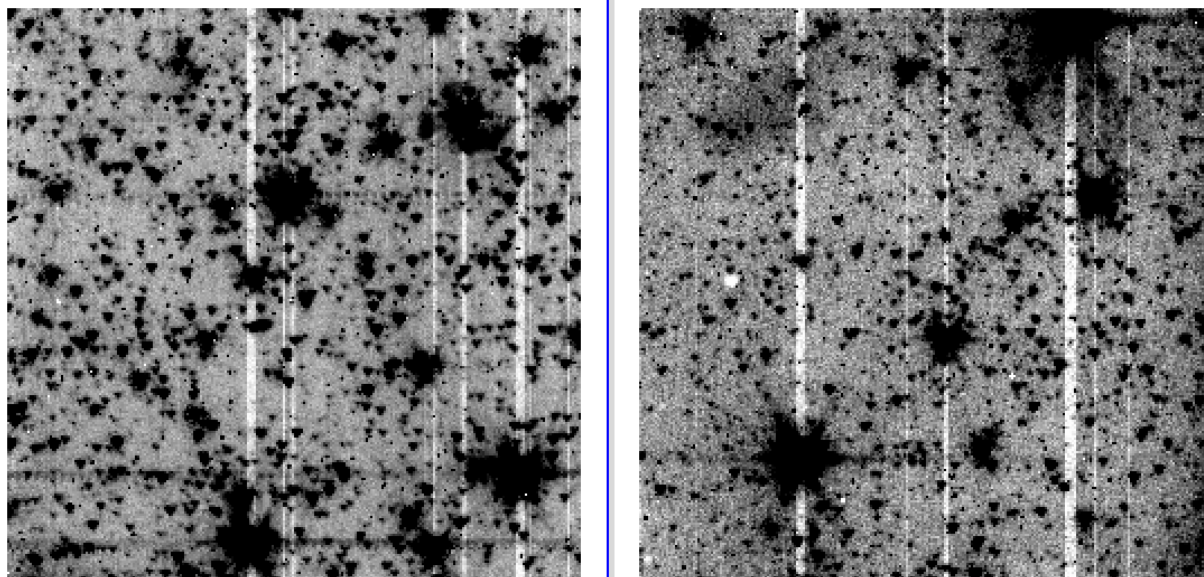
Figure 7.7: IRAC channel 1 (left) and channel 2 (right) observations of a crowded field with column pull-down apparent from the brightest sources. Note that the brighter sources affect a larger number of columns. These data were taken from program pid = 613, AORKEY = 6801408.

7.2.5   Row Pull-Up

In addition to muxbleed in channels 1 and 2, there may be electronic banding, which is manifest as a positive offset for rows that contain bright pixels. This effect is at least an order of magnitude smaller than muxbleed. Electronic banding is more significant in channels 3 and 4 but it is not as significant as the optical banding in those channels (see Section 7.3.2). The BCD pipeline mitigates against these effects. The algorithm finds instances of pull-up and banding and fits the DC offsets on either side of the triggering source to them.

7.2.6   Full-Array Pull-Up

In all four arrays, there is also an effect where an entire image is uniformly offset by some amount of DN's that is approximately proportional to the total flux or fluence integrated over the array. It is easily

noticed in a mosaic when overlap correction is turned off, and when the mosaic contains areas with and without strongly saturated stars. We call this effect "full-array pull-up," but it is also known as "droop" to the community of users of doped silicon IBC arrays. The effect can go unnoticed when overlap correction is done in the mosaic. It has no significant effect on aperture photometry of point sources or extended sources when a good background mean can be obtained within the same 5 arcmin x 5 arcmin image as the source. The effect is largest in channels 3 and 4, and if uncorrected, can lead to significant errors in the derived flux of extended objects, and especially in the brightness of the background itself. It is hard to distinguish the effect from the internal scattering in channels 3 and 4. The IRAC pipeline does not correct this effect.

7.2.7   Inter-Channel Crosstalk

We have detected electronic crosstalk between channels only in the brightest sources that have been observed. All four channels are read out simultaneously, except for the 100/200-second frames in channel 4, for which two/four 50-second frames are taken instead of the long integrations in the other channels, because IRAC is background-limited in channel 4. When a source falls on a pixel of one array, crosstalk may occur in the same pixel location in the other arrays, or in the next pixel read out. The crosstalk appears as a combination of either a positive or a negative offset in the same pixel and the derivative of the signal in the same or previous pixel. As the source is dithered, the crosstalk follows it, and therefore crosstalk appears in the mosaics. It is so weak that we have detected it so far only in channel 3, when the source is in channels 2 and 4, and in channel 4, when the source is in channels 1 and 3. Figure 7.8 shows parts of the mosaics from the off-beams in a dithered observation of a very bright star. The star was observed in channels 1 and 3 FOV first, so there are residual images in channels 1 and 3 from the bright star. The residual images appear as a diffuse glow near the center. This glow is a combination of the residual images of a very strongly saturated star observed with a Reuleaux dither pattern, thus effectively smoothed by outlier rejection. The crosstalk appears in channels 3 and 4 as a partial dark ring with a bright core.
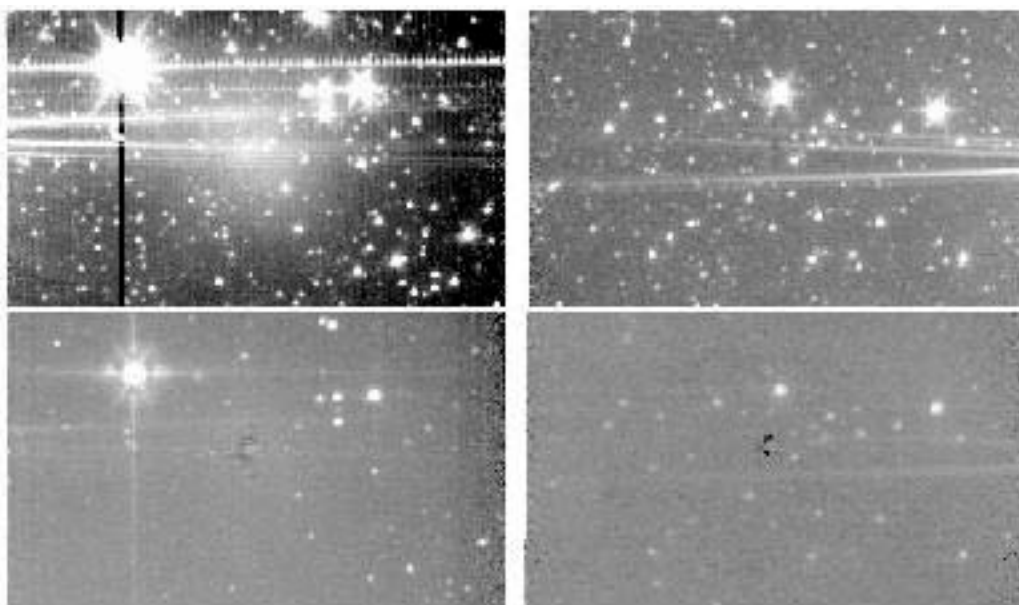
Figure 7.8: Channels 1 and 2 (top) and 3 and 4 (bottom) showing inter-channel crosstalk (dark spots near the center of the lower panels).

7.2.8   *Persistent Images*

The terms "persistent image", "residual image", and "latent image" are used interchangeably to describe the contamination of an IRAC image by a bright source from a previous exposure. When a pixel is illuminated, a small fraction of the photoelectrons become trapped. The traps have characteristic decay rates, and can release a hole or electron that accumulates on the integrating node long after the illumination has ceased. The warm mission short-term residual images are different in character than the cryogenic residuals, as the behavior of the trap populations is a function of the impurity type and array temperature. During the cryogenic mission, in all arrays, the longest e-folding decay time is about 1000 sec. For the warm mission, residuals in channel 1 are <0.01% of the fluence of the illuminating source after 60 seconds.

For extremely bright sources, residuals are produced even when the source is not imaged on the array. Residuals at 3.6 and 4.5 microns can be produced during slews from one science target to another and from one dither position to the next. These slew residuals appear as linear features streaking across IRAC images. Note that the pipeline cannot flag slew residuals, as there is no reasonable way of tracking the appearance of bright sources relative to the moving telescope pointing.

Observations contaminated by residual images can often be corrected with the data themselves. If the observations were well dithered, it is likely that the persistent image artifacts will be rejected as outliers when building the mosaic. Examining the median stack images that can be downloaded from the Spitzer Heritage Archive together with the data can often be used to identify pixels that are affected by residual images. Residual images can often be at least partially mitigated by subtracting the normalized median stack image (made with object and outlier rejection).

7.2.8.1   Cryogenic Mission Persistent Images

Tests performed during the In-Orbit Checkout (IOC) revealed that there are both short-term persistent images, with time scales of order minutes and which are present in all four arrays, and longer-term persistent images in channels 1 and 4. The short-term persistent images were known before the launch, and extensive calibrations and data analysis were performed to characterize them. The pipeline produces a mask (bit 10 of the imask) for each image that indicates whether a bright source seen by a previous exposure would have left a persistent image above three times the predicted noise in the present frame. To identify persistent images in your own data, we recommend doing a visual search on a median combined stack.

The longer-term persistent images were discovered in flight. In channel 1, the persistent images are generated by stars as faint as $K = 13$ (in very long stares). They can be generated by any long dwell time with a bright star on the array, whether or not the array is being read out. They were first noticed during a high-gain antenna downlink, when IRAC was left at a fixed position viewing the Galactic plane (by chance) for 45 minutes. The persistent images do not have the same size as a direct point source; they are significantly more diffuse (looking more like the logarithm of the point-spread function). The channel 1 long-term persistent images have time scales of order 6 hours, and they decay gradually. The cause of these persistent images has been identified as a known feature of the flight array (broken clamp) that cannot be fixed. The longer-term persistent images in channel 4 are induced by bright mid-infrared sources or bright stars. The channel 4 persistent images have very unusual properties: they have lasted for as long as two weeks, they can survive instrument power cycles, they do not decay gradually, and they can switch sign, as they decay, from positive to negative. The amplitude and decay rate of long-term persistent images is variable and no secure model exists to remove these artifacts from the data.
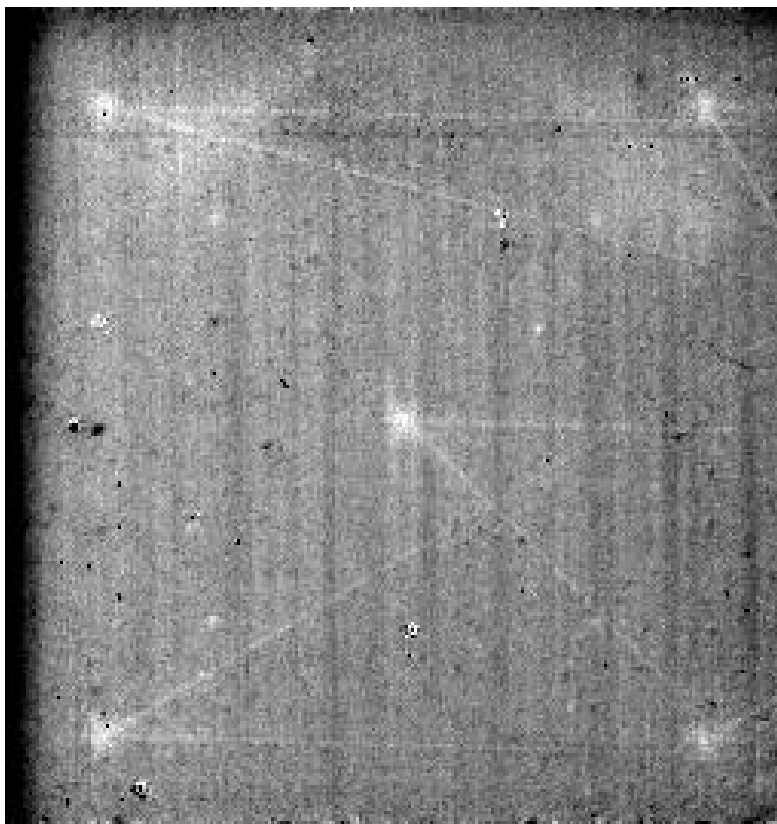
Figure 7.9: Median of channel 1 images from a calibration observation performed after observing Polaris. The 5 bright spots are persistent images from staring at the star while observing, while the set of criss-crossing lines were generated by slews between the various pointings. These observations were taken from AORKEY=3835904, in program pid=19.

We instituted a proactive and highly successful method of eliminating persistent images. Channels 1 and 4 were temporarily heated, or "annealed," briefly, with a small current running through the detector. The arrays were annealed after every telemetry downlink, which erased any persistent images built up during the downlink or during the previous 12-hour period of autonomous operations (PAO). This strategy, combined with scheduling known bright object observations immediately before downlinks, greatly decreased the possibility that preceding observations produced persistent images.

We have found that stars brighter than about magnitude −1 at 3.6 microns, when observed for more than about 6 seconds, leave a residual image that persists through an anneal, and even through multiple anneals. These latents from extremely bright objects are seldom visible in a mosaic of a science observation, but they appear in skydarks and other median-filtered stacked images of longer science observations. In channels 2, 3, and 4, all residual images are completely removed by a single anneal, and since January 2006 we annealed all 4 arrays every 12 to 24 hours.

Finally, we show an example of persistent images. Note that not all cases will be this obvious. In Figure 7.9 we see not only residual images of the star Polaris, but also residual streaks left by Polaris as the telescope moved between dither positions.

7.2.8.2 *Warm Mission Persistent Images*

Channel 1 and channel 2 have different persistent image responses in the warm mission data. There are no long-term residual images that last for weeks, such as those seen in channel 4 data during the cryogenic mission. Channel 1 residual images last for minutes to hours, depending on the brightness of the original source and the background levels in the subsequent images. The residual images in channel 1 in warm mission never exceed 1% of the illuminating source in exposures beginning immediately after the illumination of the bright source ends. Figure 7.10 shows this persistent image behavior for a first magnitude star (data taken from PID 1318). The residual image decay in channel 1 is exponential in character, as expected for trapped electron decay rates. The decay rate is constant for all sources, so that while residual images from brighter sources take longer to decay below the background level, all the persistent images decay at the same rate. These rates have been implemented for residual image flagging in the warm mission IRAC pipeline.

A consequence of the intermediate-term (hours) residual images is that it is possible for observations from a previous AOR to produce residual images. The residual image flagging module correspondingly tracks residuals from one AOR to the next. Given the original brightness of the saturation-corrected source, and the decay time calculated with the exponential decay rate, the pipeline flags all residual images until their aperture fluxes are less than three times the background noise in each image. For channel 1, each image in each AOR observed is checked for residual images from all previous observations within the observing campaign and the residual images are followed across PAOs (downlinks). Using calibration data from bright stars in channel 1 we have empirically modeled the residual flux density (in electrons) decreasing as $A \times e^{(-ltime/4.4)}$, where A is $-5614.36 + 880.12 \times \log 10$(residual causing source flux in electrons) and ltime is the time in hours since the residual causing source was observed. An example of this function is shown in Figure 7.10. We determine the background in each image by randomly selecting 100 regions in the frame, fitting a Gaussian to the electron number distribution and taking the mean from that fit as the background. If the predicted residual flux in electrons is more than 2-sigma above the background, the pixel is flagged as containing a residual image. To remove a saturated star from a possible residual image causing source list, its predicted flux in electrons needs to be below the 2-sigma background level in four consecutive images (which allows two HDR mode long exposure images to not contain a residual).

Channel 2 residual images decay much faster than those in channel 1, which last only a few minutes (<10) for even the brightest stars. Therefore, the pipeline flagging for channel 2 does not cross AORs. Channel 2 residuals start out as positive, but then become negative. The timing of the switch from positive to negative depends on the exposure time and brightness of the source. In channel 2 the decay times are much faster (minutes) and a linear function of the flux of the culprit source. More specifically, we flag pixels in channel 2 for 220 seconds after the culprit bright object has stayed on the pixels if the fluence (total number of electrons within the exposure time) of the culprit is less than 1.96×10^7 electrons, for 320 seconds if the fluence is less than 1.31×10^8 electrons, for 360 seconds if the fluence is less than 3.74×10^8 electrons and for 440 seconds if the fluence is greater than 3.74×10^8 electrons.

Table 7.3: Warm mission residual image durations.

Star K-magnitude	Channel 1 residual duration (hours)	Channel 2 residual duration (hours)
1	10	0.1
2	7	< 0.1
3	3.5	< 0.1
4	1.5	< 0.1

The arrays are not annealed during the warm mission as there is no evidence that annealing removes residual images (the arrays currently operate at nearly the old annealing temperature), and all residual images decay in a reasonably short time scale compared to those mitigated by annealing in the cryogenic mission.

Table 7.3 gives a rough idea of warm mission latent durations. Durations should not be taken as exact because they also depend on the background levels in the images that will change from one AOR to the next. This example comes from bright star observations in PID 1318 and starts with 12s observations of the bright stars.

Residual image flagging is only done for full array frames, because subarray frames do not have saturated stars tracked in the saturated star module of the pipeline, which is a necessary input to the residual image flagging routine. Residual images from non-saturated stars have not been studied.
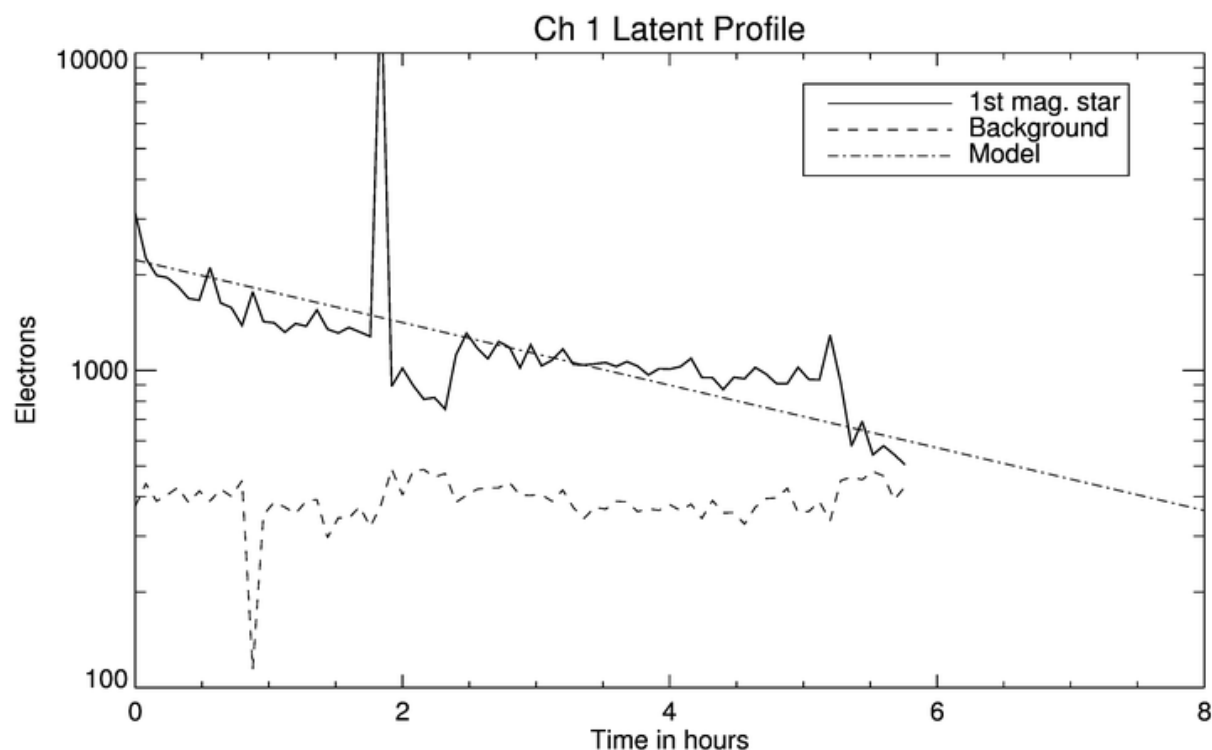
Figure 7.10: Residual image brightness decay as a function of time interval since exposure to a first magnitude source at 3.6 μm. The residual is compared to three times the noise in the sky background as measured in an equivalent aperture. The fitted exponential decay function is plotted as the dot-dashed line. These curves have been smoothed to mitigate flux jumps due to sources at the position of the original source in subsequent images.
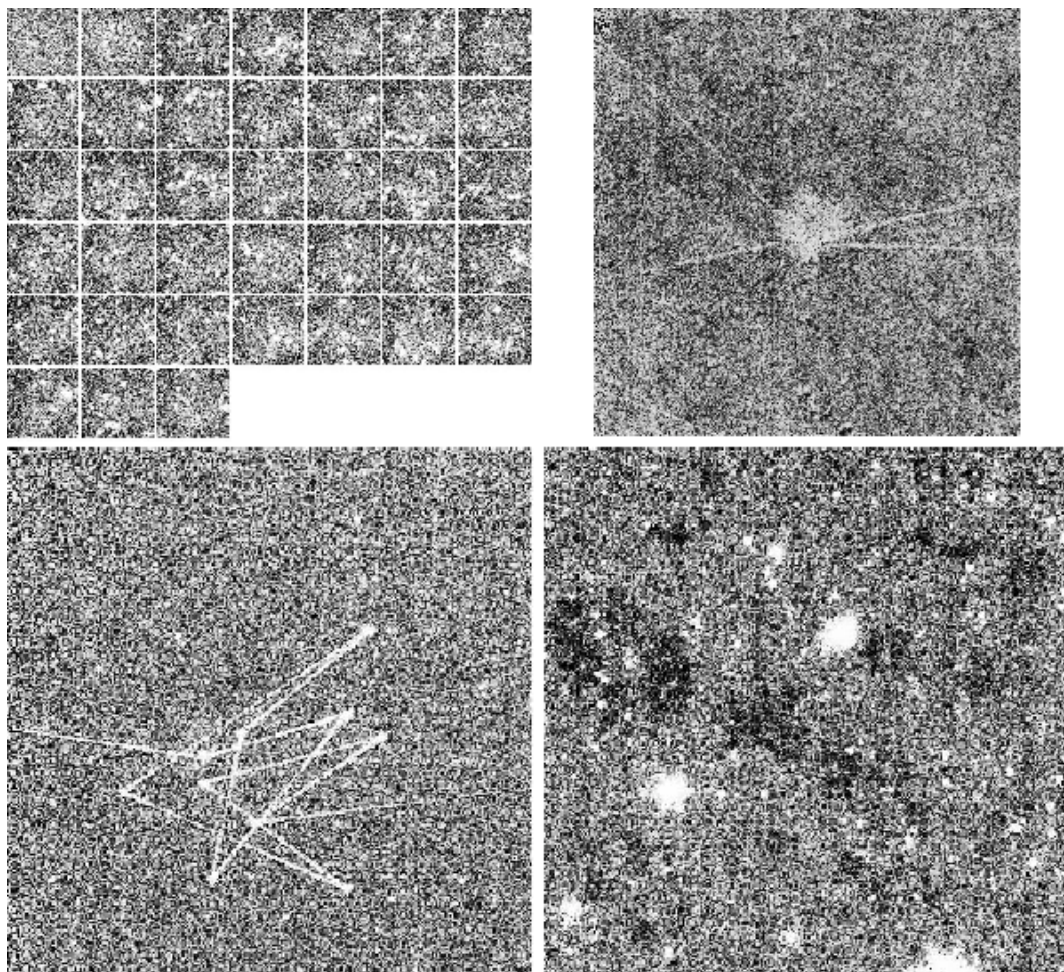
Figure 7.11. Residual image examples. From top left clockwise: ch 1, pid 90175, AORKEY 47943424; same as previous but showing the median image of the observation; ch 2, pid 90109, AORKEY 47828736; ch 1 pid 80096, AORKEY 45585920.
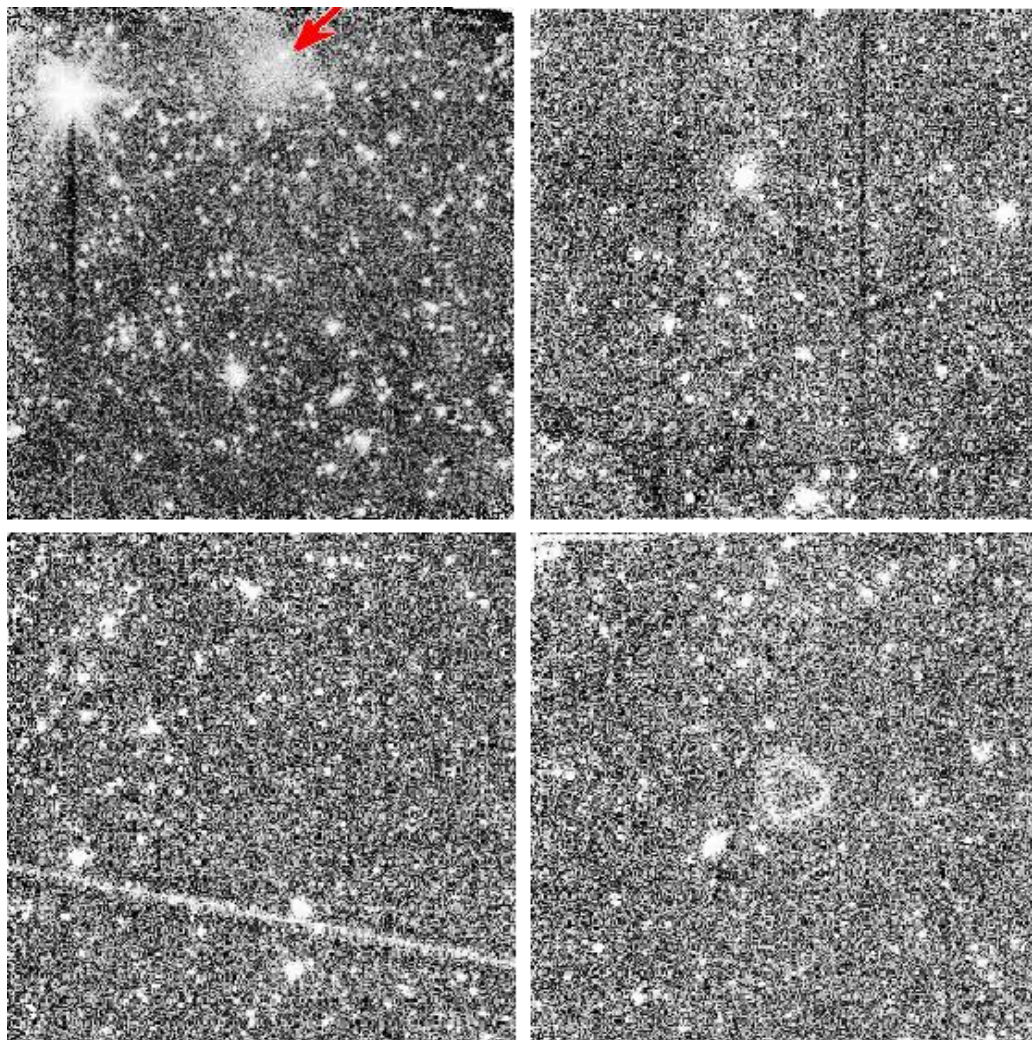
Figure 7.12. More residual image examples. From top left clockwise, ch 1, pid 90124, AORKEY 48337408; ch 2, pid 70044, AORKEY 40840192; ch 1, pid 80015, AORKEY 42191104; ch 1, pid 61009, AORKEY 35354880.

7.3   Optical Artifacts

7.3.1   *Stray Light from Array Covers*

Stray or scattered light on the arrays can be produced by illuminating regions off the edges of the arrays. Stray light from outside the IRAC fields of view is scattered into the active region of the IRAC detectors in all four channels. The problem is significantly worse in channels 1 and 2 than in channels 3 and 4. Stray light has two implications for observers. First, patches of stray light can show up as spurious sources in the images. Second, background light, when scattered into the arrays, is manifest as additions to the flatfields when they are derived from observations of the sky. The scattered light is an additive, not

a multiplicative term, so this will result in incorrect photometry when the flatfield is divided into the data unless the scattered light is removed from the flat. Stars which fall into those regions which scatter light into the detectors produce distinctive patterns of scattered light on the array. We have identified scattered light avoidance zones in each channel where observers should avoid placing bright stars if their observations are sensitive to scattered light.
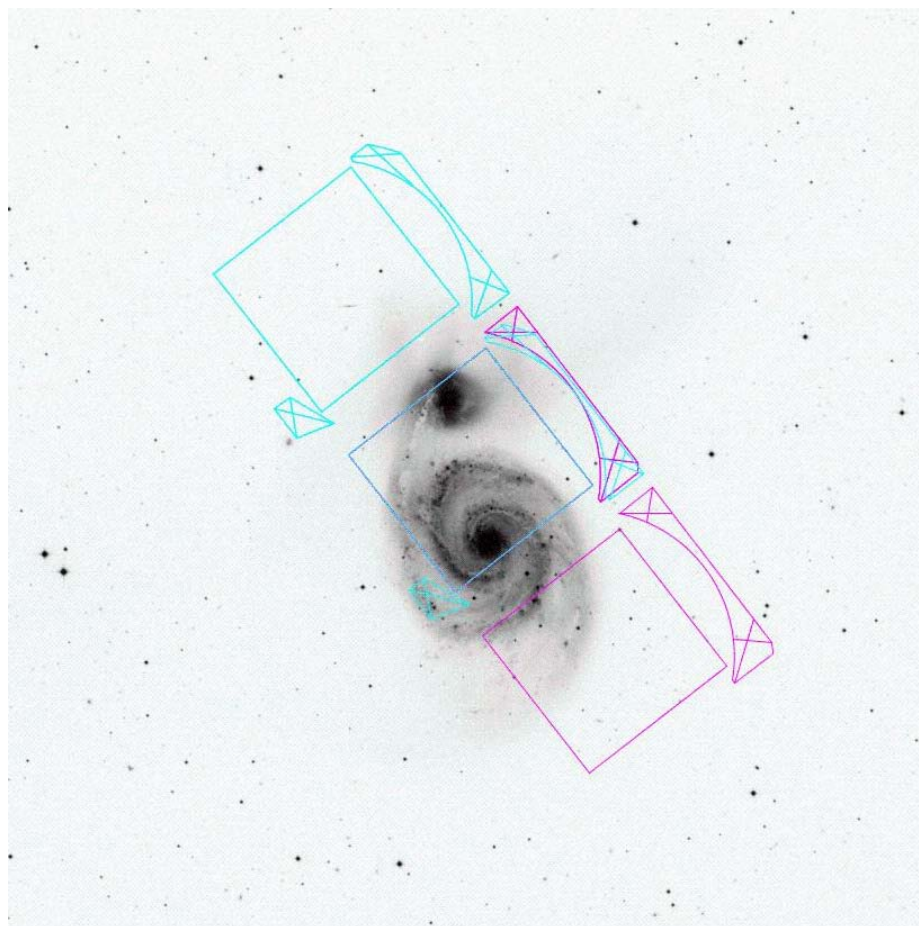
Figure 7.13: An image of the M51 system, showing an overlay of the IRAC fields of view, with the scattered light origin zones for channels 1 and 2 overlaid.

Figure 7.13 shows the zones for channels 1 and 2 with Spot overlays. Zones 1A, 1B, 2A and 2B (which produce the strongest scattered light) typically scatter about 2% of the light from a star into a scattered light "splatter pattern" which has a peak value of about 0.2% of the peak value of the star. Figure 7.14 to Figure 7.17 show examples of stray light in channels 1−4. Both point sources and the diffuse background generate stray or scattered light. Stray light due to the diffuse background is removed in the pipeline by assuming the source of illumination is uniform and has a brightness equal to the COBE/DIRBE zodiacal light model. This assumption is not true at low Galactic latitudes or through interstellar clouds, but in the 3.6–8 μm wavelength range it is nearly correct. A scaled stray light template is subtracted from each image, in both the science and calibration pipelines. Before this correction was implemented, diffuse stray

light from scattered zodiacal background contaminated the flats, which are derived from observations of high zodiacal background fields, and led to false photometric variations of 5%−10% in the portions of the array affected by stray light; this photometric error is now estimated to be less than 2%.
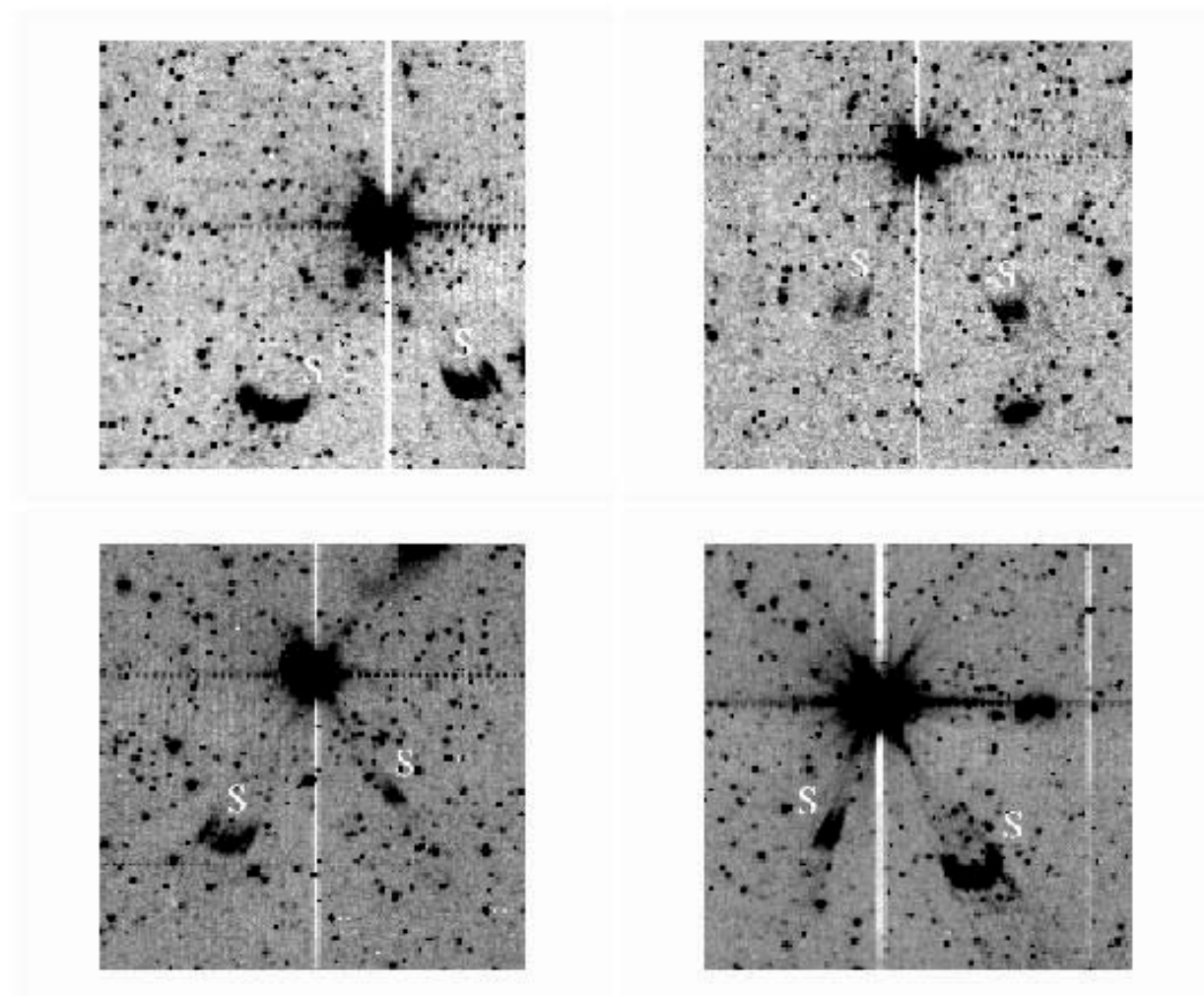
Figure 7.14: Channel 1 image showing scattered light on both sides of a bright star. The scattered light patches are marked with white "S" letters. The images were taken from program PID 30 data.

Example images of scattered light are shown here to alert you in case you see something similar in your IRAC images. The scattered light pattern from point sources is difficult to predict, and very difficult to model for removal. To the first order, you should not use data in which scattered light from point sources is expected to cover or appears to cover your scientific target. Stray light masking is done in the pipeline. This procedure incorporates our best understanding of the stray light producing regions. The procedure updates the corresponding imask for a BCD by determining whether a sufficiently bright star is in a stray light-producing region. The 2MASS point source list is used to determine the bright star positions.
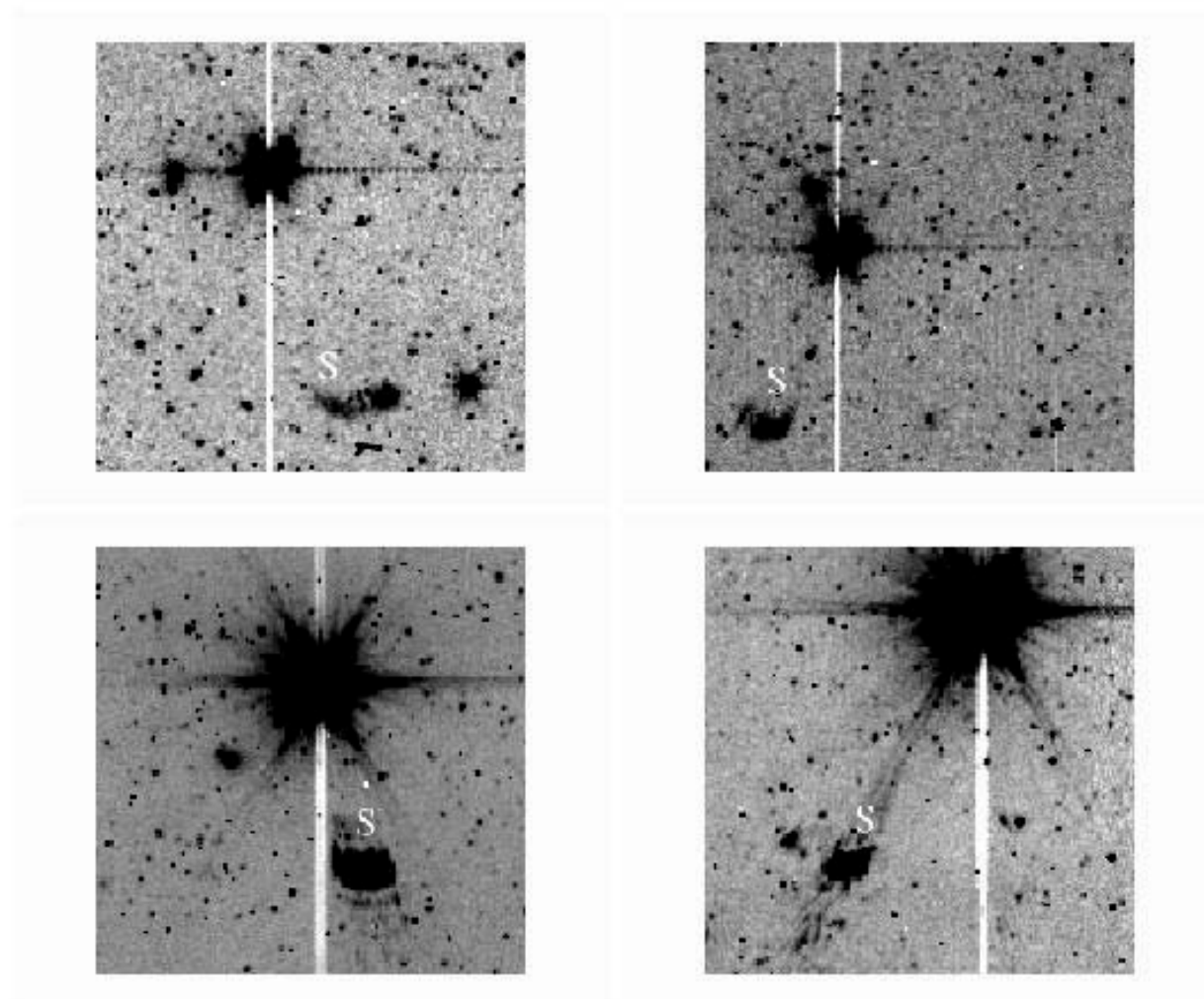
Figure 7.15: Channel 2 image showing scattered light on one side of a bright star. The scattered light patches are marked with white "S" letters. The images were taken from program PID 30 data.

Figure 7.14 to Figure 7.17 are 201 pixels (4.1') square, and have been extracted from larger mosaics produced from the IRAC GTO shallow survey (from program ID 30). This survey covers 9 square degrees with three 30-second images at each position. Because the mosaics cover large areas, the star causing the scattered light appears in many of the images. All of the sample images have the same array orientation as the BCD images. The sample images are mosaics of a BCD that contains the stray light and the BCD that contains the star that produces the stray light. Figure 7.14 and Figure 7.15 show scattered light in the two short-wavelength channels, from zones 1A, 1B, 2A, and 2B. Figure 7.16 and Figure 7.17 show examples of scattered light in channels 3 and 4.

Because stars are much fainter in these channels, and the scattering geometry is much less favorable, these scattered light spots are much less obvious than in the short-wavelength channels. Dithering by

more than a few pixels will take the bright star off the channel 3 and 4 "scattering strip," so the scattered light spots should be removed from mosaics made with adequately dithered data.
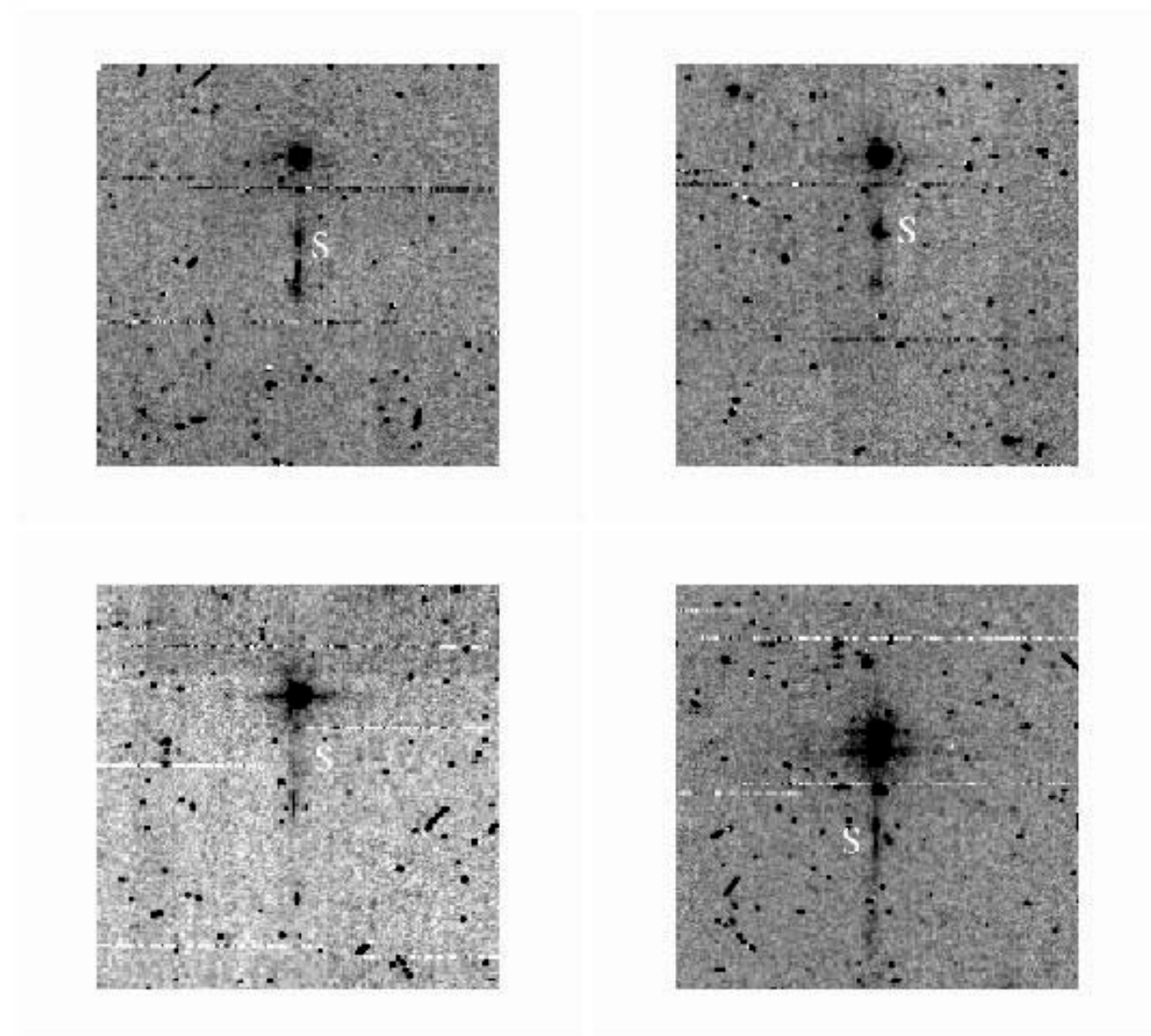
Figure 7.16: Channel 3 image showing scattered light from a scattering strip around the edge of the array where a bright star is located. The scattered light patches are marked with white "S" letters. The images were taken from program PID 30 data.

Please note that Figure 7.14 to Figure 7.17 were made with no outlier rejection. A dithered observation, combined with outlier rejection, will have much reduced stray light. Further, a diligent data analyst who recognizes and masks stray light in the individual BCDs will be able to eliminate stray light from well-planned mosaics. Observations made with little or no redundancy, or with dithers on scales smaller than the size of the stray light patches, will contain stray light and should be used with caution.
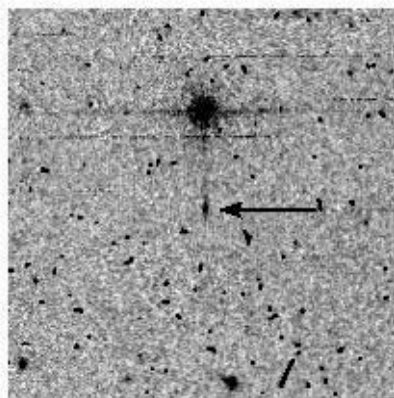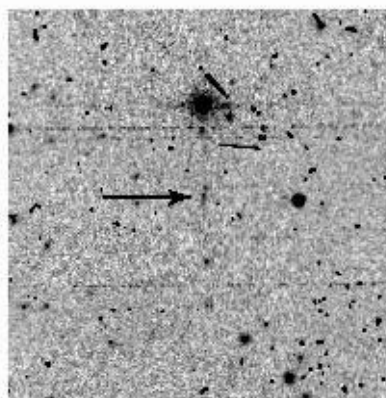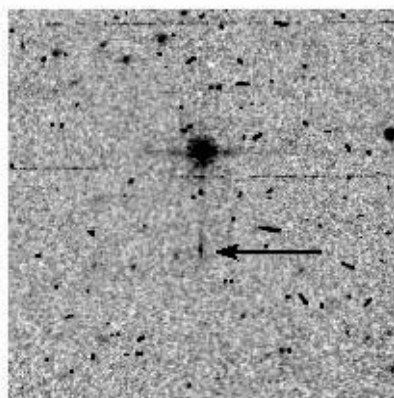
Figure 7.17: Channel 4 images showing scattered light from a scattering strip around the edge of the array where a bright star is located. The scattered light patches are pointed to by black arrows. The images were taken from program PID 30 data.

7.3.2   *Optical Banding and Internal Scattering*

The banding effect manifests itself as the rows and columns that contain a bright source having an enhanced level of brightness. This happens only in the Si:As arrays and has been shown to be due to internal optical scattering (inside the array). Both bright stellar sources and bright extended sources cause banding. It is clearly different from the optical diffraction patterns and the column pull-down effect. The SSC pipeline corrects for banding, but it does not model the flaring of banding towards the edges of the array. Therefore, the pipeline correction is not always perfect.

Banding only appears in IRAC channels 3 and 4 (5.8 and 8 micron bands), and it is stronger in channel 3. Banding probably occurs at all intensity levels, but only appears obvious around bright sources that are at or near saturation levels. Banding is seen both in row and column directions, though their relative intensities are somewhat different. In addition, there is an electronic effect. Channel 4 has a strong row pull-up, and channel 3 has a weak column pull-up. The column pull-up is uniform across the row where the source is bright. The optical banding intensity falls off with distance from the bright spot. Cosmic ray hits cause electronic banding, but not optical banding.
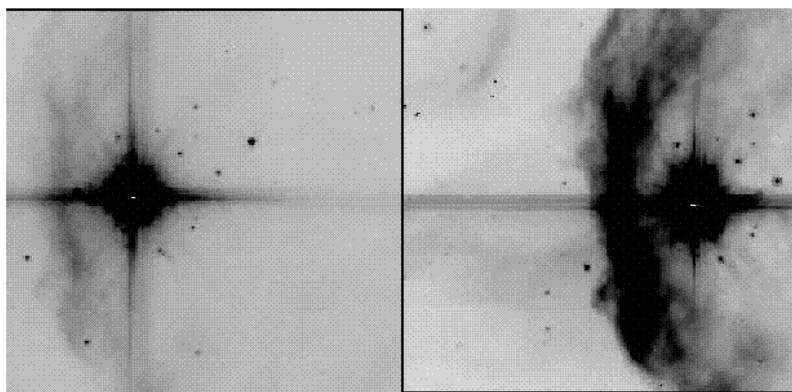
Figure 7.18: Typical image sections showing the banding effect. These are channel 3 (left) and channel 4 (right) images of the same object (S140), adopted from a report by R. Gutermuth. These data were taken from program pid 1046, AORKEY 6624768.

The optical banding is only an enhancement of the optical scattering in channels 3 and 4 near the row and column where the source is. Approximately 25% of the light incident from a point source is scattered throughout the channel 3 array. The detected scattered light falls with distance from the source. Channel 4 has the same problem to a smaller degree. Laboratory tests have confirmed the large amount of optical scattering within the Si:As arrays. At wavelengths shorter than about 10 microns, the Si:As in the channel 3 and 4 arrays is not opaque, and most of the incident photons, especially in channel 3, reach the front surface of the detector chip, where they are diffracted by the rectilinear grid of conductive pads. Many are diffracted into high angles and are multiply-reflected within the detector chip, and some can travel fully across the array before being absorbed (and detected). Other photons can pass through the detector chip and be scattered back into the detector chip where they are detected. The interference pattern tends to concentrate the scattered light along the rows and columns, causing the optical banding. The pattern is due to interference that depends on wavelength and the spatial extent of the source at each wavelength. The banding/scattering pattern does not vary much for point sources with a continuous spectrum, but a narrow-band source has a complex banding/scattering pattern.

Users should be aware of the uncertainties resulting from banding, specifically when attempting measurements of faint sources near the affected rows or columns. For bright sources with significant banding, aperture photometry may not be successful, and it would be better to measure these sources

using frames of shorter exposure times. Users are encouraged to experiment with image restoration techniques of their choice. Algorithms similar to the pull-down corrector may have some effectiveness in mitigating banding.

7.3.3   *Optical Ghosts*

There are three types of known or potential optical ghosts visible in IRAC images. The brightest and most common ghosts are produced by internal reflections within the filters. The first-order filter ghosts (one pair of internal reflections) in channels 1 and 2 are triangular, and in the BCD images they appear above and/or to the left of the star in channel 1, and above and/or to the right of the star in channel 2. The channel 1 first order filter ghost contains ~ 0.5% of the flux of the main PSF in channel 1, and the channel 2 ghost ~ 0.8% of the flux of the channel 2 PSF. Because of the increase in the optical path length, ghost images are not in focus. The separation between the main image and its ghost is roughly proportional to the distance of the main image from the Spitzer optical axis in both Y and Z directions, i.e., (Delta$_Y$, Delta$_Z$) = ($A_y y + B_y$, $A_z z + B_z$) where (y,z) are normalized coordinates in which the FPAs span the range [0,1] with the axes increasing away from the Spitzer optical axis, and the coefficients are as listed in Table 7.4 below. The +Y direction is in the IRAC (C)BCD +x direction and the +Z direction is in the IRAC (C)BCD –y direction. The peak intensity of the ghost is roughly 0.05% of the (unsaturated) peak intensity of the star. The second-order filter ghosts (two pairs of internal reflections) are much fainter (~ 25% of the flux and ~ 6% of the surface brightness of the first order ghosts), rounder, larger, and about twice as far away from the star. The separation between the star and its ghosts increases with distance from the optical axis of the telescope. The channel 3 and 4 filter ghosts appear as small crosses at a larger distance, mostly to the left or right of the star, respectively. They are offset from the primary image by approximately (+36 pix, +2 pix) and (-36 pix,+2 pix) in the Spitzer (Y,Z) directions for channels 3 and 4, respectively. The Z-offset varies slightly with position on the array. The channel 3 and 4 filter ghosts contain < 0.2% of the flux of the main PSF in these channels. The separation and orientation are different from channels 1 and 2 because of the different orientations of the filters. Examples of filter ghosts are shown in Figure 7.19.

Table 7.4. Coefficients for channel 1 & 2 ghost locations.

Channel	A_y	B_y	A_z	B_z
1	0.04351	0.00288	0.04761	0.00211
2	0.04956	0.00105	0.04964	0.00387
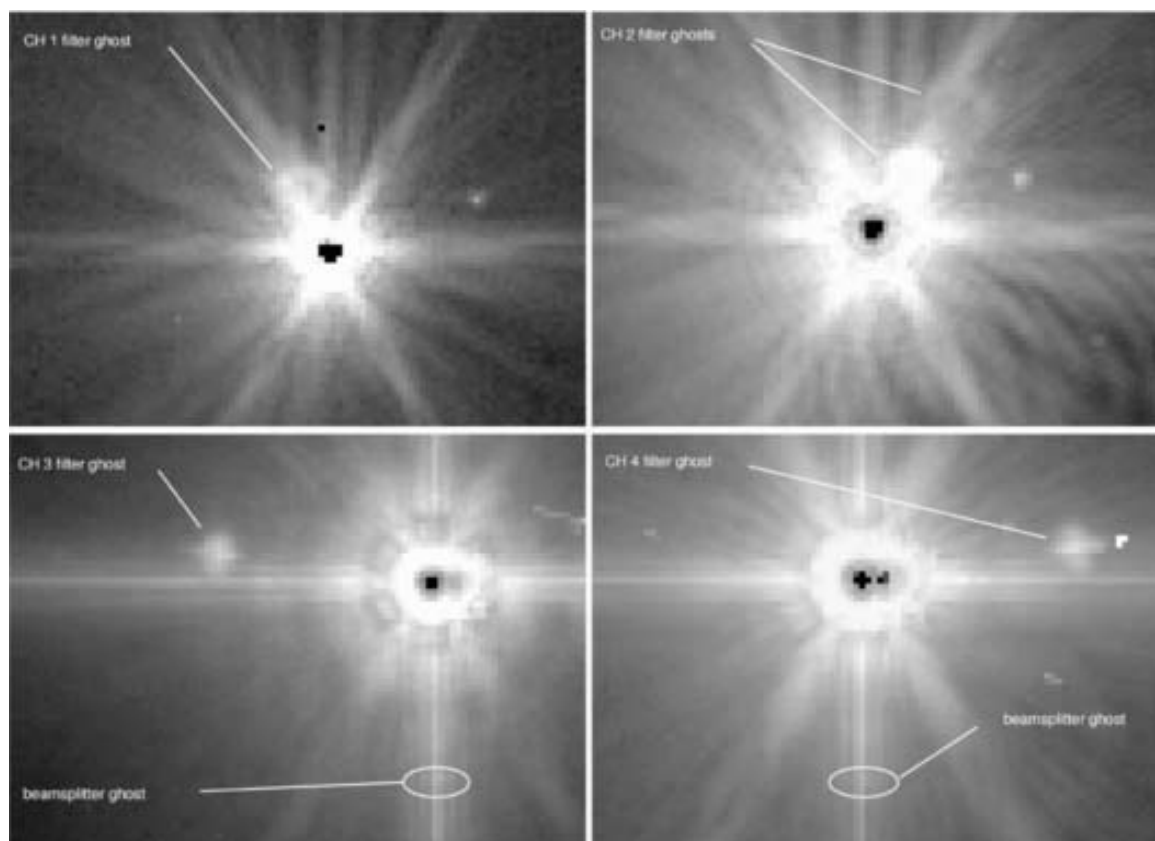
Figure 7.19: Filter and beamsplitter ghosts.

Similar ghosts are created by internal reflections within the beamsplitters. These only affect channels 3 and 4 which are transmitted through the beamsplitters. They appear as a very faint, short, horizontal bar at $\Delta y \sim -36$ pixels relative to a bright star (Figure 7.19), but are often obscured by brighter "banding" artifacts. They are slightly fainter than the filter ghosts.
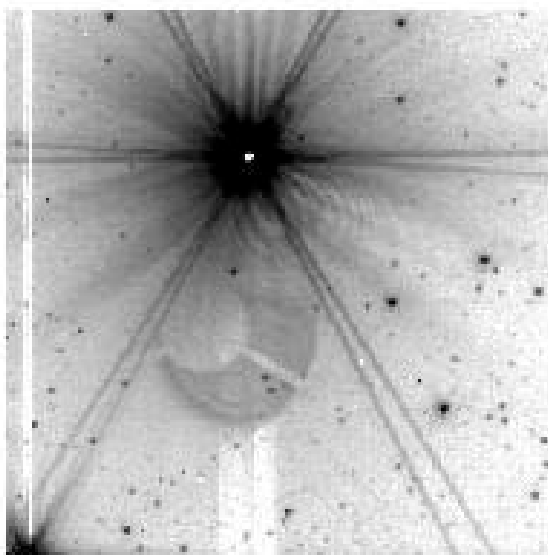
Figure 7.20: Pupil ghost in channel 2 from V416 Lac.

The faintest identified ghosts appear as images of the Spitzer entrance pupil, i.e., the primary mirror shadowed by the secondary and supports. These pupil ghosts are only found in channels 2 and 4, and require an extremely bright source (e.g., a first magnitude star in a 12-second frame) to be seen due to their low surface brightnesses. The pupil image is at a fixed location on the array (but in different locations in different channels). However, the pupil image is only partially illuminated by a single source, and the portion of the image that is illuminated depends on the source position on the array. An example of a pupil ghost is shown in Figure 7.20. This figure also shows some fringes in between the pupil ghost and the star. It is not clear if the fringes are directly related to the ghost. The total flux in these ghosts is ~ 0.05%−0.5% of the total flux in the PSF.

Currently we have no model for the exact shape and brightnesses of the ghosts, but we expect to develop models in the future. However, because the relative locations of the ghosts do vary with position on the array, sufficiently large dithering can help reduce or eliminate their effects. The stray light masking software also will flag the filter ghosts. The PRFs that we provide on our web pages include all the ghosts, and the apertures used in calibrating channels 1 and 2 include the filter ghosts. In performing photometry for channels 1 and 2, the filter ghosts should be included.

.

7.3.4   Large Stray Light Ring and Splotches

There is a faint ring of scattered light with a mean radius of about 23.7 arcminutes in channel 1 that is visible around bright objects. There is also a slightly larger, fainter ring in channel 2. They were first noticed in mosaics of a SWIRE field that was adjacent to the bright star Mira in PID 181 (see Figure 7.21). The ring was visible in channel 1 and 2 mosaics. We verified that the ring was an artifact by observing the field near Beta Gru where we observed pieces of the ring in the same places relative to the star. Starlight that is specularly reflected off the telescope mirrors cannot enter the MIC directly when the star is more than 16 arcminutes off the telescope boresight. IRAC's pupil stop is a little oversized, so the ring is probably light that is once or twice diffusely scattered at areas outside the secondary and/or near the top of the primary conical baffle. The mean surface brightness of the ring in channel 1 is 4.5×10^{-10} ($\pm 30\%$) times the mean surface brightness of the center pixel of a pixel-centered point source. Presumably there are stray light rings in channels 3 and 4, but they are too faint to see.
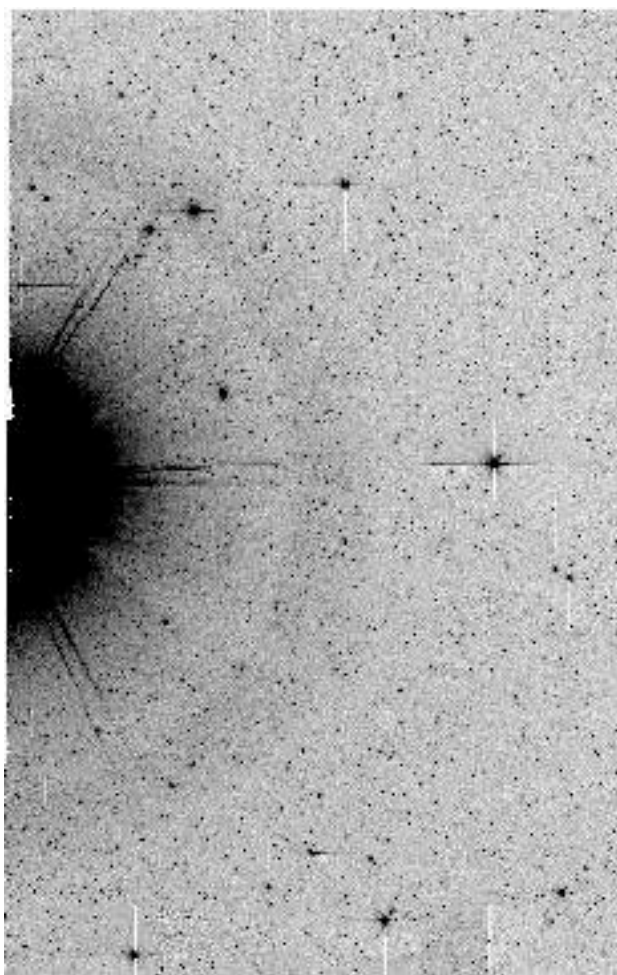
Figure 7.21: Part of the channel 1 mosaic (from observations in PID 181; AORKEYs 5838336, 5838592, 5839872 and 5840128) of the SWIRE field near Mira showing the 24 arcminute radius ring of stray light from the telescope.

The "splotches" (see Figure 7.22) are areas of more concentrated stray light that appear when a bright source is about 20–32 arcminutes off the center of the FOV, to the left or right in array coordinates. The splotches were seen in the SWIRE field near Mira and in the Beta Gru tests in channels 1, 2 and 4. The presence or absence of a splotch is very sensitive to the position relative to the bright object – a bright splotch can be present in one image and absent in an image with the telescope pointed a few pixels away. Even fainter splotches appeared in channel 2 about 1 degree away from Beta Gru, along the same directions. We thank R. Arendt for providing us with most of the information that was presented in this section.
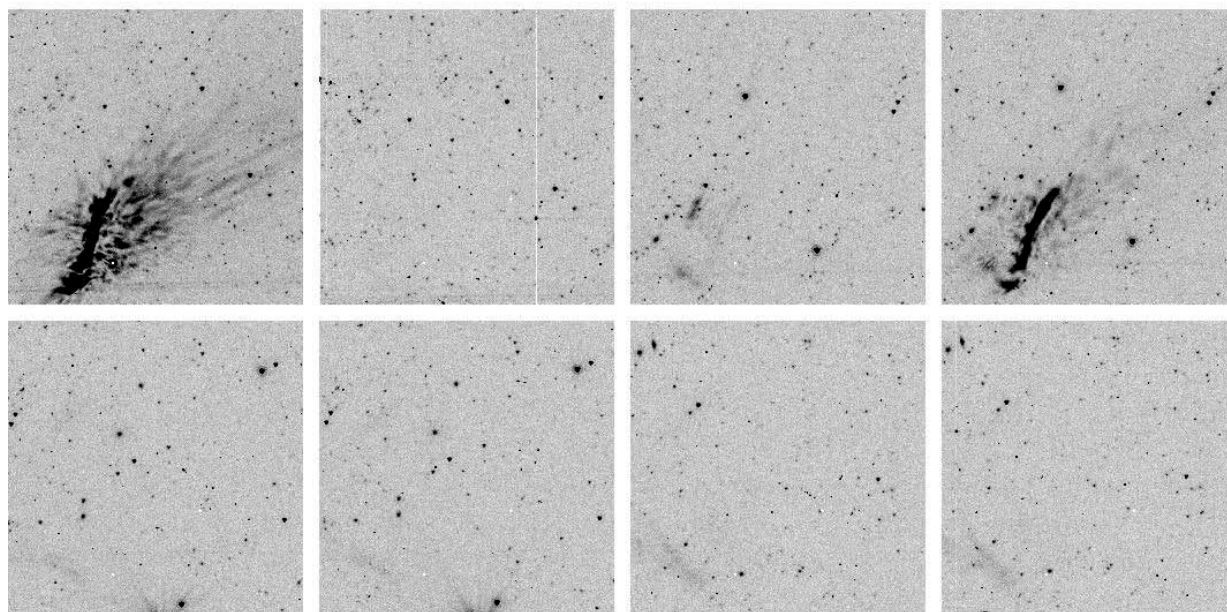
Figure 7.22: Channel 2 images from the SWIRE map showing stray light splotches from Mira, which was about 30 arcminutes away. Successive pairs of images were slightly dithered. The last pair is about 5 arcminutes from the first pair, but has a similar splotch. Note the absence of any stray light in the second image, though it was centered only a few pixels away from the first image. The images are from PID 181, AORKEY 5838336; EXPID 187 –192, 199, and 200.

7.4 Cosmic Rays and Solar Protons

The SSC mosaicker, MOPEX, identifies energetic particle hits as follows. All pixels in BCDs that contribute to a given pixel in the final mosaic are identified, and significant outliers (a user-specified number of sigmas above or below the filtered mean of all overlapping pixels of overlapping BCDs) are rejected. This method is very similar to the outlier rejection performed by shifting and adding ground based images. The rejected pixels can be inspected in the "Rmask" output files (one per input image). Outlier rejection in MOPEX can be adjusted. The parameters used in the online pipeline-generated

mosaics rely on multiple (≥3) sightings of each sky pixel. In general, a coverage of at least five is necessary to produce optimal results with the multi-frame (standard) outlier rejection.

A special outlier rejection scheme can be used for sparse (2–4x) coverage; this "dual outlier" mode can be turned on using the namelist parameter file. Dual outlier rejection identifies pixels greater than a specified threshold above the background, groups these pixels and adjacent pixels above a threshold into objects, and compares the object to objects in overlapping frames. If the object overlaps with objects in other frames (in celestial coordinates), then it is not a cosmic ray. If the object is not detected in a user-specified fraction of overlapping images, it is flagged as a cosmic ray. This information is written into the Rmask files used for mosaicking and source extraction. The dual outlier method should also be used in conjunction with the multi-frame outlier rejection method. Multi-frame rejection may throw out data around bright sources depending on the thresholding, due to pixel phase effects between BCDs. Using the dual outlier rejection and the REFINE_OUTLIER=1 option in MOPEX will prevent this.

Additionally, a single-frame radiation hit detector is run and produces bit 9 in the imask, but this bit is not used by the SSC post-BCD software and is not recommended because radiation hits cannot be uniquely separated from real sources in single images.
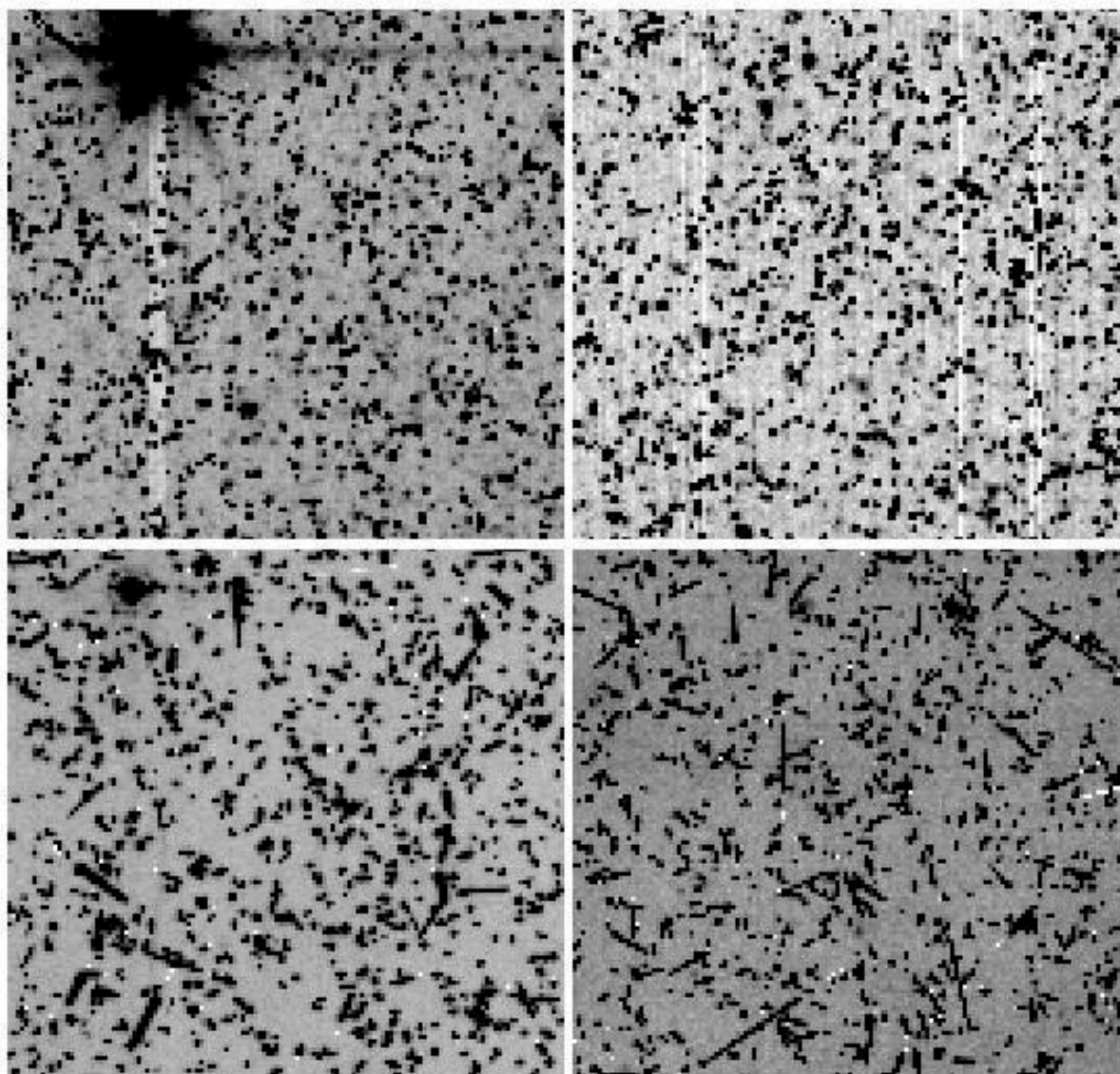
Figure 7.23: The central 128x128 pixels of IRAC 12-second images taken on January 20, 2005 during a major solar proton event. Channels 1 and 2 are top left and top right; channels 3 and 4 are bottom left and bottom right. Except for the bright star in channels 1 and 3, almost every other source in these images is a cosmic ray. These data are from observations in pid 3126.

Cosmic rays for channels 3 and 4 are larger and affect more pixels than the channel 1 and 2 cosmic rays due to the larger width of the active layer of the Si:As detectors. Some tuning of cosmic ray detection parameters may be necessary when working with deep integrations, especially for channels 3 and 4.

Each IRAC array receives approximately 1.5 cosmic ray hits per second, with ~ 2 pixels per hit affected in channels 1 and 2, and ~ 6 pixels per hit affected in channels 3 and 4. The cosmic ray flux varies randomly by up to a factor of a few over time scales of minutes but does not undergo increases larger than

that. Also, the cosmic ray flux is normally about a factor of two higher on average around solar minimum compared with solar maximum. Radiation hits do increase suddenly and dramatically during some major solar proton events. Historically, several such events have occurred over the course of the active part of a Solar cycle.

Two major solar proton events occurred during IOC, so we have experience in identifying them and their effects. Because of shielding around the instruments, only extremely energetic protons (> 100 MeV) of any origin appear as cosmic ray hits in the data. Thus, many solar weather phenomena ("storms," etc.) which do occasionally affect other spacecraft, or ground systems, are not of concern to Spitzer.

Radiation has very little effect on the IRAC arrays beyond elevating the counts in a given pixel. Some high energy cosmic rays cause persistent images, column pull-down, and muxbleed effects.

8 Introduction to Data Analysis

8.1 Post-BCD Data Processing

All processing of IRAC data beyond the individual, calibrated, 256 x 256 images produced by the BCD science pipeline is called "post-BCD." This includes combining all images from an observation (AOR) into a mosaic, detecting sources, and any cosmetic corrections, e.g., cosmic ray hits, to the images (individual or mosaic) that are not based on understood instrumental artifacts or detector physics. Two important post-BCD processes are performed routinely by the pipeline and generate results that are placed in the science archive. These include pointing refinement, wherein a set of point sources are identified in the images and are astrometrically matched to the 2MASS catalog, and mosaicking, wherein the individual images in an AOR are robustly combined into celestial coordinate mosaics for each IRAC waveband. The post-BCD processing can (and should) be performed in different ways for different observing strategies and scientific goals. The post-BCD pipeline processing was performed with a specific, conservative, set of parameters. Observers and archival researchers will very likely need to do post-BCD processing on their own. Most common will be generating mosaics from data in multiple AORs. Here we discuss some IRAC-specific issues. The post-BCD software consists of a series of modules linked by Perl wrapper scripts and controlled by namelists. Namelists need to be placed in a subdirectory called cdf and have filenames ending .nl. A (MOPEX) GUI is available as well. The namelist controls which modules are called, contain the names of the input file lists and output directories, and detailed parameter sets for each module. Input file lists should not have any blank lines, otherwise the programs will look for non-existent files. The following subsections deal with each part of the post-BCD pipeline in turn, starting with pointing refinement, then overlap correction, mosaicking and finally point source extraction.

8.1.1 Pointing Refinement

Pointing refinement corrects the pointing of each frame to the 2MASS sky. In the pipeline, the pointing refinement solutions for channels 1 and 2 are combined and applied to all four channels to produce the default pointing via the "superboresight." However, if they wish to try to improve on the supplied pointing, users may rerun the pointing refinement themselves using scripts that come with the MOPEX software package. Pointing refinement may not always be successful in channels 3 and 4, in which there are few 2MASS stars per image. Note that each run of pointing refinement overwrites any previous solutions (in the header keywords RARFND, DECRFND etc), so users should make copies of the BCDs before rerunning the pointing refinement if they wish to retain the old corrections.

8.1.2 Overlap Correction

The post-BCD software contains an overlap correction module that matches the background levels of overlapping frames in a mosaic. Generating new mosaics by running MOPEX with overlap correction turned on can remove the "patchiness" often seen in mosaics due to bias fluctuations in the array (due

both to the first-frame effect and bright source effects). Note that background matching does not always work well, especially between areas of unequal depth.

8.1.3   Mosaicking of IRAC Data

8.1.3.1   Creating a Common Fiducial Frame

Note that in the following we name the settings needed for the command line version of MOPEX. Corresponding values need to be set if using the MOPEX GUI.

As a first step in creating a mosaic, run the mosaicker with all the modules turned off except for the fiducial frame module (i.e., run fiducial image frame = 1 in the namelist), and include all the files you wish to mosaic from all four channels in the input list. This will generate the boundaries of the mosaic and will allow all channels to be mosaicked onto the exact same grid. Rename this file to, e.g., *FIF_all.tbl* to prevent it being accidently overwritten. Then, when running the mosaicker, set the fiducial frame to the file created by the fiducial frame module in this initial run using FIF_FILE_NAME = *(path)/FIF_all.tbl*, and turn off the fiducial frame module (i.e., set run_fiducial_image_frame = 0 in the namelist). The use of the common fiducial frame will ensure that the mosaics from all four channels will be accurately co-aligned. The pixel scale is controlled by the MOSAIC_PIXEL_RATIO X/Y parameters. Set Edge Padding = 100 to get a good border around the image. You can also specify CROTA2 for the output mosaic if you wish, or set CROTA2 = 'A' to get the smallest possible mosaic. The pixel size in the mosaic produced by the final pipeline is exactly 0.6 arcsec x 0.6 arcsec (CDELT1, CDELT2 = ±0.000166666667).

8.1.3.2   Outlier Rejection

The mosaicker has four outlier rejection strategies: single-frame outlier rejection, dual-outlier rejection, multi-frame outlier rejection and box outlier rejection. For IRAC, the most useful are the dual outlier and multi-frame rejections. Be sure to set THRESH_OPTION = 1 in the namelist in the multi-frame &MOSAICOUTLIERIN section. Setting the thresholds too low in the outlier modules can result in unwanted rejection of pixels in the cores of real objects. Users of these modules should carefully check the coverage maps produced by the mosaicker to ensure that the centers of real objects are not being masked out. The outlier rejection modules set bits in the rmasks. Bit 0 is set by the single-frame outlier rejection, bit 1 by the temporal (multi-frame) rejection, bit 2 by the dual outlier rejection and bit 3 by the box outlier detection. Which rmask bits are used by the mosaicker is controlled by the RMask_Fatal_BitPattern. The mosaicker takes the rmasks and makes an rmask mosaic. The switches USE_OUTLIER_FOR_RMASK, USE_DUAL_OUTLIER_FOR_RMASK and USE_BOX_OUTLIER_FOR_RMASK control which of the outlier detection modules are used. An important parameter is RM_THRESH in &MOSAICRMASKIN. When the rmask is made it is projected back onto the input images to determine which pixels will be masked in the final mosaic. An rmask pixel is divided amongst the overlapping pixels in the input image. Input image pixels with projected values of the rmask mosaic above RM_THRESH have the multi-frame outlier bit (1) set in their rmask. For channels 1 and 2 a fairly high value (e.g., 0.5) can be used. The more diffuse radhits in channels 3 and 4

---

can be more effectively rejected by setting RM_THRESH to a lower value, e.g., 0.05, which has the effect of growing the rmask and thus rejects the more diffuse edges of the radhit.

All the outlier rejection modules require uncertainty images. The BCD uncertainty images are adequate for this purpose, and the list of them should be specified with the SIGMALIST_FILE_NAME keyword in the namelist. To use them set have_uncertainties = 1 and compute uncertainties internally= 0. To compute your own uncertainty images, set compute_uncertainties_internally = 1, have_uncertainties = 0, and set the appropriate values in the &SNESTIMATORIN section of the namelist (see the mosaicker documentation for more details). Outlier rejection creates another set of masks, the rmasks. These indicate the pixels flagged by outlier rejection, and which are used by the mosaicker. A mosaic of the rmasks can be provided by setting run_mosaic_rmask = 1. As a check on the outlier rejection, it is often helpful to examine the coverage maps output by the mosaicker. If the outlier rejection has been over-zealous there will be reductions in coverage at the positions of real sources in the mosaic. Blinking the mosaics and coverage maps in, e.g., DS9 can thus be very helpful for determining whether the outlier rejection is set up correctly to reject only genuine outliers.

8.1.3.3   Mosaicker Output Files

The output directory structure after running the mosaicker looks like: BoxOutlier, Coadd, DualOutlier, Interp, ReInterp, Combine, Medfilter, Rmask, Detect, Sigma, Dmask, Outlier with "-mosaic" appended to these names, and the files in the output directory are *FIF.tbl*, *header_list.tbl*, and a namelist file with a date stamp. The directory "Combine" contains the mosaic, *mosaic.fits*, a coverage map, *mosaic_cov.fits* and an uncertainty map *mosaic_unc.fits.*

8.1.3.4   To Drizzle or Not to Drizzle?

The mosaicker has three interpolation options, set by the INTERP_METHOD keyword. The default is a linear interpolation. Drizzling is available as an option, as is a grid interpolation (useful for creating quick mosaics if the PSF quality is not important). Our experience with the drizzle option suggests that it is effective when used on datasets with many dithers per sky position, and it can reduce the point-response function (PRF) width by 10% – 20%, though at the expense of an unevenly-weighted image. The coverage map produced by the mosaicker can be used to investigate the pixel-to-pixel variation in the coverage of the drizzled image.

8.1.3.5   Mosaicking Moving Targets

Although Spitzer does track moving targets to a sub-pixel accuracy, the BCD pipeline only produces mosaics of IRAC data in fixed celestial coordinates. The user may opt to generate his or her own mosaic in a moving coordinate reference frame by setting the appropriate flags in MOPEX. The individual BCDs or CBCDs should be overlap-corrected first and then the mosaicker should be run with the flag MOVING_OBJECT_MOSAIC=1 set, using outlier rejection. Stars in the frames may be removed by outlier rejection, and the resultant composite of a moving target will be produced.

8.1.4   Source Extraction

The Spitzer source extractor, APEX, may be used to fit point sources in IRAC data. This software can be run in two modes, in a single frame mode (apex_1frame) which can be run on an individual BCD, CBCD or a mosaic, and in a multi-frame mode which uses the mosaic to detect sources, but the individual BCDs or CBCDs to measure their fluxes.

8.1.4.1   Noise Estimation

The accuracy of the fluxes from APEX is very sensitive to the noise estimates, as these affect the fitted background value. For crowded fields, it is essential to include an estimate of the confusion noise (currently not included in the BCD uncertainty image). This can be estimated by measuring the difference between the actual image RMS and the estimated RMS in the uncertainty image, and then either adding it to the uncertainty image, or using it as the confusion noise value when generating uncertainty images with the post-BCD software (see above).

8.1.4.2   PRF Estimation

The PRFs released with MOPEX should be fairly good matches to the data and a significant improvement on the previous versions. We do not recommend using the prf estimate tool to generate PRFs from the mosaics.

8.1.4.3   Background Estimation

The namelist parameter Background_Fit controls the type of background used for PRF fitting. If you give Background_Fit = 0, a median background is computed for the whole frame. A more accurate background estimate for PRF fitting, local to the source, can be generated by setting Background_Fit = 1. Note that the aperture fluxes reported by APEX are always made using the median background, and hence may be inaccurate for faint sources.

8.1.4.4   Source Extraction

Source detection and extraction are controlled by the parameters Detection max/min area and detection threshold. APEX will frequently try to split bright sources into several components. This tendency can be controlled by setting the Max_Number_PS parameter in &SOURCESTIMATE to a low number (2–3). Two files are output, *extract raw.tbl* contains all detections, and *extract.tbl*, which is a subset of extract raw.tbl containing the objects and fields which are selected by select conditions and select columns. Source extraction from the BCDs or CBCDs (multiframe mode) is recommended for IRAC data.

8.1.4.5   Outlier Rejection

By default, APEX will not perform outlier rejection. This can be gotten around by running the mosaicker with outlier rejection turned on and keeping the intermediate products (delete_intermediate files = 0).

Appendix A. Pipeline History Log

S19.2 (Warm Mission Only)

1. Recalibration of IRAC Flux Densities in Channels 1 and 2.
The absolute photometric calibration was updated using the same method that was used for the final cryogenic IRAC calibration. The uncertainty in the absolute photometric calibration is dominated by the uncertainty in the flux density of the fundamental calibrators, Vega and Sirius, and is ~ 2% in both channels.

2. Linearity Solution Improved in Channel 1.
The linearity solution was adjusted in channel 1 only. The change in flux from old to new linearity solution is <1%. Channel 2 was found to not be in need of any change.

3. Pmasks Updated
The quasi-static bad pixel masks were updated.

4. New Flatfields Derived
Newly derived flatfields are now in use with final precisions of 0.17% and 0.09% in channel 1 (3.6 microns) and channel 2 (4.5 microns), respectively.

5. Header Information Updated
Keywords for PCRS peak-up observations were added to FITS headers, including the RA, Dec, and Proper Motion of the star used for the peak-up.

6. Pointing Refinement Catalog Updated
Pointing refinement in the IRAC pipeline utilizes the 2MASS catalog. The positional information of stars in the 2MASS catalog has now been improved with UCAC4 catalog proper motions, as 22% of 2MASS sources have non-zero proper motions.

7. Readnoise Values Updated to Observed Warm Campaign Values
Previously cryogenic readnoise values were used in the (C)BCD pixel value uncertainty calculations. The readnoises have now been updated to measured warm mission readnoise values.

8. Distortion Correction Updated
The distortion correction has now been updated from a 3rd order polynomial solution to a 5th order polynomial solution, allowing an improvement of relative astrometric accuracy from 125 milliarcseconds to 30 milliarcseconds in both channels.

S19.1 (Warm Mission Only)

1. Imask Updates
Turning on the residual image ("latent") bit (10) in the imask has been updated from using only residual images created within the current AOR to include residual images left by preceding observations as well, employing algorithms that track the time decay of residual images.

2. Saturation Correction and Column Pulldown Updates
Updated saturation and column pulldown thresholds for artifact correction

S18.24

1. Recalibration of IRAC fluxes in channels 3 and 4.

In the process of performing a detailed cross comparison of the calibration of Spitzer instruments and comparing the IRAC calibration to the HST calibration database, an error was identified in the S18.18 IRAC processing. In updating the flux conversions (FLUXCONV), erroneous color corrections were used for the calibration stars. The color corrections used were incorrect for the 5.8 and 8.0 micron bands. The S18.18 flux values were multiplied by 1.000, 1.000, 0.968 and 0.973 for the 3.6, 4.5, 5.8 and 8.0 micron channels, respectively. The headers were also updated to indicate pipeline version S18.24 and revised flux conversion values.

S18.18 (Warm Mission Only)

1. Recalibration of IRAC Flux Densities in Channels 1 and 2.

The absolute photometric calibration has been updated using the first year of warm campaign calibration stars.

2. Added Header Keywords

BMJD_OBS (barycentric modified Julian Date) and AORHDR (AOR requested to be observed in HDR mode) were added to (C)BCD FITS header.

3. New Pmasks And Flatfields Created Using Only Warm Mission Data.

S18.18

1. Saturation Correction in Pipeline

Saturation is now corrected before artifacts. Artifact correction for saturated sources is now possible. The criteria for selecting sources for correction were changed. The source selection is now frame time dependent. Bit 13 in imask is changed to bit 4 after correction has been performed.

2. Imask Updates

Imask header is now formatted in a way similar to the BCD header and includes information about the various bits that may have been set.

3. ABADDATA Now Often Corrected

Frames with ABADDATA set in raw file headers are now corrected. This problem is due to shifting the data by one pixel after an extra word was read into the data. If only one such instance occurs in a frame it is now corrected. Frames with multiple instances are not corrected. The BCDs will include a header keyword BADPIX. If BADPIX = T, then another header keyword ZEROPIX gives the number of bad pixels. If ZEROPIX = 1, then header keyword ZPIXPOS gives the position of the pixel that was fixed and header keyword BADFILL gives the value (in DN) of the fixed pixel.

4. New Added Header Keywords

Barycentric Julian Date calculated with SCLK precision is now included in header keyword BMJD_OBS. Also, a new header keyword AORHDR has been added. This keyword is true if the entire AOR in which the frame was taken (not just the frame itself, such as the first frame in every AOR) was taken in the high-dynamic-range (HDR) mode.

S18.14

1. Saturation Correction Update
Only sources in the 2MASS Point Source Catalog are now corrected (extended sources, such as the nuclei of bright galaxies are not corrected). Bit 13 in imasks is now flipped to zero after the saturation has been corrected.

2. Mosaic of Imasks
Mosaics of all the imasks for a given frame time in a given AOR are now produced by the pipeline and placed in the PBCD directory (mmsk files).

3. Dmasks No Longer Archived
We no longer provide dmasks as they contain misleading and incomplete information. The imasks are more robust, include flagging of various artifacts that are not present in dmasks and make full use of the saturation correction made by the pipeline.

4. Higher Accuracy Pointing Refinement
Pointing refinement is now done with the help of the 100x sampled PRFs, leading to a more accurate pointing solution.

S18.5

1. A New Saturated Source Fitter
The pipeline now attempts to systematically find all saturated point sources in the images and fit them using an appropriate PSF that is matched to the unsaturated wings of the source. The new module replaces the saturated point source with an unsaturated point source that has the correct flux density of the point source. Please note that the new module does not successfully fit super-saturated point sources or point sources that are too close to the edge of the field of view for proper fitting. Only the CBCD files are saturation corrected (not the BCD files). The saturated pixels that have been replaced are identified within the bimsk (imask) files (bit 13).

2. A New Muxstripe Remover
Muxstriping (due to very bright objects in channel 1 or 2 fields of view, usually exhibiting itself as a depressed bias level in every fourth column in a section of an IRAC image) is now fit and corrected in a new pipeline module. The noise of the affected pixel area is compared to the unaffected pixels in the frame and a deviation is removed, without changing the background level or the flux in the pixels. Occasionally this correction fails and the muxstriping is unchanged. Only the CBCD files include this correction, not the BCD files.

3. Pmask Bits Now Included As Part of Imasks
See the imask bit definition in Section 7.1 of the IRAC Instrument Handbook for the definition of the various bits.

4. Mosaic Mask Files Now Available

The PBCD mosaics created in the pipeline now have associated mask files. The imasks associated with the CBCDs that were used for the creation of the mosaic have been combined to create the mask file, so the bit values can be deduced from the imask bit definition table.

5. Improved First-Frame Correction

More appropriate skydarks are now used in the pipeline, producing an improved first-frame effect correction.

S18.0

1. Muxbleed Correction Update

The correction of the muxbleed effect in the BCD frames was updated. After extensive testing a new functional form and scaling law was developed for muxbleed correction in channels 1 and 2. The new functional form and scaling law correct muxbleed better than before.

2. MOPEX Now Using the *bimsk.fits* Files

In creating the final mosaic image, **maic.fits*, the MOPEX pipeline now uses the **bimsk.fits* files as input, instead of the **dmsk.fits* files. The *bimsk.fits files have more relevant information useful for flagging when building mosaics and analyzing the images.

3. Header Information Updated

WCS CD matrix keywords were added to the Post-BCD file headers. The CDELT1, CDELT2, and CROTA2 keywords have been preserved but were placed in comments to avoid any confusion when handled by astronomical software. The following keywords were added to the BCD, CBCD, and Post-BCD image files: PXSCAL1, and PXSCAL2, and PA. The keywords are the pixel scale along axis 1 and axis 2 in arcsec/pixel and the position angle of axis 2 (East of North) in degrees. Keywords containing additional information on the AOR mapping parameters have been added in a separate section of the header.

S17.0

1. Artifact Mitigation Within the Pipeline

Artifact-mitigated images from the BCD pipeline and their associated uncertainty images (**cbcd.fits* and **cbunc.fits*) are now available in the archive. These images include corrections for column pulldown and banding, induced by bright sources in the images. The corrections are empirical fits to the BCDs and may not always improve the data quality. The standard BCD files (**bcd.fits*) remain available in the archive. The mosaics (post-BCD products) are now created from the **cbcd.fits* images.

2. Muxbleed Correction Updated Again

The muxbleed correction has been revised to include a better empirical fit.

3. Two-Dimensional Subarray Images

A two-dimensional image is now generated for each subarray BCD cube. Each pixel in the 2D image (**sub2d.fits*) is a robust (outlier-rejected) mean of the 64 samples of the **bcd.fits* cube. Two-dimensional masks, uncertainty images, and coverage maps are now also provided.

4. Artifacts Now Flagged For Subarray Images

The subarray imasks (*_bimsk.fits) now include masking for muxbleed, column pulldown and banding, induced by bright sources. The updated masks can be used to mitigate bright source artifacts the same way as with the full array data.

5. Darkdrift Values Written Out in the Subarray Header

The pipeline darkdrift module reduces a "jailbar" bias effect in the IRAC images. The values used for the reduction within the pipeline are included in the header of the full array data, and now in the header of the subarray data for all the planes. This allows the user to remove the correction, if desired.

6. Mosaic Header Updated

We have added more information to the mosaic header. These changes are explained in the IRAC Instrument Handbook, Section 6.

S16.0

1. Labdark Change for 100 Second HDR Data

Within 100s AORs, the channel 4 observations are split into two 50s frames. The second 50s frame received an incorrect non-HDR 50s labdark instead of an HDR labdark. This was a minor problem, and has now been corrected.

2. Muxbleed Correction Updated

The module that detects and corrects the muxbleed caused by bright sources has been updated. It now performs a more consistent and better correction than previously.

3. Artifacts Flagged Within the Pipeline

The imasks (*_bimsk.fits) now include masking for muxbleed, column pulldown and banding induced by bright sources on images. The updated masks can be used with existing contributed software to mitigate bright source artifacts, and will be used in future versions of the IRAC pipeline after mitigation algorithms have been implemented. In general, observers should not flag artifacts in mosaicking unless they have observations at various roll angles.

4. Pixel Linearization

The handling of bad and saturated pixels has been changed - they are in most cases now left with their original values, as opposed to being set equal to NaN. The method of flagging saturation in BCD mask files was changed, and now more accurately reflects the presence of saturation.

S15.0

1. Ghost Images And Scattered Light Flagged Within Pipeline

Pipeline versions of the ghost image and scattered light detection algorithms have been integrated into the IRAC pipeline. The modules use the location of bright sources upon the array (ghost image) or just outside the array, as found in 2MASS catalogs (scattered light) to predict possible optical ghosts and scattered light locations, and flag these pixels within the imask. The imask is an ancillary data product now available through the archive. IRAC observers should use the imask instead of the dmask when making mosaics etc.

2. Incorrect Group Ids in Header to Be Fixed

A bug that caused a small percentage of BCDs ($< 0.1\%$) to have an unreadable header and which were therefore not pipeline-processed, has been fixed. This should significantly decrease the number of missed BCDs in large mapping programs.

S14.0

1. Darkdrift Module Changes
As mentioned below, in S13 the darkdrift module was applied only to channel 3 data. This module is used to adjust the bias level in the four readouts in an array, thereby removing vertical striping in the data, the so-called "jailbar effect." After S13 reprocessing of IRAC data it was found that the jailbar effect can be triggered in channels 1, 2 and 4 as well. Therefore, the darkdrift module will again be applied to all four channels, and all the IRAC data will be reprocessed with pipeline version S14.

We have released a "jailbar corrector," which may be used to correct for the jailbar effect. It produces similar results to the darkdrift corrector module in the IRAC pipeline.

2. Added Keywords
Individual array readout noise (RONOISE).

S13.0

1. "Super-Boresight" Pointing Refinement (S13.2 And Thereafter)
Previous versions of the pipeline performed pointing refinement on each IRAC channel separately. The refinement was performed by matching detected point sources to 2MASS stars and registering the astrometry to minimize the positional offset between matches. In most cases, the refinement of channels 3 and 4 is less accurate as the number of stars detected in an individual frame is less than in channels 1 and 2. "Super-boresight" refinement corrects the astrometry for all four channels by simultaneously using appropriately weighted matches from all four channels and the known orientations of the FPAs. This method can dramatically improve the pointing accuracy for channels 3+4, and it removes any positional offsets between channels. The superboresight pointing is inserted into the CRVAL1 and CRVAL2 keywords in the header, while the basic (less accurate) pointing refinement remains in RARFND and DECRFND header keywords, and the original boresight pointing solution is placed in new header keywords ORIG_RA and ORIG_DEC.

2. First-Frame Effect
The interval between frames (INTRFDLY) is now maintained in a database, instead of the pipeline reading the previous image in an AOR to process the current image. This streamlines operations and handling of missing images. It is also placed in the header as a keyword.

3. Linearity Correction
New linearity corrections have been calculated from on-orbit tests and small changes will be made to channel 3 full array and all channel subarray data. The effect is roughly 2% at half-well, and 8% at 90% full-well in channel 3. The other channels are within specifications and the linearity corrections will not be changed for them.

4. Darkdrift Module Changes

Small drifts in the bias level of each of the four readouts in each array, particularly relative to the calibration labdarks, can produce a vertical striping called the "jailbar" effect. This is corrected in the pipeline software by applying a constant offset per readout channel (arranged in columns), derived from the median of those columns such that their arithmetic mean is zero. In other words, all readout channels are adjusted to a common additive bias level. In in-orbit tests, the mean offset and correction was found to be negligible, except in channel 3 data. Therefore, in S13 reprocessing, the darkdrift correction was only applied to channel 3 data. The derived correction values for each channel are located in the header in the keywords DRICORR1, DRICORR2, DRICORR3, and DRICORR4. The overall background term determined is DRIBKGND.

5. Distortion Files

The subarray distortion files were found to be derived from the incorrect place on the full array and have now been updated with correct ones. This should only make a small, but noticeable difference in pixel sizes when measuring relative separations in the subarray.

6. Super-Skyflat

A new "super-skyflat" has been derived from the first two years of flatfield data on IRAC and will be used as the flatfield for all reprocessing and further campaigns. Uncertainties in the pixel-to-pixel responsivity calibration are only 0.5%, 0.2%, 0.2%, and 0.05% for channels 1–4, respectively.

7. Flux Conversion

The flux conversion has been updated to reflect the derivation described in the IRAC calibration paper. The currently used numbers were from a nearly complete phase of this derivation, but different by 3% in ch 4.

8. Other Added Keywords

1. Median brightness of Calibration Skydark (SKYDKMED)
2. More Precise Start time of observation (SCLK_OBS).

S12.0

Since S11.0 there have been no significant changes to the IRAC pipeline affecting calibration. The majority of changes have to do with header keyword additions.

1. New observing mode: "Stellar Mode" has multiple full-array short time exposures within channel 1 and 2 and at the same time has a longer integration in channels 3 and 4. This allows for brighter objects to be observed in the longer wavelength channels to higher signal-to-noise without saturating in the shorter wavelength observations. Available frame times are 0.4/2 sec, 2x2/12 sec and 2x12 sec/30 sec. The first number(s) refer to channels 1 and 2, the last number to channels 3 and 4.
2. The median value of the frames used to create the skydark subtracted from the data will be placed in the header of the BCD: keyword SKYDKMED.
3. The name of the labdark subtracted from the data will be placed in the header: keyword LBDRKFLE.
4. The time of the observation (SCLK_OBS) will be computed using telemetry only to allow for a more exact timing. This keyword will be placed in the database and header. Further S13 changes will include calculating the first frame correction from this more exact timing.
5. Keywords PTGDIFFX, PTGDIFFY were inserted to refer to the pointing differences in actual pixels along the X & Y axis.

S11.0

1. The EQUINOX header keyword for BCDs has been fixed.
2. Other changes to the header include the addition of the First Frame Delay and Immediate Delay (FFDLAY & IMMDLAY) times, calculated from the first frame correction.
3. Previously, a DCE with a non-zero CHECKSUM from MIPL was not allowed to process through the pipeline. In S11, the CHECKSUM will now be reported within the header and the DCE processed.
4. The first frame correction has been fixed for the high-dynamic-range observations. The only remaining bug is for the intermediate frame times (12 sec) when used as part of an HDR frameset. This effect will not be noticeable except as a slight background DC-level offset from frame to frame in the 12 sec data as part of 100s or 200s HDR framesets.
5. After study of last year's worth of flat-fields and finding no noticeable change from campaign to campaign, a super skyflat has been composed of last year's worth of observations. A sub-array flat has been composed of this super skyflat, and both have been loaded into the pipeline.
6. Overlap correction is now applied in the post-BCD pipeline.
7. The mosaic image headers have been populated with more keywords.

S10.5

1. Updated the ffcorr module to use the correct delay time between frames for full array non-HDR frames. The HDR frames will be fixed in S11.

S10.0

1. New linearity model in channel 4 (full and sub). Change from quadratic to cubic (actually updated in S9.5.2).
2. Module ffcorr set to output only one plane for interpolated correction image rather than all planes.
3. FITS Keyword: Create and populate new FITS header keyword (DS_IDENT).
4. Update to readnoise in initial noise image.
5. If BCD pixel = NaN, uncertainty pixel = 0.
6. Keyword from dark ensemble placed in BCD header (SKYDRKZB; skydark zodiacal background estimate added into header of science BCD).

S9.5

1. Addition of two fields, hdrmode and numrepeats, to caldata tables. Requires a backfill script to transform and migrate current fallbacks and metadata to new tables. The HDRMODE field is in

current use. The NUMREPEATS field is to facilitate use of the external repeat number in future calibration activities.

2. In S9.5 the flux conversion will be delivered in an IPAC table, for example:

   \char Comment Calibration data file for dntoflux module.

   \char INSTRUME = 'IRAC'

   \int CHNLNUM = 4

   \char fluxconv = 'Conversion factor in MJy/sr per DN/s'

   \char fluxconvunc = 'Uncertainty in fluxconv'

   |fluxconv |fluxconvunc |

   |float |float |

   0.195 0.020

3. HDR skydarks are now delineated from non-HDR skydarks. Skydarks are now aware of channel 4 repeats and pipelines fetch skydarks for the correct repeat. This is possible due to new fields in the caldata tables.

4. Scattered light removal module ("slremove") added to science pipeline and calibration preprocessing.

5. Calibration ensemble pipelines now use "fpgen" to clean up the product header.

6. New pipeline to create subarray flats from full array flats.

7. Latent ensemble creates new request median and request average images.

8. New keywords to be added to the mosaic header: AOT_TYPE, AORLABEL, FOVID, FOVNAME, PRIMEARR, OBJECT, PAONUM, CAMPAIGN.

S9.1

Less than < 0.1% of the DCEs may not have pointing reconstruction applied to the data. BCDs with USEDBPHF=F indicate that the Boresight Pointing History File was not used, and the RA and DEC in the headers for these cases are based on pre-observation predictions which can be off by 5"–50". Do not use such data if pointing is important.

S9.0

1. Some AORs have been affected by long-term residual images from previous observations. For the most part, observers have sufficiently dithered their data, so that the impact is minimal, on processed and co-added data.

2. Note that the noise in the images and the sensitivity to point sources are not equal to our pre-launch predictions (e.g., as available from our website until December 19, 2003, or in the Observer's Manual versions before 4.0), although they are close. New sensitivity numbers are available in the revised Observer's Manual (version 4.0), which was available at our website starting ~December 19, 2003. For reference, the ratio of the new point source detection threshold to the pre-launch advertised value, for low background observations in 30 sec frames, is 0.69, 0.75, 1.60, and 1.31 in channels 1, 2, 3, and 4, respectively.

3. Persistent images in channel 1. When a bright source (K=13 mag or brighter) is stared at for a long time, for example, during a downlink, it will leave a persistent image in channel 1 that decays very slowly (persists for several hours or more). A persistent image mitigation strategy involving annealing the array after downlinks has been put in place for nominal operations. These anneals will erase the persistent images from the array, but do not protect against persistent images from bright object observations that can accumulate on the array before the next downlink. Science impact: left unmitigated, you will have extra, spurious sources in your image. These sources have a PSF that is wider than the actual true source PSF. Dithering helps to get rid of these spurious sources.

4. Persistent images in channel 4. These are different in nature from the channel 1 persistent images. A bright source leaves a persistent image that can last for more than a week and even through IRAC power cycles. These images keep building up on the array. However, the amplitude of the persistent images is rather low. Annealing has been found to erase also the channel 4 persistent images. Therefore, we will anneal both channels 1 and 4 simultaneously, every 12 hours (after each downlink), to erase persistent images. Again, dithering helps to get rid of these spurious images.

5. Diffuse stray light: All IRAC images contain a stray light pattern, resembling a "butterfly" in channels 1 and 2, and a "tic-tac-toe" board in channels 3 and 4. These artifacts are due to zodiacal light scattered onto the arrays, possibly reflected from a hole in the FPA covers above the channel 1 and 2 arrays, and from reflective surfaces outside the edges of channel 3 and 4 arrays. The stray light scales with zodiacal light, which is the light source for our flatfields, so the stray pattern contaminates the flats. As a result, the flatfields will aesthetically remove the stray light rather well from images but will induce systematic errors of approximately 5% in flux calibration for point sources that fall in the peak stray light location. Dithering will mitigate this effect, because it is unlikely that a dithered observation will keep a source within the stray light lobes. Diffuse stray light will be removed from both the flatfields and the science frames in a future version of the pipeline.

6. Stray light from point sources. Spot allows you to overlay stray light boxes on any image; if a bright star is placed in those boxes during an observation, a scattered light patch will appear on the array. We have found three more such boxes during testing, in channels 1 and 2. The new stray light boxes are included in Spot now and are also shown in the new Observer's Manual. Channels 3 and 4 have less stray light, and the stray light inducing regions are not the same as the ones we guessed (by analogy to channels 1 and 2) from the lab tests, so the channel 3 and 4 boxes were removed from Spot. In channels 3 and 4 the stray light arises when a star lands on a thin region just outside the array (the same region that causes the "tic-tac-toe" pattern from diffuse stray light in flat fields). A redundant observing strategy will help eliminate stray light problems. Observers covering fields with bright sources should inspect the individual images; this is required if the depth of coverage is less than 3, to identify spurious spots and rays that could be mistaken for real astronomical objects.

7. Dark spots on pick-up mirror. There is contamination on the mirror, which causes a dark spot about 10 pixels wide in channels 2 and 4. This is a 15% effect. Flatfields completely correct for this feature in the data.

8. Muxbleed. We have a correction algorithm, but the coefficients need fine-tuning. Furthermore, for bright sources, muxbleed does not scale linearly with source brightness, so even a

sophisticated algorithm cannot accurately remove it. Some experiments at fitting the muxbleed for bright sources indicate that the decay pattern is always the same, and only the amplitude appears to be variable.

9. Banding and column pulldown. A bright source on the array will cause its column to be pulled down by a small amount. An algorithm to cosmetically correct the images for column pulldown has been developed and is being tested. This appears to be an additive effect. An analogous effect for an extremely bright source is that the entire image appears to have a different DC level from the preceding and following images.

S8.9

1. Some AORs have been affected by long term residual images from previous observations. For the most part, observers have sufficiently dithered so that the impact is minimal, on processed and co-added data.

2. Note that the noise in the images and the sensitivity to point sources are not equal to our pre-launch predictions (e.g., as available from our website until December 19, or in the Observer's Manual versions before 4.0), although they are close. New sensitivity numbers are available in the revised Observer's Manual (version 4.0), which was available at our website starting ~December 19, 2003. For reference, the ratio of the new point source detection threshold to the pre-launch advertised value, for low background observations in 30 sec frames, is 0.69, 0.75, 1.60, and 1.31 in channels 1, 2, 3, and 4, respectively. The apparent modest decrease in sensitivity in channels 3 and 4 is under investigation.

3. Persistent images in channel 1. When a bright source (K=13 mag or brighter) is stared at for a long time, for example, during a downlink, it will leave a persistent image in channel 1 that decays very slowly (persists for several hours or more). A persistent image mitigation strategy involving annealing the array after downlinks has been put in place for nominal operations. These anneals will erase the persistent images from the array, but do not protect against persistent images from bright object observations that can accumulate on the array before the next downlink. Science impact: left unmitigated, you will have extra, spurious sources in your image. These sources have a PSF that is wider than the actual true source PSF. Dithering helps to get rid of these spurious sources.

4. Persistent images in channel 4. These are different in nature from the channel 1 persistent images. A bright source leaves a persistent image that can last for more than a week and even through IRAC power cycles. These images keep building up on the array. However, the amplitude of the persistent images is rather low. Annealing has been found to erase also the channel 4 persistent images. Therefore, we will anneal both channels 1 and 4 simultaneously, every 12 hours (after each downlink), to erase persistent images. Again, dithering helps to get rid of these spurious images.

5. Diffuse stray light: All IRAC images contain a stray light pattern, resembling a "butterfly" in channels 1 and 2, and a "tic-tac-toe" board in channels 3 and 4. These artifacts are due to zodiacal light scattered onto the arrays, possibly reflected from a hole in the FPA covers above the channel 1 and 2 arrays, and from reflective surfaces outside the edges of channel 3 and 4 arrays. The stray light scales with zodiacal light, which is the light source for our

flatfields, so the stray pattern contaminates the flats. As a result, the flatfields will aesthetically remove the stray light rather well from images but will induce systematic errors of approximately 5% in flux calibration for point sources that fall in the peak stray light location. Dithering will mitigate this effect, because it is unlikely that a dithered observation will keep a source within the stray light lobes. Diffuse stray light will be removed from both the flatfields and the science frames in a future version of the pipeline.

6. Stray light from point sources. Spot allows you to overlay stray light boxes on any image; if a bright star is placed in those boxes during an observation, a scattered light patch will appear on the array. We have found three more such boxes during testing, in channels 1 and 2. The new stray light boxes are included in Spot now and are also shown in the new Observer's Manual. Channels 3 and 4 have less stray light, and the stray light inducing regions are not the same as the ones we guessed (by analogy to channels 1 and 2) from the lab tests, so the channel 3 and 4 boxes were removed from Spot. In channels 3 and 4 the stray light arises when a star lands on a thin region just outside the array (the same region that causes the "tic-tac-toe" pattern from diffuse stray light in flat fields). A redundant observing strategy will help eliminate stray light problems. Observers covering fields with bright sources should inspect the individual images; this is required if the depth of coverage is less than 3, to identify spurious spots and rays that could be mistaken for real astronomical objects.

7. Dark spots on pick-up mirror. There is contamination on the mirror, which causes a dark spot about 10 pixels wide in channels 2 and 4. This is a 15% effect. Flatfields completely correct for this feature in the data.

8. Muxbleed. We have a correction algorithm, but the coefficients need fine-tuning. Furthermore, for bright sources, muxbleed does not scale linearly with source brightness, so even a sophisticated algorithm cannot accurately remove it. Some experiments at fitting the muxbleed for bright sources indicate that the decay pattern is always the same, and only the amplitude appears to be variable.

9. Banding and column pulldown. A bright source on the array will cause its column to be pulled down by a small amount. An algorithm to cosmetically correct the images for column pulldown has been developed and is being tested. This appears to be an additive effect. An analogous effect for an extremely bright source is that the entire image appears to have a different DC level from the preceding and following images. The physical origin of these effects and the probably related (and already known) banding effect is not yet understood. This work is in progress.

10. Mosaics produced by the online pipeline for HDR mode data incorrectly weight the short and long frame times. For long exposures (> 12s), data are effectively taken in HDR mode, and hence the pipeline produced mosaics will not be very useful.

11. Cosmic ray rejection is not functioning well.

Appendix B.   Performing Photometry on IRAC Images

This is a quick guide for performing point source photometry on IRAC images.

A. Point Source Photometry on a Mosaic

1. If you are only interested in photometry down to about 10% accuracy and have bright point sources, you can usually perform photometry on the pipeline mosaic. Set the aperture size to 10 native (~1.2 arcsec) or 20 mosaic (0.6 arcsec) pixels and the sky annulus to between 12 and 20 native (~1.2 arcsec) pixels (or between 20 and 33.3 0.6 arcsec mosaic pixels). The IRAC calibration is based on an aperture of this size, so for this aperture no aperture correction is necessary. For fainter stars, it is better to use a smaller aperture and then apply an aperture correction. Remember that the units of the images are in MJy/sr, so you need to convert your measured values into flux density units in micro-Jy, by accounting for the pixel size in steradians. Conversion into magnitudes is magnitudes = $-2.5*\log10(f/f(0))$, where f is your measured flux density and f(0) is the zero magnitude flux density. If using software such as "phot" or "qphot" in IRAF/DAOPHOT which requires a magnitude zeropoint, the "zmag" keyword in photpars should be set to 18.80 (ch1), 18.32 (ch2), 17.83 (ch3) and 17.20 (ch4) if using a mosaic pixel scale of 0.6 arcsec/pixel. Other zmag values will be needed for other pixel sizes. Note that if you require photometry to a higher accuracy than 10% – 20%, you should follow the steps listed below.
2. Examine your data (CBCDs) and identify artifacts that could affect your photometry and that need to be corrected.
3. First perform artifact mitigation on the pipeline-produced CBCDs. While the pipeline-reduced CBCD files are mostly artifact-free, some residual artifacts remain.For example, the pipeline and contributed software have difficulty recognizing very saturated pixels that produce artifacts. As a result, they will not usually correct artifacts from very saturated point sources or from extended saturated regions. Data at 5.8 and 8.0 microns exhibiting the bandwidth effect should be masked before performing photometry.
4. Make a mosaic of artifact-corrected images, for example with the MOPEX package. When creating the mosaic, the overlap correction option should be used in MOPEX, most importantly in channels 3 and 4, to match the backgrounds. Inspect the mosaic to confirm that outlier rejection is acceptable. If not, then remosaic with more appropriate MOPEX parameters. Comparing mosaics of adjacent channels on a per-pixel basis will readily identify if outliers remain in a mosaic. The mosaic coverage maps should be inspected to verify that the outlier rejection has not preferentially removed data from actual sources. If the coverage map systematically shows lower weights on actual sources, then the rejection is too aggressive and should be redone.
5. If you are interested in blue point sources (sources with spectral energy distributions, SEDs, that decline toward the longer wavelength IRAC passbands) you should create an array location-dependent photometric correction image mosaic. If you are interested in only red sources (with SEDs that rise toward the longer wavelength IRAC passbands), you do not need to apply the photometric correction images and make a mosaic out of them. We recommend making a correction mosaic, instead of multiplying the correction images with the CBCDs and then mosaicking these CBCDs together, since you may need to iterate this a few times and/or you may have both red and blue sources in the field, and thus the correction only applies to a subset of

sources. This location-dependent effect is as large as 10%. *It is the dominant source of uncertainty in the photometry of IRAC images.* For observations that well sample the array for each sky position the effect will average out. MOPEX software now is capable of creating these correction mosaics for you. If you want to make the BCD-matched photometric correction images yourself, first copy the FITS header keywords CTYPE1, CTYPE2, CRPIX1, CRPIX2, CRVAL1, CRVAL2, CD1_1, CD1_2, CD2_1, CD2_2 from the headers of the BCDs to the headers of the photometric correction images in each channel using your favorite FITS manipulation software. Thus, you make the same number of photometric correction images (otherwise identical except for the keyword information) as there are CBCDs in each channel. The correction images must be divided by the pixel solid angle correction images before mosaicking them together, because the pixel solid angle effect is essentially corrected for already in the photometric correction images and thus needs to be "canceled out" before running the images through MOPEX (which corrects for this effect). Then, copy the namelist you used to make the CBCD mosaic images into some other name, and edit the namelist to disable all the outlier rejection modules. Do not run the fiducial image frame module but instead point MOPEX to the existing *"FIF.tbl"* file used for generating the corresponding CBCD mosaic. Next, specify the RMASK_LIST file (generate a file listing the rmasks and their path, as created by the mosaicker run for the corresponding CBCDs). Finally, make the correction image mosaic with MOPEX.

6. Perform photometry with your favorite software. Aperture photometry is preferred over PRF-fitting photometry due to the undersampled nature of the data. To properly estimate the uncertainties in your photometry, the uncertainty images provided with the CBCDs can be used and mosaicked into an uncertainty mosaic. The CBCD uncertainties are slightly conservative as they take into account the uncertainties in each pipeline calibration step. For packages that estimate noise directly from the data assuming Poisson noise, you can convert the mosaic into electron units, so as to calculate the uncertainty due to source shot noise and background correctly. The conversion from MJy/sr is $*$ GAIN $*$ EXPTIME / FLUXCONV where GAIN, EXPTIME and FLUXCONV are the keywords from the CBCD header. In determining the noise, the coverage of the observation at the position of your target should also be taken into account (e.g., by entering the correct number of frames in DAOPHOT or by dividing the noise by the square root of coverage, from the coverage mosaic at the position of each target). Your aperture photometry software should of course subtract the appropriate background (usually in an annulus around the source).

7. Apply aperture correction, found in Chapter 4 of this handbook, if you perform aperture photometry in an aperture different from the 10 pixel radius aperture used for IRAC calibration or determine the background by other means than an annulus. Observers can determine their own aperture corrections by downloading IRAC calibration star observations from the Spitzer Heritage Archive, and comparing the photometry to that published in the IRAC Calibration Paper *(Reach et al. 2005, [24]).*

8. Observers should apply the array location-dependent photometric correction for blue sources and the appropriate color correction for all sources (based on the spectral energy distribution of the source). Determine the array location-dependent photometric correction (for blue compact sources) from the correction mosaic, constructed in step 5 above, by looking at the values of the pixels at the positions of the peaks of your point sources. Apply a color correction from Chapter 4 of this handbook using the tabulated values, if appropriate, or calculate the color correction for a

source spectral energy distribution as done in that chapter. To calculate a color correction, you will need the IRAC spectral response curves, available in the IRAC web pages. Color corrections are typically a few percent for stellar and blackbody sources, but can be more significant for sources with ISM-like source functions (50% – 250% depending on spectrum and passband). Measured flux density is the flux density at the effective wavelength of the array: 3.550, 4.493, 5.731 and 7.872 microns, for channels 1–4, respectively.

9. A pixel phase correction to the measured channel 1 flux densities should then be considered. More information on the pixel phase correction can be found in Chapter 4 of this Handbook. This effect is as large as 4% peak-to-peak at 3.6 microns and < 1% at 4.5 microns. To apply a correction for mosaicked data is difficult as the pixel phase correction depends on the placement of the source centroid on each CBCD. For well-sampled data the pixel phase should average out for the mosaic. For precise photometry in low coverage data, the source centroids on the CBCDs should be measured and the phase corrections averaged together and applied to the final source photometry.

B. Point Source Photometry on Individual BCDs

Although most of the time it is a good idea to use the mosaic for performing photometry, performing photometry on the (C)BCD stack is important for variability studies and can be useful for faint sources as one can measure N out of M statistics (how many times you found the source). When performing source profile fitting, performing photometry on the the (C)BCD stack is better as the phase information of the PRF is preserved.

1. Examine your data (CBCDs) and identify artifacts that could affect your photometry and that need to be corrected.

2. First perform artifact mitigation on the pipeline-produced CBCDs. While the pipeline-reduced CBCD files are mostly artifact-free, some residual artifacts remain. The pipeline and contributed software have difficultly recognizing very saturated pixels that produce artifacts. As a result they will not usually correct artifacts from very saturated point sources and extended saturated regions. Data at 5.8 and 8.0 microns exhibiting the bandwidth effect should be masked. If performing aperture photometry on the CBCDs, a particular CBCD should not be used for a source when there are masked (bad) data in the source aperture.

3. Make a mosaic of artifact-corrected images, for example with the MOPEX package. This needs to be done to create the proper rmask files to be applied to the CBCDs when performing the photometry on them, and also to get a nice comparison of CBCD-revealed and mosaic-revealed image features. When creating the mosaic, the overlap correction option should be used in MOPEX, most importantly in channels 3 and 4, to match the backgrounds. Inspect the mosaic to confirm that outlier rejection is acceptable, if not, then remosaic with more appropriate parameters. Comparing mosaics of adjacent channels on a per-pixel basis will readily identify if outliers remain in a mosaic. The mosaic coverage maps should be inspected to verify that the outlier rejection has not preferentially removed data from actual sources. If the coverage map systematically shows lower weights on actual sources, then the rejection is too aggressive and should be redone. One result of making the mosaic is the production of rmask files which identify

bad pixels in the CBCDs. One should apply the rmasks when performing the photometry in the next step so that bad pixels are not included within the apertures.

4. Perform photometry with your favorite software. The PRFs supplied can be used with APEX in multiframe mode for point source fitting. A "How To" guide and details of the validation are presented in Appendix C. The CBCD uncertainties are slightly conservative as they take into account the uncertainties in each pipeline calibration step. For packages that estimate noise directly from the data assuming Poisson noise, you can convert the CBCDs into electron units, so as to calculate the uncertainty due to source shot noise and background correctly. The conversion from MJy/sr is $*$ GAIN $*$ EXPTIME / FLUXCONV where GAIN, EXPTIME and FLUXCONV are the keywords from the CBCD header. For accurate photometry, a good background estimate is required. When performing point source fitting with APEX, the parameters of the medfilter module should be tuned to ensure good background subtraction. For aperture photometry, the background estimate can be obtained from an annulus around the source (but note that the radii of the background annulus will affect the aperture correction).

5. Apply aperture correction, found in Chapter 4 of this Handbook, if you perform aperture photometry in an aperture different from the 10 pixel radius aperture used for IRAC calibration. Observers can determine their own aperture corrections by downloading IRAC calibration star observations from the Spitzer Heritage Archive and comparing the photometry to that published in the IRAC Calibration Paper. Aperture corrections for fitted fluxes are given in Appendix C.

6. Observers should apply the array location-dependent photometric correction for blue sources and the appropriate color correction for all sources (based on the spectral energy distribution of the source). The photometric array location-dependent correction images are linked from the IRAC web pages. Apply a color correction from Chapter 4 of this Handbook, using the tabulated values, if appropriate, or calculate the color correction for a source spectral energy distribution as done in that chapter. To calculate a color correction, you will need the IRAC spectral response curves, which are also available on the IRAC web pages. Color corrections are typically a few percent for stellar and blackbody sources, but can be more significant for sources with ISM-like source functions (50%-250% depending on spectrum and passband). The measured flux density is the flux density at the effective wavelength of the array: 3.550, 4.493, 5.731 and 7.872 microns, for channels 1-4, respectively.

7. Pixel phase corrections need to be applied in channels 1 and 2. The PRFs include the pixel phase effect, so the single mean correction given in Appendix C is adequate. In the case of aperture fluxes, all the fluxes need correction. More information on the pixel phase correction can be found in Chapter 4 of this Handbook. This effect is as large as 4% peak-to-peak at 3.6 microns and $< 1\%$ at 4.5 microns.

8. Combine photometry from CBCDs, taking into account uncertainties, to generate a robust, weighted mean value. Verify that the dispersion in these measurements is comparable to the uncertainty of the individual measurements (if not, use the dispersion until you track down the source of extra error, e.g., bad pixels/cosmic rays in source).

Appendix C.   Point Source Fitting IRAC Images with a PRF

This Appendix discusses the use of point source response functions (PRFs) for fitting sources in IRAC data. For true point sources, it is possible to obtain agreement between PRF-fitted and aperture flux measurements at better than the 1% level. In this Appendix, we describe validation tests on point sources in IRAC data using the PRFs in combination with the MOPEX/APEX software. The procedure for using the PRFs in conjunction with MOPEX/APEX is given in the form of a "How To" description, and the necessary corrections to the resulting flux densities are detailed.

Point source fitting is a valuable tool for characterizing images. If the image consists of true point sources, PRF fitting can make optimal use of the information in the image, thus improving astrometric and photometric results beyond what is achievable using other techniques. PRF fitting also allows point sources to be subtracted from an image (for example, using the *apex_qa* task in MOPEX/APEX), enabling any diffuse background emission to be more easily characterized. Point source fitting is less useful in fields containing large numbers of partially-resolved objects (as typically seen in IRAC extragalactic survey fields), and aperture photometry is recommended in such fields. (In principle, model fitting could be used for extended sources by convolving a source model with the appropriate point source realizations, but such techniques lie outside the scope of this Appendix.) For isolated point sources on featureless backgrounds aperture photometry and point source fitting should give almost identical results. Point source fitting to IRAC data has proven problematic as the PSF is undersampled, and, in channels 1 and 2, there is a significant variation in sensitivity within pixels. Techniques for dealing with these problems were developed for the WFPC2 and NICMOS instruments on HST *(Lauer 1999 [19]; Anderson & King 2000, [2]*, see also *Mighell 2005, [20])*. These techniques involve building a "point response function" (PRF; Anderson & King use the alternative terminology "effective PSF"), and users interested in the detailed theory of the PRF should refer to these papers. In summary, the PRF is a table (not an image, though for convenience it is stored as a 2D FITS image file) which combines the information on the PSF, the detector sampling and the intrapixel sensitivity variation. By sampling this table at regular intervals corresponding to single detector pixel increments, an estimate of the detector point source response can be obtained for a source at any given pixel phase.

PRFs for IRAC have been created by William Hoffmann of the University of Arizona, a member of the IRAC instrument team. The starting point for these PRFs was the Code V optical models for Spitzer/IRAC, made at the Goddard Space Flight Center. These were constructed on a 5x5 grid covering each of the IRAC arrays. Observations of a calibration star made during the in-orbit checkout at each of these 25 positions per array were then deconvolved by their respective optical models. The results were averaged into a single convolution kernel per array which represents additional PRF scatter from unmodeled optical effects and spacecraft jitter. A paper on "simfit" that gives more details is included in the IRAC section of the documentation website. The intrapixel sensitivity function was estimated using a polynomial fit as a function of pixel phase. The PRFs were then transposed, and flipped in x and y to align them with the BCD coordinate system.

C.1 Use of the Five Times Oversampled PRFs Outside of APEX

As supplied in the documentation website, the PRFs are oversampled by a factor of five in *Delta_x* and *Delta_y*. This allows for 5x5=25 independent realizations of a point source, corresponding to 25 different pixel phase combinations (five each in *x* and *y*). To obtain any given point source realization (PSR), the PRF needs to be sampled every fifth pixel in *x* and *y* at the appropriate phase, i.e.,

PSR1(i,j) = PRF(5i-4,5j-4)
PSR2(i,j) = PRF(5i-4,5j-3)
PSR3(i,j) = PRF(5i-4,5j-2)
PSR4(i,j) = PRF(5i-4,5j-1)
PSR5(i,j) = PRF(5i,5j)
PSR6(i,j) = PRF(5i-3,5j-4)
……………………….……
PSR13(i,j) = PRF(5i-2,5j-2)
PSR25(i,j) = PRF(5i,5j)

where *i,j* are integers running from 1 to *n* in the case of a PRF table which is *5n* x *5n* in size. In this case, *PSR13* corresponds to the source landing in the center of a pixel. Note that the PRF should not be block averaged, as this will result in the loss of the pixel phase information.

These PRFs may be implemented directly by those willing to write their own code. In IDL, for example, a point source realization may be generated using the /SAMPLE switch in REBIN, e.g,

psr = rebin(phasedPRF,n,n,/SAMPLE)

where *phasedPRF* is the *5n* x *5n* PRF shifted to the appropriate pixel phase in both dimensions. In IRAF, use:

imcopy *PRF.fits*[1:5n-4:5,1:5n-4:5] *PSR1.fits*

Note that the PSRs are normalized to unity at infinity, not to the IRAC 10 pixel calibration aperture. Fluxes obtained with these thus need to be multiplied by the appropriate infinite aperture correction. These have been determined to be 0.943 in channel 1 and 0.929 in channel 2, based on measurements of the PRF, and can be compared to "direct" measurements of 0.944 and 0.937. Estimates from the PRF are unavailable in channels 3 and 4, but the corrections given in this Handbook are 0.772 and 0.737, respectively (Table 4.7).

C.2 Modifications to the IRAC PRFs for Use with APEX

The IRAC PRFs are centered relative to the optical axis, so they are slightly off center in array coordinates due to array distortion. APEX assumes that the PRF is centered on its array, so to use the PRFs with APEX requires them to be re-centered. APEX also requires odd-valued axes.

APEX performs PRF fitting by varying the position and flux of a source using a modified simplex technique (see the APEX manual). However, for IRAC data, particularly in channels 1 and 2, where the PRF is undersampled, the default 5x sampling of the PRF is insufficient to obtain a sufficiently accurate position for fitting.

Therefore the following transformations were applied to the PRFs:

i) The PRFs were magnified (using linear interpolation) by a factor of 20 (so the resultant PRF sampling is x100).
ii) The last row and column were removed to give odd-valued axes.
iii) The PRF was recentered on a first-moment centroid measured using the array values within a 250 (resampled) pixel border.
iv) The PRF was zeroed out in a 50 (resampled) pixel border (to avoid wrapping problems).
v) Information describing the PRFs and their modifications was added to the headers.

C.3   Results of Tests with PRF fitting

C.3.1   Test on Calibration Stars

One sample observation (AOR) was selected for each of the nine brightest IRAC calibration stars (*Reach et al. 2005, [24]*). The selected AORs were from 2005 June 05 to 2006 September. Photometry was performed on the five BCDs in each AOR and the results averaged. (C)BCD uncertainties and imasks were used. The pipeline versions were S14.0–S14.4. The central PRF, modified for APEX use as described above, was used as the stars were close to the center of the array in each of the images.

APEX_1frame was used with current default parameters in the namelists provided in the cdf/ sub-directory of the MOPEX distribution, e.g., *apex_1frame_I1.nl* etc, with one change. A Normalization Radius for the PRF is needed to correspond to the IRAC calibration radius of 10 pixels. This was placed in the parameter block for *sourcestimate*: Normalization_Radius = 1000 (since it is in units of PRF pixels, and the sampling is 100x).

We performed aperture photometry using a 10 pixel (calibration) radius for IRAC channels 1 and 2, and a 3 pixel radius for IRAC channels 3 and 4, and a 12–20 pixel background annulus for all. Aperture corrections from this Handbook were applied to IRAC channels 3 and 4. The use of smaller apertures at longer wavelengths is not critical but reduces the effect of background noise. No aperture corrections were needed for IRAC channels 1 and 2 for this aperture/annulus combination as it is used to define the flux calibration. The IRAC channel 1 aperture photometry was divided by the empirical pixel-phase flux correction from Chapter 4 in this Handbook:

$$Corr = 1 + 0.0535 \times [\frac{1}{\sqrt{2\pi}} - p] \qquad\qquad (C.1)$$

where p is the radial pixel phase, defined as the distance of the centroid of the stellar image from the center of its peak pixel. This corrects to an average pixel phase of $p = \dfrac{1}{\sqrt{2\pi}} \approx 0.4$ pix.

The average PRF-fitted fluxes compared to aperture photometry are shown in Figure C.1. The weighted average differences between PRF fluxes and (corrected) aperture fluxes are shown as long blue dashes. There are offsets in all four channels between the aperture and fitted fluxes. In IRAC channels 3 and 4, the offset is due to the fact that in these channels, the PSFs are wide and there is significant flux in the 12–20 pixel background annulus subtracted out in the IRAC calibration. APEX does not know about this in its PRF normalization, so the PRF fluxes are too high. We examined the "core" PRFs and estimated this factor. The estimated effect of the annulus on the PRF fluxes is shown in Fig. C.1 as black, short dashes. These are within 1% of the IRAC channel 3 and 4 estimates from the calibration stars. For IRAC channels 1 and 2, these annulus terms appear to be small, so we assume zero correction for the present time. The annulus correction factors (divide PRF fluxes by these) are 1.022 for IRAC channel 3, and 1.014 for IRAC channel 4 (Table C.1).

C.3.2   Subpixel Response in Channels 1 and 2

The offset for IRAC channel 1 in Figure C.1 is due to a completely different effect, namely the pixel phase effect described above. Aperture sums on the channel 1 IRAC PRFs match reasonably well the pixel phase relation in Eqn. C.1 if we sum a 10 pixel radius aperture.

APEX performs normalization on the "center-of-pixel" (pixel phase [0,0]) PRF, and applies this normalization factor to all sub-pixel positions. This results in an offset of the photometry relative to the mean pixel phase of $p = \dfrac{1}{\sqrt{2\pi}}$. We need to "back out" APEX's center normalization. Setting $p=0$ in Eqn. C.1 gives us the required factor: divide the PRF fluxes by 1.021. Similarly, using the pixel phase slope of 0.0301 in IRAC channel 2 leads to a correction factor of 1.012.

With these corrections, the PRF fitting on single CBCDs matches aperture results with any systematics less than a percent in all IRAC channels (Fig. C.2). The remaining scatter is most likely due to residual pixel phase effect not removed by the one-dimensional correction applied to the aperture photometry. The true pixel phase effect has two dimensional structure which is included in the PRF (see also *Mighell et al. 2008, [21]*).

Table C.1. Correction factors for PRF flux densities

Band	PRF aperture corrections			Correction to mean	Total
	From Core PRFs	From Cal Stars	Adopted	pixel phase	correction
IRAC1	1.004		1.000	1.021	1.021
IRAC2	1.004		1.000	1.012	1.012
IRAC3	1.021	1.023±0.002	1.022	1.000	1.022
IRAC4	1.014	1.014±0.002	1.014	1.000	1.014

Divide PRF fluxes by the last column.
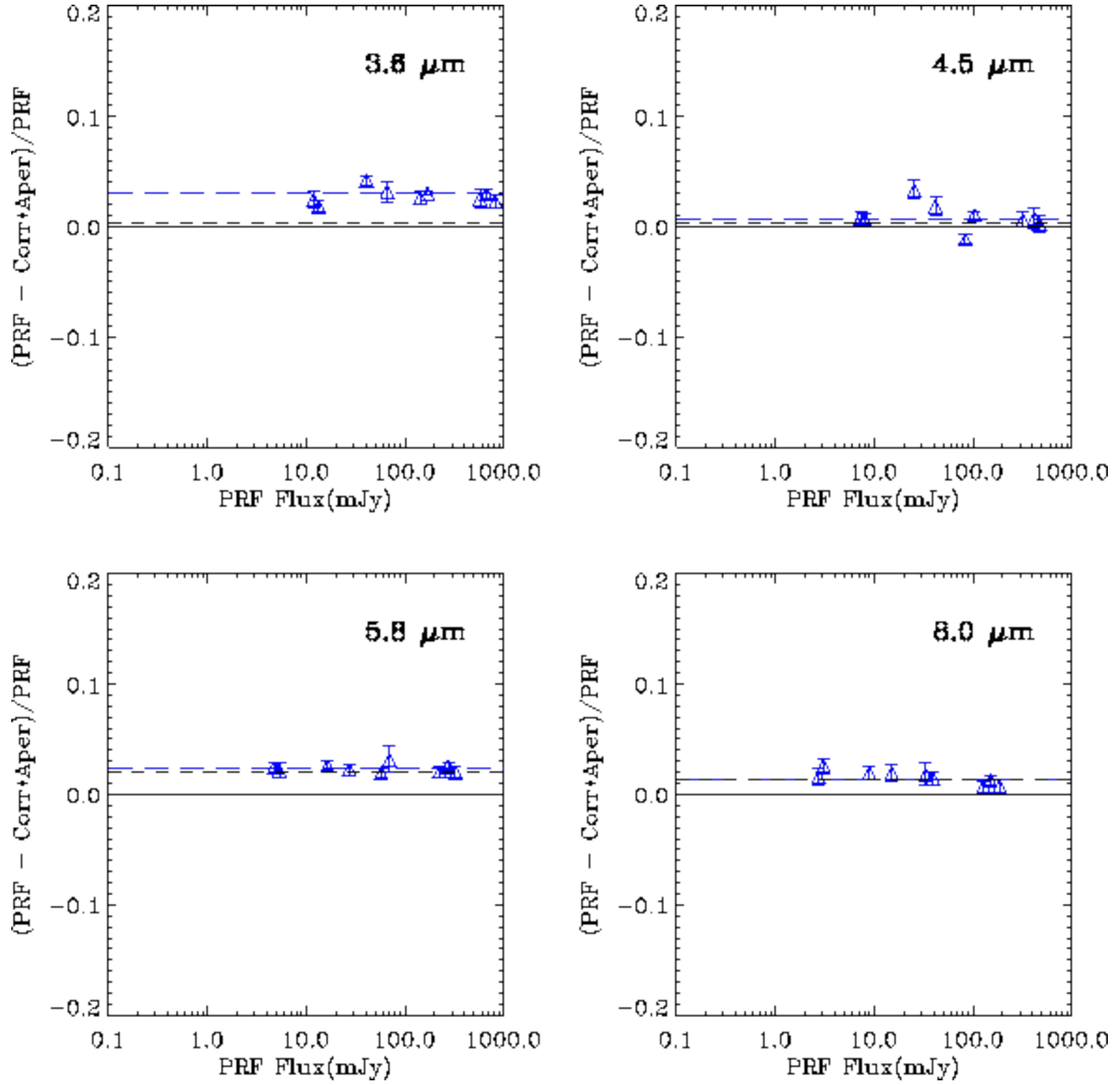
Figure C.1: PRF fits *vs.* aperture photometry for selected IRAC calibration star CBCDs. The vertical axis is the fractional difference between the PRF fit and corrected aperture photometry. The aperture photometry for IRAC channels 3 and 4 is in a 3 pixel radius with a 12–20 pixel background annulus and an aperture correction factor from this Handbook. For IRAC channels 1 and 2, it is in a 10 pixel radius with the same annulus. Short black dashed lines are the expected annulus correction needed. Long blue dashed line is the offset estimated from a weighted average of the data. Note this is essentially the expected value for IRAC channels 3 and 4. But IRAC channel 1 (and IRAC channel 2 to a lesser extent) requires a pixel-phase correction (see text).
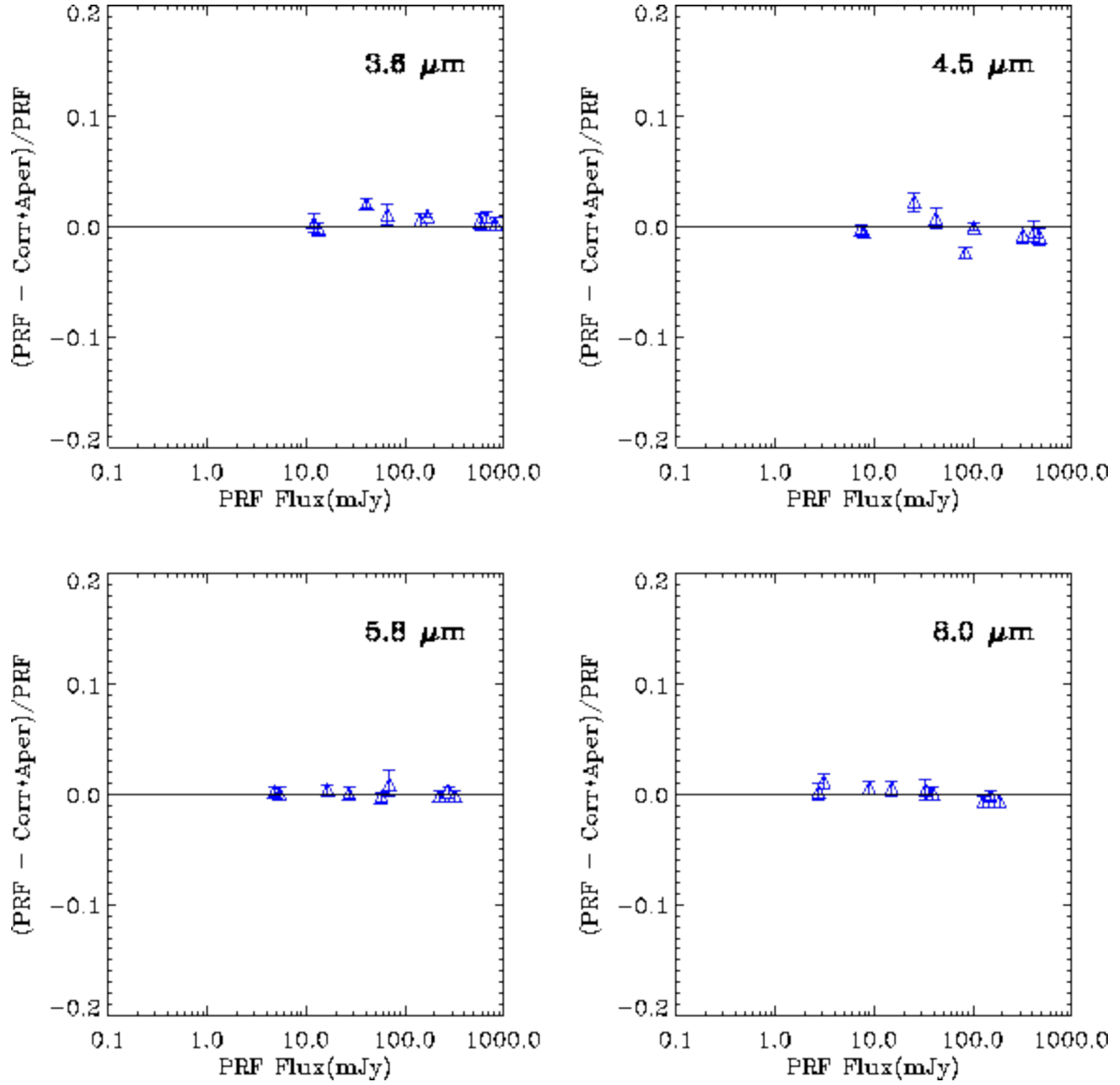
Figure C.2: Data from Fig. C.1, with IRAC channels 3 and 4 corrected for the annulus contribution, and IRAC channels 1 and 2 corrected for the pixel-phase effect.

C.3.3 The Serpens Test Field

Data for this test is a "C2D" off-cloud field (OC3) near Serpens, AORKEY 5714944 (S14.0). The observation is HDR mode data (0.6 and 12 sec) from all four IRAC channels. The observation used two repeats of two dithers, so the typical coverage is 4. The observation consisted of a 3x4 map. The field was chosen to be a crowded, predominantly stellar, field. The BCD data were run through artifact mitigation to correct muxbleed, column pulldown/pullup, electronic banding and the first frame effect. No pixel replacement was done. Long and short HDR data were handled separately. The tests here are with the long frames.

APEX multiframe was used with the Hoffmann PRFs, using a complete set of 25 array-location-dependent PRFs. Note that APEX does aperture photometry on the mosaic, but PRF fits on the stack (individual images). Final extracted sources shown are those with SNR > ~ 8.

Figure C.3 shows the comparison of PRF-fitted fluxes to aperture-corrected aperture photometry in a 3 pixel radius aperture. For IRAC channels 1 and 2, this is without pixel-phase corrections; for IRAC channels 3 and 4 it is *with* correction for the PRF aperture (Table C.1), but *without* correction for mosaic smear. Mosaicking involves an interpolation process which smears out point sources. Aperture corrections for aperture photometry off the mosaics need therefore to be made either based on point sources in the mosaic itself, or using values for CBCDs with a correction for mosaic smear. The amount of smearing depends on the pixel sampling in the final mosaic.
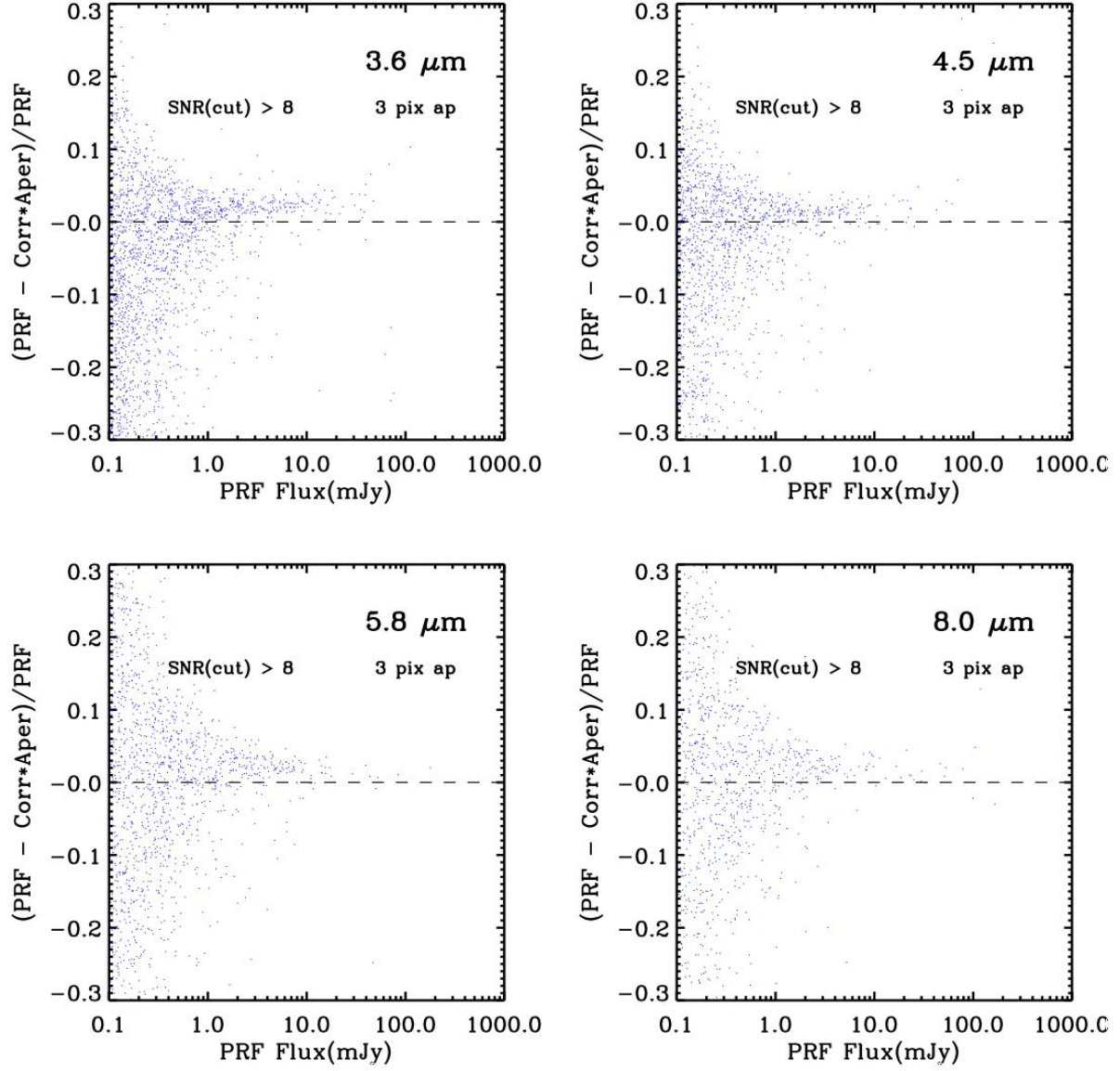
Figure C.3: APEX PRF-fitted photometry in the Serpens test field, with array-location-dependent PRFs vs. aperture photometry. The aperture has a 3 pixel radius, the background annulus is 12–20 pixels. The aperture fluxes have been corrected using the aperture corrections in this Handbook. The IRAC channel 3 and 4 PRF fluxes have been corrected for annulus contribution.

Figure C.4 shows the data with the remaining corrections discussed above applied. PRF fluxes for IRAC channels 1 and 2 were corrected for the pixel phase effect (Table C.1). Mosaic smear corrections for the aperture fluxes were determined empirically by comparing BCD and mosaic aperture fluxes. In IRAC channels 1 and 2 they were negligible, but IRAC channel 3 and 4 fluxes were corrected by 2.8% and 1.5%, respectively.

The results (Fig. C.4) show generally good agreement with aperture photometry, with any systematic offset < 1%.
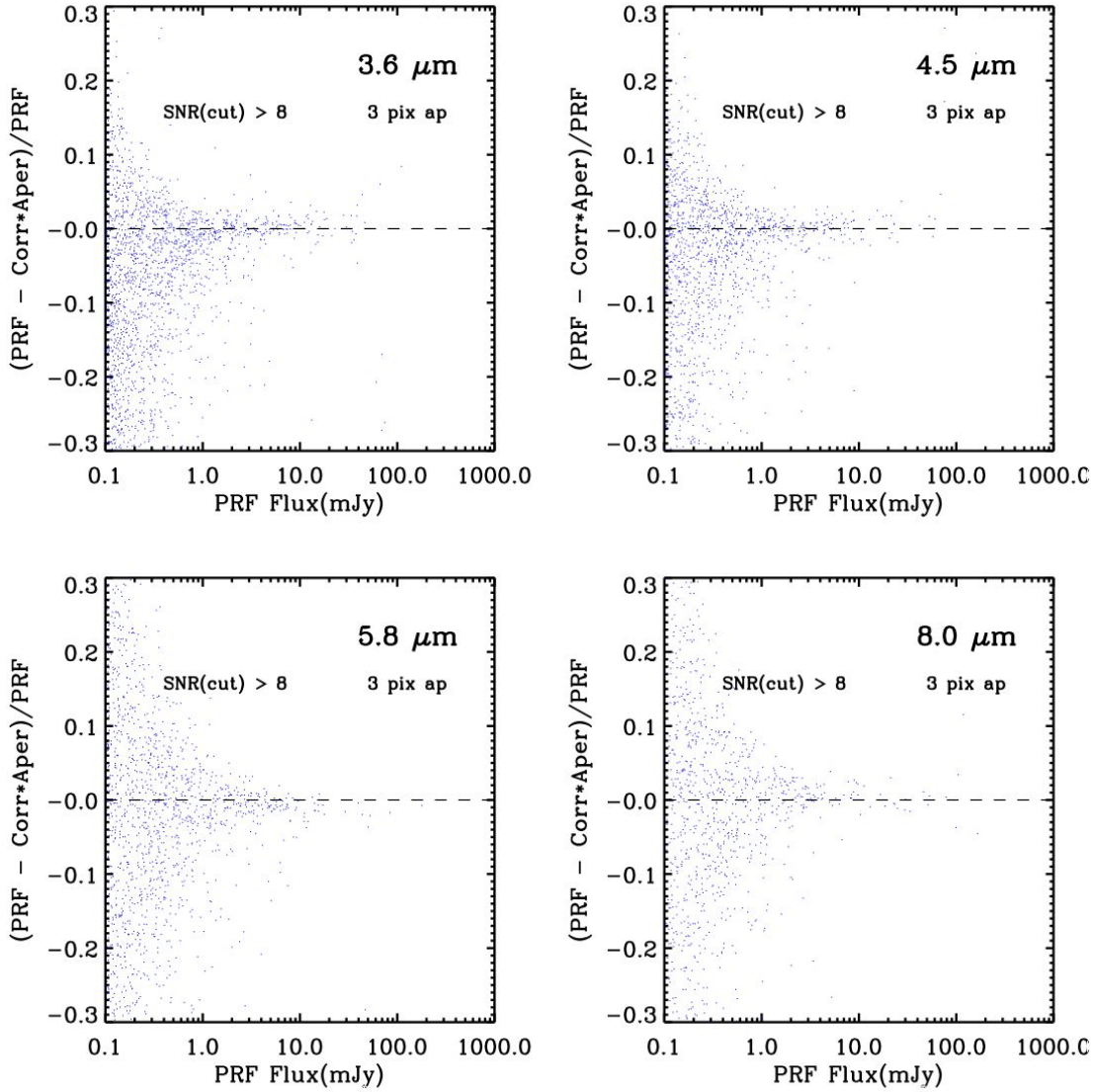
Figure C.4: APEX PRF-fitted photometry with a PRF Map vs. aperture photometry in the Serpens test field. PRF and aperture fluxes have been corrected as described in the text.

C.3.4   The GLIMPSE Test Field

We also analyzed the GLIMPSE AORKEY 9225728 in a similar manner. This produced similarly good agreement between the aperture and fitted fluxes. In addition, we stacked the residuals of the brighter sources in an attempt to determine the size of any systematics, and plotted out the ratio of the residuals to the uncertainties for the inner four pixels closest to the source position. No significant residual could be found in a stack of 111 sources with channel 1 fluxes between 50 and 100 mJy, corresponding to a limit of ~0.1% on the size of any systematic residual. Similarly, no significant difference could be found for the

distribution of the ratio of residual to uncertainty between the pixels near to the peak star position and pixels in the remainder of the image.

C.3.5 *Photometry of Moderately-Resolved Sources*

Point source fitting is most appropriate for true point sources. The flux of astronomical objects that are extended will be underestimated by such a procedure. Nearly all fields observed by IRAC have a substantial population of faint (10s of micro-Jy) background sources, which are in fact galaxies, and in a typical 100-second exposure these can approach 100 galaxies per IRAC frame at 3.6 microns. Although a casual visual inspection of the IRAC data would seem to indicate that the majority of these sources are compact and point-like, in fact treating them as such will lead to substantial errors in photometry, as these objects are typically resolved on a scale of ~1 arcsecond (e.g., *Lacy et al. 2005, [18]*).

This issue has been studied in substantial detail in the IRAC Dark Field, which is the dark current calibration field for IRAC. This is an extremely deep IRAC pointing of approximately 200 square arcminutes near the north ecliptic pole, and which reaches the confusion limit in all IRAC bands. More importantly, there is also deep high spatial resolution HST optical imaging over the same field, which can provide prior information on true source sizes and shapes.

Point source fitting was used to extract photometry for the IRAC Dark Field. An examination of the point-source subtracted residual images shows clearly that the residuals mimic the HST source morphology, conclusively demonstrating that IRAC does in fact resolve the majority of the faint galaxies. This result is strongest at the shorter IRAC wavelengths, where the spatial resolution is higher and the galaxies may be slightly more extended. This result was hardly unexpected - calculations of expected galaxy angular sizes assuming a modern cosmology indicated that most galaxies would be marginally resolved by IRAC almost regardless of distance, modulo changes in galaxy morphology with redshift and the ability to detect faint extended emission.

Curves of growth were generated for the galaxies, and when used in conjunction with the optical priors, the amount of error associated with point source fitting was quantified. Sources below a few micro-Jy start to be affected by confusion issues, so we describe here results for galaxies brighter that this. At 3.6 microns, roughly 50% of all galaxies are demonstrably resolved by IRAC. In 20% of the objects, the use of point source fitting will underestimate the true flux by a factor of two or more.

A much more effective solution is to use aperture photometry for such sources. The SWIRE survey performed detailed analyses to determine an "ideal" extraction aperture such that it minimized noise. This aperture was 1.9 arcseconds in radius, or roughly twice the FWHM. Most other survey groups have found similar results, and this mirrors well-known ideas about aperture photometry of small sources. When such an aperture is used, even though some objects may be larger than this the number where the flux differs by a factor of 2 falls to only 3%. This improvement over the PSF-fitting reflects the fact that the summation over an aperture larger than the PSF FWHM will always capture a better representation of the true flux of an extended object, even if that is more extended than the aperture itself. A more ideal solution is to use Kron-like apertures (which are dynamically sized based on moments derived from the image) which are either derived from the data themselves or from image priors in some other band.

We may thus conclude that for the extragalactic background, which is present in nearly all IRAC data, at least half the objects are resolved by IRAC in a meaningful fashion. Ideally, measurements should dynamically use shape information determined from the data themselves, or from priors derived from other, higher resolution datasets. Barring the use of shape parameters, use of aperture photometry in circular apertures somewhat larger than the PSF provides a more accurate result than PRF fitting.

C.3.6   Positional Accuracy

Tests were performed on GLIMPSE AORKEY 9225728, which contained approximately 10000 point sources in channels 1 and 2. Comparisons were made with respect to SExtractor Gaussian-windowed centroids XWIN_WORLD, YWIN_WORLD using both the pipeline mosaics, and mosaics made with the original pointing. Using the 100x oversampled PRFs recentered as previously described we found that the source positions agreed with SExtractor to within ~0.1". Systematic shifts with respect to 2MASS are ~0.2" in the pipeline (superboresight) pointing, and ~0.4" in the original pointing. Recentering the PRF has no effect on photometry. The shifted and unshifted PRFs gave nearly identical photometric results in channels 1–4.

C.3.7   A How-To-Guide for IRAC Point Source Photometry with APEX

It is recommended that APEX in point source fitting mode should be used only directly on the BCD data using the Hoffmann PRFs modified for use with APEX as described above. Trying to fit point sources on the mosaic is not recommended as the mosaicking process both blurs the undersampled point sources, and loses the pixel phase information. We also do not recommend using the *prf_estimate* tool to derive a PRF from IRAC data, as it does not deal correctly with the undersampling of the PRF.
We list below the steps towards producing a point source list using APEX in multiframe mode (i.e., on the stack of individual [C]BCDs).

1. Source fitting versus aperture fluxes: ask yourself if point source photometry is appropriate for your sources of interest. If in doubt after reading about photometry of moderately resolved sources above, use aperture photometry with APEX or Sextractor.
2. Artifact correction: use CBCDs or preprocess your IRAC BCD data to remove or mask artifacts as necessary.
3. Rmasks: assuming the data were taken with overlapping (C)BCDs, make a mosaic with MOPEX, doing outlier rejection, and creating Rmasks. Then include the appropriate Rmasks with your input data to APEX.
4. PRF: put the center Hoffmann 100x PRF (the one with ...col129_row129...) in your MOPEX cal/ subdirectory for command-line (this will be PRF_FILE_NAME in the namelist file), or type it into the GUI. Although you can run APEX with just the center PRF, we recommend using the whole PRF Map set, as it noticeably improves the quality of the fits for sources outside of the central region of the arrays. To do this, create a table like the one linked from the PSF/PRF section of the IRAC web pages (substituting appropriate filenames and paths). PRF position

refers to the bottom-left corner of the region of size NAXIS1, NAXIS2 over which the PRF is valid (in native pixels). This will be PRFMAP_FILE_NAME in a namelist, or you can type it into the GUI. Figure C.5 shows how the PRFs are distributed over the arrays.

5. Normalization Radius: the Hoffmann PRFs require a normalization that matches the IRAC calibration radius. In the *Sourcestimate* block, set *Normalization_Radius = 1000* (since it is in PRF pixels and the sampling is 100x).

6. Run APEX. If doing command-line for IRAC1, edit the default namelist for your data and run: *apex.pl -n apex_I1_yourdata.nl*

7. PRF Flux: The PRF flux column is called "flux" in the *extract.tbl* output file, and the units are micro-Jy. These need to be divided by the appropriate photometric correction factors from Table C.1: 1.021 (IRAC 1), 1.012 (IRAC2), 1.022 (IRAC3) and 1.014 (IRAC4).

8. PRF Flux Uncertainty: The column labelled "delta_flux" is the formal uncertainty from the least-squares fit. It will in general underestimate the flux uncertainty. Do not use the column labelled "SNR"' for IRAC, as it only takes into account the background noise, and ignores the Poisson (shot) noise term which typically dominates the error. The best estimate is the aperture uncertainty (calculated from the data uncertainties) in a 3 pixel radius. This covers the majority of the PSF without going too far out. (For the default namelist, the relevant uncertainty is in column "ap_unc2" [microJy].)

9. Array Location-Dependent Photometric Corrections: Multiply the (C)BCDs by the correction image ("...photcorr...") and run APEX on the resulting images. The fluxes will be correct for "blue" sources (where blue means having the colors of an early-type stellar photosphere). For "red" sources (objects with colors close to that of the zodiacal light) use fluxes derived from running APEX on unmodified CBCDs.

10. Color Correction: This is the correction needed to get the right monochromatic flux if your source spectrum is different from the reference spectrum used to calibrate the IRAC filters

($\nu F_\nu =$ constant). There is a good discussion of this in Chapter 4 of this Handbook.

If all these steps are followed, then the systematic error in the flux measurement for bright, isolated point sources should be ~1%. A comparable systematic error exists in the flux density scale. Background estimation errors will contribute significantly to the error budget for fainter sources and in confused fields.

Row
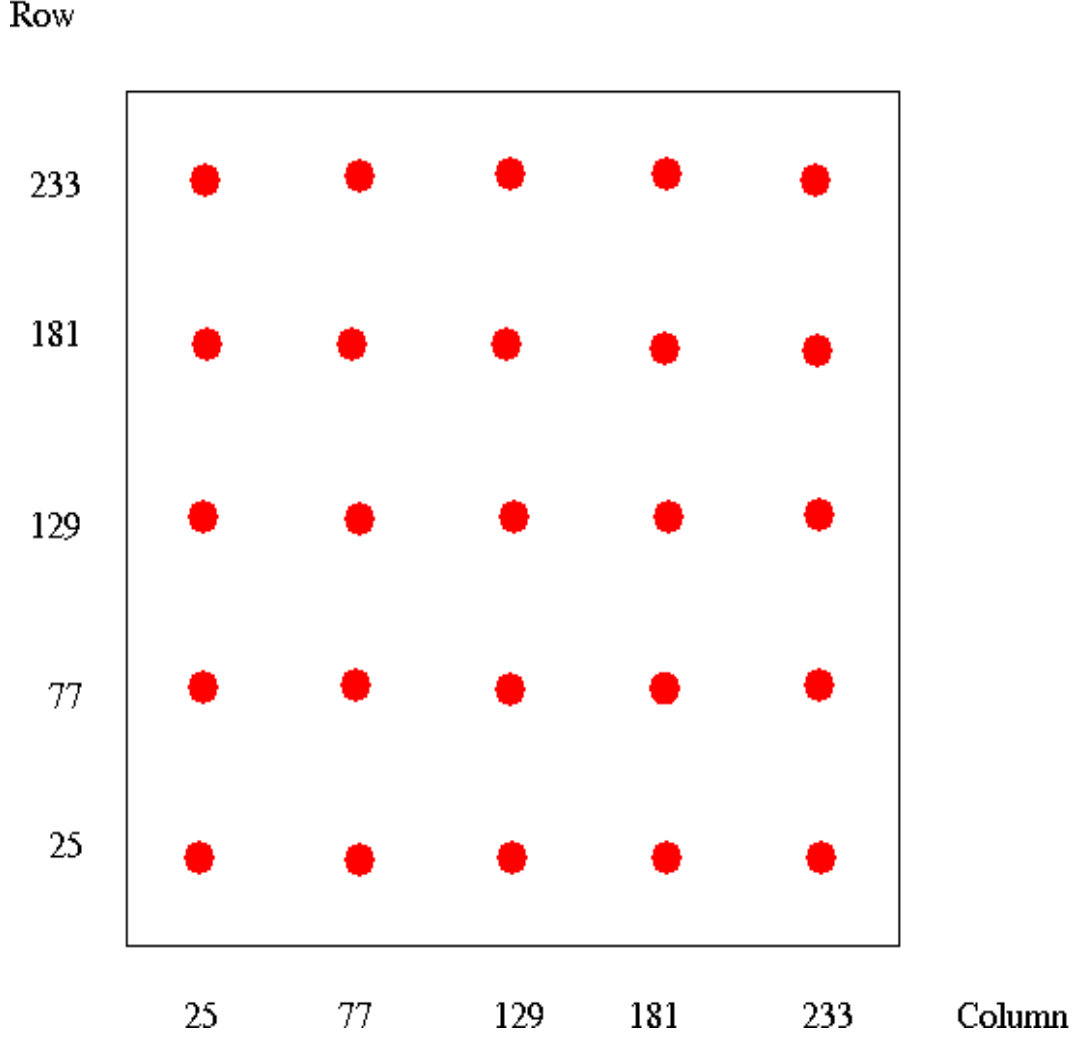
Figure C.5: The 25 PRF positions on an IRAC BCD.

C.3.8 Pixel Phase

We define pixel phase as the offset between the centroid of a stellar image and the center of the pixel in which that centroid lies. For example, an object whose centroid has pixel coordinates 128.23, 127.85 has a pixel phase of Dx,Dy=(-0.27, 0.35). The pixel phase effect in aperture photometry in Chapter 4 is characterized in terms of the radial pixel phase $p = \sqrt{D_x^2 + D_y^2}$). To shift a PRF to a given pixel phase we have adopted the following technique:

i) Magnify the PRFs by a large factor, e.g. 20, using linear interpolation (so the resultant PRF sampling is x100).
ii) Re-center the PRF by shifting it to its centroid. (Note that the estimate of the centroid of a source is itself a function of the method used to determine the centroid, so ideally you would use equivalent

algorithms to find centroids in the (C)BCDs as you do to centroid the PRF. Note also that some of the IDL centroiding functions perform poorly with the very undersampled IRAC data at 3.6 and 4.5 microns).
ii) Shift the PRF array (in the example above a shift by 27, -35 resampled pixels would move the desired PRF to the center of the array).
iii) Extract the point source realization by sampling the PRF at intervals corresponding to native pixel increments (every 100 oversampled pixels in this example), making sure to pick up the center of the central pixel.

In IDL the commands would be:
i) Use rebin on the 128^2, 5x oversampled PRF to produce the magnified PRF:
magPRF = rebin(PRF,2560,2560).
ii) Re-center the PRF. We find that calculating the first moments is usually a robust way to find the centroids. Set xmin, xmax and ymin and ymax to approximately the same values in native pixels as you use to estimate the centroids in your data:
xx = float(lindgen(2560,2560) mod 2560)
yy = float(lindgen(2560,2560)/2560)
xcen = total(xx[xmin:xmax,ymin:ymax]*magPRF[xmin:xmax,ymin:ymax])/total(magPRF[xmin:xmax,ymin:ymax])
ycen = total(yy[xmin:xmax,ymin:ymax]*magPRF[xmin:xmax,ymin:ymax])/total(magPRF[xmin:xmax,ymin:ymax])
xcensh = nx/2 - round(xcen)
ycensh = ny/2 - round(ycen)
cenPRF = shift(magPRF,xcensh,ycensh)
ii) Shift the re-centered PRF to the center of the central PRF pixel and trim to an integer multiple of the 100x oversampling factor such that the central pixel (1280,1280) is moved to (1200,1200), the center of the trimmed array:
shiftedPRF = shift(cenPRF,27,-35)
phasedPRF = fltarr(2500,2500)
trimmedPRF = shiftedPRF[80:2559,80:2559]
phasedPRF[0:2479,0:2479] = trimmedPRF
iii) Sample the trimmed PRF to produce the point source realization:
PSR = rebin(trimmedPRF,25,25,/SAMPLE)
The center of the zero phase PSR in this example should be IDL pixel (12,12).

Appendix D.   IRAC BCD File Header

```
SIMPLE  =                     T / Fits standard
BITPIX  =                   -32 / FOUR-BYTE SINGLE PRECISION FLOATING POINT
NAXIS   =                     2 / STANDARD FITS FORMAT
NAXIS1  =                   256 / STANDARD FITS FORMAT
NAXIS2  =                   256 / STANDARD FITS FORMAT
ORIGIN  = 'Spitzer Science Center' / Organization generating this FITS file
CREATOR = 'S18.18.0'             / SW version used to create this FITS file
TELESCOP= 'Spitzer '            / SPITZER Space Telescope
INSTRUME= 'IRAC    '            / SPITZER Space Telescope instrument ID
CHNLNUM =                     3 / 1 digit instrument channel number
EXPTYPE = 'sci     '            / Exposure Type
REQTYPE = 'AOR     '            / Request type (AOR, IER, or  SER)
AOT_TYPE= 'IracMap '            / Observation template type
AORLABEL= 'IRAC_calstar_NPM1p67.0536_spt4l2 - copy' / AOR Label
FOVID   =                    67 / Field of View ID
FOVNAME = 'IRAC_Center_of_3.6&5.8umArray' / Field of View Name

        / PROPOSAL INFORMATION

OBSRVR  = 'William Reach'       / Observer Name (Last, First)
OBSRVRID=                   125 / Observer ID of Principal Investigator
PROCYCL =                     3 / Proposal Cycle
PROGID  =                  1181 / Program ID
PROTITLE= 'SIRTF IRAC Calibration Program' / Program Title
PROGCAT =                    32 / Program Category

        / TIME AND EXPOSURE INFORMATION

DATE_OBS= '2009-03-23T00:39:17.567' / Date & time (UTC) at DCE start
UTCS_OBS=       291040757.567 / [sec] DCE start time from noon, Jan 1, 2000 UTC
MJD_OBS =       54913.0272867 / [days] MJD in UTC at DCE start (,JD-2400000.5)
HMJD_OBS=        54913.027367 / [days] Corresponding Helioc. Mod. Julian Date
BMJD_OBS=       54913.0273674 / [days] Solar System Barycenter Mod. Julian Date
ET_OBS  =       291040823.752 / [sec] DCE start time (TDB seconds past J2000)
SCLK_OBS=       922236194.809 / [sec] SCLK time (since 1/1/1980) at DCE start
SPTZR_X =    -116152405.204261 / [km] Heliocentric J2000 x position
SPTZR_Y =      87280111.04679 / [km] Heliocentric J2000 y position
SPTZR_Z =      37591123.947116 / [km] Heliocentric J2000 z position
SPTZR_VX=          -18.879473 / [km/s] Heliocentric J2000 x velocity
SPTZR_VY=          -21.032571 / [km/s] Heliocentric J2000 y velocity
SPTZR_VZ=           -9.762563 / [km/s] Heliocentric J2000 z velocity
SPTZR_LT=          500.593938 / [sec] One-way light time to Sun's center
AORTIME =                   2. / [sec] Frameset selected in IRAC AOT
SAMPTIME=                  0.2 / [sec] Sample integration time
FRAMTIME=                   2. / [sec] Time spent integrating (whole array)
COMMENT   Photons in Well = Flux[photons/sec/pixel] * FRAMTIME
EXPTIME =                  1.2 / [sec] Effective integration time per pixel
COMMENT   DN per pixel = Flux[photons/sec/pixel] / GAIN * EXPTIME
FRAMEDLY=                  18. / [sec] Frame Delay Time
FRDLYDET= 'T       '            / Frame Delay Time Determinable (T or F)
```

```
INTRFDLY=                    18. / [sec] Inter Frame Delay Time
IMDLYDET= 'T       '            / Immediate Delay Time Determinable (T or F)
AINTBEG =            1114427.07 / [Secs since IRAC turn-on] Time of integ. start
ATIMEEND=            1114429.03 / [Secs since IRAC turn-on] Time of integ. end
AFOWLNUM=                     4 / Fowler number
AWAITPER=                     2 / [0.2 sec] Wait period
ANUMREPS=                     1 / Number of repeat integrations
AREADMOD=                     0 / Full (0) or subarray (1)
AORHDR  =                     F / Requested AOT is HDR mode
HDRMODE =                     F / DCE taken in High Dynamic Range mode
ABARREL =                     2 / Barrel shift
APEDSIG =                     0 / 0=Normal, 1=Pedestal, 2=Signal


            / TARGET AND POINTING INFORMATION


OBJECT  = 'NPM1p67.0536'       / Target Name
OBJTYPE = 'TargetFixedCluster' / Object Type
CRPIX1  =                  128. / Reference pixel along axis 1
CRPIX2  =                  128. / Reference pixel along axis 2
CRVAL1  =      269.646261212312 / [deg] RA at CRPIX1,CRPIX2 (using Pointing Recon
CRVAL2  =       67.789551215035 / [deg] DEC at CRPIX1,CRPIX2 (using Pointing Reco
CRDER1  = 6.19688778419269E-05 / [deg] Uncertainty in CRVAL1
CRDER2  =  6.4255687707609E-05 / [deg] Uncertainty in CRVAL2
RA_HMS  = '17h58m35.1s'        / [hh:mm:ss.s] CRVAL1 as sexagesimal
DEC_DMS = '+67d47m22s'         / [dd:mm:ss] CRVAL2 as sexagesimal
RADESYS = 'ICRS    '           / International Celestial Reference System
EQUINOX =                 2000. / Equinox for ICRS celestial coord. system
CD1_1   = -0.000214831469601829 / Corrected CD matrix element with Pointing Reco
CD1_2   = -0.000262955698252767 / Corrected CD matrix element with Pointing Reco
CD2_1   = -0.000264515231791188 / Corrected CD matrix element with Pointing Reco
CD2_2   = 0.000215085880792259 / Corrected CD matrix element with Pointing Recon
CTYPE1  = 'RA---TAN-SIP'       / RA---TAN with distortion in pixel space
CTYPE2  = 'DEC--TAN-SIP'       / DEC--TAN with distortion in pixel space
PXSCAL1 =     -1.22673962032422 / [arcsec/pix] Scale for axis 1 at CRPIX1,CRPIX2
PXSCAL2 =      1.22298117494211 / [arcsec/pix] Scale for axis 2 at CRPIX1,CRPIX2
PA      =     -50.7183862658392 / [deg] Position angle of axis 2 (E of N) (was OR
UNCRTPA = 0.000575824424074831 / [deg] Uncertainty in position angle
CSDRADEC= 2.27476132413713E-06 / [deg] Costandard deviation in RA and Dec
SIGRA   =     0.033918650300932 / [arcsec] RMS dispersion of RA over DCE
SIGDEC  =    0.0233826859041868 / [arcsec] RMS dispersion of DEC over DCE
SIGPA   =    0.0180000000057134 / [arcsec] RMS dispersion of PA over DCE
PA      =     -50.7183862658392 / [deg] Position angle of axis 2 (E of N) (was OR
RA_RQST =     269.646397245074 / [deg] Requested RA at CRPIX1, CRPIX2
DEC_RQST=     67.7896310093685 / [deg] Requested Dec at CRPIX1, CRPIX2
PM_RA   =                   0. / [arcsec/yr] Proper Motion in RA (J2000)
PM_DEC  =                   0. / [arcsec/yr] Proper Motion in Dec (J200)
RMS_JIT =  0.00414784151698205 / [arcsec] RMS jitter during DCE
RMS_JITY=  0.00293095487000397 / [arcsec] RMS jitter during DCE along Y
RMS_JITZ=  0.00293497747861887 / [arcsec] RMS jitter during DCE along Z
SIG_JTYZ= -0.00102057552390795 / [arcsec] Costadard deviation of jitter in YZ
PTGDIFF =     0.341735121617664 / [arcsec] Offset btwn actual and rqsted pntng
PTGDIFFX=     0.339553396668735 / [pixels] rqsted - actual pntng along axis 1
PTGDIFFY=    0.0374044542123624 / [pixels] rqsted - actual pntng along axis 2
RA_REF  =     269.727166666669 / [deg] Commanded RA (J2000) of ref. position
DEC_REF =     67.7936944444455 / [deg] Commanded Dec (J2000) of ref. position
```

```
USEDBPHF=                        T / T if Boresight Pointing History File was used
BPHFNAME= 'SBPHF.0922233600.041.pntg' / Boresight Pointing History Filename
FOVVERSN= 'BodyFrames_FTU_14a.xls' / FOV/BodyFrames file version used
RECONFOV= 'IRAC_Center_of_5.8umArray' / Reconstructed Field of View
ORIG_RA =     269.646270751953 / [deg] Original RA from raw BPHF (without pointi
ORIG_DEC=      67.7895202636719 / [deg] Original Dec from raw BPHF (without point
ORIGCD11=      -0.0002148321219 / [deg/pix] Original CD1_1 element (without point
ORIGCD12=      -0.0002629551745 / [deg/pix] Original CD1_2 element (without point
ORIGCD21=      -0.0002645147033 / [deg/pix] Original CD2_1 element (without point
ORIGCD22=       0.0002150865184 / [deg/pix] Original CD2_2 element (without point



          / DISTORTION KEYWORDS

A_ORDER =                    3 / polynomial order, axis 1, detector to sky
A_0_2   =         -4.3447E-06 / distortion coefficient
A_0_3   =          -1.016E-09 / distortion coefficient
A_1_1   =          3.5897E-05 / distortion coefficient
A_1_2   =         -1.5883E-07 / distortion coefficient
A_2_0   =         -1.6032E-05 / distortion coefficient
A_2_1   =         -1.0378E-09 / distortion coefficient
A_3_0   =         -1.5738E-07 / distortion coefficient
A_DMAX  =               1.641 / [pixel] maximum correction
B_ORDER =                    3 / polynomial order, axis 2, detector to sky
B_0_2   =          2.5424E-05 / distortion coefficient
B_0_3   =         -1.6169E-07 / distortion coefficient
B_1_1   =          -9.977E-06 / distortion coefficient
B_1_2   =          7.6924E-09 / distortion coefficient
B_2_0   =         -7.8167E-06 / distortion coefficient
B_2_1   =         -1.6873E-07 / distortion coefficient
B_3_0   =         -1.1593E-08 / distortion coefficient
B_DMAX  =               1.184 / [pixel] maximum correction
AP_ORDER=                    3 / polynomial order, axis 1, sky to detector
AP_0_1  =         -2.3883E-07 / distortion coefficient
AP_0_2  =           4.406E-06 / distortion coefficient
AP_0_3  =          6.4348E-10 / distortion coefficient
AP_1_0  =         -1.5761E-05 / distortion coefficient
AP_1_1  =         -3.6428E-05 / distortion coefficient
AP_1_2  =            1.64E-07 / distortion coefficient
AP_2_0  =          1.6243E-05 / distortion coefficient
AP_2_1  =         -9.3393E-10 / distortion coefficient
AP_3_0  =          1.5989E-07 / distortion coefficient
BP_ORDER=                    3 / polynomial order, axis 2, sky to detector
BP_0_1  =         -1.6807E-05 / distortion coefficient
BP_0_2  =         -2.5772E-05 / distortion coefficient
BP_0_3  =          1.6546E-07 / distortion coefficient
BP_1_0  =         -8.8532E-07 / distortion coefficient
BP_1_1  =          1.0173E-05 / distortion coefficient
BP_1_2  =         -8.7895E-09 / distortion coefficient
BP_2_0  =          7.8383E-06 / distortion coefficient
BP_2_1  =          1.7089E-07 / distortion coefficient
BP_3_0  =          1.2114E-08 / distortion coefficient

          / PHOTOMETRY
```

```
BUNIT   = 'MJy/sr  '           / Units of image data
FLUXCONV=             0.6074 / Flux Conv. factor (MJy/sr per DN/sec)
GAIN    =                3.8 / e/DN conversion
RONOISE =                9.1 / [Electrons] Readout Noise from Array
ZODY_EST=           1.977768 / [MJy/sr] Zodiacal Background Estimate
ISM_EST =          0.1727364 / [MJy/sr] Interstellar Medium Estimate
CIB_EST =                 0. / [MJy/sr] Cosmic Infrared Background Estimate
SKYDRKZB=           1.934454 / [MJy/sr] Zodiacal Background Est of Subtracted
SKYDKMED=          -1.472912 / [MJy/sr] Median of Subtracted Skydark
SKDKRKEY=           29840640 / Skydark AOR Reqkey
SKDKTIME=                 2. / [sec] Skydark AOR Duration Time
SKDKFDLY=              11.97 / [sec] Average Frame Delay Time of Skydark
SKDKIDLY=              11.97 / [sec] Average Immediate Delay Time of Skydark


        / IRAC MAPPING KEYWORDS


READMODE= 'FULL    '           / Readout mode (full or sub)


        / INSTRUMENT TELEMETRY DATA


ASHTCON =                  2 / Shutter condition (1:closed, 2: open)
AWEASIDE=                  0 / WEA side in use (0:B, 1:A)
ACTXSTAT=                  0 / Cmded transcal status
ATXSTAT =                  0 / transcal status
ACFLSTAT=                  0 / Cmded floodcal status
AFLSTAT =                  0 / floodcal status
AVRSTUCC=               -3.4 / [Volts] Cmded VRSTUC Bias
AVRSTBEG=         -3.3878126 / [Volts] VRSTUC Bias at start integration
AVDETC  =                -4. / [Volts] Cmded VDET Bias
AVDETBEG=         -3.9877046 / [Volts] VDET Bias at start of integration
AVGG1C  =              -3.45 / [Volts] Cmded VGG1 Bias
AVGG1BEG=         -3.4382206 / [Volts] VGG1 Bias at start of integration
AVDDUCC =                -3. / [Volts] Cmded VDDUC Bias
AVDDUBEG=         -2.9828275 / [Volts] VDDUC Bias at start integration
AVGGCLC =                 0. / [Volts] Cmnded VGGCL clock rail voltage
AVGGCBEG=                 0. / [Volts] VGGCL clock rail voltage
AHTRIBEG=          150.05788 / [uAmps] Heater current at start of integ
AHTRVBEG=          1.9357675 / [Volts] Heater Voltage at start integ.
AFPAT2B =          6.0626999 / [Deg_K] FPA Temp sensor #2 at start integ.
AFPAT2BT=          1114416.9 / [Sec] FPA Temp sensor #2 time tag
AFPAT2E =          6.0626999 / [Deg_K] FPA temp sensor #2, end integ.
AFPAT2ET=          1114416.9 / [Sec] FPA temp sensor #2 time tag
ACTENDT =          20.925428 / [Deg_C] C&T board thermistor
AFPECTE =           18.04231 / [Deg_C] FPE control board thermistor
AFPEATE =          21.025127 / [Deg_C] FPE analog board thermistor
ASHTEMPE=           22.11418 / [Deg_C] Shutter board thermistor
ATCTEMPE=          23.272451 / [Deg_C] Temp. controller board thermistor
ACETEMPE=          20.864466 / [Deg_C] Calib. electronics board thermistor
APDTEMPE=           20.98639 / [Deg_C] PDU board thermistor
ACATMP1E=           1.302006 / [Deg_K] CA Temp, Foot 2
ACATMP2E=          1.2846904 / [Deg_K] CA Temp, Foot 1
ACATMP3E=          1.3177339 / [Deg_K] CA Temp, Shutter
ACATMP4E=          1.3142446 / [Deg_K] CA Temp, Top OMH
ACATMP5E=          1.3122628 / [Deg_K] CA Temp, Bottom OMH
```

```
ACATMP6E=            1.3106288 / [Deg_K] CA Temp, Top TxCal Sphere
ACATMP7E=            1.3093235 / [Deg_K] CA Temp, Bottom TxCal Sphere
ACATMP8E=            1.3022636 / [Deg_K] CA Temp, Foot 3


           / DATA FLOW KEYWORDS


ORIGIN0 = 'JPL_FOS '           / Site where RAW FITS file was written
CREATOR0= 'J5.3    '           / SW system that created RAW FITS
DATE    = '2010-08-17T21:59:39' / [YYYY-MM-DDThh:mm:ss UTC] file creation date
AORKEY  =            29850368 / AOR or EIR key. Astrnmy Obs Req/Instr Eng Req
DS_IDENT= 'ads/sa.spitzer#0029850368' / Data Set Identification for ADS/journals
EXPID   =                   9 / Exposure ID (0-9999)
DCENUM  =                   0 / DCE number (0-9999)
TLMGRPS =                   1 / expected number of groups
FILE_VER=                   1 / Version of the raw file made by SIS
RAWFILE = 'IRAC.3.0029850368.0009.0000.01.mipl.fits' / Raw data file name
CPT_VER = '3.1.11  '           / Channel Param Table FOS versioN
CTD_VER = '3.0.94S '           / Cmded telemetry data version
EXPDFLAG=                   T / (T/F) expedited DCE
MISS_LCT=                   0 / Total Missed Line Cnt in this FITS
MANCPKT =                   F / T if this FITS is Missing Ancillary Data
MISSDATA=                   F / T if this FITS is Missing Image Data
BADTRIG =                   F / Bad data (zero pixel) was located in raw frame
CHECKSUM=                   0 / MIPL computed checksum
PAONUM  =                3383 / PAO Number
CAMPAIGN= 'IRAC013100'         / Campaign
DCEID   =           117913164 / Data-Collection-Event ID
DCEINSID=            24298735 / DCE Instance ID
DPID    =           318707046 / Data Product Instance ID
PIPENUM =                 107 / Pipeline Script Number
SOS_VER =                   2 / Data-Product Version
PLVID   =                   6 / Pipeline Version ID
CALID   =                   8 / CalTrans Version ID
SDRKEPID=             6906663 / Sky Dark ensemble product ID
PMSKFBID=                1878 / Pixel mask ID
LDRKFBID=                 852 / Fall-back lab dark ID
LINCFBID=                1021 / Fall-back Linearity correction ID
FLATFBID=                1161 / Fall-back flat ID
FLXCFBID=                1801 / Flux conversion ID
LBDRKFLE= 'FUL_2s_2sf4d1r1_ch3_v1.2.0_dark.txt' / Labdark File Used
LBDRKTD = 'T         '         / Labdark Time Dependent (T or F)



           / PROCESSING HISTORY


HISTORY job.c ver: 1.50
HISTORY TRANHEAD                 v.          13.1, ran Tue Aug 17 14:58:33 2010
HISTORY CALTRANS                 v.           4.0, ran Tue Aug 17 14:58:44 2010
HISTORY cvti2r4          v. 1.31 A61025, generated  8/17/10 at 14:58:47
HISTORY hdrupd8          v. 1.6  A70821,  updated   8/17/10 at 14:58:52
HISTORY hdrupd8          v. 1.6  A70821,  updated   8/17/10 at 14:58:55
HISTORY hdrupd8          v. 1.6  A70821,  updated   8/17/10 at 14:58:59
HISTORY hdrupd8          v. 1.6  A70821,  updated   8/17/10 at 14:59:02
HISTORY hdrupd8          v. 1.6  A70821,  updated   8/17/10 at 14:59:05
```

```
HISTORY hdrupd8              v.  1.6  A70821,  updated   8/17/10 at 14:59:08
HISTORY hdrupd8              v.  1.6  A70821,  updated   8/17/10 at 14:59:11
HISTORY FFC                  v.            1.0, ran Tue Aug 17 14:59:13 2010
HISTORY FOWLINEARIZE         v.       4.900000, ran Tue Aug 17 14:59:13 2010
HISTORY hdrupd8              v.  1.6  A70821,  updated   8/17/10 at 14:59:16
HISTORY BGMODEL              v.            1.0, ran Tue Aug 17 14:59:16 2010
HISTORY SLREMOVE             v.            1.0, ran Tue Aug 17 14:59:17 2010
HISTORY hdrupd8              v.  1.6  A70821,  updated   8/17/10 at 14:59:19
HISTORY hdrupd8              v.  1.6  A70821,  updated   8/17/10 at 14:59:22
HISTORY hdrupd8              v.  1.6  A70821,  updated   8/17/10 at 14:59:24
HISTORY hdrupd8              v.  1.6  A70821,  updated   8/17/10 at 14:59:27
HISTORY hdrupd8              v.  1.6  A70821,  updated   8/17/10 at 14:59:30
HISTORY hdrupd8              v.  1.6  A70821,  updated   8/17/10 at 14:59:33
HISTORY DARKSUBNG            v. 1.000, ran Tue Aug 17 14:59:34 2010
HISTORY DARKDRIFT            v.            4.1, ran Tue Aug 17 14:59:35 2010
HISTORY FLATAP               v. 1.500   Tue Aug 17 14:59:35 2010
HISTORY DNTOFLUX             v.            4.2, ran Tue Aug 17 14:59:39 2010
HISTORY CALTRANS             v.        4.0, ran Thu Aug 19 04:55:27 2010
HISTORY PTNTRAN              v.          1.4, ran Thu Aug 19 04:55:34 2010
HISTORY FPGen                v.          1.26, ran Thu Aug 19 04:55:40 2010
HISTORY PTGADJUST            v.          1.0, ran Thu Aug 19 05:01:12 2010
HISTORY SATCORR Module version 1.7  image created Thu Aug 19 19:58:27 2010
SATSRCFX=                    T / Saturated sources corrected with estimate
SATSRCS =                    0 / number of saturated sources fixed
CLPLDNFX=                    T / Column Pulldown artifact corrected
HISTORY pulldown_correction  v.   1.2   Thu Aug 19 19:59:16 2010
BANDNGFX=                    T / Banding artifact corrected
HISTORY bandingcorr          v.   1.1   Thu Aug 19 19:59:38 2010
END
```

Appendix E.   Acronyms

ADC

Analog-to-Digital Converter

AOR

Astronomical Observation Request - an individual observation.

AORKEY

Astronomical Observation Request Key - a unique numerical identification of an observation.

AOT

Astronomical Observation Template - the IRAC observing mode.

BCD

Basic Calibrated Data, the Level 1 data product from each DCE that has been pipeline-processed and is fully calibrated.

CBCD

Corrected Basic Calibrated Data. This should be the starting point for further scientific analysis in most cases.

Campaign

Unbroken time period when an instrument is powered on. Most instrument IRAC campaigns are expected to be on the order of one week in length.

CTE

Charge Transfer Efficiency.

DCE

Data Collection Event, for IRAC a single 256x256 pixel image from a single detector.

DN

Data Number.

FET

Field Effect Transistor.

FOS

Flight Operations System.

FPA

Focal Plane Assembly, housing one IRAC detector.

IER

Instrument Engineering Request - like an AOR, but for specific engineering tasks that cannot be accomplished with an AOR.

InSb

Indium Antimonide, the detector material used in the short wavelength channels of IRAC (1 and 2).

IOC

In-Orbit Checkout, the two-month long testing period of the telescope following its launch.

ISSA

IRAS Sky Survey Atlas.

IWIC

IRAC Warm Instrument Characterization, the two-month long testing period of the telescope at the beginning of the warm mission and immediately following the end of the cryogenic mission.

JPL

Jet Propulsion Laboratory

MIC

Multiple Instrument Chamber.

PAO

Period of Autonomous Operation, the interval between ground contacts for uplinking commands and downlinking data, normally 12–24 hours.

PCS

Pointing Control System.

PRF

Point Response Function. The PRF is essentially the convolution of a box the size of the image pixel with the PSF.

ROIC

Read-Out Integrated Circuit. It is the chip that contains the multiplexer (column and row scanners and the buses), the unit cell amplifiers, and the output amplifiers. The chip containing the detector diodes is bonded to it. It is often called simply the "mux."

SAO

Smithsonian Astrophysical Observatory, Cambridge, MA.

SSC

Spitzer Science Center, Caltech, Pasadena, CA.

Si:As

Arsenic-doped Silicon, the detector material in the IRAC long-wavelength channels (3 & 4).

SV

Science Verification, a 35-day period after the IOC during which the science instruments and their observational modes were commissioned.

SWIRE

Spitzer Wide Area Infrared Survey.

WCS

World Coordinate System.

Appendix F.   Acknowledgments

IRAC would not have been the successful instrument it was without the enthusiastic and capable contribution of many colleagues (see the lists of collaborators and laboratories below). Support for the IRAC instrument was provided by NASA through contract 960541 issued by JPL.

Principal Investigator

Dr. Giovanni Fazio (SAO, Harvard)
Dr. Gary J. Melnick, Deputy Principal Investigator (SAO, Harvard)
Dr. Joseph L. Hora, Project Scientist (SAO, Harvard)
Richard S. Taylor, Project Manager (SAO, Harvard)

Co-Investigators

The co-investigators played a central role in defining the technical characteristics of IRAC in order to carry out the science programs agreed upon by all of them. Lynne Deutsch, a co-investigator of IRAC, died on April 2, 2004, after a long illness. Lynne was a dear friend and a close colleague. The IRAC team deeply misses her presence.

Dr. William F. Hoffmann (University of Arizona)
Dr. Craig R. McCreight (Ames Research Center)
Dr. S. Harvey Moseley (Goddard Space Flight Center)
Dr. Judith L. Pipher (University of Rochester)
Dr. Lori E. Allen (SAO, Harvard)
Dr. Matthew L. N. Ashby (SAO, Harvard)
Dr. Pauline Barmby (SAO, Harvard)
Dr. Lynne K. Deutsch (SAO, Harvard)
Dr. Peter Eisenhardt (JPL, Caltech)
Dr. Jiasheng Huang (SAO, Harvard)
Dr. David I. Koch (SAO, Harvard)
Dr. Massimo Marengo (SAO, Harvard)
Dr. S. Thomas Megeath (SAO, Harvard; University of Toledo)
Dr. Michael Pahre (SAO, Harvard)
Dr. Brian Patten (SAO, Harvard)
Dr. Howard Smith (SAO, Harvard)
Dr. John R. Stauffer (SAO, Harvard; SSC, Caltech)
Dr. Eric V. Tollestrup (SAO, Harvard)
Dr. Zhong Wang (SAO, Harvard)
Dr. Steven P. Willner (SAO, Harvard)
Dr. Edward L. Wright (UCLA)
Dr. William F. Hoffmann (U. Arizona)
Dr. William J. Forrest (University of Rochester)
Dr. Daniel Gezari (GSFC)

Collaborators

Construction and ground calibration phase

People listed here include those that participated in the mechanical, optical and cryo-mechanical studies that led to the definition of IRAC, as well as those who designed and built the on-board electronic subsystems, developed the on-board software and worked on the Ground Support Equipment. Others participated in the development of the extensive software systems and procedures later used for the in-flight calibration, system tests and uplink subsystems or in the Off-Line pipeline.

Dr. Jon Chappell, Data Systems Analyst (SAO, Harvard)
Dr. Martin Cohen, Calibration Scientist (SAO, Harvard)
Dr. Steven Kleiner, IT Specialist (SAO, Harvard)
Dr. John Spitzak, Data Systems Analyst (SAO, Harvard)
SAO IRAC PROJECT OFFICE
Christina M. Arabadjis, Project Administrator
Jo-Ann Campbell-Cameron, Group Secretary
Mary L. Horan, Project Administrator
Ralph Paganetti, Management Support
S. Douglas Smith, Project Administrator
Jane I. Wamback, Group Administrator
SAO CENTRAL ENGINEERING
John P. Polizotti, IRAC Systems Engineer
Vaman S. Bawdekar, Quality Assurance Engineer
David A. Boyd, Thermal Engineer
John Boczenowski, Quality Assurance Manager
Kathy Daigle, Documentation Control Engineer
Leslie Frazier, Quality Assurance Engineer
Thomas Gauron, Mechanical Engineer
Joaquim J. Gomes, Electrical Engineer
Everett Johnston, Electrical Engineer
Maggie Kanouse, Documentation Specialist
Warren Martell, Quality Assurance Engineer
Paul Okun, Electrical Engineer
Joel Rosenberg, Electrical Engineer

AMES RESEARCH CENTER
Dr. Craig R. McCreight, Lead Si:As Scientist
Roy R. Johnson, Detector Test Engineer
Roderick N. McHugh, Electronic Technician
Mark E. McKelvey, Detector Test Lead
Robert E. McMurray, Jr., Detector Scientist
Nicolas N. Moss, Programmer

Margaret Drennan, Graduate Student
Mike Dunham, Undergraduate Student
Kevin Flaherty, Undergraduate Student
Rob Gutermuth, Graduate Student
Alaina Henry, Undergraduate Student
Osa Igbinosun, Undergraduate Student
Angela Lowell, Undergraduate Student
Rebecca Madson, Undergraduate Student
Dawn Peterson, Graduate Student

RAYTHEON VISION SYSTEMS
SANTA BARBARA RESEARCH CENTER
InSb AND Si:As DETECTOR DEVELOPMENT, FABRICATION AND TEST

Dr. Alan Hoffman, Project Manager
Dr. George Domingo, Si:As Development Lead, Project Manager
Conrad Anderson, IBC Detector & Test
Jim Asbrock, Readout Design
Virginia Bowman, Si:As Processing
George Chapman, Detector Test
Elizabeth Corrales, Business Manager
Arnold Estrada, Array Test
Bruce Fletcher, Hybridization Engineer
Peter Love, System Engineer
Dr. Larry Lum, Readout Engineer
Dr. Nancy Lum, Multiplexer Designer
Susan Morales, Production Control
Olivia Moreno, Quality Assurance
Heidi Mosel-Riedo, Business Manager
Joseph Rosbeck, InSb Detector Engineer
Kiomi Schartz, IBC Processing
Michael S. Smith, Detector Test Engineer
Steve Solomon, Array Test Engineer
Kevin Sparkman, Test Engineer
Andrew S. Toth, IBC Detector Engineer
Peter S. Villa, Hybridization Engineer
Sharon E. Woolaway, Hybridization Engineer

GODDARD SPACE FLIGHT CENTER

INSTRUMENT MANAGEMENT
Lois Workman, Instrument Manager
Felicia Jones-Selden, Instrument Engineer/Manager
Juan Rivera, Instrument Engineer/Manager

Rich Barney, Instrument Manager, Branch Head

SCIENCE TEAM
Dr. S. Harvey Moseley, Instrument Scientist
Dr. Richard Arendt, Science Support
Dr. Sean Casey, Science Support
Dr. Dale Fixsen, Science Support
Dr. Daniel Gezari, Instrument Scientist
Dr. Alexander Kutyrev, Science Support
Tim Powers, Electronics Technician

REVIEW TEAM
William T. Tallant, Review Team Chairman
Steve Bartel, Review Team
James Caldwell, Review Team
Robert Coladonato, Review Team
Michael Dipirro, Review Team
Pam Davila, Review Team,
Gene Gochar, Review Team
Frank Kirchman, Review Team
Robert Martineau, Review Team
Ian Mclean, Review Team
Vern Weyers, Review Team

INSTRUMENT SYSTEM ENGINEERS
Gabe Karpati, Instrument System Engineer
Neil Martin, Instrument System Engineer
Robert Maichle, Instrument System Engineer
Kevin Brenneman, System Engineer
Robert Kichak, Chief Engineer, Electrical
John Wolfgang, Verification Lead

MECHANICAL SYSTEMS
Claef Hakun, Mechanical System Lead
Willie Blanco, Mechanical Branch Head
Willie Barber, Mechanical Technician
Carlos Bernabe, Mechanical Engineer
Ken Blumenstock, Mechanical Engineer
Gary Brown, Mechanical Engineer
Dr. Philip Chen, Contamination Engineer
Rainer Fettig, Mechanical Engineer
Bryan Grammer, Designer
Paul Haney, Mechanical Technician
Tom Hanyok, Designer

Darron Harris, Mechanical Technician
Mike Hersh, Mechanical Engineer
Sid Johnson, Mechanical Technician
Ben Lewit, Mechanisms Engineer
Carlos Lugo, Mechanical Engineer
Dave Pfenning, Electro/Mechanical Tech
George Reinhardt, Mechanical Engineer
Scott Schwinger, Mechanical Engineer
Ryan Simmons, Systems Analyst
Dr. Michael G. Ryschkewitsch, Designer, 1988-1989
Charles Tomasevich, Mechanical Engineer, 1997-2000
George Voellmer, Mechanical Engineer, 1995-1996
Steve Wood, Mechanical Technician, 1997-2000

ELECTRICAL SYSTEMS
Jose Florez, Electrical System Lead
Harlan Bowers, OSC Task Manager
Vicky Brocius, Parts Procurement
Robert Clark, Parts Procurement
Tracy Clay, WEA Enclosure Supervisor
Jim Cook, PWA Assembly
Glenn Davis, Polymerics
Mitch Davis, ESE Engineer
Bob Demme, PWA Assembly Manager
Melissa Eberhardinger, Parts Procurement
Majed El Alami, Parts Procurement
Patricia Gilbertson, Parts Procurement
Steve Graham, Electrical Engineer
David Hessler, Electrical Engineer
Gina Kanares, Parts Stock
Richard Katz, Electrical Engineer
Igor Kleiner, BTE S/W
Tracie Lampke, PWA Assembly
David Liu, Electrical Engineer
Jim Lohr, Parts Engineer
Bill Long, WEA Enclosure Supervisor
Jack Lorenz, WEA Enclosure Designer
John McCloskey, Electrical Engineer
Charlie McClunin, WEA Enclosure Designer
Margaret McVicker, PWA Assembly
Tim Miralles, WEA Test Engineer
Keyvan Mortazavi, J&T Task Manager
Kim Moats, PWA Assembly
Trang Nguyen, Electrical Engineer

J. R. Norris, Litton Task Manager
Larry Pack, Packaging Lead
Laddawan Ruamsuwan, Electrical Engineer
Allen Rucker, WEA Test Engineer
Kamdin Shakoorzadeh, Electrical Engineer
Narenda Shukla, DC-DC Converter
Kevin Smith, WEA PWA Designer
Steve Smith, WEA Test Engineer
John Stewart, Electronics Technician
Victor Torres, Electrical Engineer
Yen Tran, WEA PWA Designer
Steven Van Nostrand, WEA PWA Designer
Sherry Wagner, PWA Assembly
Banks Walker, WEA PWA Designer
Mark Walter, DC-DC Converter
Richard Williams, Parts Engineer

SOFTWARE SYSTEMS
Raymond Whitley, Software Manager
Louise Bashar, Software Engineer
Craig Bearer, Ground Software Engineer
Glenn Cammarata, Software Engineer
Jenny Geiger, Software Engineer
Bob Koehler, Software Engineer
Steve Mann, Software Engineer
Dave McComas, Software Engineer
Janet McDonnell, Software Engineer
Ken Rehm, Software Engineer
Jann Smith, Software Engineer
Carlos Trujillo, Software Engineer
David Vavra, Software Engineer

CRYOGENICS
Dan McHugh, Cryogenics Technician,
John Bichell, Cryogenics Technician
Rob Boyle, Cryogenics Engineer
Susan Breon, Cryogenics Engineer
Michael Dipirro, Cryogenics Engineer
Darrell Gretz, Cryogenics Technician
Ed Quinn, Cryogenics Technician
Peter Shirron, Cryogenics Engineer

FLIGHT ASSURANCE
Ted Ackerson, Systems Assurance Manager

Dick Bolt, Flight Assurance
Jerry Bushman, Flight Assurance
Jack Galleher, System Reliability
Steve Hull, Parts Assurance
Ron Kolecki, Flight Assurance Manager
Norman Lee, Flight Assurance
Shirley Paul, Flight Assurance

OPTICAL SYSTEMS
Peter Maymon, Lead Optics, Optics Consultant, Branch Head
Catherine Marx, Optical Designer, Optics Lead
Pat Losch, Lead Optics, Optics I&T
Bill Eichorn, Lead Optics, Optical I&T
Julie Crooke, Optical Engineer
Andy Dantzler, Optical Designer
Dr. Bruce Dean, Optical Analyst
Dennis Evans, Optical Design
Thomas French, Optical Technician
Dr. David Glenar, Calibration Optics
Dr. Qian Gong, Optical Engineer
Paul Hannan, Optical Designer
Dr. Donald Jennings, Optics Engineer
Jay Jett, Optical Technician
Linette Kolos, Plating Technician
Dr. Ritva Keski-Kuha, Optics Engineer
James Lyons, Optical Technician
Eric Mentzell, Optical Analyst
Joseph McMann, Optics Engineer
Dr. Ray Ohl, Optical Engineer
Dean Osgood, Optical Technician
Grant Piegari, Optical Technician
Dr. Manuel Quijada, Optics Engineer
Steve Rice, Thin Films Technician
Kevin Redman, Optical Technician
Vicki Roberts, Optical Technician
Dr. Frederick Robinson, Optics Engineer
Dr. Kenneth Stewart, Optics Engineer
Carl Strojny, Optical Technician
Felix Threat, Thin Films Technician
Larry White, Mechanical Technician
Mark Wilson, Optical Designer
Lou Worrel, Optics Technician

THERMAL SYSTEMS

Rick Stavely, Lead Thermal Engineer
Carol Mosier, Lead Thermal Engineer
Mike Choi, Thermal Engineer
Raymond Trunzo, Thermal Engineer

FOCAL PLANE ASSEMBLIES
Dr. Danny Krebs, FPA Lead
Dr. Murzy D. Jhabvala, FPA Lead
Christine Allen, FPA Engineer
Sachi Babu, Detector Assembly Technician
Mark Cushman, Detector Assembly Tech
John Godfrey
Steve Graham, Electronics Engineer
Anh La, Test Engineer
Gerald Lamb, FPA Engineer
Kim Moats, Electronics Technician
Trang Nguyen, Electronics Engineer
Frank Peters, Detector Technician
David Rapchun, Detector Technician
Peter Shu, Science Team
Robert Stanley, Electronics Technician
Jeff Travis, Electronics Engineer

INTEGRATION AND TEST
Ray Jungo, Integration and Test Manager
Michael Alexander, Test Conductor
Maureen Armbruster, Test Conductor
Craig Bearer, S/C Simulator Programmer
Marty Brown, Test Conductor
Jamie Britt, Environmental Test Engineer
Frank Carroll, Test Conductor
James E. Golden, Programmer
Peter Gorog, Programmer
Shirley M. Jones, Harness Technician
Don Kirkpatrick, Harness Technician
Juli Lander, Test Conductor
Matthew E. (Ed) Lander, Test Conductor
Jim MacLeod, Test Conductor
Rudy Manriquez, Harness Technician
Ayman Mekhail, Test Conductor
James Mills, Harness Fabrication Supervisor
Brian Ottens, Environmental Test Engineer
Ramjit Ramrattan, Harness Technician
Marco Rosales, Harness Technician

Charles Stone, Harness Technician

INSTRUMENT TEAM SUPPORT
John Anders, Configuration Manager
Kim Brecker, Web Page Manager
Walt Carel, Transportation
Ron Colvin, Web Server
John Davis, Scheduler
Robert Dipalo, Transportation
Cristina Doria-Warner, Resource Analyst
Steve Ford, Program Analyst
Toni Hegarty, Configuration Manager
Ken Lathan, Web Page Support
Lois Pettit, Configuration Manager
Bob Read, Support Team Supervisor
Chris Romano, Program Analyst
Sharmaine Stewart, Resource Analyst
Lynette Sullivan, Configuration Manager
Catherine Traffanstedt, Transportation
Debra A. Yoder, Configuration Manager

Operations phase

The following are the people who participated in the operational phase of IRAC. The list includes those actively involved with the day-to-day operations within the IRAC Instrument Support Team (IST) at SSC, and those in the "home team" within the IRAC Instrument Team (IT) at SAO, Harvard, and anyone that contributed to a better understanding of IRAC by producing software code used in the online and offline pipelines.

IRAC INSTRUMENT SUPPORT TEAM (IST) AT SPITZER SCIENCE CENTER, CALTECH

Dr. William Reach, Team Lead
Dr. Sean Carey, Team Lead
Dr. Patrick Lowrance, Team Lead
Dr. Jason Surace, Deputy Lead
Dr. Bidushi Bhattacharya
Heidi Brandenburg
Dr. Peter Capak
Dr. David Cole
Dr. William Glaccum
Dr. Carl Grillmair
Dr. Myungshin Im
Dr. James Ingalls
Dr. Thomas Jarrett

Iffat Khan
Dr. Jessica Krick
Dr. Mark Lacy
Dr. Seppo Laine
Wen-Piao Lee
Dr. Brant Nelson
Dr. JoAnn O'Linger-Luscusk
Dr. Inseok Song
Dr. Gillian Wilson

IRAC INSTRUMENT TEAM AT SAO/HARVARD
Dr. Giovanni Fazio, IRAC Principal Investigator
Dr. Joseph L. Hora, Instrument Scientist
Dr. Lori E. Allen
Dr. Matthew L. N. Ashby
Dr. Pauline Barmby
Dr. Jiasheng Huang
Dr. Massimo Marengo
Dr. S. Thomas Megeath
Dr. Michael Pahre
Dr. Brian Patten
Dr. Howard Smith
Dr. Zhong Wang
Dr. Steven P. Willner

SPITZER SCIENCE CENTER OBSERVER SUPPORT/SCIENCE USER SUPPORT
Dr. Seppo Laine
Dr. Solange Ramirez

IRAC IOC/SV
Dr. Peter Eisenhardt (JPL)
Dr. Daniel Stern (JPL)

IRAC CALIBRATION/SOFTWARE CONTRIBUTORS
Dr. Stefano Casertano (STScI)
Dr. Mark Dickinson (STScI; NOAO)
Dr. David Elliott (JPL)
Dr. Robert Gehrz (U. Minnesota)
Dr. William Hoffmann (U. Arizona)
Dr. Leonidas Moustakas (JPL)
Edward Romana (JPL)

Post-Operations phase
The Post Operations phase is expected to last 6 months.

List of Laboratories

Caltech (California Institute of Technology, Pasadena, CA)

SAO (Smithsonian Asttrophysical Observatory, Harvard, MA)

SBRC (RaytheonVision Systems/Santa Barbara Research Center, Santa Barbara, CA)

GSFC (Goddard Space Flight Center, Greenbelt, MD)

JPL (Jet Propulsion Center, Pasadena, CA)

Steward Observatory, University of Arizona,Tucson, AZ

NASA Ames Research Center, Moffett Field, CA

University of Rochester, Rochester, NY

Appendix G. List of Figures

Appendix H.   List of Tables

Appendix I. Version Log

Version 2.1.2, November 2015:

S 18.18 warm mission information added to Appendix A.

Typo in equation in section 2.2.2 corrected

Version 2.1.1, October 2015:

S 19.2 added to Appendix A.

Version 2.1, February 2015:

Added information about the warm mission to several sections and updated the aperture corrections.

Version 2.0.3, February 2013:

Typo in Table 4.7 fixed: the 3.6 micron infinite value should have been 0.944 instead of 0.994

Version 2.0.2, March 2012:

S 18.24 added to Appendix A

Version 2.0.1, June 2011:

Reference to Krick et al. added to Section 4.11.5

Version 2.0, April 2011:

Discussion about artifact mitigation was added to Chapter 5 (5.3).

A new processing version S18.18 BCD FITS header replaced the old header file in Appendix D.

Discussion of a few new header keywords, including timing keywords and bad data value keywords, was added in Section 6.2.

The filenames in Table 6.1 were updated.

Added information about warm mission persistent images and edited the information on cryogenic mission persistent images in Section 7.2.8.

Added information about the effect of very deep surface brightness level observations in Section 4.11.

Added an Index at the end of the document.

Version 1.0, February 2010:

The first version of the IRAC Instrument Handbook, which includes information from the old IRAC Data Handbook, the old IRAC Pipeline Description Document, the cryogenic Spitzer Observer's Manual (SOM), and Spitzer Science Center web pages.

Bibliography

[1] Abraham, P., Leinert, C., & Lemke, D. 1997, Search for Brightness Fluctuations in the Zodiacal Light at 25 μm with ISO, A&A, 328, 702

[2] Anderson, J. & King, I. R. 2000, Toward High-Precision Astrometry with WFPC2. I. Deriving an Accurate Point-Spread Function, PASP, 112, 1360

[3] Arendt, R. G., Fixsen, D. J., & Moseley, S. H. 2000, Dithering Strategies for Efficient Self-Calibration of Imaging Arrays, Ap.J., 536, 500

[4] Beichman, C. A., Neugebauer, G., Habing, H. J., Clegg, P. E., Chester, T. J. 1988, *Infrared Astronomical Satellite (IRAS) Catalogs and Atlases. Volume I: Explanatory Supplement*, §VI.C.3

[5] Blommaert et al. 2003, CAM – *The ISO Camera ISO Handbook, Vol. 2, Ver 2.0* (Noordwijk: ESA), (http://iso.esac.esa.int/manuals/HANDBOOK/cam_hb/)

[6] Charbonneau, D., et al. 2005, Detection of Thermal Emission from an Extrasolar Planet, ApJ, 626, 523

[7] Cohen, M., Megeath, S. T., Hammersley, P. L., Martín-Luis, F., Stauffer, J. 2003, Spectral Irradiance Calibration in the Infrared. XIII. "Supertemplates" and On-Orbit Calibrators for the SIRTF Infrared Array Camera, AJ, 125, 2645

[8] Estrada, A. D., et al. 1998, Si:As IBC IR Focal Plane Arrays for Ground-Based and Space-Based Astronomy, Proc. SPIE, 3354, 99

[9] Fazio, G. G., et al. 2004, The Infrared Array Camera (IRAC) for the Spitzer Telescope, ApJS, 154, 10

[10] Franceschini, A., Toffolatti, L., Mazzei, P., Danese, L., & de Zotti, G., 1991, Galaxy Counts And Contributions to the Background Radiation from 1 micron to 1000 Microns, A&AS, 89, 285

[11] Fruchter, A. S., & Hook, R. N. 2002, Drizzle: A Method for the Linear Reconstruction of Undersampled Images, PASP, 114, 144

[12] Hauser, M. G., et al. 1998, *COBE Diffuse Infrared Background Experiment (DIRBE) Explanatory Supplement,* (Washington: GSFC) (http://lambda.gsfc.nasa.gov/product/cobe/dirbe_exsup.cfm)

[13] Hoffmann, W. F., Hora, J. L., Fazio, G. G., Deutsch, L. K., & Dayal, A. 1998, MIRAC2: a Mid-Infrared Array Camera for Astronomy, Proc. SPIE, 3354, 24

[14] Hoffmann, W. F., Hora, J. L., Mentzell, J. E., Marx, C. T., Eisenhardt, P. R., Carey, S. J., Megeath, S. T., & Schwenker, J. T. 2004, Determination of Spitzer Space Telescope Focus from IRAC Images Without A Focus Slew, Proc. SPIE, 5487, 186

[15] Hora, J. L, et al. 2008, Photometry Using the Infrared Array Camera on the Spitzer Space Telescope, PASP, 120, 1233

[16] Hora, J. L. et al. 2004, In-Flight Performance And Calibration of the Infrared Array Camera (IRAC) for the Spitzer Space Telescope, SPIE, 5487, 244

[17] Krick, J., et al. 2011, Spitzer IRAC Low Surface Brightness Observations of the Virgo Cluster, ApJ, 735, 76

[18] Lacy, M., et al. 2005, The Infrared Array Camera Component of the Spitzer Space Telescope First Look Survey, ApJS, 161, 41

[19] Lauer, T. R. 1999, The Photometry of Undersampled Point-Spread Functions, PASP, 111, 1434

[20] Mighell, K. J. 2005, Stellar Photometry And Astrometry with Discrete Point Spread Functions, MNRAS, 361, 861

[21] Mighell, K. J., Glaccum, W., Hoffmann, W. 2008, Improving the Photometric Precision of IRAC Channel *1*, Proc. SPIE, Vol 7010, p. 70102W

[22] Quijada, M. A., Marx, C. T., Arendt, R. G., & Moseley, S. H. 2004, Angle-of-Incidence Effects in the Spectral Performance of the

Infrared Array Camera of the Spitzer Space
Telescope, Proc. SPIE, 5487, 244

[23] Reach W. T., Morris, P., Boulanger, F., &
Okumura, K. 2003, The Mid-infrared Spectrum
of the Zodiacal and Exozodiacal Light, Icarus,
164, 384

[24] Reach, W. T., et al. 2005, Absolute
Calibration of the Infrared Array Camera on the
Spitzer Space Telescope, PASP, 117, 978

[25] Schuster, M. T., Marengo, M., & Pattern, B.
M. 2005, Proc. SPIE, Vol 6270, 20

[26] Shupe, D., Moshir, M., Li, J., Makovoz, D.,
Narron, R., Hook, R. N. 2005, The SIP
Convention for Representing Distortion in FITS
Image Headers, ASP Conf. Series, Vol 347, San
Francisco: PASP, p. 491, available at:
http://irsa.ipac.caltech.edu/data/SPITZER/docs/f
iles/spitzer/shupeADASS.pdf

Index